Measurement of Branching Fractions and CP Asymmetries in $\mathrm{B} \to \omega\mathrm{K}$ Decays and First Observation of the $\mathrm{B}^0 \to \psi(2\mathrm{S})\pi^0$ Decay

Veronika Chobanova

München 2015

Measurement of Branching Fractions and CP Asymmetries in $\mathrm{B} \to \omega\mathrm{K}$ Decays and First Observation of the $\mathrm{B}^0 \to \psi(2\mathrm{S})\pi^0$ Decay

Veronika Chobanova

Dissertation
an der Physik
der Ludwig–Maximilians–Universität
München

vorgelegt von
Veronika Chobanova
aus Sofia

München, den 29.05.2015

Erstgutachter: Prof. Dr. Christian Kiesling
Zweitgutachter: Prof. Dr. Thomas Kuhr
Tag der mündlichen Prüfung: 27.07.2015

Contents

Zusammenfassung

Wir präsentieren eine Messung der Verzweigungsverhältnisse und CP-Asymmetrien in $B^0 \to \omega K^0_S$ und $B^\pm \to \omega K^\pm$ Zerfällen, sowie des $B^0 \to \psi(2S)\pi^0$ Verzweigungsverhältnisses. Es wird der komplette vom Belle-Detektor am e^+e^--KEKB-Beschleuniger (Japan) aufgenommenen Datensatz von 772×10^6 $B\overline{B}$-Ereignissen ($710\,fb^{-1}$) benutzt.

Die Verzweigungsverhältnisse sind bestimmt in einer Messung der Signalausbeute unter Benutzung der bekannten Anzahl an $B\overline{B}$-Paaren und der Zerfallsrekonstruktionseffizienzen. Aus der Verteilung der Eigenzeitintervalle zwischen einem B^0-Meson-Zerfall in den ωK^0_S Endzustand und einem anderen Flavour-bestimmten B^0- or $\overline{B}^0$-Meson-Zerfall messen wir die Parameter $\mathcal{A}_{\omega K^0_S}$ and $\mathcal{S}_{\omega K^0_S}$, die jeweils ein Maß für die CP-Verletzung in den Zerfallsamplituden und in der Interferenz zwischen dem Zerfall und der Oszillationsphasen sind. Im $B^\pm \to \omega K^\pm$ Zerfall wird der ensprechende $\mathcal{A}_{\omega K^\pm}$-Parameter von der Differenz der B^+- und B^-- Meson-Zerfallsraten bestimmt.

Auf Quarkebene sind die $B^0 \to \omega K^0$ Zerfälle vom Loopprozess dominierte $b \to s q\overline{q}$ Übergänge. Geht man nur vom Loopprozess aus, sagt das Standardmodell (SM) $\mathcal{A}_{\omega K^0_S} = 0$, $\mathcal{A}_{\omega K^\pm} = 0$ und $\mathcal{S}_{\omega K^0_S} = \sin 2\phi_1$ voraus, wo ϕ_1 eine messbare Phase ist, die mit den Einträgen der Quark-Mischungsmatrix zusammenhängt. Zieht man SM-Prozesse zweiter Ordnung in Betracht, erwarten man einen leicht höheren Wert von $\sin 2\phi_1$ in $b \to s q\overline{q}$ Übergängen zu messen als in den theoretisch sauberen $b \to c\bar{c}q$ Zerfällen. Jede signifikante gemessene Abweichung von den SM-Vorhersagen könnte ein Indiz für neue Physik sein.

Wir erhalten die weltweit genaueste Messung der Verzweigungsverhältnisse

$$\begin{aligned} \mathcal{B}(B^0 \to \omega K^0) &= (4.5 \pm 0.4\ (\text{stat}) \pm 0.3\ (\text{syst})) \times 10^{-6}, \\ \mathcal{B}(B^\pm \to \omega K^\pm) &= (6.8 \pm 0.4\ (\text{stat}) \pm 0.4\ (\text{syst})) \times 10^{-6}. \end{aligned}$$

Es werden folgende CP-Verletzungsparameter gemessen:

$$\begin{aligned} \mathcal{A}_{\omega K^0_S} &= -0.36 \pm 0.19\ (\text{stat}) \pm 0.05\ (\text{syst}), \\ \mathcal{S}_{\omega K^0_S} &= +0.91 \pm 0.32\ (\text{stat}) \pm 0.05\ (\text{syst}), \\ \mathcal{A}_{\omega K^\pm} &= -0.03 \pm 0.04\ (\text{stat}) \pm 0.01\ (\text{syst}). \end{aligned}$$

Wir finden kein Indiz für CP-Verletzung in $B^\pm \to \omega K^\pm$ Zerfällen; dennoch erhalten wir die erste Evidenz auf CP-Verletzung in $B^0 \to \omega K^0_S$ Zerfällen mit einer Signifikanz von 3.1 Standardabweichungen. Die Ergebnisse stimmen mit den SM-Vorhersagen überein.

Zusätzlich präsentieren wir die erste Beobachtung des $B^0 \to \psi(2S)\pi^0$ Zerfalls mit Signifikanz von 7.2 Standardabweichungen. Wir messen das Verzweigungsverhältnis

$$\mathcal{B}(B^0 \to \psi(2S)\pi^0) = (1.17 \pm 0.18\ (\text{stat}) \pm 0.08\ (\text{syst})) \times 10^{-5}.$$

Abstract

We present a measurement of the branching fractions and the CP asymmetries in $\mathrm{B}^0 \to \omega\mathrm{K}^0_\mathrm{S}$ and $\mathrm{B}^\pm \to \omega\mathrm{K}^\pm$ decays and the $\mathrm{B}^0 \to \psi(2\mathrm{S})\pi^0$ branching fraction. We use the full data set of 772×10^6 ($710\,\mathrm{fb}^{-1}$) $\mathrm{B\overline{B}}$ events recorded by the Belle detector at the $\mathrm{e^+e^-}$ KEKB accelerator (Japan).

The branching fractions are determined in a signal yield measurement, using the knowledge of the number of $\mathrm{B\overline{B}}$ pairs and the decay reconstruction efficiencies. From the distributions of the proper-time intervals between a B^0 meson decay into the $\omega\mathrm{K}^0_\mathrm{S}$ final state and another, flavour-tagged B^0 or $\overline{\mathrm{B}}^0$ meson decay, we measure the parameters $\mathcal{A}_{\omega\mathrm{K}^0_\mathrm{S}}$ and $\mathcal{S}_{\omega\mathrm{K}^0_\mathrm{S}}$, which reflect the amount of CP violation in the decay amplitudes and in the interference between the decay and the mixing phases, respectively. In the $\mathrm{B}^\pm \to \omega\mathrm{K}^\pm$ decay, the corresponding $\mathcal{A}_{\omega\mathrm{K}^\pm}$ parameter is extracted from the difference between the B^+ and B^- meson decay rates.

At the quark level, the $\mathrm{B}^0 \to \omega\mathrm{K}^0$ decays are loop-dominated $\mathrm{b} \to \mathrm{s}q\overline{q}$ transitions. Assuming only a loop amplitude, the Standard Model (SM) predicts $\mathcal{A}_{\omega\mathrm{K}^0_\mathrm{S}} = 0$, $\mathcal{A}_{\omega\mathrm{K}^\pm} = 0$ and $\mathcal{S}_{\omega\mathrm{K}^0_\mathrm{S}} = \sin 2\phi_1$, where ϕ_1 is an observable phase related to the elements of the Cabibbo-Kobayashi-Maskawa quark mixing matrix. Taking into account second-order SM processes, the measured value of $\sin 2\phi_1$ in $\mathrm{b} \to \mathrm{s}q\overline{q}$ transitions is expected to be slightly higher than that in the theoretically clean $\mathrm{b} \to \mathrm{c\bar{c}}q$ decays. Any significant measured deviation with respect to the SM prediction could hint at new physics.

We obtain the world's most accurate measurement of the branching fractions

$$\begin{aligned}\mathcal{B}(\mathrm{B}^0 \to \omega\mathrm{K}^0) &= (4.5 \pm 0.4\ (\mathrm{stat}) \pm 0.3\ (\mathrm{syst})) \times 10^{-6},\\ \mathcal{B}(\mathrm{B}^\pm \to \omega\mathrm{K}^\pm) &= (6.8 \pm 0.4\ (\mathrm{stat}) \pm 0.4\ (\mathrm{syst})) \times 10^{-6}.\end{aligned}$$

For the CP violating parameters we obtain,

$$\begin{aligned}\mathcal{A}_{\omega\mathrm{K}^0_\mathrm{S}} &= -0.36 \pm 0.19\ (\mathrm{stat}) \pm 0.05\ (\mathrm{syst}),\\ \mathcal{S}_{\omega\mathrm{K}^0_\mathrm{S}} &= +0.91 \pm 0.32\ (\mathrm{stat}) \pm 0.05\ (\mathrm{syst}),\\ \mathcal{A}_{\omega\mathrm{K}^\pm} &= -0.03 \pm 0.04\ (\mathrm{stat}) \pm 0.01\ (\mathrm{syst}).\end{aligned}$$

We find no indication of CP violation in $\mathrm{B}^\pm \to \omega\mathrm{K}^\pm$ decays; however, we obtain the first evidence of CP violation in $\mathrm{B}^0 \to \omega\mathrm{K}^0_\mathrm{S}$ decays at the level of 3.1 standard deviations. These results are in agreement with the SM predictions.

We also present the first observation of the $\mathrm{B}^0 \to \psi(2\mathrm{S})\pi^0$ decay with a significance of 7.2 standard deviations. We measure the branching fraction

$$\mathcal{B}(\mathrm{B}^0 \to \psi(2\mathrm{S})\pi^0) = (1.17 \pm 0.18\ (\mathrm{stat}) \pm 0.08\ (\mathrm{syst})) \times 10^{-5}.$$

Introduction

According to the prevailing cosmological model, the Big Bang, the Universe originates from a singularity with infinite density and temperature and it has been expanding and cooling down since its beginning, reaching its current temperature of 2.7 K. In the early, very hot and energetically dense stage of the Universe, large amounts of particle-antiparticle pairs were produced. Assuming that matter and antimatter behave the same way in weak interaction processes, one would expect that as the Universe cooled down, the two would either annihilate entirely, leaving behind a vast amount of photons, or they would continue to exist in spatially separate regions. The Universe we observe today is in contradiction with both expectations: Neither does it consist only of photons, nor do we find antimatter-dominated regions. Due to an asymmetry in the interactions of matter and antimatter, one out of $\sim 10^{10}$ particles overpassed the annihilation. This surplus of particles is the baryonic matter in today's Universe.

To explain this phenomenon, A. Sakharov postulated in 1976 three conditions [1] that would generate this cosmological matter-antimatter asymmetry: (1) non-conservation of baryonic charge; (2) C-symmetry and CP-symmetry violation; (3) interactions outside of the thermal equilibrium. Interactions, violating the baryonic charge, have never been observed by now. The weak interaction holds a maximum violation of the C symmetry. In 1964, J. Cronin and V. Fitch observed for the first time a CP-violating process in the neutral kaon system [2]. This work won them the Nobel Prize in 1980. Based on N. Cabibbo's theory of quark mixing from 1963 [3], M. Kobayashi and T. Maskawa postulated the Cabibbo-Kobayashi-Maskawa (CKM) CP-violating mechanism in the weak interaction in 1973 [4]. The CP violation manifests itself as a complex phase in the quark-mixing CKM matrix. After their predictions were confirmed experimentally, Kobayashi and Maskawa were awarded the Nobel Prize in 2008.

The CKM mechanism is an integral part of the Standard Model (SM), which is a theory that encapsulates our best understanding of how the elementary particles and three of the fundamental forces of nature – strong, weak and electromagnetic – are related to each other. It was postulated and developed in the 60's and 70's years of the 20th century by S. L. Glashow [5], A. Salam [6] and S. Weinberg [7], for which they were awarded the Nobel Prize in 1979. The SM assumes three generations of fermions, which are the fundamental matter particles and possess spin $1/2$. These particles interact with each other via exchange of field quanta, called gauge bosons. Many SM predictions have been verified with a high precision [8–13].

Despite its indisputable success, the SM fails to explain some physical observations.

Such are the neutrino masses, the gravity, the dark matter and dark energy, which are the constituents of our Universe [14, 15], and many more. This is why the effort of the particle physics community is increasingly turning towards the search for physics beyond the SM, also called new physics (NP).

The B meson system provides a perfect environment for precise tests of the SM and with this for the search for NP. In 1980, based on the observation of a surprisingly long lifetime of the B mesons, I. I. Bigi, A. B. Carter and A. I. Sanda pointed out that the B^0-$\overline{B}^0$ system may show large time-dependent CP asymmetries [16–18]. Following this idea, two experiments were built to measure the CP-violating parameters of the SM – BaBar [19] at SLAC, USA, and Belle [20] at KEKB, Japan. The LHCb experiment at the Large Hadron Collider [21] was also designed for the measurement of CP violation in B decays. The BaBar and Belle experiments are referred to as the B factories due to the large number of $e^+e^- \to \Upsilon(4S) \to B^0\overline{B}^0$ events they have produced. They have provided a range of precise measurements of the CP asymmetries in the B sector and especially of the CP-violating phase ϕ_1. After this parameter has been estimated very accurately in the theoretically clean tree $b \to c\bar{c}q$ transitions [22, 23], attention has turned towards measurements of ϕ_1 in loop-dominated decays. These can be produced through a so-called penguin diagram which contains an internal loop and is therefore an excellent place for new exotic particles to show up in a virtual manner. A measured asymmetry that has a large deviation with respect to the SM prediction can be a sign of NP.

Such decays are for example $B^0 \to \omega K^0_S$ and $B^\pm \to \omega K^\pm$, which occur via $b \to sq\overline{q}$ transitions. In this work, the measurement of the branching fractions and CP-violating parameters of the rare $B^0 \to \omega K^0$ decays at Belle is presented. In addition, the results from the $B^0 \to \psi(2S)\pi^0$ branching fraction measurement are shown. $B^0 \to \psi(2S)\pi^0$ proceeds mainly through a $b \to c\bar{c}q$ transition and is thus sensitive to ϕ_1.

In the first chapter of this thesis, we present the theoretical aspects of the Standard Model and the theory of CP violation.

In the second chapter, the apparatus is described. This includes the KEKB accelerator, which produces the e^+e^- collisions, and the Belle detector installed around the interaction point, which measures them.

In the third chapter, we give an overview of the main techniques used in the $B \to \omega K$ and $B^0 \to \psi(2S)\pi^0$ analyses.

The fourth chapter is devoted to the measurement of the $B \to \omega K$ branching fraction and CP asymmetries and includes the decay phenomenology, reconstruction, event model, results and the systematic uncertainties.

In the fifth chapter, in a similar way, the $B^0 \to \psi(2S)\pi^0$ branching fraction measurement is presented, which has a significance of 7σ and is the decay's first observation.

Chapter 1

Physics Motivation

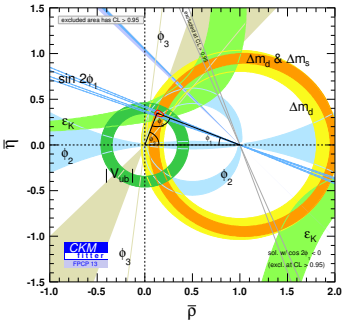

In this chapter, the phenomenology of CP violation is explained, focusing on the B meson system. First, a brief introduction to the Standard Model is given. Next, the basic symmetry operations and the CP violation mechanism in the Standard Model are explained. Afterwards,the time evolution of the neutral B meson is presented.

1.1 The Standard Model of Particle Physics

The Standard Model (SM) of particle physics is a theory that describes the elementary particles and the fundamental forces acting on them. The theory is consistent with both quantum mechanics and special relativity. In this section, we give a basic outline of the Standard Model. For more detailed information, the reader is referred to [24].

The Standard Model successfully describes three of the four fundamental interactions of matter: strong, weak and electromagnetic. It does not contain a theoretical description of the fourth one – gravity. Nevertheless, because the experimental results on these three forces so far have been consistent with the SM predictions, it is a very successful theory. Still, the Standard Model has some open issues, which are discussed in Section 1.1.2

1.1.1 A Brief Introduction to the Standard Model

In the core of the Standard Model lays the principle of the building blocks of matter, the elementary particles leptons and quarks, interacting with each other via mediator bosons. The interaction mechanism in the SM is based on a gauge theory of $SU(3)_C \times SU(2)_L \times U(1)_Y$ groups. The $SU(3)_C$ group describes the strong interaction by quantum chromodynamics (QCD). The strong force is mediated by massless gluons (see Table 1.1) and couples to the

colour charge of particles. There are three colours (red, green, blue) and their corresponding anticolours (antired, antigreen, antiblue). A gluon itself carries a colour-antincolour pair. In total, eight different gluons can exist with different colour combinations. Since the gluons interact with each other, the range of the strong interaction is not unlimited but in the order of 10^{-15} m.

The $SU(2)_L$ and $U(1)_Y$ groups form together a unified theory of the electroweak interaction, which is a combination of the weak and the electromagnetic interactions. The electromagnetic interaction is described by quantum electrodynamics (QED) and mediated through photons (see Table 1.1), acting on the electrical charge. Since the photons are massless and do not interact with each other, the range of the electromagnetic interaction is infinite. There are two types of weak interactions – charged current interactions mediated by the W boson and neutral current interactions mediated by the Z boson (see Table 1.1). Due to the large masses of the W and Z bosons ($m_W = 80\,\mathrm{GeV}/c^2$ and $m_Z = 91\,\mathrm{GeV}/c^2$), the range of the weak force is limited to the order of 10^{-18} m. The weak interaction is the weakest force of the three and acts on the flavofur of quarks and leptons. It is the only interaction that can change the particle flavour.

The mediator particles of the weak interaction are produced by a spontaneous symmetry breaking of the electroweak symmetry, caused by the Higgs mechanism. Without it, the Z and the W bosons would be massless. The fermion masses are also created through the spontaneous symmetry breaking, as they interact through the Yukawa coupling with the Higgs field. The spontaneous symmetry breaking also gives rise to a scalar boson, the Higgs boson. Postulated in 1963 [25, 26], a Higgs boson with mass $m_H \approx 126\,\mathrm{GeV}/c^2$ was found by the LHC experiments ATLAS and CMS [12, 13] in 2012. For this prediction, F. Englert and P. Higgs received the Nobel Prize in 2013.

All elementary particles have spin 1/2 and are thus fermions. They are subdivided into quarks and leptons. Both types of particles exist in so-called generations, which correspond to different mass scales. There are two quarks and two fermions in a generation. One of the quarks is an up-type and the other one is a down-type. The up-type quarks are the up quark (u), the charm quark (c) and the top quark (t). They have electrical charge $+2/3$ of the elementary charge. The down-type quarks have electrical charge $-1/3$ of the elementary charge and are respectively the down quark (d), the strange quark (s) and the bottom quark (b). The main properties of the elementary particles are summarized in Table 1.2.

Quarks do not exist in an isolated state but combine in groups of two or three to form a real physical particle, a hadron. This property is called colour confinement. There are two types of hadrons: the ones that contain a quark-antiquark pair are called mesons and the ones that contain three quarks are called baryons. Mesons are for example the kaon K ($s\bar{d}/\bar{s}d/s\bar{u}/\bar{s}u$), the D ($c\bar{d}/\bar{c}d/c\bar{u}/\bar{c}u$) and the B ($b\bar{d}/\bar{b}d/b\bar{u}/\bar{b}u$) mesons. Baryons are for instance the proton p (uud) and the neutron n (udd).

1.1.2 Open Issues of the Standard Model

Although the Standard Model made many predictions, which are in agreement with numerous experimental results, a big number of issues in physics is still open, such as

Interaction	Strong	Weak	EM	Gravity
mediator	g	$W^{\pm}, Z^0$	γ	graviton(?)
range (m)	10^{-15}	10^{-18}	∞	∞
long-distance behaviour	const	$e^{-m_{Z,W}r}/r$	$1/r^2$	$1/r^2$
relative strength	1	10^{-13}	1/137	10^{-38}

Table 1.1: The fundamental interactions.

Gen.	**Quark**	Mass [MeV]	Charge [e]	**Lepton**	Mass [MeV]	Charge [e]
1	**u**	$1.7 - 3.1$	$+2/3$	**e**	0.5	-1
1	**d**	$4.1 - 5.7$	$-1/3$	$\boldsymbol{\nu_e}$	< 0.002	0
2	**c**	≈ 1290	$+2/3$	$\boldsymbol{\mu}$	105.6	-1
2	**s**	≈ 100	$-1/3$	$\boldsymbol{\nu_\mu}$	< 0.19	0
3	**t**	≈ 173000	$+2/3$	$\boldsymbol{\tau}$	1776.8	-1
3	**b**	≈ 4000	$-1/3$	$\boldsymbol{\nu_\tau}$	< 18.2	0

Table 1.2: The Standard Model elementary particles. Values taken from [27].

- gravity is not explained by the SM
- can the strong and the electroweak forces be further unified to one Grand Unified Theory, as already achieved with the electromagnetic and weak interactions?
- the hierarchy problem: Why is the weak force 10^{32} times stronger than the gravity?
- what are dark matter and dark energy?
- in order to explain the imbalance of matter and antimatter in nature CP, violation larger than that of the SM is needed
- are there other particles than those in the SM? Does supersymmetry exist?
- does nature have more than the four known space-time dimensions? If so, what is their size?
- why are there exactly three lepton families and four fundamental interactions?
- is the neutrino its own antiparticle?

All these issues point to the incompletion of the Standard Model. Perhaps there is still a big amount of new physics beyond it. Huge efforts have already been made in explaining what the SM cannot. One important issue is the asymmetry between matter and antimatter in the Universe today. The SM expectations concerning the range of this asymmetry are insufficient to explain the ratio of $\sim 10^{-10}$ antiparticles per particle. A. Sakharov postulated in 1976 three conditions [1] that would generate this cosmological matter-antimatter asymmetry:

- non-conservation of baryonic charge
- C-symmetry and CP-symmetry violation
- interactions outside of the thermal equilibrium.

While there is no observation of non-conservation of baryonic charge until now, C and CP violation have been observed in weak decays. As shown later on in this chapter, CP violation is also incorporated in the Standard Model. The asymmetry can be produced outside thermal equilibrium. With this, CP violation could be the key to explaining the matter-antimatter asymmetry in the Universe. However, both the experimental observation and the theoretical prediction from the Standard Model can just explain the existence of the amount of matter in one galaxy but not in the entire Universe. This is one of the reasons why physics beyond the Standard Model is needed.

The B meson system offers a perfect environment for SM CP violation measurements and new physics search. B mesons contain a b antiquark and a light quark (u, d or s). Just like other mesons, for example the kaon K and the D meson, the bound quarks in them interact with each other via the weak force, which allows one quark to change its flavour. One particular case of this interaction, where asymmetry between mesons and antimesons is observed, is the transition between particles and antiparticles in the neutral meson systems. This asymmetry arises from the different probabilities of particle to antiparticle transition for the neutral mesons and their antimesons. Another source of asymmetry are the different decay rates of a particle and its antiparticle into a certain (conjugated) final state. By measuring the difference in the decay rates of the mesons and the antimesons one can obtain the CP violation parameters, which will also be explained in the following sections. Three experiments are dedicated to CP violation measurements in the B sector – the B factories Belle in Japan and BaBar in the USA, and the LHCb experiment at CERN.

1.2 General Formalism of CP Violation

In the following sections, the basic formalism of CP violation is described. We first introduce the discrete C, P and T symmetries. Next, we introduce the Cabibbo-Kobayashi-Maskawa mechanism and then study the time-dependent evolution of the neutral meson-antimeson system from a quantum-mechanical point of view. Following that, the mixing and decay mechanism along with the possible appearances of CP violation in the neutral meson system are explained and an example of CP violation in the kaon system is given.

1.2.1 Discrete Symmetries

Symmetries are an important aspect of physics. Noether's theorem [28], published in 1918, shows that symmetries lie at the basis of any conservation law. For example, the conservation of energy is a consequence of the invariance of physical laws under a time shift; rotational symmetry corresponds to the conservation of angular momentum. The

study presented in this thesis is a search for violation of the discrete CP symmetry. The CP operator is the product of the parity operator P and the charge-conjugation operator C. CP is also closely related to the time reversal operator T. The properties of these discrete symmetries and the non-conservation of the CP asymmetry are discussed in this section.

1.2.1.1 Parity Conjugation

The parity operator, P, creates a mirror image of the space. According to the behaviour under parity transformation, it can be distinguished between tensors and pseudotensors. Tensors $\mathcal{T}$ change sign under parity transformation while pseudotensors $\mathcal{P}$ are invariant,

$$\mathcal{T} \xrightarrow{P} -\mathcal{T} \qquad\qquad \mathcal{P} \xrightarrow{P} \mathcal{P}. \tag{1.1}$$

Examples for tensors are the scalars, such as the time and the electrical charge, and the vectors, such as the momentum and the space coordinate. Psedotensors are the pseudoscalars $S = \overrightarrow{V} \cdot \overrightarrow{A}$, where $\overrightarrow{V}$ is a vector and $\overrightarrow{A} = \overrightarrow{V'} \times \overrightarrow{V''}$ is a pseudovector. Pseudoscalars are for example the magnetic charge and the helicity and pseudovectors are the angular momentum and the magnetic field.

Parity holds in particle physics when the mirror image of a process is indistinguishable from a real process. For example,

$$(\pi^+ \to \mu_R^+ + \nu_L) \xrightarrow{P} (\pi^+ \to \mu_L^+ + \nu_R). \tag{1.2}$$

Parity conservation implies that nature makes no distinction between right- and left-handed rotations. Thus, two particles rotating in opposite direction μ_L^+ and μ_R^+ are identical in their physical behaviour if parity conservation holds. The decay on the right side in Eq. 1.2 has never been observed, as the weak interaction violates parity maximally.

1.2.1.2 Charge Conjugation

The charge operator transforms a particle q into its antiparticle $\bar{q}$, leaving its mass, momentum and spin invariant, but inverting quantum numbers like flavour and electric charge,

$$C\,|q\rangle \to |\bar{q}\rangle\,. \tag{1.3}$$

In the physics example of the pion decay,

$$(\pi^+ \to \mu_R^+ + \nu_L) \xrightarrow{C} (\pi^- \to \mu_R^- + \overline{\nu}_L). \tag{1.4}$$

The decay on the right side in Eq. 1.4 does not occur in nature and so the C symmetry is maximally violated in the weak interaction.

Until the 1950s, it was assumed that P and C are universal symmetries and therefore always conserved in physics interactions. In 1956, trying to explain the $\theta - \tau$ puzzle (C.F. Powell, 1949), Tsung-Dao Lee and Chen Ning Yang (Nobel prize 1957) pointed out that parity conservation had never been tested in weak decays [29]. In the same year,

Chien-Shiung Wu demonstrated [30] that parity conjugation is maximally violated in weak decays and that weak interaction only couples to left-handed particles and right-handed antiparticles. This was also confirmed by the experiment of Goldhaber [31].

The combined operator of C and P, CP, acts on the pion decay as follows

$$(\pi^+ \to \mu_R^+ + \nu_L) \xrightarrow{CP} (\pi^- \to \mu_L^- + \overline{\nu}_R). \tag{1.5}$$

This process has been observed. Combining C and P transformations, the pion decay becomes symmetric again and CP is conserved.

1.2.1.3 Time Reversal

The time conjugation operator, T, reflects the time t to $-t$ but has no effect on the space coordinates, $\overrightarrow{x}$,

$$T((\overrightarrow{x}, t)) = (\overrightarrow{x}, -t), \tag{1.6}$$

and thus represents the reversal of motion in time. For the pion decay this means

$$(\pi^+ \to \mu_R^+ + \nu_L) \xrightarrow{T} (\mu_R^+ + \nu_L \to \pi^+). \tag{1.7}$$

C, P, T, CP, CT, PT and CPT symmetries are conserved in the strong and electromagnetic interactions. CPT is assumed to be a conserved global symmetry, since its violation would be in conflict with well-established theories such as the theory of relativity. Therefore, the lifetime and mass of a particle and antiparticle must be equal. CP violation has been observed for the first time in the weak decays of the kaon [2] and later also in the B meson system [32, 33].

1.2.2 *CP* Violation in the Standard Model

1.2.2.1 Weak Charged Current

CP violation can arise in charged current weak interactions, mediated through a $\mathrm{W}^{\pm}$ boson. The weak charged current can change a left-handed up-type quark, u_L, into a left-handed down-type quark, d_L. These transitions are governed by coupling constants V_{ij} with different strengths, which are combined in a $N \times N$ matrix, $\mathbf{V}$, where N is the number of quark generations. The Lagrangian that describes these charged-current interactions can be written as

$$\mathcal{L} = \frac{-G_W}{\sqrt{2}} \left(V_{ij} \bar{u}_{Li} \gamma^\mu d_{Lj} W_\mu^\dagger + V_{ij}^* \bar{d}_{Li} \gamma^\mu u_{Lj} W_\mu \right), \tag{1.8}$$

where G_W is a coupling constant. The CP-conjugated Lagrangian is given by

$$\tilde{\mathcal{L}} = \frac{-G_W}{\sqrt{2}} \left(V_{ij}^* \bar{u}_{Li} \gamma^\mu d_{Lj} W_\mu^\dagger + V_{ij} \bar{d}_{Li} \gamma^\mu u_{Lj} W_\mu \right). \tag{1.9}$$

For CP to be conserved, $\mathcal{L}$ needs to be equal to $\tilde{\mathcal{L}}$ and hence $V_{ij} = V_{ij}^*$. Thus, at least one complex phase in the $\mathbf{V}$ matrix is needed for CP violation to be possible.

To conserve probability, $\mathbf{V}$ is a unitary matrix and as such has N^2 independent parameters. $2N-1$ of these parameters are not physically significant, because one phase can be absorbed into each quark field [34]. Therefore, the total number of free parameters is $N^2-(2N-1)=(N-1)^2$. Of these, $N(N-1)/2$ are mixing angles and $(N-1)(N-2)/2$ are complex phases, which allow CP violation. To make CP violation possible, at least three quark generations are needed, as this gives one complex phase in the $\mathbf{V}$ matrix.

1.2.2.2 Cabibbo-Kobayashi-Maskawa (CKM) Mechanism

In the 1963, as only the u, d and the s quarks were known, Cabibbo postulated a theory that explained the flavour transitions in the weak interaction [3]. According to it, the weak eigenstates of the quarks are linear combinations of their mass eigenstates, more precisely a rotation by the Cabibbo angle $\theta_C = 13.04°$. This relation can be represented by a 2×2 matrix. The idea was later extended from two to three quark generations by Kobayashi and Maskawa [4] to incorporate CP violation. The result was a 3×3 matrix, the Cabibbo-Kobayashi-Maskawa (CKM) matrix,

$$\begin{pmatrix} d' \\ s' \\ b' \end{pmatrix}_{weak} = \mathbf{V_{CKM}} \begin{pmatrix} d \\ s \\ b \end{pmatrix}_{mass} \equiv \begin{pmatrix} V_{ud} & V_{us} & V_{ub} \\ V_{cd} & V_{cs} & V_{cb} \\ V_{td} & V_{ts} & V_{tb} \end{pmatrix} \begin{pmatrix} d \\ s \\ b \end{pmatrix}_{mass} . \tag{1.10}$$

A parametrization in terms of three Euler angles ($\theta_{12}=\theta_C$, θ_{23}, θ_{13}) and one CP-violating phase, δ, is given by

$$\mathbf{V_{CKM}} = \begin{pmatrix} c_{12}c_{13} & s_{12}c_{13} & s_{13}e^{-i\delta} \\ -s_{12}c_{23} - c_{12}s_{23}s_{13}e^{i\delta} & c_{12}c_{23} - s_{12}s_{23}s_{13}e^{i\delta} & s_{23}c_{13} \\ s_{12}s_{23} - c_{12}c_{23}s_{13}e^{i\delta} & -c_{12}s_{23} - s_{12}c_{23}s_{13}e^{i\delta} & c_{23}c_{13} \end{pmatrix}. \tag{1.11}$$

s_{ij} and c_{ij} denote the sine and cosine of the respective angles. However, a more convenient and instructive parametrization is the one proposed by Wolfenstein [35]. Experimental results showed that the matrix elements can be grouped according to their size. The diagonal elements are close to one, while the off-diagonal elements that represent a transition over two generations are close to zero. This characteristic is used in the Wolfenstein parametrization, in which the CKM matrix is expanded in terms of the parameter $\lambda \equiv V_{us} = \sin\theta_C \approx 0.23$ and three more real parameters: A, ρ and η,

$$\mathbf{V_{CKM}} = \begin{pmatrix} 1-\lambda^2/2 & \lambda & A\lambda^3(\rho - i\eta) \\ -\lambda & 1-\lambda^2/2 & A\lambda^2 \\ A\lambda^3(1-\rho-i\eta) & -A\lambda^2 & 1 \end{pmatrix} + \mathcal{O}(\lambda^4). \tag{1.12}$$

This parametrization is unitary to all orders of λ. While the parameters λ and $A = 0.81^{+0.02}_{-0.01}$ are well known [27], there are still rather large experimental uncertainties on ρ and η. The estimated values for these are $\bar{\rho} \equiv (1-\lambda^2/2+\mathcal{O}(\lambda^4))\rho = 0.13^{+0.03}_{-0.01}$ and $\bar{\eta} \equiv (1-\lambda^2/2+\mathcal{O}(\lambda^4))\eta = 0.35 \pm 0.01$. It is the term $i\eta$ that gives rise to the complex phase and induces CP violation when non-zero.

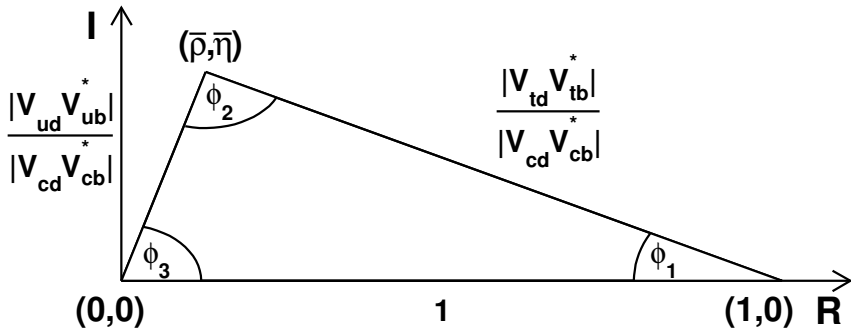

Figure 1.1: Unitarity triangle in the complex plane.

1.2.2.3 Unitarity Triangle

From the $\mathbf{V_{CKM}}$ unitarity follows that

$$\sum_k V_{ik} V_{jk}^* = 0. \tag{1.13}$$

These relations between the CKM matrix elements can be represented as triangles in the complex plane with the sides $V_{ik}V_{jk}^*$. As the lengths of the triangle sides are products of $\mathbf{V_{CKM}}$ elements, they can be obtained from measuring proper decay rates, while the angles can be accessed by CP eigenstate asymmetry measurements. It can be shown that all unitarity triangles have the same area [36], which is proportional to the amount of CP violation in the SM.

Of particular interest is the triangle that follows from the relation relevant for B meson

$$\begin{array}{l} V_{ud}V_{ub}^* + V_{cd}V_{cb}^* + V_{td}V_{tb}^* = 0, \\ \mathcal{O}(\lambda^3) \quad \mathcal{O}(\lambda^3) \quad \mathcal{O}(\lambda^3), \end{array} \tag{1.14}$$

since all its sides are of the same order in λ and with this its angles are large. Therefore, large CP asymmetry effects are expected in the B sector. In the following, we refer to this triangle as "the unitarity triangle".

It is more practical to rescale the unitarity triangle by dividing its sides by $V_{cd}V_{cb}^*$, so that one of the sides is aligned with the real axis and has a length of one, as shown in Figure 1.1. The coordinates of the top corner are $(\bar{\rho}, \bar{\eta})$ and the three angles ϕ_1, ϕ_2 and ϕ_3 are defined as

$$\phi_1 \equiv \arg\left(-\frac{V_{cd}V_{cb}^*}{V_{td}V_{tb}^*}\right) \qquad \phi_2 \equiv \arg\left(-\frac{V_{td}V_{tb}^*}{V_{ud}V_{ub}^*}\right) \qquad \phi_3 \equiv \arg\left(-\frac{V_{ud}V_{ub}^*}{V_{cd}V_{cb}^*}\right). \tag{1.15}$$

By measuring decay rates and CP asymmetries in particular B meson decay modes along with the mass ratio of the two mass eigenstates in the B^0 meson system, we can

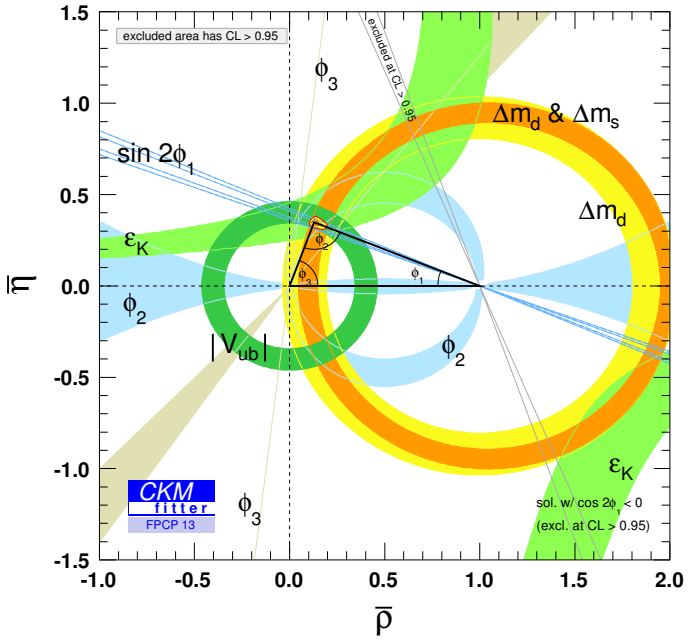

Figure 1.2: Current constraints the unitarity triangle [37].

access the angles and sides of the unitarity triangle. If $\mathbf{V_{CKM}}$ is unitary, meaning that the SM description of CP violation is correct and complete, then the triangle closes. Hence, observing a deviation from unitarity will be a hint at physics beyond the SM. Considering that a triangle is unambiguously defined by either three sides, two sides and one angle or one side and two angles, this problem is overconstrained from the experimental point of view, as two sides and three angles can be measured. Thus, the B meson system provides an excellent environment for tests of the SM. Many experiments have measured the elements of the CKM matrix. The CKM fitter collaboration [37] collects the measurement results and summarizes them on the $(\bar{\rho}, \bar{\eta})$ plane, as shown in Figure 1.2.

1.2.3 The Neutral Meson-Antimeson System

We consider a neutral meson, P^0, and its antiparticle, $\overline{\mathrm{P}}^0$. Both are eigenstates of the strong and electromagnetic interactions such that

$$(H_s + H_{em})\,|\mathrm{P}^0\rangle = m\,|\mathrm{P}^0\rangle \qquad (H_s + H_{em})\,|\overline{\mathrm{P}}^0\rangle = \bar{m}\,|\overline{\mathrm{P}}^0\rangle\,, \tag{1.16}$$

where H_s and H_{em} are the Hamiltonians of the strong and electromagnetic interactions, respectively. m and $\bar{m}$ are the P^0 and $\overline{\mathrm{P}}^0$ masses, respectively. Assuming CPT conservation of H_s and H_{em}, $m = \bar{m}$.

Let $|f\rangle$ be any eigenstate of the strong and electromagnetic interactions with eigenvalue

E_f such that

$$(H_s + H_{em})\,|f\rangle = E_f\,|f\rangle\,. \tag{1.17}$$

$|f\rangle$ is also required to be accessible as a weak decay final state of P^0 and $\overline{\mathrm{P}}^0$. Let us assume that until time $t = 0$, only the strong and the electromagnetic interactions act on P^0 and $\overline{\mathrm{P}}^0$ and that the two particles are stable under these forces. At $t > 0$, the weak interaction is switched on. Hence, the time evolution of the P^0-$\overline{\mathrm{P}}^0$ system, including its decays $f(t)$, is given by a vector in Hilbert space,

$$|\tilde{\Psi}(t)\rangle = a(t)\,|\mathrm{P}^0\rangle + b(t)\,|\overline{\mathrm{P}}^0\rangle + \sum_f c_f(t)\,|f(t)\rangle, \tag{1.18}$$

where $a(t)$, $b(t)$ and $c_f(t)$ are the time-dependent amplitudes. To determine $\tilde{\Psi}(t)$, the Schrödinger equation must be solved

$$i\hbar\frac{\partial}{\partial t}\tilde{\Psi}(t) = (H_s + H_{em} + H_w)\tilde{\Psi}(t), \tag{1.19}$$

where H_w is the Hamiltonian of the weak interaction. The exact time dependency of $\tilde{\Psi}(t)$ cannot be obtained without a knowledge in strong electrodynamics beyond our current capabilities. However, the problem can be significantly simplified by introducing some additional assumptions and reducing our demands:

- $|\tilde{\Psi}(0)\rangle = a(0)\,|\mathrm{P}^0\rangle + b(0)\,|\overline{\mathrm{P}}^0\rangle$
- we are only interested in $a(t)$ and $b(t)$, not in $c_f(t)$
- we only consider times larger than a typical strong interaction scale (Wigner-Weisskopf approximation [38]).

For a more detailed calculation, we refer to [34]. We can write the Schrödinger equation as

$$i\hbar\frac{\partial}{\partial t}\Psi(t) = \mathbf{H}\Psi(t), \tag{1.20}$$

where $\Psi(t)$ is restricted to the subspace of P^0 and $\overline{\mathrm{P}}^0$,

$$\Psi(t) = a(t)\,|\mathrm{P}^0\rangle + b(t)\,|\overline{\mathrm{P}}^0\rangle\,. \tag{1.21}$$

The Hamiltonian $\mathbf{H}$ is given by

$$\mathbf{H} = \mathbf{M} - \frac{i}{2}\mathbf{\Gamma} = \begin{pmatrix} \mathrm{M}_{11} & \mathrm{M}_{12} \\ \mathrm{M}_{21} & \mathrm{M}_{22} \end{pmatrix} - \frac{i}{2}\begin{pmatrix} \Gamma_{11} & \Gamma_{12} \\ \Gamma_{21} & \Gamma_{22} \end{pmatrix}, \tag{1.22}$$

where $\mathbf{M}$ is the mass matrix and $\mathbf{\Gamma}$ is the decay matrix.

$\mathbf{M}$ has diagonal elements

$$\begin{aligned} \mathrm{M}_{11} &= m + \langle \mathrm{P}^0|\,H_w\,|\mathrm{P}^0\rangle + \sum_f \mathcal{P}\left(\frac{\langle \mathrm{P}^0|\,H_w\,|f\rangle\,\langle f|\,H_w\,|\mathrm{P}^0\rangle}{m - E_f}\right), \\ \mathrm{M}_{22} &= m + \langle \overline{\mathrm{P}}^0|\,H_w\,|\overline{\mathrm{P}}^0\rangle + \sum_f \mathcal{P}\left(\frac{\langle \overline{\mathrm{P}}^0|\,H_w\,|f\rangle\,\langle f|\,H_w\,|\overline{\mathrm{P}}^0\rangle}{m - E_f}\right), \end{aligned} \tag{1.23}$$

where $\mathcal{P}$ is the principal part.

The diagonal elements of $\mathbf{\Gamma}$ are

$$\begin{aligned}\Gamma_{11} &= 2\pi \sum_f |\langle \mathrm{P}^0| H_w |f\rangle|^2 \delta(m - E_f),\\ \Gamma_{22} &= 2\pi \sum_f |\langle \overline{\mathrm{P}}^0| H_w |f\rangle|^2 \delta(m - E_f),\end{aligned} \tag{1.24}$$

where the term $\delta(m - E_f)$ assures energy conservation. This means that although in the sum over f all possible real and virtual states are considered, only the terms with real physical states are non-zero.

The off-diagonal elements of the two matrices are given by

$$\begin{aligned}\mathrm{M}_{12} = \mathrm{M}_{21}^* &= \langle \mathrm{P}^0| H_w |\overline{\mathrm{P}}^0\rangle + \sum_f \mathcal{P}\left(\frac{\langle \mathrm{P}^0| H_w |f\rangle \langle f| H_w |\overline{\mathrm{P}}^0\rangle}{m - E_f}\right),\\ \Gamma_{12} = \Gamma_{21}^* &= 2\pi \sum_f \langle \mathrm{P}^0| H_w |f\rangle \langle f| H_w |\overline{\mathrm{P}}^0\rangle \, \delta(m - E_f).\end{aligned} \tag{1.25}$$

If $\mathbf{H}$ is Hermitian and invariant under C, CP and CPT transformation, then

- CPT or CP conserved $\Rightarrow \mathrm{M}_{11} = \mathrm{M}_{22}$, $\Gamma_{11} = \Gamma_{22}$
- CP or T conserved $\Rightarrow \mathrm{Im}\,\mathrm{M}_{12} = 0 = \mathrm{Im}\,\Gamma_{12}$.

As we assume CPT conservation, we can use the following notation for the diagonal elements of the matrices: $\mathrm{M}_{11} = \mathrm{M}_{22} \equiv \mathrm{M}$, $\Gamma_{11} = \Gamma_{22} \equiv \Gamma$ and $\mathrm{H}_{11} = \mathrm{H}_{22} \equiv \mathrm{H}$.

Having obtained a considerable simplification of Eq. 1.18 and Eq. 1.19, we can now easily solve Eq. 1.20 by using the ansatz

$$a(t) = C_+ e^{-i\mu_+ t} + C_- e^{-i\mu_- t}, \tag{1.26}$$

where $\mu_\pm$ are the eigenvalues of $\mathbf{H}$,

$$\mu_\pm \equiv \mathrm{M} - \frac{i}{2}\Gamma \pm \sqrt{\left(\mathrm{M}_{12} - \frac{i}{2}\Gamma_{12}\right)\left(\mathrm{M}_{12}^* - \frac{i}{2}\Gamma_{12}^*\right)}. \tag{1.27}$$

Next we find

$$b(t) = \frac{q}{p}(C_+ e^{-i\mu_+ t} - C_- e^{-i\mu_- t}), \tag{1.28}$$

with

$$\frac{q}{p} = \sqrt{\frac{\mathrm{M}_{12}^* - \frac{i}{2}\Gamma_{12}^*}{\mathrm{M}_{12} - \frac{i}{2}\Gamma_{12}}} \qquad \text{and} \qquad \sqrt{p^2 + q^2} = 1. \tag{1.29}$$

Note that if CP is conserved, M_{12} and Γ_{12} are real and thus $q = p$. The $\mathbf{H}$ eigenstates are determined by diagonalising $\mathbf{H}$,

$$\mathbf{H} |\mathrm{P}_\pm(t)\rangle = \mu_\pm |\mathrm{P}_\pm(t)\rangle, \tag{1.30}$$

and are related to $|\mathrm{P}^0\rangle$ and $|\overline{\mathrm{P}}^0\rangle$ as

$$\begin{aligned} |\mathrm{P}_+(t)\rangle &= e^{-i\mu_+ t}\,|\mathrm{P}_+\rangle = e^{-i\mu_+ t}(p\,|\mathrm{P}^0\rangle + q\,|\overline{\mathrm{P}}^0\rangle), \\ |\mathrm{P}_-(t)\rangle &= e^{-i\mu_- t}\,|\mathrm{P}_-\rangle = e^{-i\mu_- t}(p\,|\mathrm{P}^0\rangle - q\,|\overline{\mathrm{P}}^0\rangle). \end{aligned} \tag{1.31}$$

These eigenstates represent physical mass-eigenstates. Their masses, $m_\pm$, and lifetimes, $\Gamma_\pm$, can be obtained from the eigenvalues

$$m_\pm = \mathrm{Re}(\mu_\pm) \qquad \text{and} \qquad \Gamma_\pm = -2\,\mathrm{Im}(\mu_\pm). \tag{1.32}$$

We will use the notation

$$\begin{aligned} \Delta m &\equiv m_- - m_+ = -2\,\mathrm{Re}\left(\sqrt{\left(\mathrm{M}_{12} - \frac{i}{2}\Gamma_{12}\right)\left(\mathrm{M}^*_{12} - \frac{i}{2}\Gamma^*_{12}\right)}\right), \\ \Delta\Gamma &\equiv \Gamma_- - \Gamma_+ = 4\,\mathrm{Im}\left(\sqrt{\left(\mathrm{M}_{12} - \frac{i}{2}\Gamma_{12}\right)\left(\mathrm{M}^*_{12} - \frac{i}{2}\Gamma^*_{12}\right)}\right) \\ \bar{m} &\equiv \frac{m_+ + m_-}{2} \\ \bar{\Gamma} &\equiv \frac{\Gamma_+ + \Gamma_-}{2}. \end{aligned} \tag{1.33}$$

Eq. 1.26 and 1.28 can be solved by using the initial condition at $t = 0$ that $\Psi(t)$ is a pure P^0 state

$$\begin{aligned} a(t=0) &= C_+ + C_- = 1, \\ b(t=0) &= \frac{q}{p}(C_+ - C_-) = 0, \end{aligned} \tag{1.34}$$

which has a solution $C_+ = C_- = 1/2$ and with this,

$$\begin{aligned} a(t) &= \frac{1}{2}(e^{-i\mu_+ t} + e^{-i\mu_- t}), \\ b(t) &= \frac{q}{p}\frac{1}{2}(e^{-i\mu_+ t} - e^{-i\mu_- t}). \end{aligned} \tag{1.35}$$

For the sake of visibility, we redefine $a(t) = g_+$ and $b(t) = \frac{q}{p}g_-$ or explicitly

$$\begin{aligned} g_\pm(t) &= \frac{1}{2}(e^{-i\mu_+ t} \pm e^{-i\mu_- t}) \\ &= \frac{1}{2}e^{i\bar{m}t}e^{-\bar{\Gamma}t/2}\left(e^{i\Delta m t/2}e^{-\Delta\Gamma t/4} \pm e^{-i\Delta m t/2}e^{\Delta\Gamma t/4}\right). \end{aligned} \tag{1.36}$$

The time evolution of an initially pure $|\mathrm{P}^0\rangle$ and $|\overline{\mathrm{P}}^0\rangle$ state, respectively, can be written as

$$\begin{aligned} |\mathrm{P}^0(t)\rangle &= g_+(t)\,|\mathrm{P}^0\rangle + \frac{q}{p}g_-(t)\,|\overline{\mathrm{P}}^0\rangle\,, \\ |\overline{\mathrm{P}}^0(t)\rangle &= g_+(t)\,|\overline{\mathrm{P}}^0\rangle + \frac{p}{q}g_-(t)\,|\mathrm{P}^0\rangle\,, \end{aligned} \tag{1.37}$$

from which is visible that the time evolution of the neutral meson P^0 is an oscillation between the flavours P^0 and $\overline{\mathrm{P}}^0$.

1.2.4 Types of CP Violation

In the following, we describe the three types of CP violation, which arise from the oscillation and the decay.

1.2.4.1 CP Violation in the Oscillation Between Particle and Antiparticle

CP violation can take place before a decay process occurs. Assuming Eq. 1.37, the probability of obtaining a final state $|\mathrm{P}^0\rangle$ and $|\overline{\mathrm{P}}^0\rangle$, respectively, starting with an initial state $|\mathrm{P}^0\rangle$ after a time t is given by

$$\begin{aligned}\left|\langle \mathrm{P}^0|\mathrm{P}^0(t)\rangle\right|^2 &= |g_+(t)|^2 = \frac{1}{4}\left(e^{-\Gamma_+ t} + e^{-\Gamma_- t} + 2e^{-\Gamma t}\cos\left(\Delta m t\right)\right), \\ \left|\langle \overline{\mathrm{P}}^0|\mathrm{P}^0(t)\rangle\right|^2 &= \left|\frac{q}{p}g_-(t)\right|^2 = \frac{1}{4}\left|\frac{q}{p}\right|^2\left(e^{-\Gamma_+ t} + e^{-\Gamma_- t} - 2e^{-\Gamma t}\cos\left(\Delta m t\right)\right). \end{aligned} \quad (1.38)$$

In order to conserve the CP symmetry during the oscillation, the following equality must be satisfied

$$\left|\langle \overline{\mathrm{P}}^0|\mathrm{P}^0(t)\rangle\right|^2 = \left|\langle \mathrm{P}^0|\overline{\mathrm{P}}^0(t)\rangle\right|^2 \quad (1.39)$$

or

$$\left|\frac{q}{p}g_-(t)\right|^2 = \left|\frac{p}{q}g_-(t)\right|^2 \quad \Rightarrow \quad \left|\frac{q}{p}\right|^2 = \left|\frac{p}{q}\right|^2 \quad \Rightarrow \quad \left|\frac{q}{p}\right| = 1. \quad (1.40)$$

The violation of this condition is referred to as "indirect CP violation". One note that only in this case P_+ and P_- are orthogonal to each other.

1.2.4.2 CP Violation in the Decay

Consider a final state f ($\bar{f}$) accessible through a weak decay of P^0 ($\overline{\mathrm{P}}^0$). The respective decay amplitudes are

$$\begin{aligned} A_f &= \langle f|\,\mathbf{H}\,|\mathrm{P}^0\rangle\,, \\ \bar{A}_{\bar{f}} &= \langle \bar{f}|\,\mathbf{H}\,|\overline{\mathrm{P}}^0\rangle\,. \end{aligned} \quad (1.41)$$

If CP is not conserved,

$$|A_f| \neq |\bar{A}_f|. \quad (1.42)$$

This is called direct CP violation.

1.2.4.3 CP Violation in the Interplay between Oscillation and Decay

A third source of CP violation arises in the interplay of the oscillation and decay mechanisms. CP violation occurs when the same final state f is accessible both from the particle P^0 and its antiparticle $\overline{\mathrm{P}}^0$. Then P^0 ($\overline{\mathrm{P}}^0$) can oscillate to $\overline{\mathrm{P}}^0$ (P^0) before it decays. For example, this is possible when the final state is a CP eigenstate. However, this is not

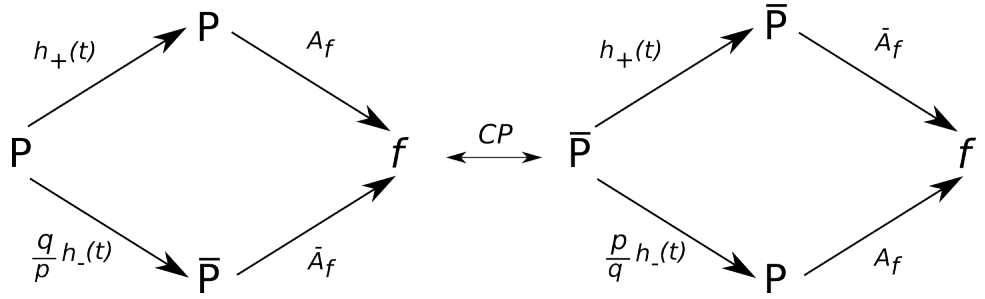

Figure 1.3: Oscillation and decay interference for an initial particle P (left) and its CP conjugated process (right).

a necessary condition. CP violation can also occur in processes like $\overline{(\mathrm{B})}^0 \to \mathrm{D}^{\pm}\pi^{\mp}$, which are not CP eigenstates.

The decay amplitudes can then be written as

$$\begin{aligned} A_f &\equiv \langle f|\,\mathbf{H}\,|\mathrm{P}^0\rangle\,, \\ \bar{A}_f &\equiv \langle f|\,\mathbf{H}\,|\overline{\mathrm{P}}^0\rangle\,. \end{aligned} \tag{1.43}$$

The total probability amplitude of obtaining a final state f after a time t when the initial state is $|\mathrm{P}^0\rangle$ or $|\overline{\mathrm{P}}^0\rangle$, respectively, is

$$\begin{aligned} P_f(t) &\propto A_f g_+(t) + \bar{A}_f \frac{q}{p} g_-(t), \\ \bar{P}_f(t) &\propto \bar{A}_f g_+(t) + A_f \frac{p}{q} g_-(t). \end{aligned} \tag{1.44}$$

We introduce the parameter

$$\lambda_{CP} \equiv \frac{q}{p}\frac{\bar{A}_{CP}}{A_{CP}}. \tag{1.45}$$

$P_f(t)$ can be accessed through a measurement of the time-dependent decay-rate, $\Gamma_f(t) = |P_f(t)|^2$. CP violation occurs when $\Gamma_f(t) \neq \bar{\Gamma}_f(t)$. For the two types of processes described above, the time-dependent decay rates can be written as

$$\begin{aligned} \Gamma_f(t) &\propto |A_f|^2\,|g_+(t)|^2 + \left|\bar{A}_f\right|^2 \left|\frac{q}{p}\right|^2 |g_-(t)|^2 + 2\,|A_f|^2\,\mathrm{Re}\left(\lambda_{CP} g_+^*(t) g_-(t)\right), \\ \bar{\Gamma}_f(t) &\propto \left|\bar{A}_f\right|^2 |g_+(t)|^2 + |A_f|^2 \left|\frac{p}{q}\right|^2 |g_-(t)|^2 + 2\left|\bar{A}_f\right|^2 \mathrm{Re}\left(\frac{1}{\lambda_{CP}} g_+^*(t) g_-(t)\right). \end{aligned} \tag{1.46}$$

Assuming that no direct and indirect CP violation occur, the sum of the two first terms in both equations would be equal, since $|A_f|^2 = \left|\bar{A}_f\right|^2$ and $|p|^2 = |q|^2$. In this case, $|\lambda_{CP}|^2 = 1$. CP violation could still arise in the third term. We consider

$$\begin{aligned} \mathrm{Re}\left(\lambda_{CP} g_+^*(t) g_-(t)\right) &= \mathrm{Re}\,(\lambda_{CP})\,\mathrm{Re}\left(g_+^*(t) g_-(t)\right) - \mathrm{Im}\,(\lambda_{CP})\,\mathrm{Im}\left(g_+^*(t) g_-(t)\right), \\ \mathrm{Re}\left(\frac{1}{\lambda_{CP}} g_+^*(t) g_-(t)\right) &= \mathrm{Re}\left(\frac{1}{\lambda_{CP}}\right)\mathrm{Re}\left(g_+^*(t) g_-(t)\right) - \mathrm{Im}\left(\frac{1}{\lambda_{CP}}\right)\mathrm{Im}\left(g_+^*(t) g_-(t)\right). \end{aligned} \tag{1.47}$$

Since $|\lambda_{CP}|^2 = 1$, the first terms in both equations are equal. From this follows that even in the absence of direct and indirect CP violation, there could be a difference in the decay rates of the CP conjugated processes if $\mathrm{Im}(\lambda_{CP}) \neq 0$. This third type of CP violation is referred to as "mixing-induced CP violation".

1.2.4.4 CP Violation in the Kaon System

CP violation was first observed in neutral kaon decays [2]. The K^0-$\overline{\mathrm{K}}^0$ system is an example of an oscillating meson-antimeson pair. The mass eigenstates K^0_S and K^0_L correspond to P_- and P_+ (see Eq. 1.31), respectively. $|\mathrm{K}^0_\mathrm{S}\rangle$ and $|\mathrm{K}^0_\mathrm{L}\rangle$ depend on the eigenstates of the CP operator, $|\mathrm{K}_1\rangle$ and $|\mathrm{K}_2\rangle$, as follows

$$\begin{aligned} |\mathrm{K}^0_\mathrm{S}\rangle &= \frac{1}{\sqrt{1+|\epsilon|^2}}\left(|\mathrm{K}_1\rangle - \epsilon\,|\mathrm{K}_2\rangle\right), \\ |\mathrm{K}^0_\mathrm{L}\rangle &= \frac{1}{\sqrt{1+|\epsilon|^2}}\left(|\mathrm{K}_1\rangle + \epsilon\,|\mathrm{K}_2\rangle\right), \end{aligned} \tag{1.48}$$

where ϵ is a complex mixing parameter which depends on p and q as

$$p = \frac{1+\epsilon}{\sqrt{2\left(1+|\epsilon|^2\right)}} \qquad q = \frac{1-\epsilon}{\sqrt{2\left(1+|\epsilon|^2\right)}}. \tag{1.49}$$

Experiments have shown that $|\epsilon| = (2.23 \pm 0.01) \times 10^{-3}$ [27].

1.3 CP Violation in the B Meson System

B mesons consist of a $\overline{\mathrm{b}}q$ pair, where $\overline{\mathrm{b}}$ is the antibottom quark and q is a u, d, s or c quark. The respective B mesons are called B^+, B^0, B^0_s, B^+_c. It also exists a $\mathrm{b}\overline{\mathrm{b}}$ bound state referred to as "bottomonium". A bottom-top quark-antiquark bound state is considered impossible because of the top quark's short lifetime. Unless stated otherwise, in the following we use the term "B meson" for B^+ and B^0 mesons only. These have a mass of $m_\mathrm{B} = 5.279\,\mathrm{GeV}/c^2$ [27].

B mesons decay weakly dominantly into quarks with lower mass than the b quark. A decay into a t quark is not possible because of its large mass ($m_\mathrm{t} \approx 173\,\mathrm{GeV}/c^2$). Decays into u, d, s and c quarks are CKM suppressed by at least $|V_{cb}| \sim \lambda^2$ (cf. 1.12). This is the reason for the comparably long lifetime of the B meson,

$$\begin{aligned} \tau_{\mathrm{B}^0} &= (1.519 \pm 0.007) \times 10^{-12}\,\mathrm{s}, \\ \tau_{\mathrm{B}^\pm} &= (1.641 \pm 0.008) \times 10^{-12}\,\mathrm{s}. \end{aligned} \tag{1.50}$$

The long lifetime of the B meson offers good conditions for CP violation studies in the B sector.

1.3.1 Time Evolution of Neutral B Mesons

The lowest-order quark transitions through which B^0 meson oscillation takes place, proceed through so-called box diagrams, shown in Figure 1.4. In the box, a virtual u, c or t (anti-)quark can occur, with a probability depending on the square of its mass and its corresponding coupling constant, which makes the top quark contribution the largest. The B^0-$\overline{B}^0$ time evolution is given by Eq. 1.37,

$$\begin{aligned} |B^0(t)\rangle &= g_+(t)\,|B^0\rangle + \frac{q}{p} g_-(t)\,|\overline{B}^0\rangle\,, \\ |\overline{B}^0(t)\rangle &= g_+(t)\,|\overline{B}^0\rangle + \frac{p}{q} g_-(t)\,|B^0\rangle\,. \end{aligned} \tag{1.51}$$

For the B meson system, $g_\pm$ (see Eq. 1.36) can be simplified further by taking into account that $\Delta\Gamma/\Gamma \approx \mathcal{O}(10^{-3})$ and thus $\Delta\Gamma$ can be ignored. For convenience, we redefine $\bar{\Gamma} = \Gamma$. Furthermore, $e^{i\bar{m}t}$ can be ignored by a phase convention. With this,

$$g_\pm(t) = \frac{1}{2} e^{-\Gamma t/2} \left(e^{i\Delta m t/2} \pm e^{-i\Delta m t/2} \right). \tag{1.52}$$

For the off-diagonal decay matrix element, Γ_{12}, and the off-diagonal mass matrix element, M_{12}, the relation is valid [16],

$$\frac{\Gamma_{12}}{M_{12}} \propto \frac{M_B^2}{M_t^2} \approx \mathcal{O}(10^{-3}) \qquad \Rightarrow \qquad |\Gamma_{12}| \ll |M_{12}|. \tag{1.53}$$

With this, the CP parameter for the oscillation becomes [39]

$$\frac{q}{p} = \sqrt{\frac{M_{12}^* - \frac{i}{2}\Gamma_{12}^*}{M_{12} - \frac{i}{2}\Gamma_{12}}} \overset{|\Gamma_{12}| \ll |M_{12}|}{\approx} \frac{M_{12}^*}{|M_{12}|} = e^{-i\phi_M}. \tag{1.54}$$

This means that $|q/p| \approx 1$ and that the CP violation in the B^0-$\overline{B}^0$ oscillation is very small. However, $|q/p|$ can still have a large complex phase ϕ_M.

Taking these considerations into account, the B meson time evolution can be written as

$$\begin{aligned} |B^0(t)\rangle &= e^{-\Gamma t/2} \left(\cos\left(\frac{\Delta m t}{2}\right) |B^0\rangle + i\frac{q}{p} \sin\left(\frac{\Delta m t}{2}\right) |\overline{B}^0\rangle \right), \\ |\overline{B}^0(t)\rangle &= e^{-\Gamma t/2} \left(\cos\left(\frac{\Delta m t}{2}\right) |\overline{B}^0\rangle + i\frac{p}{q} \sin\left(\frac{\Delta m t}{2}\right) |B^0\rangle \right). \end{aligned} \tag{1.55}$$

This result indicates that with time, an initial pure flavour state will develop into an opposite flavoured component as long as Δm is not zero. Starting with an initial state $|B^0\rangle$, the probabilities of finding a state $|B^0\rangle$ or a state $|\overline{B}^0\rangle$ after time t are therefore

$$\begin{aligned} P(|\,\langle B^0|B^0(t)\rangle\,|^2) &= e^{-\Gamma t} \cos^2\left(\frac{\Delta m t}{2}\right) |B^0\rangle\,, \\ P(|\,\langle B^0|\overline{B}^0(t)\rangle\,|^2) &\overset{\left|\frac{q}{p}\right| \approx 1}{=} e^{-\Gamma t} \sin^2\left(\frac{\Delta m t}{2}\right) |\overline{B}^0\rangle\,. \end{aligned} \tag{1.56}$$

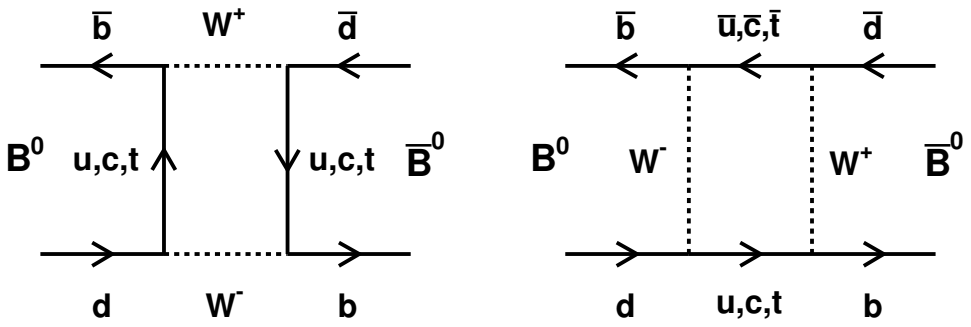

Figure 1.4: B^0-$\overline{B}^0$ mixing diagrams.

1.3.2 B^0 Decay into a CP Final State

In CP violation studies, the decays of the B meson are divided into four categories depending on the final state:

- the final state is a pure CP eigenstate, for example $J/\psi K^0_S$
- the final state is a mixture of CP eigenstates, such as $D^{*+}D^{*-}$
- flavour specific final states, for example $\ell^{\pm}\nu X^{\mp}$
- flavour non-specific final states, such as $D^{\pm}\pi^{\mp}$.

Topic of this work are the decays $B^0 \to \omega K^0_S$ and $B^0 \to \psi(2S)\pi^0$, which are pure CP eigenstates. This is why in the following we focus on this decay category.

We assume that f_{CP} is a CP final state accessible by both B^0 and $\overline{B}^0$. The respective decay amplitudes are given by

$$\begin{aligned} A_{CP} &\equiv \langle f_{CP}| \mathbf{H} |B^0\rangle , \\ \bar{A}_{CP} &\equiv \langle f_{CP}| \mathbf{H} |\overline{B}^0\rangle . \end{aligned} \tag{1.57}$$

Since f_{CP} is a CP final state,

$$|\bar{f}_{CP}\rangle = \eta_{CP} |f_{CP}\rangle , \tag{1.58}$$

where η_{CP} is the CP eigenvalue of f_{CP}. One can show that [40]

$$A_{CP} = \eta_{CP} e^{i\phi_D} \bar{A}_{CP}, \tag{1.59}$$

where ϕ_D is a weak phase difference between the decay amplitudes. Taking this and Eq. 1.54 into consideration and assuming that there is only one decay mechanism (amplitude) that contributes to the decay process, the parameter λ_{CP} can be written as

$$\lambda_{CP} = \frac{q}{p}\frac{\bar{A}_{CP}}{A_{CP}} = \eta_{CP} e^{-i\phi_M} e^{-i\phi_D}. \tag{1.60}$$

In this case, $|\lambda_{CP}| = 1$.

Considering that $|q/p| \approx 1$ and that $\Delta\Gamma \approx 0$, we can simplify Eq. 1.46,

$$\begin{aligned}
\Gamma(\mathrm{B}^0(t) \to f_{CP}) &= \left|\langle f_{CP}|\mathrm{B}^0(t)\rangle\right|^2 \\
&\propto |A_{CP}|^2 \frac{e^{-\Gamma t}}{2}\left[1 + |\lambda_{CP}|^2 + \left(1 - |\lambda_{CP}|^2\right)\cos(\Delta m t) - 2\,\mathrm{Im}(\lambda_{CP})\sin(\Delta m t)\right], \\
\Gamma(\overline{\mathrm{B}}^0(t) \to f_{CP}) &= \left|\langle f_{CP}|\overline{\mathrm{B}}^0(t)\rangle\right|^2 \\
&\propto |A_{CP}|^2 \frac{e^{-\Gamma t}}{2}\left[1 + |\lambda_{CP}|^2 - \left(1 - |\lambda_{CP}|^2\right)\cos(\Delta m t) + 2\,\mathrm{Im}\left(\frac{1}{\lambda_{CP}}\right)\sin(\Delta m t)\right].
\end{aligned} \tag{1.61}$$

We define the time-dependent CP asymmetry as

$$\begin{aligned}
a_{CP} &\equiv \frac{\Gamma(\overline{\mathrm{B}}^0(t) \to f_{CP}) - \Gamma(\mathrm{B}^0(t) \to f_{CP})}{\Gamma(\overline{\mathrm{B}}^0(t) \to f_{CP}) + \Gamma(\mathrm{B}^0(t) \to f_{CP})} \\
&= \frac{|\lambda_{CP}|^2 - 1}{|\lambda_{CP}|^2 + 1}\cos(\Delta m t) + \frac{2\,\mathrm{Im}(\lambda_{CP})}{|\lambda_{CP}|^2 + 1}\sin(\Delta m t).
\end{aligned} \tag{1.62}$$

We introduce the parameters

$$\mathcal{A}_{CP} \equiv \frac{|\lambda_{CP}|^2 - 1}{|\lambda_{CP}|^2 + 1} \qquad \text{and} \qquad \mathcal{S}_{CP} \equiv \frac{2\,\mathrm{Im}(\lambda_{CP})}{|\lambda_{CP}|^2 + 1}. \tag{1.63}$$

$\mathcal{A}_{CP}$ is a measure of the direct CP violation, since $\mathcal{A}_{CP} = 0$ when $|A_{CP}| = |\bar{A}_{CP}|$ and, respectively, $|\lambda_{CP}|^2 = 1$. $\mathcal{S}_{CP}$ reflects the amount of mixing-induced CP violation, since it can be unequal to zero even if $|A_{CP}| = |\bar{A}_{CP}|$ and $|q/p| = 1$.

We represent a_{CP} as

$$\boxed{a_{CP}(t) = \mathcal{A}_{CP}\cos(\Delta m t) + \mathcal{S}_{CP}\sin(\Delta m t)}. \tag{1.64}$$

One note that there is still a third CP parameter that has been neglected in this formula due to the $\Delta\Gamma = 0$ approximation,

$$\mathcal{A}_{\Delta\Gamma} = \frac{2\,\mathrm{Re}(\lambda_{CP})}{|\lambda_{CP}|^2 + 1} \overset{\Delta\Gamma=0}{\approx} 0. \tag{1.65}$$

The three parameters are related as

$$\mathcal{A}^2_{\Delta\Gamma} + \mathcal{A}^2_{CP} + \mathcal{S}^2_{CP} = 1 \quad \Rightarrow \quad \mathcal{A}^2_{CP} + \mathcal{S}^2_{CP} \leq 1. \tag{1.66}$$

We can conclude that in the neutral B^0 system direct and mixing-induced CP parameters can be measured from the time-dependent CP asymmetry for decays to a CP eigenstate.

Chapter 2

The Belle Experiment at KEKB

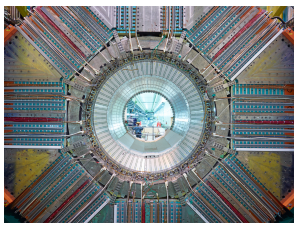

In this chapter, we introduce the Belle experiment at the asymmetric-energy e^+e^- accelerator KEKB in Tsukuba, Japan. The main features of the accelerator and the detector are presented.

The Belle Experiment at the KEKB accelerator in Tsukuba, Japan, has been primarily designed to study CP violation in the B meson sector. It has the worldwide highest luminosity of $2.11 \times 10^{34}\,\mathrm{cm^2 s^{-1}}$ [41], which exceeds twice its design luminosity. In more than ten years of running until its shutdown in June 2010, the Belle detector accumulated an integrated luminosity of over $1\,\mathrm{ab^{-1}}$ at five Υ(nS) resonances and below them, as shown in Figure 2.1. $0.7\,\mathrm{ab^{-1}}$ of data were collected at the Υ(4S) resonance, which corresponds to approximately 772×10^6 $\mathrm{B\overline{B}}$ meson pairs.

2.1 Υ(4S) Production at Belle

Five bottomonium resonances are produced at Belle. The production cross-section in $\mathrm{e^+e^-}$ collisions of four of them is illustrated in Figure 2.2. The three lowest-energy resonances, Υ(1S), Υ(2S) and Υ(3S), are very narrow, with a measured width dominated by the energy resolution of the detector. The Υ(4S) state has an energy just 20 MeV above the threshold for $\mathrm{B\overline{B}}$ production and has a mass $m(\Upsilon(4S)) = 10.579\,\mathrm{GeV}/c^2$ [27]. The highest-energy bottomonium reached at Belle is Υ(5S), at which $\mathrm{B_s^0}$ mesons are produced. Figure 2.2 also shows that the $\mathrm{e^+e^-}$ annihilation does not only create Υ(nS) states, but also non-resonant contributions, referred to as "continuum" or "$q\bar{q}$ background". It consists of lighter pairs of the u, d, s and c quarks. These events are about three quarters of the total electron-positron cross-section at the Υ(4S) resonance.

Over 96% of the Υ(4S) decays are into a $\mathrm{B\overline{B}}$ pair, which is either a $\mathrm{B^0\overline{B}^0}$ or a $\mathrm{B^+B^-}$ pair. This makes the Υ(4S) resonance a practical state for CP violation studies.

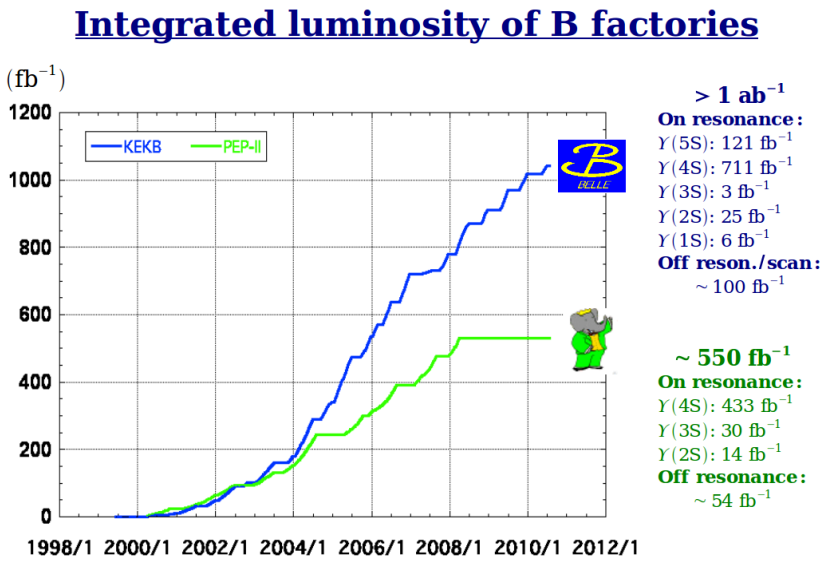

Figure 2.1: Integrated luminosity at the B factories [42].

Besides Belle, also the BaBar experiment at SLAC, USA, uses the same B meson production method and is also dedicated to CP violation measurements. The LHCb experiment at CERN measures CP violation using B mesons created at a proton-proton accelerator.

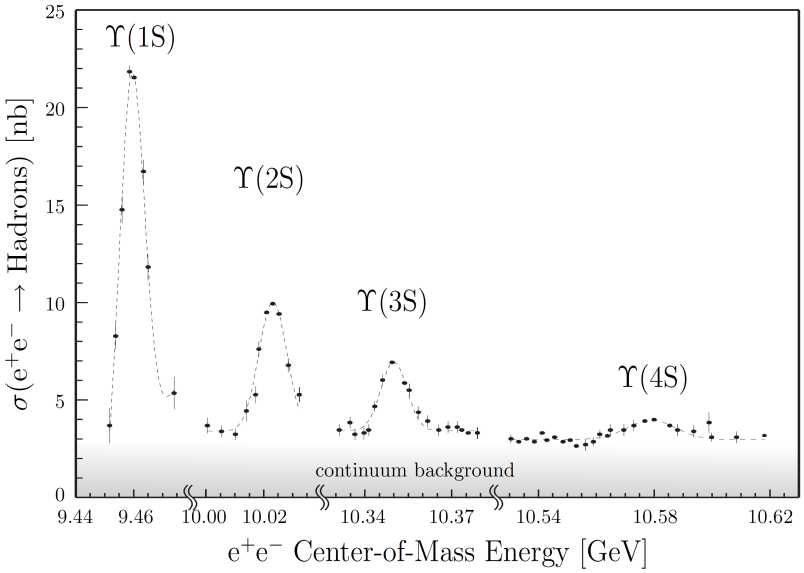

Figure 2.2: Hadronic cross-section for e^+e^- collisions as a function of the e^+e^- center-of-mass energy in the region at and above the $\Upsilon(1S)$ [43].

2.2 The KEKB Accelerator

The KEKB accelerator [44, 45] is an asymmetric e^+e^- collider. It consists of a high-energy electron ring (HER) at $E_- = 8\,\text{GeV}$ and a low-energy positron ring (LER) at $E_+ = 3.5\,\text{GeV}$, both supplied by a linear accelerator, Linac, as shown in Figure 2.3. The rings have a circumference of 3 km and are placed at about 10 m underground. At the interaction point (IP), the two beams collide at an angle of 22 mrad in order to reduce beam-interference background, as shown in Figure 2.4. Since 2004, KEK used a "continuous injection" mode, at which either electrons or positrons are injected continuously, while the two beams are colliding and data is being taken. This method significantly increases the integrated luminosity. To increase the specific luminosity, crab-cavities were installed to tilt the head-to-tail of the bunch just before the IP (see Figure 2.4).

The KEKB center of mass energy is $\sqrt{s} = 2\sqrt{E_- E_+} = 10.58\,\text{GeV}$ at the $\Upsilon(4S)$ resonance. $\Upsilon(4S)$ is produced with a boost $\beta\gamma$ in beam (z) direction,

$$\beta = \frac{p_{\Upsilon(4S)}c}{E_{\Upsilon(4S)}} = \frac{E_- - E_+}{E_- + E_+}, \quad \gamma = \frac{1}{\sqrt{1-\beta^2}}, \quad \beta\gamma = \frac{E_- - E_+}{\sqrt{s}} = 0.425. \tag{2.1}$$

Since the B mesons have very low momentum in the $\Upsilon(4S)$ rest frame, they have nearly the same boost value and direction and propagate 200 µm on average before decaying.

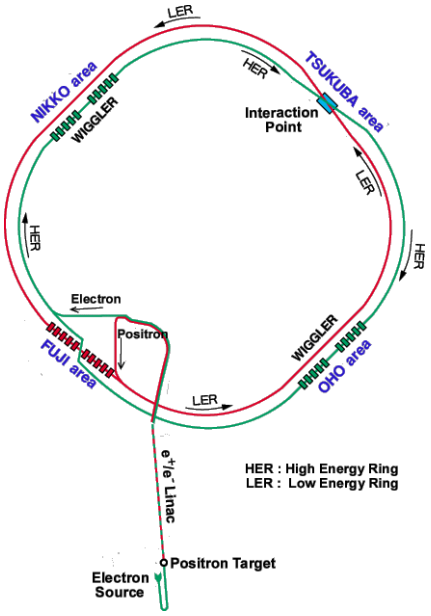

Figure 2.3: Schematic view of the KEKB accelerator.

2.3 The Belle Detector

After having created a $B\overline{B}$ pair, it is necessary to accurately measure the daughter particles and the decay time of both B mesons. In the study presented in this dissertation, we

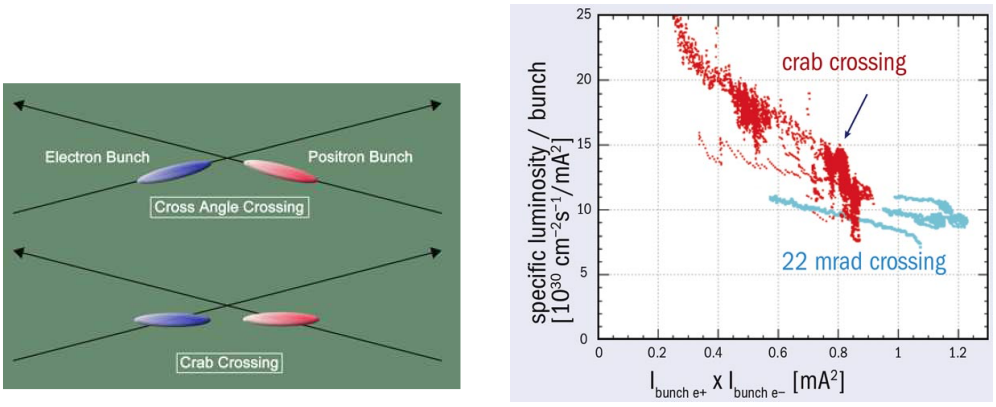

Figure 2.4: Left: The finite crossing angle of 22 mrad with and without crab cavity. Right: Using a crab cavity, a clear improvement in the luminosity is visible, especially at low bunch currents [44].

reconstruct the decay of a neutral B meson to ωK^0_S or $\psi(2S)\pi^0$ and the decay of a charged B meson to ωK^+. For the neutral case, we refer to these B mesons as B_{CP}, while the other meson in the $B^0\overline{B}^0$ pair is referred to as "B_{tag}" and is crucial for the determination of the B_{CP} flavour as will be explained in the next chapter. The apparatus used to measure the properties of the decay particles is the Belle detector. In the following, we give an overview of its design.

The Belle detector [20, 46] is a large solid-angle magnetic spectrometer. It is reconstructed around the accelerator interaction point and aims to measure the properties of particles created in e^+e^- collisions. Most of these particles have a very short lifetime and decay before they can be detected. They are reconstructed combining their light, long-living decay products that can be measured in the detector. These are electrons, muons, protons, pions, kaons and photons.

At Belle, a right-handed Cartesian coordinate system is used. The x, y and z axes have their origin at the IP. The x axis is the radial horizontal axis from the centre of the accelerator outwards. The y axis points upwards. The z axis follows the direction opposite to the positron beam. Often cylindrical coordinates are used: the radial distance is defined as $r = \sqrt{x^2 + y^2}$; the polar angle ϕ is measured with respect to the z axis and the azimuthal angle θ is measured with respect to the x axis.

A scheme of the Belle detector is shown in Figure 2.5. It consists of multiple subdetector layers and has a total acceptance of 91% of the total solid angle. Each one of them specialises on particular type of measurement. By combining the signals from all subdetectors, one obtains the necessary information to reconstruct a physics event. The two innermost subdetectors are the Silicon Vertex Detector (SVD) followed by the Central Drift Chamber (CDC). These measure the track position along the particle's flight direction. The SVD is also used to determine the decay vertex positions of the particles. In addition, the CDC measures the particle's energy loss, used to identify pions, kaons and electrons. With this, the CDC is a part of the particle identification system (PID), together with the Aerogel Cherenkov Counter (ACC) and the Time-of-Flight detector

(TOF). The ACC measures the Cherenkov light emitted by highly energetic charged particles. The TOF measures the time between the interaction and the moment it detects the particle. Combined with the measured momentum, ACC and TOF give access to the mass of the particle and allow separation of kaons from pions. The Electromagnetic Calorimeter (ECL), in which the energy of electrons and photons is measured, is installed around these inner detectors. The trajectories of the charged particles are bent in a 1.5 T magnetic field provided by the superconducting solenoid, placed outside the ECL. The extreme forward calorimeter (EFC), is positioned close to extend the spatial coverage of the ECL and to reduce the beam pipe background in the CDC. The outermost detector is the K^0_L/μ detector (KLM). The individual elements of the Belle detector are described in the following.

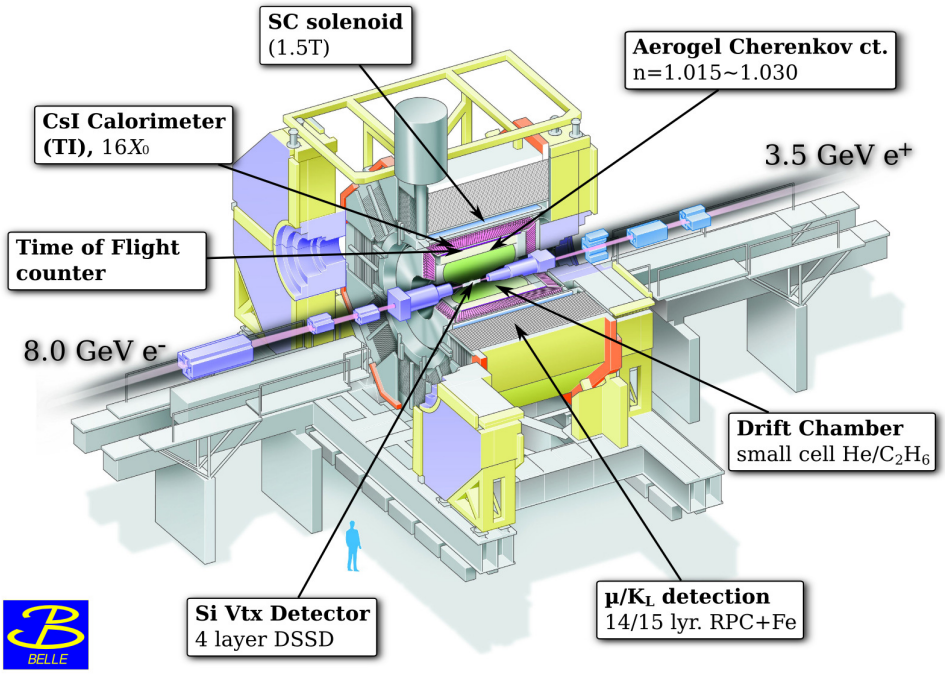

Figure 2.5: A schematic view of the Belle detector.

2.3.1 Beam Pipe

The beam interaction point is in vacuum, assured by the beam pipe. The z track vertex resolution is limited by the multiple Coulomb scattering in the beam pipe wall, which is why the beam pipe's material is reduced to minimum. Furthermore, the vertex resolution is inversely proportional to the distance between the SVD and the IP and with this the radius of the beam pipe needs to be as small as possible. This is not a trivial task because of the beam-induced heating, which can reach up to a few hundred Watts. Initially, the beam pipe was made of a double-wall beryllium cylinder with an inner radius of 2 cm. The gap between the two layers is 2.5 mm and is filled with helium for cooling. In 2003,

the detector was upgraded with a new SVD, which had a smaller beam pipe opening. For this reason, the inner radius of the beam pipe was reduced to 1.5 cm. A 20 µm gold foil covers the outer surface to shield low energy X-ray background (< 5 keV) in the vertex detectors. The total material thickness of the beryllium section is 0.3% of a radiation length and the one of the gold foil is 0.6%.

2.3.2 Silicon Vertex Detector

The Silicon Vertex Detector is the innermost subsystem of the Belle detector. Its main purpose is to assure a high vertex resolution, which is essential for the CP violation measurement. Additionally, SVD improves the momentum resolution of charged particles.

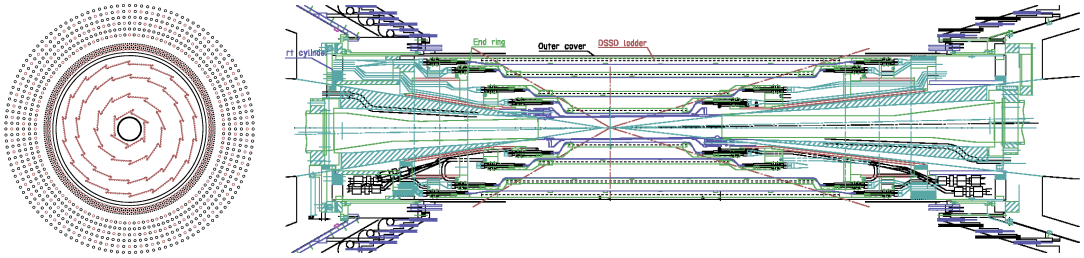

(a) front view (b) side view

Figure 2.6: Structure of the SVD2 [47]. The front view also shows the inner wires of the drift chamber.

The data used in this analysis is taken with two different types of SVD. The first one, referred to as SVD1, was replaced in 2003 with another detector, SVD2. SVD1 consisted of three layers of double sided silicon strip detectors (DSSD), while SVD2 has four layers.

A scheme of SVD2 is shown in Figure 2.6. Each layer is constructed from independent ladders. Each ladder comprises DSSDs, reinforced by boron-nitride support ribs. A DSSD consists of a p- and an n-strip. A bias voltage of 75 V is applied to the n-side, while the p-side is grounded. A charged particle, which traverses the pn-junction of the detector, creates electron-hole pairs. The electrons and holes drift to their corresponding biased side of the DSSD, which creates a two-dimensional hit signal.

A comparison between the most important parameters of SVD1 and SVD2 is shown in Table 2.1. In SVD2, the number of modules increased by more than a factor of two. To keep the number of readout channels compatible with the existing hardware, the readout channels of all modules in the forward/backward half of one ladder were added together. As a result, complete tracking is required to determine the position of an SVD2 cluster, since it may originate from up to three modules.

We estimate the SVD performance with two quantities [48]. One is the SVD-CDC track matching efficiency, defined as the probability that a CDC track passing through the SVD acceptance has associated SVD hits in at least two layers, and at least one two dimensional hit. $K^0_S \to \pi^+\pi^-$ are excluded because the long K^0_S lifetime means that

		SVD1	SVD2
Beam pipe radius	[mm]	20	15
Layers		3	4
Radii of layers	[mm]	30.0/45.5/60.5	20.0/43.5/70.0/88.8
Ladders per layer		8/10/14	6/12/18/18
Modules per ladder		2/3/4	2/3/5/6
Number of modules		102	246
Module width	[mm]	32.0	25.6 (33.28 for layer 4)
Module length	[mm]	54.5	76.8 (74.75 for layer 4)
Module thickness	[µm]	300	300
Pitch $r\phi$	[µm]	25	50 (65 for layer 4)
Pitch z	[µm]	84	75 (73 for layer 4)

Table 2.1: Parameters of the two different vertex detector configurations [20, 47].

these tracks do not necessarily pass through the SVD. In that case, the average matching efficiency is better than 97%.

The second estimate of the SVD performance is the impact parameter resolution of tracks with associated SVD hits. The impact parameter is the distance of closest approach to the IP and its resolution is measured as a function of the track's momentum, p, velocity, β, and polar angle, θ,

$$\sigma_{r\phi} = 22 \oplus 36/\left(p\beta\sin(\theta)^{3/2}\right)\,\mu\text{m}, \qquad \sigma_z = 28 \oplus 32/\left(p\beta\sin(\theta)^{5/2}\right)\,\mu\text{m}, \tag{2.2}$$

where $\oplus$ indicates a quadratic sum. Figure 2.7 shows the momentum and angular dependence of the impact parameter resolution. A clear improvement in the vertex resolution is visible after the upgrade to SVD2. The z separation between the two B meson vertices is measured with a precision of about 60 µm, which makes a time-dependent CP analysis possible.

2.3.3 Central Drift Chamber

The Central Drift Chamber measures particle track momenta from their curvature in the magnetic field, induced by the solenoid magnet. The CDC also measures the energy loss per unit length, dE/dx, of charged tracks to provide particle identification information together with the dedicated ACC and TOF subdetectors (explained in the next sections).

A scheme of the CDC is shown in Figure 2.8. For precise momentum measurement, especially for low-momentum tracks, the Coulomb scattering in the CDC has to be minimized. Therefore, it is filled with low-Z gas, consisting of 50% helium and 50% ethane. The CDC contains 8400 drift cells organized in 50 cylindrical layers around the z axis. A drift cell consists of eight negatively biased field wires, which surround a positively biased sense wire. Approximately half of the wires are parallel to the z axis to provide measurement of the transversal momentum, p_t, while the other half is slanted by a small

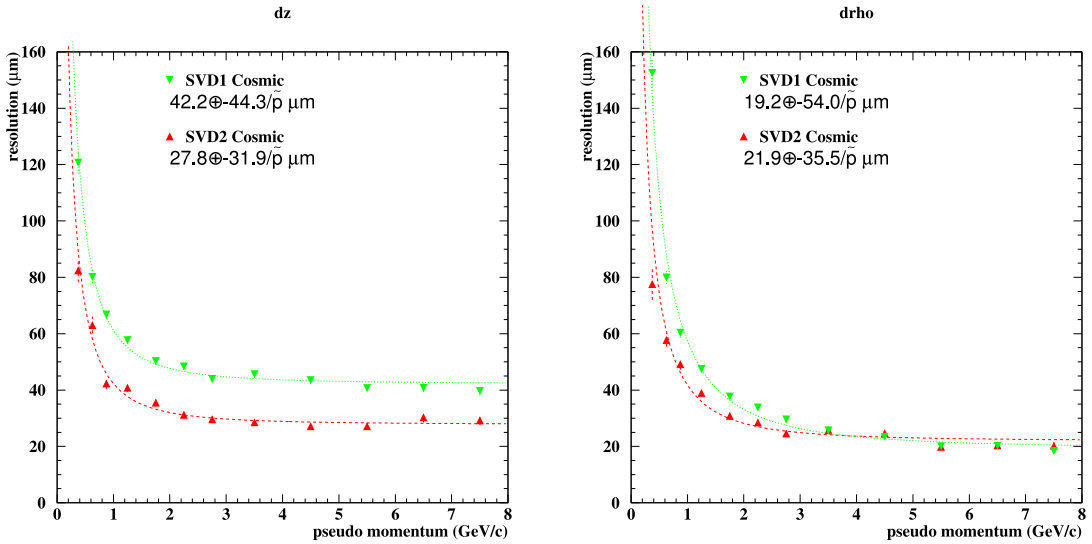

Figure 2.7: Distribution of SVD1 and SVD2 impact parameters $\sigma_{r\phi}$ and σ_z [48].

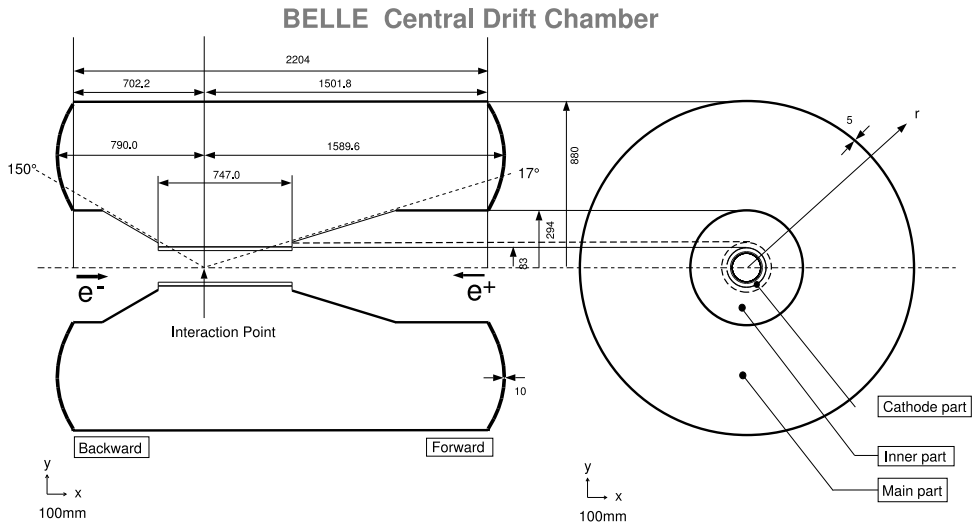

Figure 2.8: Layout of the Central Drift Chamber [20].

angle of ±50 mrad. This configuration allows a polar angle measurement of the track and with this an access to its longitudinal momentum.

A charged particle passing through the drift cell causes gas ionisation. The created gas electrons drift towards the sensor wires. Due to the very small diameter of the sense wires (30 µm), the strong electric field close to the wire accelerates the electrons sufficiently to cause an ionisation cascade. This process, called gas amplification, increases the signal by more than 10^6 times. Before amplification, the electrons have a specific drift velocity, so the measured pulse height and drift time are related to the energy deposit and distance from the sense wire, respectively. The resolution of the transverse momenta in dependence of its transversal momentum, p_t, and velocity, β, is given by [47]

$$\sigma(p_t, \beta) = 0.201\% p_t \oplus 0.290\% \beta.$$

The energy loss, dE/dx, in the CDC can be calculated from the energy deposition in the CDC and the particle drift distance. dE/dx is an important component for the particle identification, since its distribution in dependence of the momentum varies for different particle types, as shown in Figure 2.9. For kaons and pions with a momentum between 0.4 GeV/c and 0.6 GeV/c, a separation of three standard deviations can be obtained.

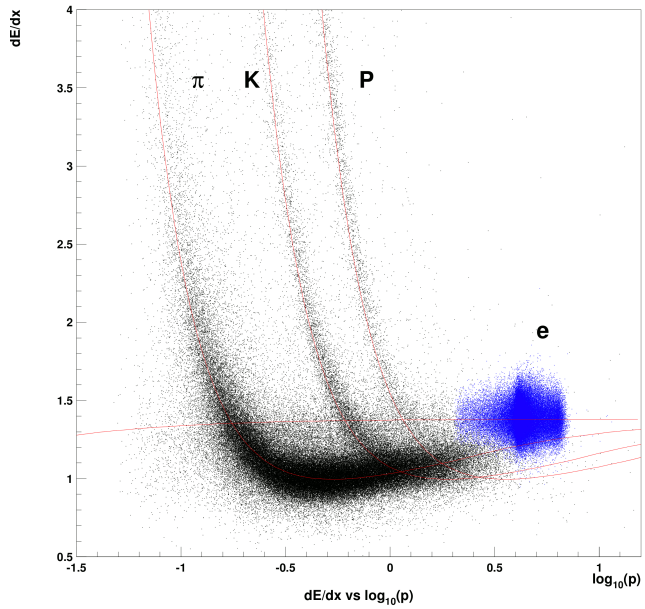

Figure 2.9: Measured dE/dx versus momentum in the CDC [20].

The CDC was also upgraded in 2003. Due to the larger outer dimensions of the SVD2, the CDC's inner radius had to be increased. This was done by removing three inner CDC layers and replacing them by two layers of smaller, so-called small-cell CDC modules, such that the inner radius became 140 mm. The measurements provided by the CDC are combined with the SVD signal in order to improve the overall track resolution.

2.3.4 Aerogel Cherenkov Counter

The purpose of the Aerogel Cherenkov Counter is to enhance the particle identification by distinguishing charged pions from charged kaons in a momentum range between 1.2 GeV/c and 3.5 GeV/c. This extends the momentum coverage beyond the reach of the CDC dE/dx measurement (see Section 2.3.3) and the time-of-flight measurement (see Section 2.3.5).

The particle identification in the ACC is based on the Cherenkov light emittance by particles travelling faster than the speed of light in the aerogel medium. The speed of light v_l depends on the aerogel refractive index n as

$$v_l = \frac{c}{n}, \tag{2.3}$$

where c is the speed of light in vacuum. When the speed of a particle exceeds the speed of light in the medium,

$$n \geq \frac{c}{v_l} = \frac{1}{\sqrt{1 + \left(\frac{m}{p}\right)^2}}, \tag{2.4}$$

a cone of light (Cherenkov radiation) is emitted with an angle, inversely proportional to its velocity. The particle velocity at which this effect occurs depends on the particle mass, m. By choosing an appropriate refractive index, there is a range of velocities for which pions emit Cherenkov radiation, while kaons do not.

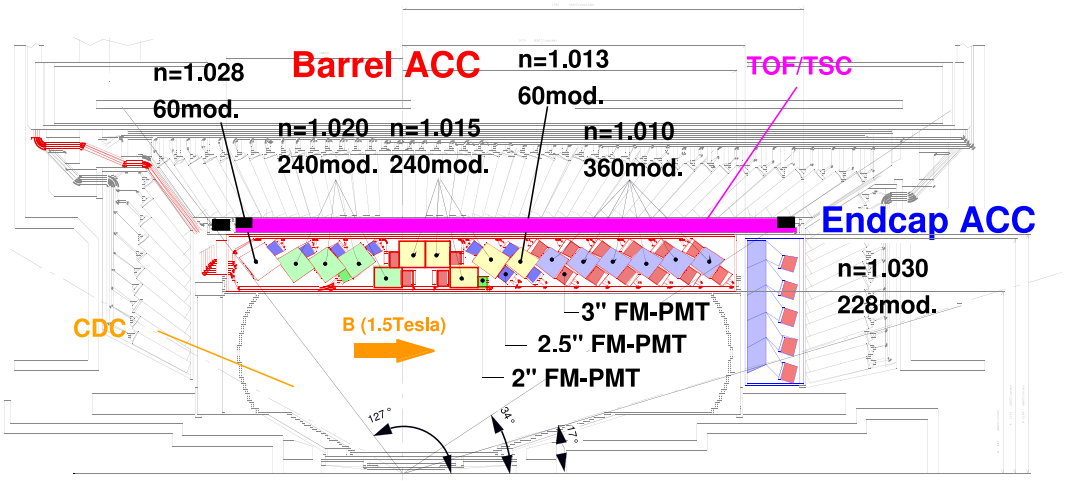

Figure 2.10: Arrangement of the ACC modules [20].

Figure 2.10 shows the side-view of the ACC. The detector system is divided into a barrel and a forward endcap parts. The barrel ACC is composed of 960 counter modules, segmented into 60 cells in the ϕ direction. The endcap ACC is composed of 228 counter modules, arranged in five concentric layers. The aerogel refractive index, n, ranges from 1.010 to 1.028 for the barrel ACC, depending on the polar angle. For the endcap ACC, $n = 1.030$ has been chosen. To measure the produced light, each counter module is

equipped with one or two fine-mesh photo-multiplier tubes with diameter of either 2, 2.5 or 3 in.

For particles with momenta up to 4 GeV/c, the kaon identification efficiency is 80 % or more, while the pion fake rate remains below 10 %. Below the pion threshold of 1 GeV/c, also electron identification is possible.

2.3.5 Time-Of-Flight Counter

The time-of-flight counter provides PID information in the energy region below 1.2 GeV, which encloses about 90% of the particles produced at Belle. The TOF measures the time the particle takes to travel from the IP to the TOF barrel. The flight time T for a particle with a mass m, which travels a length of L is given by

$$T = \frac{L}{c}\sqrt{1 + \left(\frac{mc}{p}\right)^2}. \tag{2.5}$$

By combining the momentum measurement from the CDC with the measured velocity by the TOF, one can calculate the corresponding mass of the particle and with this identify its type. The mass distribution calculated from TOF measurements is shown in Figure 2.11.

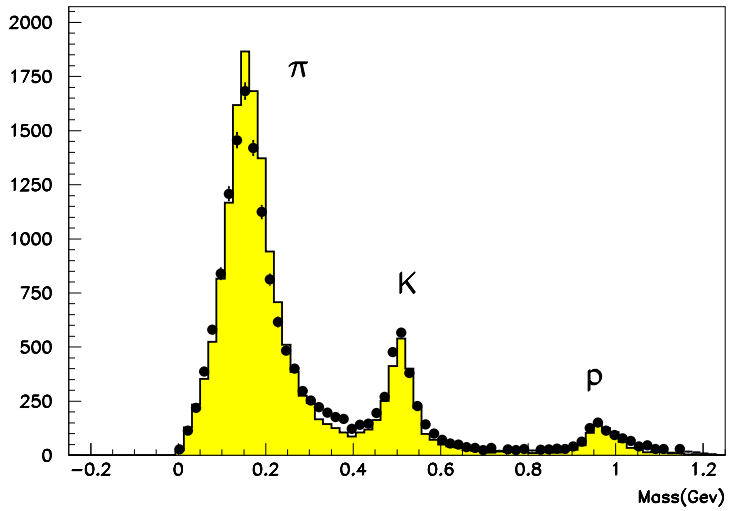

Figure 2.11: Particle identification using TOF measurements showing a clear separation between kaons, pions and protons [20].

The TOF consists of 64 modules in the barrel region, covering the polar region of $33° < \theta < 121°$. Each of them includes two plastic scintillation counters attached to photomultiplier tubes and has a time resolution of 100 ps. The TOF also provides fast timing signals for the trigger system. In order to sustain high trigger rates, thin trigger scintillation counters (TSC) are connected to the TOF counters.

After combining the information from the TOF measurement with the ACC and CDC information on dE/dx described in the previous sections, a 3σ separation between charged kaons and pions is obtained for momenta up to $3.5\,\mathrm{GeV}/c$.

2.3.6 The Electromagnetic Calorimeter

The electromagnetic calorimeter is used for photon detection and electron identification. Although most photons originate from π^0 and radiative B meson decays and have energies below 500 MeV, certain B meson decays, such as $B^0 \to \pi^0\pi^0$, produce photons with energies above 4 GeV. Thus, an ECL with a good resolution in a large energy range is needed. For the detection of high momentum neutral pions, the energies of the two decay photons as well as their opening angle need to be measured accurately, which requires a fine-grained segmentation in the calorimeter.

The geometry of the ECL is shown in Figure 2.12. It consists of 8736 thallium-doped Caesiumiodide (CsI(Tl)) crystal counters. The tower-shaped CsI(Tl) crystals are 30 cm long, which corresponds to 16.2 radiation lengths. Each crystal is positioned to point roughly towards the IP. The ECL is divided into a barrel and an end cap part. The barrel part consists of 6624 crystals and the end cap part contains 1152 (960) crystals in the forward (backward) directions.

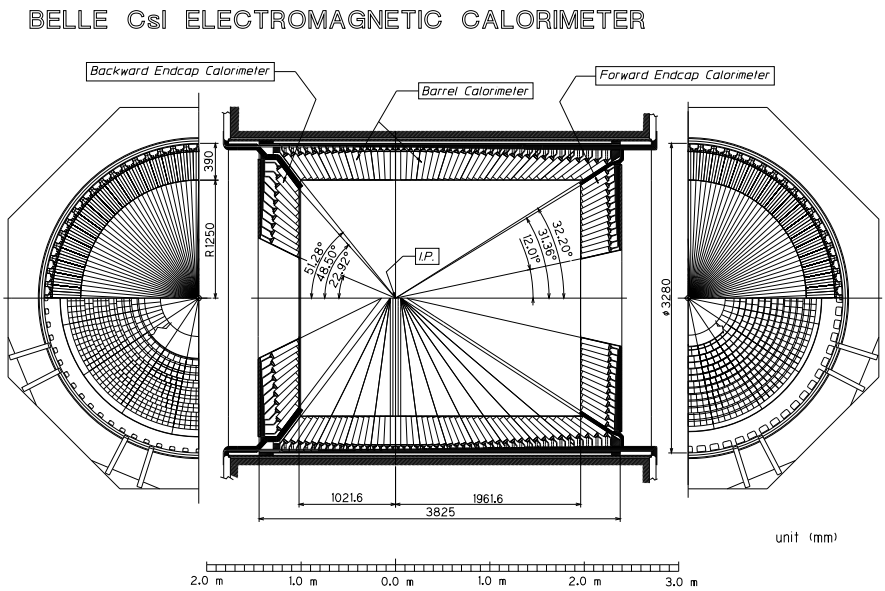

Figure 2.12: Schematics of the Belle Electromagnetic Calorimeter [20].

The ECL energy resolution ranges from 4% at 100 MeV to about 1.6% at 8 GeV. The angular resolution is between 13 mrad and 3 mrad at low, respectively, high energies. In total, a π^0 mass resolution of about $4.5\,\mathrm{MeV}/c^2$ is obtained. The crystal is then read out by a pair of silicon positive-intrinsic-negative photodiodes mounted at the rear end of the

crystal. A total solid angle of $12° < \theta < 155°$ is covered, which corresponds to 92% of the full solid angle.

The ECL provides the main parameter for electron/hadron separation: the ratio E/p of the shower energy to the track momentum. When an electron or a photon hits a CsI(Tl) crystal, most of its energy is deposited in electromagnetic showers produced by bremsstrahlung and pair production, while heavy charged particles, such as protons and pions, deposit only a small amount of energy by ionisation.

2.3.7 The Extreme Forward Calorimeter

The extreme forward calorimeter extends the polar angle coverage of the ECL in the forward ($6.4° < \theta < 11.5°$) and backward ($163.3° < \theta < 171.2°$) directions. It detects photons and electrons based on the same principle as the ECL. Since the EFC is installed around the beam pipe, close to the IP, it is exposed to large amounts of radiation. This is why radiation hard bismuth germanate crystals are chosen as the scintillating material, corresponding to 12 (11) radiation lengths in the forward (backward) direction. The produced scintillating light is captured by photodiodes. The 160 crystals are segmented in 32 (5) sections in ϕ (θ) as shown in Figure 2.13. The EFC has an energy resolution of 7.3% at 8 GeV and 5.8% at 3.5 GeV. In addition, this detector has the function to shield the CDC from the beam background. The EFC plays also an important role in the measurement of the delivered luminosity to Belle.

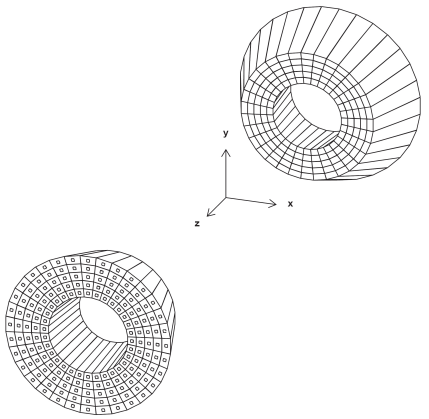

Figure 2.13: The extreme forward calorimeter at Belle [20].

2.3.8 The Solenoid

The superconducting solenoid provides a magnetic field of 1.5 T in a cylindrical volume measuring 3.4 m in diameter and 4.4 m in length that is parallel to the z direction. The coil consists of a single layer niobium-titanium-copper alloy embedded in a high purity

aluminium stabilizer and is wound around the inner surface of an aluminium support cylinder. Cooling is provided by liquid helium in a tube on the inner surface of the aluminium cylinder.

2.3.9 K_L^0/μ Detector

The KLM detector is placed outside the magnet solenoid. Its purpose is to detect K_L^0 mesons and muons with a transverse momentum of over 600 MeV/c. Since these particles have a small interaction probability with matter, dense material is needed to detect them. This is realised by iron plates providing a total of 3.8 interaction lengths. A K_L^0 particle traversing these iron plates produces a hadronic shower, creating a cluster of hits in the KLM. Muons can be discriminated from K_L^0 mesons using their signal shape, which is linear for muons and shower-shaped for kaons. In addition, a muon can be distinguished from a neutral kaon, since it triggers a signal in the inner detectors. Muons with a momentum above 1 GeV/c are detected with an efficiency of over 90%.

The KLM's barrel-shaped region around the interaction point covers a polar angular range of $45° < \theta < 125°$, while the forward and backward end caps extend this range between 20° and 155°. The KLM configuration is shown in Figure 2.14. The detector consists of alternating layers of 15 Resistive Plate Counters (RPC) and 14 layers of 4.7 cm thick iron plates. In the end-cap region there are only 14 RPCs. The layers are then grouped in a so-called super layer, which consists of two RPC planes sandwiched between cathode strips that provide ϕ and θ information. The K_L^0 direction from the IP can be measured using its shower but the resolution on the energy deposition does not allow for an accurate energy determination. The position resolution for K_L^0 mesons is 30 mrad in both angular directions. The time resolution is around a few nanoseconds. The iron plate is also used as return yoke for the magnetic field produced by the superconducting solenoid.

2.3.10 The Trigger System

During normal accelerator operation with an instant luminosity of 10^{34} cm^{-2}s^{-1}, the total event rate in the Belle detector is around 200 Hz. Approximately half of these events are not of interest as they originate from background processes, such as cosmic ray events, synchrotron radiation, beam gas and beam-beam interactions. Besides hadronic events, which could originate from a $B\overline{B}$ pair, events of importance are the Bhabha, $\gamma\gamma$ processes and muon pair production as these are used for luminosity determination.

A trigger system is used to distinguish between events which should be recorded and such to be discarded. It consists of a level 1 hardware trigger, a real-time level 3 software trigger and an offline level 4 software trigger. The trigger system obtains an efficiency of more than 99.5% for hadronic events.

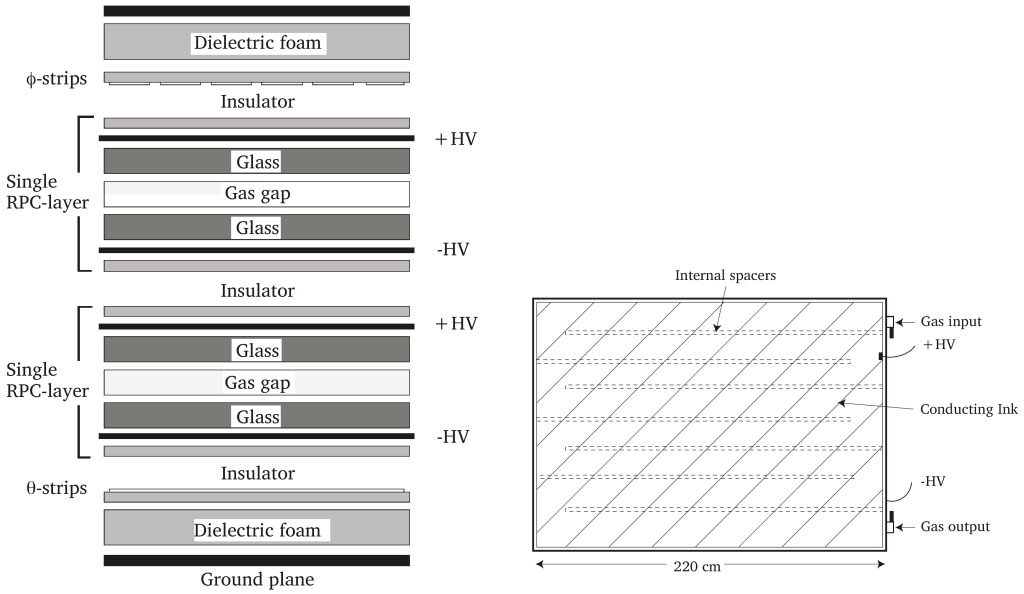

Figure 2.14: The KLM detector [20].

2.3.10.1 The Level-1 Trigger

The Global Decision Logic (GDL) is a central trigger-system that collects trigger signals from each subdetector and issues a level-1 decision. The subtriggers arrive at the GDL 1.85 µs after the beam crossing, and the trigger decision is issued by the GLD 0.35 µs later. The CDC and TOF produce charged particle triggers. In addition, the CDC provides $r-\phi$ and $r-z$ track trigger signals. The ECL issues a trigger based on the deposited energy and the number and timing of ECL cluster hits. The EFC subdetector triggers on Bhabha and two-photon events. The KLM detector trigger provides a signal when muons are detected. For the hadronic trigger, there are five main strategies:

- The two-track trigger requires two tracks with $r-\phi$ measurements and one measurement of a hit in the z-direction. The opening angle needs to be larger than 135°. There must be also hits in the TOF and ECL clusters.

- The three-track trigger is similar to the two-track trigger but requires three or more $r-\phi$ CDC triggers and has no condition for the opening angle. There are further trigger types depending on the number of tracks.

- The isolated cluster counting trigger requires four or more isolated ECL clusters to avoid Bhabha events.

- The total energy trigger requires the total energy deposited in ECL to be larger than 1 GeV. It is vetoed by the Bhabha events detected in the ECL and cosmic triggers.

- Combined trigger: this is a combination of the track, energy and cluster triggers. When using the overlap of these triggers, an efficiency of over 99% is obtained for $B\overline{B}$ events. A detailed description of the Level-1 trigger can be found in [49].

The normal trigger rate is $200-250\,\mathrm{Hz}$ but the system is designed to sustain a maximum trigger rate of $500\,\mathrm{Hz}$.

2.3.10.2 The Level-3 and Level-4 Triggers

The level-3 trigger is an offline, software-based trigger used to further reduce the number of events to be stored. It performs a fast track reconstruction to discard events that do not contain a track originating close to the IP. All events that pass the level-3 criteria are stored. After that, a level-4 trigger is applied. This trigger works similiar to level-3 but can impose stricter requirements. The level-4 trigger rejects around 78% of the events, while keeping almost 100% of the $B\overline{B}$ events.

2.3.11 The Data Acquisition System

The data acquisition system needs to record events that passed the level-1 and level-3 trigger requirements with a rate of up to $500\,\mathrm{Hz}$ and a dead time of less than 10%. Therefore, the signals from the subdetectors are processed in parallel. The data is then sent to the mass storage system of the KEK computing center and stored on data summary tapes (DST) in the PANTHER format. A typical hadronic $B\overline{B}$ or $q\overline{q}$ event has a data size of about 30 kB corresponding to a maximum data transfer rate of 15 MB/s.

Events are further classified in so-called skims. These are subsamples of the total data set and are submitted to a handful of loose selection criteria in order to enhance the fraction of certain physics events. Most analyses, including the ones presented in this thesis, are performed on the HadronB(J) data skim, which contains a larger fraction of standard hadron events. The software for simulation and reconstruction of data as well as the analysis code is run in the C++-based Belle Analysis Framework (BASF).

Chapter 3

Analysis Methods for the Branching Fraction and CP Violation Parameters Measurement

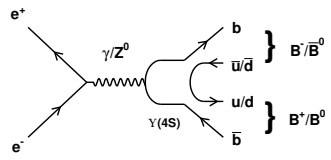

This chapter is about the analysis methods used to extract the branching fractions and CP asymmetries of the decays presented in this thesis. First, the blind analysis and the unbinned maximum likelihood method are explained. Next, it is shown how the branching fraction and the CP asymmetries are extracted from the Belle data. At the end, the determination of the Belle luminosity and data preparation for analysis are reviewed.

In the two analyses presented in this thesis, we measure the $B \to \omega K$ and $B^0 \to \psi(2S)\pi^0$ branching fractions and the $B \to \omega K$ time-dependent CP parameters shown in Eq. 1.64. These are determined from data fits to a set of observables. In the following, we give an overview of some general analysis methods used for these measurements.

3.1 The Blind Analysis Method

Both analyses presented in this thesis are performed using the so-called blind analysis method. It includes signal and background observable shape studies based entirely on Monte Carlo (MC) simulations and data outside the signal region. The shapes are then combined into a common model which aims to first describe a set of MC pseudoexperiments. These consist of a mixture of randomly generated signal and background MC events, which simulate the expected event content in the data. Once the model is verified with this test, it is applied to the real data to extract the physics parameters of interest. The purpose of the blind analysis is to protect from biased results due to the influence of the analyser's preferences and expectations.

3.2 Unbinned Extended Maximum Likelihood Method

The event shapes are described by probability density functions (PDF). These are combined to form an unbinned extended likelihood which is maximized to determine the physics parameters. In a data set with N events, described by a model with multiple components C, where each of them has a probability density function $\mathcal{P}_C(x;\theta)$ and a yield Y_C, the likelihood for a given set of parameters θ and yields Y_C is defined as

$$\mathcal{L}(\theta, Y_C) = \frac{\left(\sum_C Y_C\right)^N e^{-\sum_C Y_C}}{N!} \prod_{i=1}^{N} \frac{\sum_C Y_C \mathcal{P}_C(x_i;\theta)}{\sum_C Y_C}. \tag{3.1}$$

However, for computation time reasons, it is more convenient to transform $\mathcal{L}(\theta, Y_C)$ using a logarithmic function

$$\ln \mathcal{L}(\theta, Y_C) = \sum_{i=0}^{N} \ln \left(\sum_C Y_C \mathcal{P}_C(x_i;\theta) \right) - \sum_C Y_C - \ln N! \tag{3.2}$$

where we leave out the constant term $\ln N!$ and finally minimize the objective function,

$$-2 \ln \mathcal{L}(\theta) = 2 \left(\sum_C Y_C - \sum_{i=0}^{N} \ln \left(\sum_C Y_C \mathcal{P}_C(x_i;\theta) \right) \right), \tag{3.3}$$

using the MINUIT software [50].

Using the unbinned extended likelihood method, one can extract the signal yield, N_{sig}, and from it the branching fraction as described in the following.

3.3 Branching Fraction Measurement

In a sample of $N_{\mathrm{B\overline{B}}}$ events ($\mathrm{B\overline{B}}$ pairs), the signal branching ratio, $\mathcal{B}$, is obtained from N_{sig} using

$$\mathcal{B} = \frac{N_{Sig}}{N_{\mathrm{B\overline{B}}} \epsilon_{Sig} \eta}, \tag{3.4}$$

with the reconstruction efficiency ϵ_{Sig}, and an efficiency correction factor η, accounting for the difference between data and MC. ϵ_{Sig} is a feature of the reconstruction algorithm. η is obtained from independent Belle studies. Both parameters will be discussed in the $\mathrm{B} \to \omega\mathrm{K}$ and $\mathrm{B}^0 \to \psi(2\mathrm{S})\pi^0$ analysis chapters.

3.4 Measurement of CP Violation at Belle

To determine the time-dependent CP asymmetry and from it extract the $\mathcal{A}_{CP}$ and $\mathcal{S}_{CP}$ parameters, two observables need to be measured: The time of decay and the flavour of the B meson. Because of the short lifetime of the B meson, which is in the order of picoseconds, a direct time measurement is experimentally impossible. In the case where

both B^0 and $\overline{B}^0$ decay into the same CP final state f_{CP}, the B flavour cannot be deduced from its decay products. Therefore, the time-dependent CP asymmetry measurement is not a trivial experimental task.

These issues are resolved at the B factories, Belle and BaBar, where quantum-entangled pairs of B^0-$\overline{B}^0$ mesons are created with a large momentum boost in the laboratory frame. This allows a precise determination of the flavour and the decay time of the B meson. In the following, we explain how this is achieved.

3.4.1 Flavour Identification

At Belle, $B\overline{B}$ pairs are created in e^+e^- annihilation at the $\Upsilon(4S)$ resonance, as shown in Figure 3.1. $\Upsilon(4S)$ is a bottomonium with a mass $M(\Upsilon(4S)) = 10.579\,\mathrm{GeV}/c^2$ [27], which is exactly at the threshold for $B\overline{B}$ pair production. It has quantum numbers $J^{PC} = 1^{--}$ and hence the pair of spinless B mesons ($S = 0$) is produced in a p-wave ($L = 1$) to conserve the total angular momentum, $J = L + S$. The $B\overline{B}$ wave function must be antisymmetric and therefore Bose-Einstein statistics forbids the states B^0B^0 and $\overline{B}^0\overline{B}^0$, which are symmetric. As a consequence, the two B mesons oscillate so that a state B^0B^0 or $\overline{B}^0\overline{B}^0$ cannot occur at any time,

$$|B_1(t_1), B_2(t_2)\rangle = \frac{1}{\sqrt{2}}\left(|B_1^0(t_1)\rangle\,|\overline{B}_2^0(t_2)\rangle - |\overline{B}_1^0(t_1)\rangle\,|B_2^0(t_2)\rangle\right). \tag{3.5}$$

This property is used for the determination of the neutral B meson flavour. A $\Upsilon(4S)$ decay into two B mesons is shown in Figure 3.2. The B meson of interest, whose parameters we aim to measure, is referred to as "CP-side" B or "B_{CP}". The other one is called "tag-side" B or "B_{tag}". In this case, B_{CP} decays into ωK_S^0, which is accessible to both B^0 and $\overline{B}^0$ and thus its flavour cannot be determined from the decay products. However, the B_{tag} flavour can be obtained using flavour-specific decays. The flavour of the B_{CP} is known to be the opposite at the time of the decay, since the $B\overline{B}$ pair is entangled. The exact procedure, called "flavour tagging", will be explained later in this thesis.

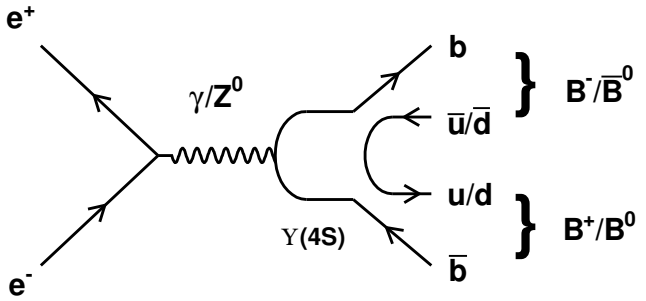

Figure 3.1: $B\overline{B}$ meson production at the $\Upsilon(4S)$ resonance.

We define $\Delta t = t_2 - t_1$, where t_1 and t_2 are the decay times of the two B mesons.

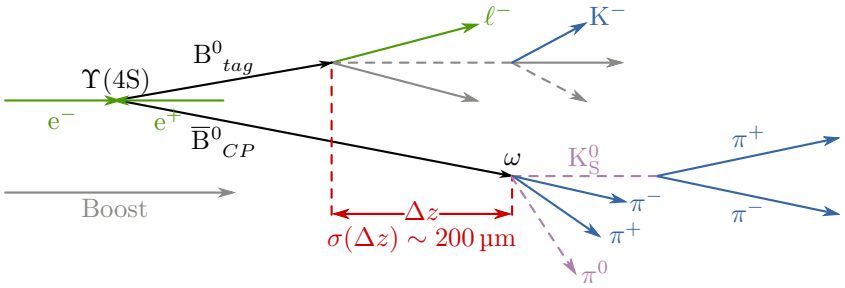

Figure 3.2: A scheme of a $B^0\overline{B}^0$ decay.

Using this, we can rewrite Eq. 1.64 as

$$a_{CP}(\Delta t) = \mathcal{A}_{CP}\cos(\Delta m \Delta t) + \mathcal{S}_{CP}\sin(\Delta m \Delta t). \tag{3.6}$$

The CP-violating parameters $\mathcal{A}_{CP}$ and $\mathcal{S}_{CP}$ can be extracted as a physical observable if Δt and the flavour of B_{tag} can be determined. The probability of B_{CP} decaying into a final state f_{CP} at time Δt, after having measured the flavour tag $q = +1(-1)$ for $B_{tag} = B^0(\overline{B}^0)$, is given by

$$\mathcal{P}(\Delta t, q) = \frac{e^{-|\Delta t|/\tau_{B^0}}}{4\tau_{B^0}}\left[1 + q\left(\mathcal{A}_{CP}\cos\left(\Delta m \Delta t\right) + \mathcal{S}_{CP}\sin\left(\Delta m \Delta t\right)\right)\right]. \tag{3.7}$$

3.4.2 Decay Time Measurement

The $\Upsilon(4S)$ resonance is produced with a boost in beam (z) direction. Since $M(\Upsilon(4S))$ is only slightly larger than the double B meson mass, the produced B mesons are in good approximation at rest in the center of mass system (CMS). Thus, they have very low momenta in the $\Upsilon(4S)$ frame and propagate almost parallel to the boost direction. This makes it possible to extract Δt from a measurement of the distance Δz between the decay vertices of the two B mesons, using the relation

$$\Delta t = \frac{\Delta z}{\langle\beta\gamma\rangle c}, \tag{3.8}$$

where $\langle\beta\gamma\rangle$ is the system boost and c is the speed of light. At Belle, $\langle\beta\gamma\rangle = 0.425$. For this boost value, we obtain $\Delta z \approx 200\,\mu m$.

3.5 The Belle Data

The analyses presented in this thesis are based on the full Belle data set, which contains 772×10^6 $B\overline{B}$ pairs. In the following, we describe how the number of $B\overline{B}$ pairs is obtained.

The full energy of a e^+e^- collision is known, since the two particles are elementary and dispose their full energy in an interaction process. This major advantage of a e^+e^-

accelerator over a hadron collider allows amongst other things to determine the number of $B\overline{B}$ pairs, which is an essential observable in the measurement of exclusive branching fractions (see Section 3.3).

3.5.1 Determination of the Number of $B\overline{B}$ Pairs in the Data

The first step to the calculation of the number of $B\overline{B}$ pairs is the determination of the accelerator luminosity. This is a property entirely dependent on the parameters of the colliding beams and independent of the actual physics processes. Its measurement is done on two levels – online and offline. The online luminosity is measured during data taking and is necessary to optimize the beam parameters during operation. The offline luminosity is determined from the fully reconstructed DST files and is used for the normalization of experimental data for physics analysis and for collider performance optimisation.

In e^+e^- colliders, the online luminosity is mostly measured by determining the rate of $e^+e^- \to e^+e^-$ (Bhabha scattering) or $e^+e^- \to e^+e^-\gamma$ (single bremsstrahlung) interactions, as for these QED processes the cross sections can be calculated with a precision better than 1%. The outgoing Bhabha particles are produced under a very low angle [51], which is why these events are detected using signals in the EFC and in the end caps of the ECL. Single bremsstrahlung interactions are characterized by a sharp angular distribution of the radiated photon, in the direction of the incoming $e^{\pm}$. This is measured by a zero degree luminosity monitor [52].

For offline luminosity measurement, a more sophisticated analysis on the Bhabha events is performed. The method has an accuracy of around 1.4%. A detailed explanation of these measurements is found in [53] and [54].

Having obtained the luminosity, one can calculate the number of $B\overline{B}$ events. The hadronic events produced at the $\Upsilon(4S)$ resonance are either continuum $q\overline{q}$ events or $B\overline{B}$ events. The number of continuum events can be estimated with the data samples collected at 60 GeV below the $\Upsilon(4S)$ mass (off-resonance), where no $B\overline{B}$ events are produced. Since the cross-section of these events depends on the the center-of-mass energy, $\sqrt{s}$, its value at the $\Upsilon(4S)$ energy (on-resonance) needs to be corrected accordingly. The number of $B\overline{B}$ events produced at the $\Upsilon(4S)$ resonance, $N_{B\overline{B}}$, can be calculated using the formula

$$N_{B\overline{B}} = \frac{1}{\epsilon^{B\overline{B}}_{\Upsilon(4S)}} \cdot \left(N^h_{\Upsilon(4S)} - N^h_{q\overline{q}} \cdot \frac{\mathcal{L}_{\Upsilon(4S)}}{\mathcal{L}_{q\overline{q}}} \cdot \frac{E^2_{q\overline{q}}}{E^2_{\Upsilon(4S)}} \cdot \frac{\epsilon_{\Upsilon(4S)}}{\epsilon_{q\overline{q}}}, \right) \tag{3.9}$$

where $N^h_{\Upsilon(4S)}$ and $N^h_{q\overline{q}}$ are the number of hadrons in the on- and off-resonance, respectively; $\mathcal{L}_{\Upsilon(4S)}$ is the luminosity at the $\Upsilon(4S)$ resonance and $\mathcal{L}_{q\overline{q}}$ – the offline luminosity; $E_{q\overline{q}}$ and $E_{\Upsilon(4S)}$ are the center-of-mass energies below and at the $\Upsilon(4S)$ resonance, respectively; $\epsilon_{\Upsilon(4S)}$ denotes the reconstruction efficiency of the continuum background on-resonance and $\epsilon_{q\overline{q}}$ that off-resonance; $\epsilon^{B\overline{B}}_{\Upsilon(4S)}$ is the reconstruction efficiency of the $B\overline{B}$ events at the $\Upsilon(4S)$ resonance.

With this, we obtain a total of $(771.581 \pm 10.566) \times 10^6$ $B\overline{B}$ pairs, of which $(151.965 \pm 1.241) \times 10^6$ were collected using the SVD1 and the remaining $(619.620 \pm 9.441) \times 10^6$ –

with SVD2.

3.5.2 Non-Hadronic Event Suppression in the Data

To reduce the non-hadronic background originating from QED processes, $\tau^+\tau^-$ pairs, $\gamma\gamma$ processes and beam-gas interactions, a hadronic skim is performed on the data before the actual B meson analysis. In this section, we give a brief overview of the skim. The full procedure is described in [55].

The events are required to fulfill the following criteria.

- The event must contain at least three "good" charged tracks, which have a transverse momentum $p_T < 0.1$ GeV/c and $dr < 2$ cm and $|dz| < 4$ cm, where dr and dz are the radial and the z distance of the closest approach to the IP, respectively
- The primary vertex obtained from a fit of the "good" charged tracks must satisfy $dr < 1.5$ cm and $|dz| < 3.5$ cm
- There must be at least two "good" clusters in the ECL barrel region, defined as clusters with energy $E_{cluster} > 0.1$ GeV and polar angle $-0.7 < \cos\theta < 0.9$
- The sum of momentum magnitudes in the z direction in the $\Upsilon(4S)$ rest frame must be less than half the total beam energy, $\sqrt{s}$
- Assuming the pion mass for "good" charged tracks, the total visible energy in the $\Upsilon(4S)$ rest frame, $E_{vis}^{CMS} = \sum p^{trk} + \sum E^{cluster}$, must be $E_{vis}^{CMS} > 0.18\sqrt{s}$ $0.1\sqrt{s} < E_{CMS}^{cluster} < 0.8\sqrt{s}$, which suppresses QED processes, τ pair production, beam gas and two-photon events with low energy sum
- To suppress τ events, the invariant mass of the particles in each hemisphere perpendicular to the boost, M_{jet}, must satisfy $M_{jet} > 1.8$ GeV/c^2 or $M_{jet}/E_{vis}^{CMS} > 0.25$.

These selection criteria retain more than 99% of the $B\overline{B}$ events, while reducing the contamination from non-hadronic processes to less than 5%. The fraction of continuum events is reduced by 20%.

3.5.3 Monte Carlo Generation

An important analysis tool are the Monte Carlo simulations. These contain generated physics events, which are passed through a virtual copy of the Belle detector geometry to simulate its response. The purpose of the MC simulations is to study the detector effects on the measurements, which, due to the complexity of the detector, is a task that cannot be resolved analytically.

Throughout the analysis, we use MC samples many times: to define the selection cuts, to parametrize the detector response on certain variables or to compare data with MC distributions that contain considerably more events, so that statistical fluctuations are reduced.

The production of MC data takes place in two stages: the generation of physics events and the simulation of the detector response. In the first step, particles are generated from the e^+e^- collision to the subsequent decays of very short-lived daughters. The EvtGen package [56] used for this purpose is an event generator developed by the BABAR and CLEO collaborations.

The EvtGen module contains particle and decay properties, such as decay rates and angular distributions, based on the world averages of the corresponding physics observables. Also relevant properties from the KEKB accelerator are incorporated, such as the electron and positron beam energies. The second step is the simulation of the detector response, in which the detailed detector geometry, its response and inefficiencies are taken into account. A BASF module, called GSIM, simulates the detector response using the CERN GEANT3 package [57]. The interactions between the final state particles and the detector are simulated and the events are then reconstructed in the same way as the data events. The produced Mini-DST (MDST) files contain additional generation information to identify the originally generated process. Background events are added by taking random trigger events with their corresponding noise hits. At the end, evolution in subdetectors, dead channels or the change in the size or position of interaction regions in time are also incorporated.

Chapter 4

Measurement of Branching Fractions and CP Asymmetries in B $\rightarrow \omega$K Decays

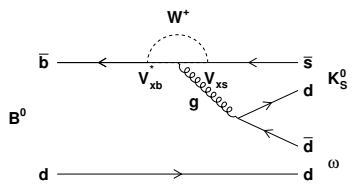

In the following, an overview of the theoretical predictions and previous measurements of the $B \rightarrow \omega K$ decays are given. Next, the method and results of the $B \rightarrow \omega K$ branching fractions and CP asymetries measurement are presented, including the event reconstruction algorithm, the event model and the background studies. At the end, we give an overview of the results, their systematic uncertainties and significance.

4.1 Phenomenology and Previous Measurements of B $\rightarrow \omega$K Decays

The main subjects of this thesis are the neutral decay $B^0 \rightarrow \omega K^0_S$ and the charged decay $B^{\pm} \rightarrow \omega K^{\pm}$. The leading-order decay processes are represented by Feynman diagrams in Figure 4.1. The dominant contribution is a colour-suppressed b $\rightarrow$ s$q\overline{q}$ transition that proceeds through a loop-process (so-called penguin), mediated by a W meson. A CKM-suppressed, so-called tree process, also contributes to the decay. It takes place through a b $\rightarrow$ u$q\overline{q}$ transition. In the case of the neutral decay, the tree process is additionally colour-suppressed.

Decays that proceed dominantly through a loop diagram are sensitive to new physics, since an unobserved particle can enter the loop and introduce an additional amplitude to the decay. This potentially affects the decay rate and the CP asymmetry. Thus, a measured deviation from the SM predictions for the branching fractions and CP asymmetries of b $\rightarrow$ s$q\overline{q}$ dominated decays could be a hint at new physics.

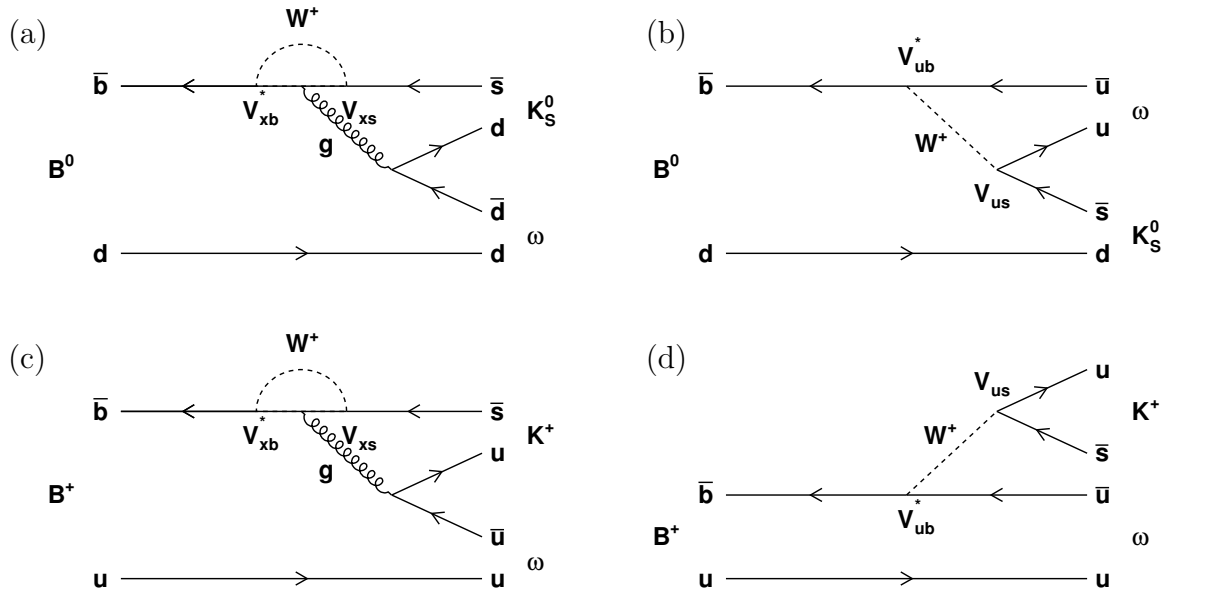

Figure 4.1: Leading-order Feynman diagrams for B $\to \omega$K decays. For $B^0 \to \omega K^0_S$, (a) shows the loop (penguin) while (b) shows the tree diagram. For $B^\pm \to \omega K^\pm$, (c) and (d) are the corresponding diagrams. In the penguin diagrams, the subscript x in V_{xb} refers to the flavour of the intermediate-state up-type quark ($x = u, c, t$).

ωK^0_S is a CP final state. Its CP eigenvalue is determined as

$$\eta_{CP} = CP(K^0_S) \cdot CP(\omega) \cdot (-1)^L = 1 \cdot 1 \cdot (-1)^1 = -1, \tag{4.1}$$

where $L = 1$ is the relative angular momentum of ω and K^0_S. Assuming only a loop decay contribution and neglecting the tree process, the parameter λ_{CP} is given by

$$\lambda_{CP} = \eta_{CP} \cdot \left(\frac{p}{q}\right)_B \cdot \frac{\bar{A}_{\omega K^0_S}}{A_{\omega K^0_S}} \cdot \left(\frac{p}{q}\right)_K = -\frac{V_{td}V^*_{tb}}{V^*_{td}V_{tb}} \cdot \frac{V_{tb}V^*_{ts}}{V^*_{tb}V_{ts}} \cdot \frac{V_{cs}V^*_{cd}}{V^*_{cs}V_{cd}}. \tag{4.2}$$

This equation can be simplified using the unitarity constraint $V^*_{ub}V_{us} + V^*_{cb}V_{cs} + V^*_{tb}V_{ts} = 0$. Since $V^*_{ub}V_{us} \propto \lambda^4$ and $V^*_{cb}V_{cs} \propto \lambda^2$, $V^*_{ub}V_{us} \ll V^*_{cb}V_{cs}$ and thus $V^*_{tb}V_{ts} \approx V^*_{cb}V_{cs}$. With this,

$$\frac{\bar{A}_{\omega K^0_S}}{A_{\omega K^0_S}} = \frac{V_{tb}V^*_{ts}}{V^*_{tb}V_{ts}} = \frac{V_{cb}V^*_{cs}}{V^*_{cb}V_{cs}}. \tag{4.3}$$

Inserting Eq. 4.3 into Eq. 4.2 and taking into account that $\frac{V_{cd}V^*_{cb}}{V^*_{cd}V_{cb}} = 1$,

$$\lambda_{CP} = -\frac{V_{td}V^*_{tb}}{V^*_{td}V_{tb}} \cdot \frac{V_{cb}V^*_{cd}}{V^*_{cb}V_{cd}} = e^{2i\phi_1}. \tag{4.4}$$

Parameter	pQCD	QCDF	SCET 1	SCET 2
$\mathcal{B}(\mathrm{B}^0 \to \omega\mathrm{K}^0)$	$9.8^{+8.6}_{-4.9}$	$4.1^{+4.2+3.3}_{-1.7-2.2}$	$4.1^{+2.1+0.8}_{-1.7-0.7}$	$4.9^{+1.9+0.7}_{-1.6-0.6}$
$\mathcal{B}(\mathrm{B}^\pm \to \omega\mathrm{K}^\pm)$	$10.6^{+10.4}_{-5.8}$	$4.8^{+4.4+3.5}_{-1.9-2.3}$	$5.1^{+2.4+0.9}_{-1.9-0.8}$	$5.9^{+2.1+0.8}_{-1.7-0.7}$
$\mathcal{A}_{\omega\mathrm{K}^0_\mathrm{S}}$	-3^{+2}_{-4}	$-4.7^{+1.8+5.5}_{-1.6-5.8}$	$5.2^{+8.0+0.6}_{-9.2-0.6}$	$3.8^{+5.2+0.3}_{-5.4-0.3}$
$\mathcal{S}_{\omega\mathrm{K}^0_\mathrm{S}}$	84^{+3}_{-7}	84^{+5+4}_{-5-6}	51^{+5+2}_{-6-2}	80^{+2+1}_{-2-1}
$\mathcal{A}_{\omega\mathrm{K}^\pm}$	32^{+15}_{-17}	$22.1^{+13.7+14.0}_{-12.8-13.0}$	$11.6^{+18.2+1.1}_{-20.4-1.1}$	$12.3^{+16.6+0.8}_{-17.3-1.1}$

Table 4.1: pQCD [59, 60], QCDF [61], SCET 1 [62] and SCET 2 [62] theoretical predictions for the $\mathrm{B}^0 \to \omega\mathrm{K}^0_\mathrm{S}$ and $\mathrm{B}^\pm \to \omega\mathrm{K}^\pm$ branching fractions (in units of 10^{-6}) and CP parameters (in units of 10^{-2}).

With this, we expect

$$\begin{aligned} \mathcal{A}_{CP}(\mathrm{B}^0 \to \omega\mathrm{K}^0_\mathrm{S}) \equiv \mathcal{A}_{\omega\mathrm{K}^0_\mathrm{S}} &= \frac{|\lambda_{CP}|^2 - 1}{|\lambda_{CP}|^2 + 1} = 0, \\ \mathcal{S}_{CP}(\mathrm{B}^0 \to \omega\mathrm{K}^0_\mathrm{S}) \equiv \mathcal{S}_{\omega\mathrm{K}^0_\mathrm{S}} &= \frac{2\,\mathrm{Im}(\lambda_{CP})}{|\lambda_{CP}|^2 + 1} = \sin 2\phi_1. \end{aligned} \tag{4.5}$$

Since in the charged mode no mixing is possible due to charge conservation, the expected CP asymmetry in the single process approximation is

$$a_{CP}(\mathrm{B}^\pm \to \omega\mathrm{K}^\pm) \equiv \mathcal{A}_{\omega\mathrm{K}^\pm} = 0. \tag{4.6}$$

The current world average for $\sin 2\phi_1$ is $\sin 2\phi_1 = 0.689 \pm 0.019$ [37], obtained from $\mathrm{b} \to \mathrm{c\bar{c}s}$ transitions. These decays and in particular the so-called "golden mode" $\mathrm{B} \to \mathrm{J}/\psi\mathrm{K}^0_\mathrm{S}$ provide a clean environment for $\sin 2\phi_1$ measurements, both in the theoretical and experimental sense. In SM theory, $\mathrm{b} \to \mathrm{c\bar{c}s}$ decays are dominated by tree contributions and the loop transitions are very strongly suppressed, which allows direct access to $\sin 2\phi_1$. Experimentally, these modes are rather free from background and thus their physical properties can be extracted accurately.

In $\mathrm{b} \to \mathrm{s}q\overline{q}$ transitions, CKM-suppressed amplitudes with a different weak phase introduce additional weak phases, whose contribution may not be negligible. As a consequence, the measured S_{CP} is expected to be higher than $\sin 2\phi_1$ within the SM. Measurements so far show the opposite tendency, as illustrated in Figure 4.2.

The predictions for the branching fractions, $\mathcal{B}$, and the CP parameters of $\mathrm{B} \to \omega\mathrm{K}$ decays are summarized in Table 4.1. They are estimated in several theoretical approaches – quantum chromodynamics factorization (QCDF), perturbative QCD and soft collinear effective theory (SCET). These methods use the world average values for the CKM parameters, unitarity triangle angles and hadron decay constants. The Belle and BaBar experiments have already performed measurements of $\mathrm{B}^0 \to \omega\mathrm{K}^0_\mathrm{S}$ and $\mathrm{B}^\pm \to \omega\mathrm{K}^\pm$. They are summarized in Table 4.2. The predictions and the measurements are mostly in agreement but their high uncertainties are a motivation for both more precise theoretical calculations and more precise measurements.

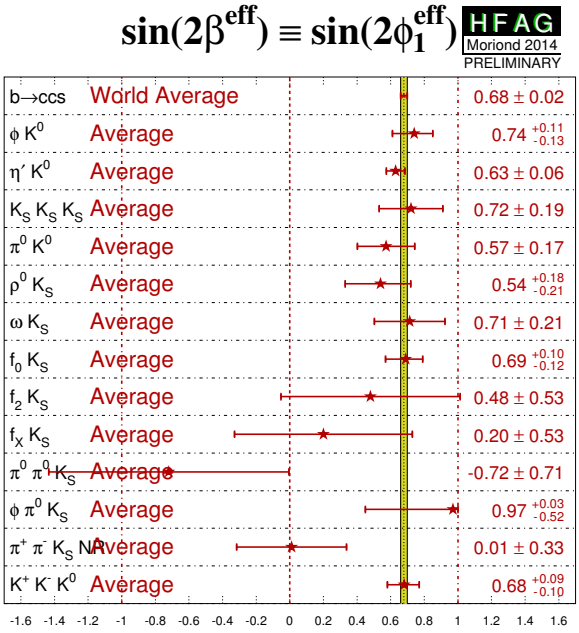

Figure 4.2: Current status of the measurements of $\sin 2\phi_1$ in $b \to s\bar{q}q$ transitions [58].

Parameter	Belle (388×10^6 $B\overline{B}$ pairs)	Belle (535×10^6 $B\overline{B}$ pairs)	BaBar (467×10^6 $B\overline{B}$ pairs)
$\mathcal{B}(B^0 \to \omega K^0_S)$	$(4.4^{+0.8}_{-0.7} \pm 0.4) \times 10^{-6}$	-	$(5.4 \pm 0.8 \pm 0.3) \times 10^{-6}$
$\mathcal{A}_{\omega K^0_S}$	-	$-0.09 \pm 0.29 \pm 0.06$	$0.52^{+0.20}_{-0.22} \pm 0.03$
$\mathcal{S}_{\omega K^0_S}$	-	$0.11 \pm 0.46 \pm 0.07$	$0.55^{+0.26}_{-0.29} \pm 0.02$

Parameter	Belle (388×10^6 $B\overline{B}$ pairs)	BaBar (383×10^6 $B\overline{B}$ pairs)
$\mathcal{B}(B^\pm \to \omega K^\pm)$	$(8.1 \pm 0.6 \pm 0.6) \times 10^{-6}$	$(6.3 \pm 0.5 \pm 0.3) \times 10^{-6}$
$\mathcal{A}_{\omega K^\pm}$	$0.05^{+0.08}_{-0.07} \pm 0.01$	$-0.01 \pm 0.07 \pm 0.01$

Table 4.2: Summary of $B \to \omega K$ branching fractions and CP violation parameters obtained by Belle [63, 64] and BaBar [65, 66]. For all parameters, the first uncertainty is statistical and the second is systematic.

4.2 Signal Reconstruction

A set of selection criteria are applied to the Belle data to successfully filter out the decays $B^0 \to \omega K^0_S$ and $B^\pm \to \omega K^\pm$ on the CP side (see Section 3.4). In this analysis, B_{CP} is reconstructed completely, while on the tag side only the B meson decay vertex and flavour

are determined to allow for measurement of the CP parameters.

To develop and optimise the selection cuts, which aim to enhance the signal purity, and to study the fit observables' shapes, signal and background Monte Carlo events as well as data outside of the signal region are used. The exact content of these MC and data samples are explained in the following sections.

4.2.1 Decay Channels

We reconstruct the decays $B^0 \to \omega K^0_S$ and $B^\pm \to \omega K^\pm$ from selected subdecays of the corresponding B meson daughters. $B^0 \to \omega K^0_S$ is reconstructed from $\omega \to \pi^+\pi^-\pi^0$, which has a branching fraction of 89.2%, and from $K^0_S \to \pi^+\pi^-$ with a decay probability of 69.5% [27]. The neutral pion candidate in the ω meson decay is built from two photons. The charged pion and kaon candidates are reconstructed from charged tracks in the detector.

4.2.2 Monte Carlo and Data Samples

Besides signal events, also background events, such as $e^+e^- \to q\overline{q}$ (see Section 2.1) and B meson decays to other modes, pass our selection criteria. To study the signal and background distributions in the data, we use three types of Monte Carlo samples and real data outside of the signal region referred to as "sideband data".

- Signal MC: It consists of two samples containing exclusively $B\overline{B}$ pairs, in which one of the B mesons decays either as $B^0 \to \omega K^0_S$ or as $B^\pm \to \omega K^\pm$ and the other one follows the world average B meson decay probabilities. 2 000 000 events were generated in each of the two samples – 1 000 000 for each SVD configuration.

- Charm B MC: This sample contains all known B meson decays occurring via $b \to cq\overline{q}$ transitions, with $q = u, d, s$. There are two charm MC samples – one with neutral and one with charged B meson pairs. The number of events in these MC samples is 10 times their expected contribution to the full data taken by Belle.

- Charmless B MC: It contains B meson decays which proceed through a $b \to (u/d/s)q\overline{q}$ transition. Just like the charm MC sample, it is divided into a neutral and a charged samples. This kind of processes is rare and to obtain enough events to be able to model their shape, the charmless samples are 100 times larger than their expected contribution to the on-resonance data.

- On-resonance data: This is the full data set of 772×10^6 $B\overline{B}$ events recorded by Belle at the $\Upsilon(4S)$ resonance. In the signal region, it is used for the branching fractions and the CP parameters measurement; in the sideband region, which is defined further in the thesis, the study of the major background, $e^+e^- \to q\overline{q}$, is performed.

4.2.3 CP Side Reconstruction

The selection criteria used in the data and in the MC aim to enhance the signal in respect to the background. They are first applied to the final-state particles, which in this case are photons, pions and kaons. Their four-momenta are then combined to first form possible π^0 and later ω and K^0_S candidates. More quality and selection requirements are applied to the ω and K^0_S candidates before they are combined into B meson candidates. Furthermore, filters are applied based on the event shape variables to separate $B\overline{B}$ events from continuum background events. The following sections will discuss in more detail the chosen filters.

4.2.3.1 $\pi^\pm$ and $K^\pm$ Candidates Reconstruction

The charged pions and kaons are reconstructed from charged tracks in the detector. A loose cut on the charged-track origin is applied, requiring the track impact parameters (see Section 2.3.2) to be fulfill $dr < 0.4\,\text{cm}$ and $|dz| < 4\,\text{cm}$.

Pions and kaons cannot be distinguished unambiguously in the detector. They are identified using a likelihood ratio $\mathcal{L}_{K/\pi}$ constructed from CDC (see Section 2.3.3), ACC (see Section 2.3.4) and TOF (see Section 2.3.5) information. $\mathcal{L}_{K/\pi}$ is the likelihood that a track is a kaon given the pion hypothesis. It is defined as

$$\mathcal{L}_{K/\pi} = \frac{\mathcal{L}_K}{\mathcal{L}_K + \mathcal{L}_\pi}, \tag{4.7}$$

where $\mathcal{L}_i$ ($i = \pi, K$) is the likelihood that a particle is of type i.

$$\mathcal{L}_i = \mathcal{L}_i^{CDC} \times \mathcal{L}_i^{ACC} \times \mathcal{L}_i^{TOF}, \tag{4.8}$$

where $\mathcal{L}_i^{DET}$ is the likelihood that the particle is of type i in the respective subdetector.

The resulting likelihood ratio for all reconstructed tracks ranges from zero to unity and is shown in Figure 4.3. The pion and kaon candidates are required to satisfy $\mathcal{L}_{K/\pi} \leq 0.9$ and $\mathcal{L}_{K/\pi} \geq 0.6$, respectively. Thus, in the overlap region of $0.6 \leq \mathcal{L}_{K/\pi} \leq 0.9$, one and the same track is identified both as a kaon and a pion. However, when reconstructing a B meson, a track can only be used once. For instance, it is not possible to have a B^- meson candidate containing the same track once as a π^- and once as a K^- candidate.

To separate pions and kaons from electrons, a similar likelihood is used, built upon CDC, ACC and ECL information. Pions and kaons with $\mathcal{L}_{e/h} = \mathcal{L}_e/(\mathcal{L}_e + \mathcal{L}_h) < 0.9$ are accepted, where "e" represents an electron and "h" a hadron.

4.2.3.2 π^0 Candidate Reconstruction

Neutral pion candidates are reconstructed from two photons, required to have energies above 50 MeV in the ECL barrel and above 100 MeV in the ECL end cap. The reconstructed invariant mass must be in the range $118\,\text{MeV}/c^2 \leq M(\gamma\gamma) \leq 150\,\text{MeV}/c^2$, which is $15\,\text{MeV}/c^2$ around the world average π^0 mass, $M_{\pi^0} = 135\,\text{MeV}/c^2$ [27]. This is the cut on which the general Belle reconstruction systematic uncertainty is based [67]. The π^0 candidates' mass distribution is shown in Figure 4.4.

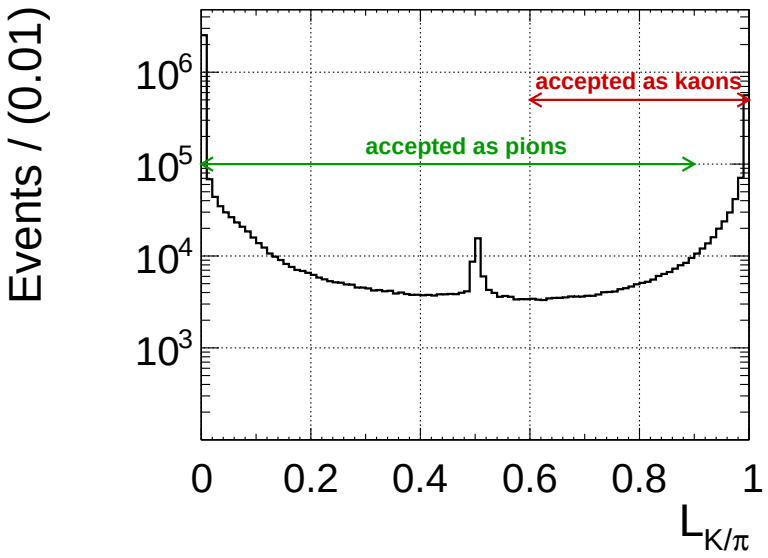

Figure 4.3: Particle identification likelihood ratio for $B^{\pm} \to \omega K^{\pm}$. The peak at 0.5 is caused by tracks for which no particle ID information is available, such as tracks reconstructed only in the SVD.

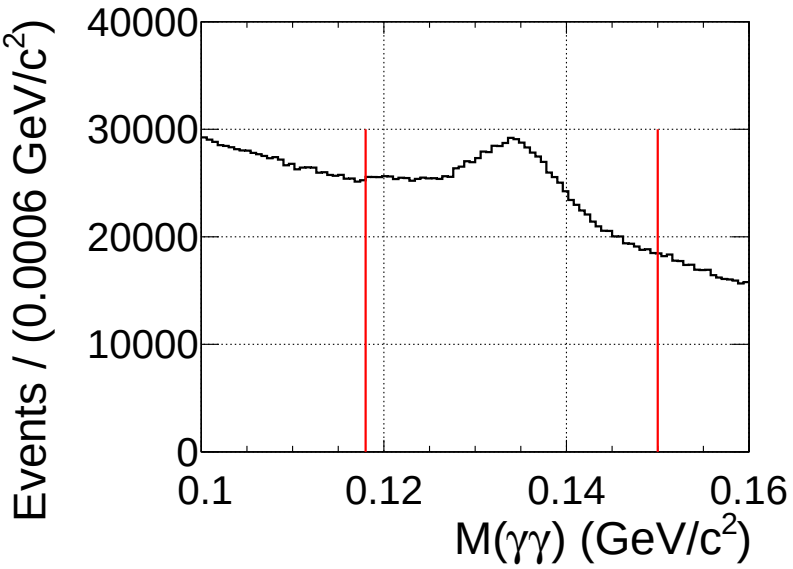

Figure 4.4: Mass distribution of the π^0 candidates in $B^0 \to \omega K^0_S$ MC before the application of the selection criteria. The mass cut (red lines) corresponds to approximately 2.5 experimental widths.

4.2.3.3 K^0_S Candidate Reconstruction

The K^0_S candidates are reconstructed from two oppositely charged pions. The reconstructed invariant mass is required to be $482\,\mathrm{MeV}/c^2 \leq M(\pi^+\pi^-) \leq 514\,\mathrm{MeV}/c^2$, which is $16\,\mathrm{MeV}/c^2$ around the nominal K^0_S mass, $M_{K^0_S} = 498\,\mathrm{MeV}/c^2$ [27], and assures an inclusion of almost 100% of the K^0_S candidates. Cuts dependent on the K^0_S momentum are applied on the displacement of the $\pi^+\pi^-$ vertex to the IP, since the neutral kaon transverses a distance of approximately $1-3$ cm in the detector before it decays. This standard Belle algorithm for K^0_S reconstruction is referred to as "GoodKs" [68] and has an efficiency of 83.5% for K^0_S particles with a momentum over 1.5 GeV/c. 100% of the K^0_S originating from $B^0 \to \omega K^0_S$ are in this momentum range. The K^0_S candidates' mass distribution is shown in Figure 4.5.

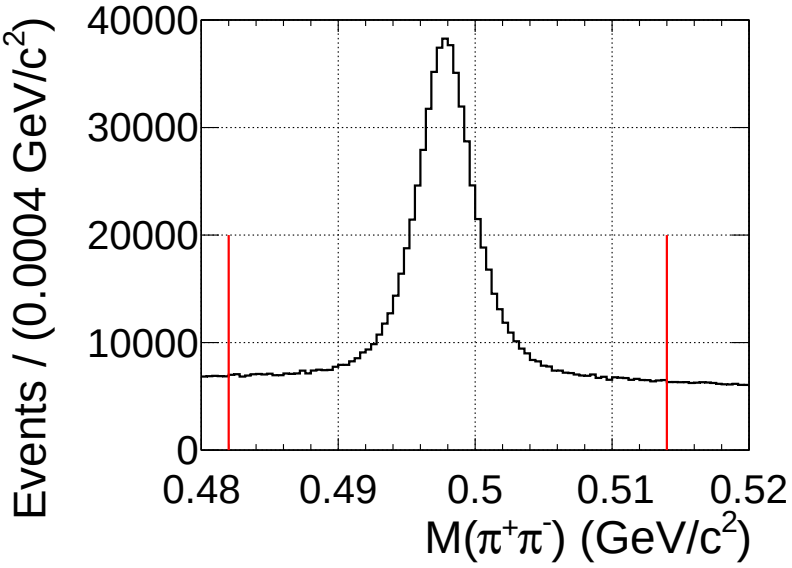

Figure 4.5: Mass distribution of the K^0_S candidates in $B^0 \to \omega K^0_S$ MC before the application of the selection criteria. The mass cut (red lines) corresponds to three experimental widths.

4.2.3.4 ω Candidate Reconstruction

The ω candidates are built from a π^+, a π^- and a π^0 candidate. The reconstructed mass is required to be $730\,\mathrm{MeV}/c^2 \leq M(\pi^+\pi^-\pi^0) \leq 830\,\mathrm{MeV}/c^2$ which is $50\,\mathrm{MeV}/c^2$ (five experimental widths) around the nominal ω mass, $M_\omega = 782\,\mathrm{MeV}/c^2$ [27]. The ω candidates' mass distribution is shown in Figure 4.6.

4.2.3.5 B Meson Candidate Reconstruction

Once the ω, K^0_S and $K^\pm$ candidates are reconstructed, they are combined into B meson candidates. For the measurement of the CP parameters, it is necessary to know the

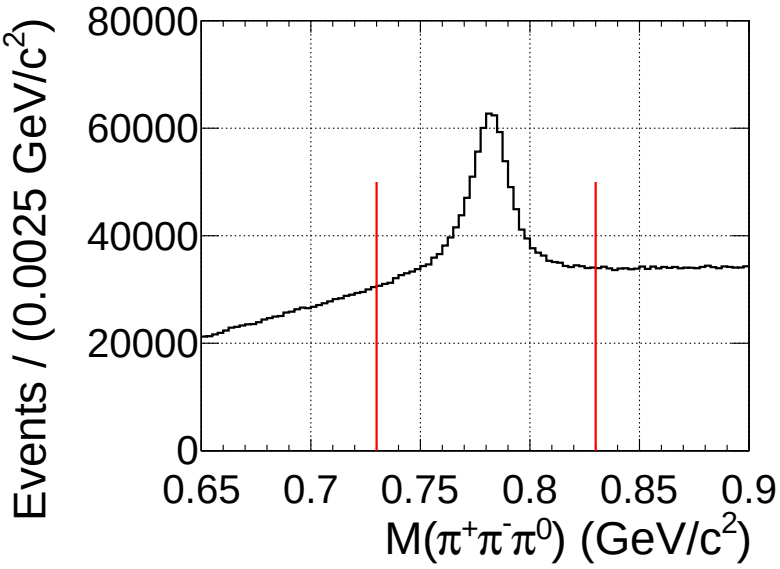

Figure 4.6: Mass distribution of the ω candidates in $B^0 \to \omega K^0_S$ MC before the application of the selection criteria. The mass cut (red lines) corresponds to five experimental widths.

position of the B meson decay vertex (see Section 3.4).

B Meson Vertex

Due to its short lifetime of $\tau_\omega = 7.75 \times 10^{-23}$ s [27], the ω meson has the same decay vertex as the B meson from the experimental point of view. This is why, in this analysis, the B meson decay vertex is obtained directly from a fit [69] to the charged tracks of the ω meson, π^+ and π^-. These are required to have at least one $r-\phi$ layer hit in the SVD and, to assure a good Δz resolution, at least two z layer hits. If a track does not fulfill this requirement, it is excluded from the vertex fit.

To improve the vertex position, the fit is constrained to be consistent with the IP profile, which is modeled as a three-dimensional Gaussian distribution (see Appendix A.1) and determined from hadronic events every 10 000 to 60 000 events [70]. Its widths, σ, are typically

$$\sigma_x = 100\,\mu\text{m} \qquad \sigma_y = 5\,\mu\text{m} \qquad \sigma_z = 3\text{ mm}.$$

To account for the finite flight length of the B meson and avoid a bias on the z position of the vertex, the IP profile is added to the fit as a virtual straight track along the boost axis. Using this virtual track, it is possible to obtain a vertex with only one charged track of the B meson decay. The difference in the Δz resolution between single- and two-track vertices is taken into account in the Δt resolution function (see Section 3.4.2), presented later in the thesis.

The position uncertainty of the track is the IP profile size in the xy-plane, smeared by an additional

$$\text{IP}_{\text{smear}} = 21\,\mu\text{m}$$

to account for the transverse B decay length. After the vertex fit, the excluded K^0_S and $K^\pm$ are constrained to come from the same vertex and the B meson momentum is calculated using these updated momenta.

The vertexing algorithm has an efficiency of 91% and provides a vertex resolution of approximately 50 µm.

ΔE and $M_{\rm bc}$

The next step in the reconstruction is to constrain the B meson candidate mass and energy. Because of energy conservation, the $B\overline{B}$ pair has the same energy as the total one of the two beams. The two B mesons have equal masses and, since they originate from a two-body decay, they also have the same momenta and the same energies in the CMS, which are equal to half the total beam energy. Using this knowledge, the resolution of the invariant B meson mass can be increased by substituting the measured energy with the beam energy. This observable is called beam-constrained mass and is defined as

$$M_{\rm bc} = \sqrt{\left(E^{CMS}_{\rm beam}\right)^2 - \left(\overrightarrow{p}^{CMS}_{\rm B}\right)^2}, \tag{4.9}$$

where $E^{CMS}_{\rm beam}$ is half the beam energy and $\overrightarrow{p}^{CMS}_{\rm B}$ is the reconstructed B meson momentum in the CMS system, computed from the measured momenta of its daughter particles.

The $M_{\rm bc}$ resolution is dominated by the beam energy,

$$\sigma^2(M_{\rm bc}) = \sigma^2\left(E^{CMS}_{beam}\right) + \left(|\overrightarrow{p}^{CMS}_{\rm B}|/M_{\rm B}\right)^2 \sigma^2\left(\overrightarrow{p}^{CMS}_{\rm B}\right) \tag{4.10}$$

with $(|\overrightarrow{p}^{\rm CMS}_{\rm B}|/M_{\rm B}) = 0.34/5.29 \simeq 0.064$ and $\sigma(\overrightarrow{p}^{\rm CMS}_{\rm B}) \leq \sigma(E^{\rm CMS}_{\rm beam})$ [71]. Because of the strong suppression of the $\sigma^2\left(\overrightarrow{p}^{CMS}_{\rm B}\right)$ term through $(|\overrightarrow{p}^{\rm CMS}_{\rm B}|/M_{\rm B})^2$, the spread in $M_{\rm bc}$ is dominated by the spread in beam energy rather than by the uncertainty in momentum or energy measurements of the decay products. In Figure 4.7, the distributions of $M_{\rm bc}$ and the B meson mass, $M_{\rm B}$, reconstructed from the energies of the decay products are shown. It is obvious that the $M_{\rm bc}$ resolution is much better than that of $M_{\rm B}$, which makes $M_{\rm bc}$ the better observable for discrimination against the $q\overline{q}$ background. Due to the interactions in the detector, a small part of the B meson daughter particle energy and momentum, mostly of the photons, is not entirely reconstructed. This leads to a "tail" in the $M_{\rm bc}$ distribution towards lower energies.

Another variable used to identify the B meson is the energy difference $\Delta E = E^{CMS}_{\rm B} - E_{\rm beam}$, where $E^{CMS}_{\rm B}$ is the reconstructed B meson energy. $E^{CMS}_{\rm B}$ is obtained from the four-momenta of the daughter particles. The ΔE resolution is dominated by the uncertainty of the reconstructed energy,

$$\sigma^2\left(\Delta E\right) = \sigma^2\left(E^{CMS}_{\rm B}\right) + \sigma^2\left(E^{CMS}_{beam}\right), \tag{4.11}$$

where $\sigma^2(E^{CMS}_{\rm B}) \gg \sigma^2(E^{CMS}_{beam})$ [71].

We retain only candidates which satisfy

$$M_{\rm bc} \geq 5.25\,{\rm GeV}/c^2 \qquad \text{and} \qquad -0.15\,{\rm GeV} \leq \Delta E \leq 0.10\,{\rm GeV}. \tag{4.12}$$

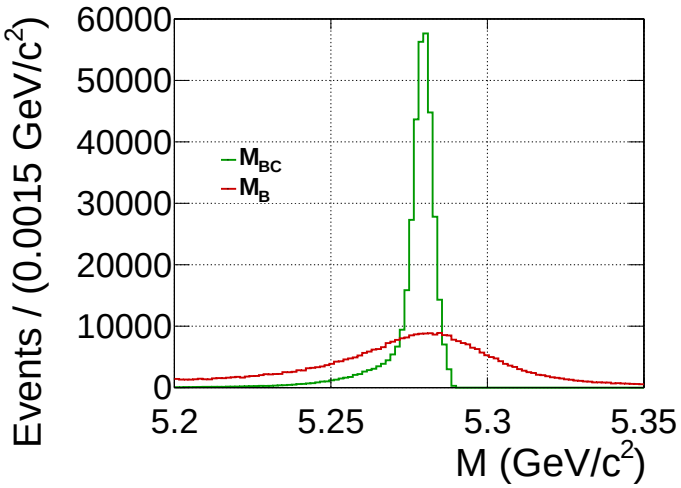

Figure 4.7: Comparison between the beam constrained mass, M_{bc}, (green) and the invariant mass of the B candidate, M_{B}, (red) for $\mathrm{B}^0 \to \omega \mathrm{K}^0_{\mathrm{S}}$ signal MC events.

M_{bc} is naturally limited up to less than $5.30\,\mathrm{GeV}/c^2$ by the maximum beam energy. The reason for the asymmetric cut in ΔE is the "tail" in the distribution towards lower energies (see ΔE in Figure 4.15) originating from incomplete photon energy reconstruction.

Best B Candidate Selection

Due to the combinatorial nature of the reconstruction, there is the possibility that more than one B meson is reconstructed per event. The number of reconstructed B mesons per event is referred to as "event multiplicity". Its distribution for the two decay modes is shown in Figure 4.8. The mean multiplicity per event for $\mathrm{B}^0 \to \omega \mathrm{K}^0_{\mathrm{S}}$ and $\mathrm{B}^\pm \to \omega \mathrm{K}^\pm$ is 1.1. However, there can only be one correct B meson per event at most[1]. Thus, we choose only one possible B candidate, aiming for the correct one. This procedure is referred to as "best B selection".

A common best B selection criterion would be to choose the B candidate with M_{bc} closest to the B meson mass world average or to pick the B candidate with the best reconstructed vertex (lowest fit χ^2). However, both criteria prove to be unsuitable for the purposes of this analysis. If we choose the best M_{bc} criterion, we would introduce a bias in M_{bc}, which is a fit observable in the event model. In addition, it would create an artificial peak in the otherwise flat $q\bar{q}$ M_{bc} distribution (see M_{bc} in Figure 4.27). The choice of the best vertex is known to bias the Δt distribution, which is also a part of the event model. Having this consideration in mind together with the relatively low multiplicity, we decide to choose a reproducible arbitrary B meson candidate.

Using MC information, one can find out how often the correct B meson is reconstructed. We define a "correctly reconstructed" B meson as one which has a vertex obtained from

[1]The case where both the CP and the tag-side decay into $\mathrm{B}^0 \to \omega \mathrm{K}^0_{\mathrm{S}}$ has a probability of about 10^{-12} and with this is extremely rare.

the charged tracks of its associated ω meson pions. This definition allows us to extract the correct Δt distribution for $B^0 \to \omega K^0_S$ events, which requires a correct B_{CP} vertex on the CP side. Note that events with a π^0 and a K borrowed from the tag side are still considered correctly reconstructed. Events with a wrong vertex are referred to as "misreconstructed" and their fraction is found to be 1.8-1.9% of all signal events for both decay channels. This amount is only negligibly higher than if we use the best $M_{\rm bc}$ or the best vertex as a best B criterion, proving that our selection method has no noticeable disadvantage compared to these alternative two.

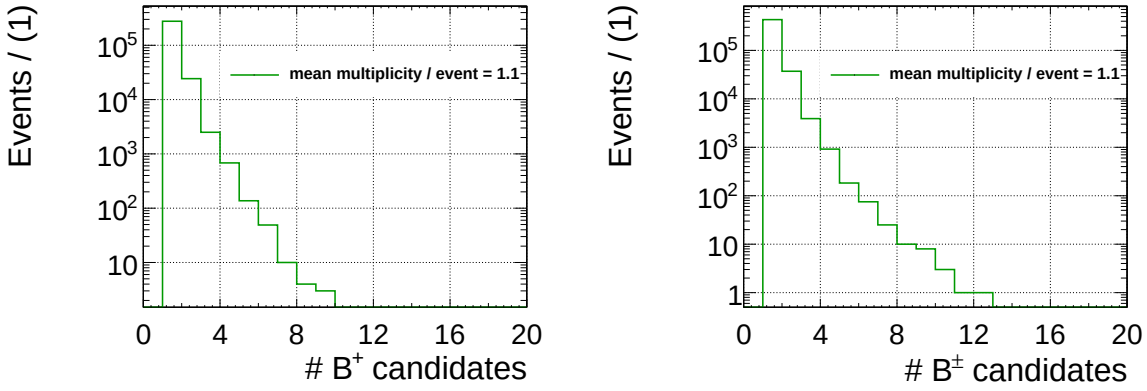

Figure 4.8: Number of reconstructed B^0 candidates per event in $B^0 \to \omega K^0_S$ signal Monte Carlo (left) and number of reconstructed $B^\pm$ candidates per event in $B^\pm \to \omega K^\pm$ signal Monte Carlo (right).

4.2.4 Tag-Side Reconstruction

After a successful reconstruction of the CP side, all remaining tracks are assumed to belong to the tag-side meson $B_{\rm tag}$. As already mentioned in Section 3.4, to be able to extract CP information, the $B_{\rm tag}$ flavour and decay vertex position need to be determined. Note that this is necessary for the neutral decay mode only, since $B^\pm \to \omega K^\pm$ is a self-tagging decay.

4.2.4.1 Flavour Tagging

We give a brief overview of the flavour tagging procedure, in which the flavour of the $B_{\rm tag}$ meson is determined. The full method description can be found in [72].

At Belle, six types of events are used for flavour tagging:

- Primary leptons: In events such as $b \to c\ell\overline{\nu}$ (primary leptons), the a $\overline{\ell}$ (ℓ), which can be either electron or muon, indicates a B^0 ($\overline{B}^0$) on the tag side.
- Secondary leptons: Leptons from cascade decays (secondary leptons) occurring via the transition $b \to W^- c[s\bar{\ell}\nu]$ carry tagging information as well: a ℓ ($\bar{\ell}$) hints at a B^0 ($\overline{B}^0$) on the tag side. Secondary leptons are characterized by a much softer momentum spectrum than primary leptons

- Kaons: A K^+ (K^-) in decays such as $B^0 \to \overline{D}[K^+X]X$ tags a B^0 ($\overline{B}^0$)
- Slow pions: Low-momentum π^- (slow pions) from transitions such as $D^{*+} \to D^0[K^-X]\pi^+$ provide another source of tagging information
- High-momentum pions: A high-momentum π^+ (π^-) in decays such as $\overline{B}^0 \to D^{*+}\pi^-$ indicates a B^0 ($\overline{B}^0$) decay
- Λ baryon events: The flavour of a Λ baryon produced in B_{tag} decays carries tagging information because it likely contains an s quark produced in the cascade decay $b \to c \to s$. Therefore, the presence of a Λ ($\overline{\Lambda}$) will indicate a $\overline{B}^0$ (B^0).

The flavour tagging algorithm uses a binned multidimensional likelihood method to estimate the flavour q and the expected flavour dilution factor r. q can be either 1 if B_{tag} is a B^0 or -1 if it is a $\overline{B}^0$. r ranges from zero for no discrimination to one for unambiguous flavour assignment. Using a multidimensional lookup table, the signed probability $q \cdot r$ is given by

$$q \cdot r = \frac{N(B^0) - N(\overline{B}^0)}{N(B^0) + N(\overline{B}^0)} \tag{4.13}$$

where $N(B^0)\Big(N(\overline{B}^0)\Big)$ is the number of $B^0(\overline{B}^0)$ events in the corresponding bin of the lookup table prepared from a large sample of simulated events.

The flavour-tagging algorithm works in two stages: the track stage and the event stage. In the track stage, all tracks are classified into four categories: lepton-like, kaon-like, slow-pion-like and Λ-like. For each category, $(q \cdot r)_X$ is estimated using a set of kinematic variables, such as track momentum, angle and particle identification information. In the event stage, the $(q \cdot r)_X$ with the largest absolute value is taken from the slow-pion-like and lepton-like categories while the kaon-like and Λ-like categories are combined into a common $(q \cdot r)$ to account for the cases with multiple s quarks in an event. These variables are used to estimate the final event $q \cdot r$ from a second MC-based lookup table.

Depending on the flavour dilution factor $(q \cdot r)$, the flavour tagging procedure provides a wrong flavour tag for a certain fraction of events. This fraction is referred to as the wrong tag fraction w, with the difference $\Delta w = w(q = +1) - w(q = -1)$. The values of these two parameters are obtained from data-based studies.

Since the flavour tagging result is independent of the CP side, one can determine w by looking at flavour-specific decays on the CP side and compare the flavour tag to the reconstructed flavour. The wrong tag fractions, w, and differences, Δw, are determined directly from the data for six out of seven different regions of r, using semi-leptonic ($B^0 \to D^{*-}\ell^+\nu$) and hadronic ($B^0 \to D^{(*)-}\pi^+$, $B^0 \to D^{*-}\rho^+$) decays and their charge conjugates. The results are summarized in Table 4.3. The value of r is related to w through $r = 1 - 2w$. For events in the seventh r region ($|r| \leq 0.1$), the flavour discrimination is negligible and thus the wrong tag fraction is set to $w_0 = 0.5$. The effective flavour tagging efficiency is $\epsilon_{eff} = \epsilon(1-2w)^2$, where ϵ is the raw tagging efficiency. The average effective tagging efficiency is $\epsilon_{eff} = (28.8 \pm 0.6)\%$.

	SVD1		SVD2	
region of r	w	Δw	w	Δw
0.0 – 0.1	0.500	0.000	0.500	0.000
0.1 – 0.25	0.419	0.057	0.419	-0.009
0.25 – 0.5	0.330	0.013	0.319	0.010
0.5 – 0.625	0.234	-0.015	0.223	-0.011
0.625 – 0.75	0.171	-0.001	0.163	-0.019
0.75 – 0.875	0.100	0.009	0.104	0.002
0.875 – 1.0	0.023	0.005	0.025	-0.004

Table 4.3: Wrong tag fractions, w, and differences, Δw, for SVD1 and SVD2 determined from $B^0 \to D^{*-}\ell^+\nu$ and its charge conjugate decay.

A very important consequence of the tagging procedure is that the probability density function of the proper-time difference for events, in which B_{CP} is tagged as a B^0 or $\overline{B}^0$, given in 3.7, is diluted due to the wrong-tag fraction,

$$\mathcal{P}(\Delta t, q) = \frac{e^{-|\Delta t|/\tau_{B^0}}}{4\tau_{B^0}} [1 + q\Delta w + q(1-2w)\left(\mathcal{A}_{CP}\cos\left(\Delta m \Delta t\right) + \mathcal{S}_{CP}\sin\left(\Delta m \Delta t\right)\right)] \quad (4.14)$$

After the flavour-tagging algorithm has been applied, 99.8% of all signal candidates remain. The few events that get rejected are such in which there are either no tracks on the tag side or the observables needed for the flavour tagging are in regions of the lookup tables with missing information.

4.2.4.2 Tag-Side Vertexing

After a successful flavour tagging, the tag-side vertex is determined. This is a non-trivial procedure mainly for two reasons. First, in only a small fraction of events, all decay products of B_{tag} are inside the acceptance of the detector, hence a strategy based on a full reconstruction is excluded. Second, the majority of the B_{tag} decays proceed through a decay to open charm, leading to at least one secondary vertex in the B_{tag} decay topology. The decay length of the charmed daughter is not negligible in comparison to that of the B meson and also the number of tracks originating from the vertex is similar. Thus, the assignment of charmed daughter tracks to the B_{tag} vertex leads to a bias in the B_{tag} position and to a resolution deterioration [73].

The first step in the algorithm is the selection of an optimal set of tracks. All tracks that are associated with the CP side are removed. In order to obtain a good resolution in z direction, from the remaining tracks, only those are retained that have at least one SVD-r-ϕ hit and two SVD-z hits. Also tracks with large impact parameters are removed. After a series of additional cuts, all remaining tracks together with the IP profile constraint (see Section 4.2.3.5) are fitted on a combined vertex. If the χ^2 per degree of freedom, χ^2/NDF, is larger than 20, the track with the highest contribution to the χ^2 is removed and the vertex is refitted. The procedure is repeated until a vertex with $\chi^2/NDF < 20$ is

found or only one track is left. In the second case, the algorithm fails. Tracks identified as leptons with a high transverse momentum are never discarded as they have a high probability to originate from the B_{tag} vertex.

The B_{tag} vertex resolution is in the range $100 - 200\,\mu m$ and with this 2-4 times worse than that of B_{CP}. Thus, the main contribution to the the Δz resolution comes from the tag side.

4.2.5 From Vertex Positions to Δt

Time-dependent CP parameters are extracted from the Δt distribution, which can be calculated from the z distance between the B_{CP} and B_{tag} vertices. Under the assumption that the B meson momentum in the CMS system is negligible, the dependency is given by

$$\Delta t = \frac{\Delta z}{\langle\beta\gamma\rangle c} = \frac{z_{CP} - z_{\text{tag}}}{\langle\beta\gamma\rangle c} \tag{4.15}$$

where $\langle\beta\gamma\rangle = 0.425$ is the Lorentz boost of the $\Upsilon(4S)$.

Normally, the quality of the vertex fit is determined by its standard χ^2/NDF. However, this value is correlated with the z-position of the vertex due to the IP constraint in the xy-plane and would bias the Δt distribution if used as quality indicator. We therefore introduce a new measure of vertex quality

$$h = \frac{1}{2(n-1)} \sum_{i=1}^{n} \left[\frac{z^i_{after} - z^i_{before}}{\epsilon^i_{before}} \right]^2 \tag{4.16}$$

where n is the number of tracks used in the fit, z^i_{before} and z^i_{after} are the z positions of each track before and after the vertex fit and ϵ^i_{before} is the error on z^i_{before}. h corresponds to a reduced χ^2 without the IP constraint taken into account, which has been shown to be unbiased [74].

Figure 4.9 shows the distributions of the difference between the reconstructed vertex position and its true position for single- and multi-track vertices for the CP- and the tag-side based on MC events. There is an obvious difference in their resolutions, which is why we threat them differently in the event selection and Δt resolution function.

Loose selection criteria are imposed on the vertex quality for both CP-side and tag-side vertices [75]. These aim to remove only events with a very low quality of the vertex. The criteria are:

- $h < 50$
- the z-error of the vertex, σ_z, has to fulfill $\sigma_z < 0.2\,\text{mm}$ for multi-track vertices to reduce the possible Δt resolution function (see next section) bias due to different vertex error distributions in signal and $q\bar{q}$ background, also known as the Punzi effect [76]
- for single track vertices, we require $\sigma_z < 0.5\,\text{mm}$.

In addition, we impose $-70\,\text{ps} \leq \Delta t \leq 70\,\text{ps}$, which corresponds to $\Delta z \approx 1$ cm. These requirements reject in total 0.2% of all signal events.

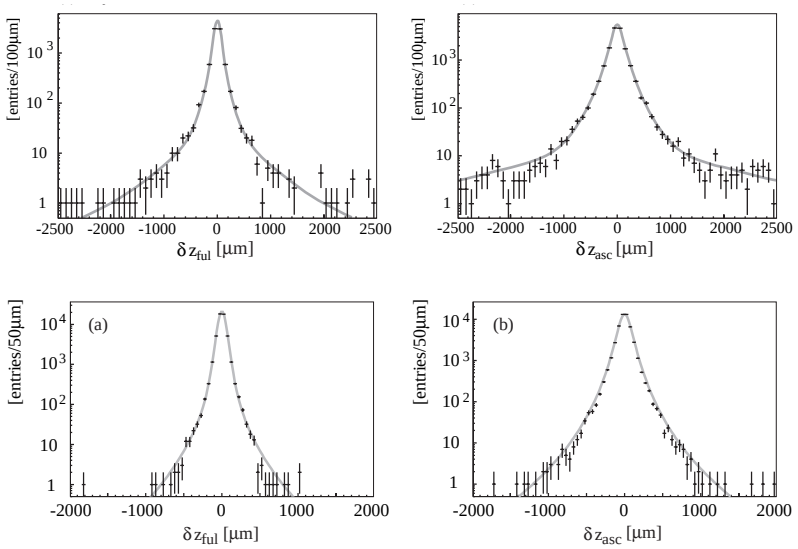

Figure 4.9: Distribution of the difference between the reconstructed vertex position and its true position for single-track vertices for the CP (upper left) and tag side (upper right) and for multi-track CP (lower left) and tag side (lower right) vertices. The plots are based on $B^0 \to J/\psi K^0_S$ MC events [70].

4.2.6 Δt Resolution Function

The Δt distribution function for B mesons in Eq. 4.14 is a theoretical description and does not include the detector response. To model the detector effects on Δt, resolution functions for $B\overline{B}$ and $q\overline{q}$ events have been developed.

For both $B\overline{B}$ and $q\overline{q}$, the corresponding resolution function, $\mathcal{R}$, smears the true Δt distribution $\mathcal{P}(\Delta t)$ as

$$\mathcal{P}(\Delta t) = \int_{-\infty}^{+\infty} \mathcal{P}(\Delta t')\mathcal{R}(\Delta t - \Delta t')d(\Delta t'). \tag{4.17}$$

In the following, we explain the main features of the two types of resolution functions and refer to [70] for more information.

4.2.6.1 Δt Resolution Function for $B\overline{B}$ Events

The $B\overline{B}$ resolution function, $\mathcal{R}_{sig}$, was determined using a large sample of decays such as $\overline{B}^0 \to D^+\pi^-$, $D^{*+}\pi^-$, $D^{*+}\rho^-$, $J/\psi K^0_S$, $J/\psi \overline{K}^{*0}$, $B^- \to D^0\pi^-$, $J/\psi K^-$ and their charge conjugates. The vertex selection criteria are the same as the ones described in the previous sections. The functional form of the resolution function was determined from a detailed MC simulation study, while its parameters were obtained from data lifetime fits. The resolution function has different parameters for events in which the CP/tag-side vertex is reconstructed with only one B_{CP}/B_{tag} meson track and for events with more. In addition,

there are separate resolution functions for $B^0\overline{B}^0$ and B^+B^- events with the same shape but with different parameters.

$\mathcal{R}_{sig}$ is a convolution of four different resolution functions

$$\mathcal{R}_{sig}(\Delta t) = \int\int\int_{-\infty}^{\infty} \mathcal{R}_{det}^{CP}(\Delta t - \Delta t')\mathcal{R}_{det}^{tag}(\Delta t' - \Delta t'') \cdot \mathcal{R}_{np}(\Delta t'' - \Delta t''')\mathcal{R}_{kin}(\Delta t)\Delta t'\Delta t''\Delta t'''. \quad (4.18)$$

The four contributions to $\mathcal{R}_{sig}(\Delta t)$ are described in the following.

Detector Resolutions $\mathcal{R}_{det}^{CP}$ and $\mathcal{R}_{det}^{tag}$

The B_{CP} vertex detector resolution, $\mathcal{R}_{det}^{CP}$, and the B_{tag} vertex detector resolution, $\mathcal{R}_{det}^{tag}$, describe the smearing of primary tracks originating from the two B mesons. The two resolutions are studied using a special MC simulation in which all short-lived ($\tau < 10^{-9}$ s) secondary particles are forced to decay with zero lifetime at the B meson decay points. Because the resolution of multi-track vertices is better than single-track vertices, they are treated separately. All distributions are symmetric around zero.

The single-track vertex resolution function for both the CP and the tag side is given by a sum of two Gaussians,

$$\mathcal{R}_i^{single}(\delta z_i) \equiv (1 - f_{det}^{tail})G(\delta z_i; S_{det}^{main}\sigma_i) + f_{det}^{tail}G(\delta z_i; S_{det}^{tail}\sigma_i), \;\; i = CP,\, tag, \quad (4.19)$$

where δz_i is defined as the difference between the reconstructed vertex position and its true position, σ_i is the vertex position error, f_{det}^{tail} is the fraction of the tail part, which describes poorly reconstructed tracks, and S_{det}^{main} and S_{det}^{tail} are global scale factors, which are common to all single-track vertices.

For multi-track vertices, the CP- and tag-side vertex resolution functions are described by a single Gaussian,

$$\mathcal{R}_i^{multi}(\delta z_i) \equiv G(\delta z_i; (S_i^0 + S_i^1 h)\sigma_i), \;\; i = CP,\, tag, \quad (4.20)$$

where S_i^0 and S_i^1 are scale factors obtained from the data, which account for the correlation between the vertex quality, h (see Eq. 4.16), and the vertex position error, σ_i.

Tag-Side Smearing Due to Non-Primary Tracks $\mathcal{R}_{np}$

As already mentioned in Section 4.2.4.2, also tracks that do not originate from the B_{tag} decay point are included to the B_{tag} vertex leading to its smearing.

The functional form of this non-prompt component and its parameters are determined from the difference between z_{tag} obtained from a MC in which the tag side is simulated taking into account the secondary decay vertices and z_{tag} determined from the MC in which all short-lived secondary particles are forced to decay with zero lifetime at the B decay point (see the $\mathcal{R}_{det}^{CP}$ and $\mathcal{R}_{det}^{tag}$ description).

The resulting resolution function, $\mathcal{R}_{np}$, is then given by

$$\mathcal{R}_{np}(\delta z_{tag}) \equiv f_\delta\delta(\delta z_{tag}) + (1 - f_\delta)\left[f^+E^+(\delta z_{tag}; \tau_{np}^+) + (1 - f^+)E^-(\delta z_{tag}; \tau_{np}^-)\right], \quad (4.21)$$

where f^+ is the fraction of events with $\delta z_{tag} > 0$. The function consists of two parts. The first component has a fraction f_δ and represents the vertices without non-primary track contamination. It is given by the Dirac δ function. The second part describes the lifetimes of secondary vertices, E^+ and E^-, on both sides of the δz_{tag} distribution,

$$E^+(\delta z_{tag}) \equiv \begin{cases} \frac{1}{\tau_{np}^+} e^{-\delta z_{tag}/\tau_{np}^+} & \text{if} \quad \delta z_{tag} > 0 \\ 0 & \text{if} \quad \delta z_{tag} < 0 \end{cases}, \tag{4.22}$$

$$E^-(\delta z_{tag}) \equiv \begin{cases} 0 & \text{if} \quad \delta z_{tag} > 0 \\ \frac{1}{\tau_{np}^-} e^{-\delta z_{tag}/\tau_{np}^-} & \text{if} \quad \delta z_{tag} < 0 \end{cases}, \tag{4.23}$$

where the effective decay lengths, $\tau_{np}^\pm$, depend on the vertex quality, h_{tag}, because secondary tracks from longer lived particles give a larger distortion of the vertex and its error. For a multi-track $\mathrm{B_{tag}}$ vertex, accounting for the correlation with σ_{np} and h_{tag}, $\tau_{np}^\pm$ are parametrized as

$$\begin{aligned} \tau_{np}^+ &\equiv \tau_0^+ + \tau_1^+ \left[S_{tag}^0 + S_{tag}^1 h_{tag} \right] \sigma_{tag}/c(\beta\gamma) \\ \tau_{np}^- &\equiv \tau_0^- + \tau_1^- \left[S_{tag}^0 + S_{tag}^1 h_{tag} \right] \sigma_{tag}/c(\beta\gamma). \end{aligned} \tag{4.24}$$

For single-track vertices, the vertex quality, h_{tag}, is not defined. Instead, we consider the correlation between the vertex position shift and the z vertex-position error, σ_{tag}^z. Since for single-track vertices the detector resolution, $\mathcal{R}_{det}^{tag}$, is defined as a sum of a main and a tail Gaussian (see Eq. 4.19), we introduce two separate $\mathcal{R}_{np}$, $\mathcal{R}_{np}^{main}$ and $\mathcal{R}_{np}^{tail}$, according to Eq. 4.21. The $\tau_{np}^\pm$ parametrization used is given by

$$\begin{aligned} \tau_{np,main}^\pm &\equiv \tau_0^\pm + \tau_1^\pm S_{np}^{main} \sigma_{tag}/c(\beta\gamma) \\ \tau_{np,tail}^\pm &\equiv \tau_0^\pm + \tau_1^\pm S_{np}^{tail} \sigma_{tag}/c(\beta\gamma). \end{aligned} \tag{4.25}$$

Kinematic Approximation $\mathcal{R}_{kin}$

The proper-time interval calculated as Eq. 4.15 is equal to the true proper-time interval when the CMS motion of the B mesons is neglected. The difference between Δt and the true proper-time interval, $\Delta t_{true} = t_{CP} - t_{tag}$, is calculated from the kinematics of the $\Upsilon(4S)$ two-body decay:

$$x \equiv \Delta t - \Delta t_{true} = \frac{\Delta z}{\langle \beta\gamma \rangle c} = \frac{z_{CP} - z_{\mathrm{tag}}}{\langle \beta\gamma \rangle c} - (t_{CP} - t_{tag}). \tag{4.26}$$

It can be shown that

$$x \approx 0.165 \cos\theta_{\mathrm{B}} (t_{CP} - t_{tag}), \tag{4.27}$$

where $\cos\theta_{\mathrm{B}}$ is the cosine of the angle between the B meson flight direction in the CMS system and the detector z axis.

The resolution function, $\mathcal{R}_{kin}$, that accounts for Δt_{true} can be parametrized in terms of x as

$$\mathcal{R}_{kin}(x)=\begin{cases} E^{+}\left(x-\left[\left(\frac{E_{\rm B}^{CMS}}{m_{\rm B}}-1\right)\Delta t_{true}+\frac{p_{\rm B}^{CMS}\cos\theta_{\rm B}}{\beta m_{\rm B}}|\Delta t_{true}|;\left|\frac{p_{\rm B}^{CMS}\cos\theta_{\rm B}}{\beta m_{\rm B}}\right|\tau_{\rm B}\right]\right) & (\cos\theta_{\rm B}>0) \\ \delta\left(x-\left(\frac{E_{\rm B}^{CMS}}{m_{\rm B}}-1\right)\right) & (\cos\theta_{\rm B}=0)\ , \\ E^{-}\left(x-\left[\left(\frac{E_{\rm B}^{CMS}}{m_{\rm B}}-1\right)\Delta t_{true}+\frac{p_{\rm B}^{CMS}\cos\theta_{\rm B}}{\beta m_{\rm B}}|\Delta t_{true}|;\left|\frac{p_{\rm B}^{CMS}\cos\theta_{\rm B}}{\beta m_{\rm B}}\right|\tau_{\rm B}\right]\right) & (\cos\theta_{\rm B}<0) \end{cases}$$

where $E^{\pm}$ are defined as in Eq. 4.22 and Eq. 4.23.

In addition, Gaussian distributed outlier events with a very broad width are included in the Δt distribution function. Taking into account the detector resolution, the complete Δt resolution function is given by

$$\begin{aligned}\mathcal{P}(\Delta t,q) \;=\; & (1-f_{out})\,\frac{e^{-|\Delta t|/\tau_{\rm B}}}{4\tau_{\rm B}}\Big\{1-q\Delta w+q(1-2w)\times\Big[\mathcal{A}_{CP}\cos\Delta m\Delta t+\mathcal{S}_{CP}\sin\Delta m\Delta t\Big]\Big\} \\ & \otimes\mathcal{R}_{sig}(\Delta t)+f_{out}\,\frac{1}{2}G(\Delta t;0,\sigma_{out}),\end{aligned} \tag{4.28}$$

where f_{out} and σ_{out} are the outlier fraction and width, respectively.

4.2.6.2 Δt Resolution Function for $q\overline{q}$ Events

The background proper-time distribution function consists of a prompt component and a lifetime component with a lifetime τ_{bkg}. The prompt component models the Δt shape for $q\overline{q}$ events, where q is an u, d, c or s quark. In these events, all tracks originate from the same point, which can be described by a Dirac delta function, $\delta(x)$. The second part of the physics component describes the $\mathrm{B\overline{B}}$ combinatorial background events, which can be modeled by an exponential decay function with a lifetime τ_{bkg},

$$\mathcal{P}_{q\overline{q}}(\Delta t,q)=\frac{1}{2}\left[(1-f_{\delta})\frac{e^{-|\Delta t|/\tau_{q\overline{q}}}}{2\tau_{q\overline{q}}}+f_{\delta}\;\delta(\Delta t-\mu_{\delta})\right]\otimes\mathcal{R}_{q\overline{q}}(\Delta t). \tag{4.29}$$

The resolution function, $\mathcal{R}_{q\overline{q}}$, is parametrized by

$$\mathcal{R}_{q\overline{q}}(\Delta t)=(1-f^{tail})G(\Delta t;\mu_{mean},S^{main}\sigma)+f^{tail}G(\Delta t;\mu_{mean},S^{main}S^{tail}\sigma), \tag{4.30}$$

where $\sigma=\sqrt{\sigma_{CP}^2+\sigma_{tag}^2}$ is the quadratic sum of the vertex errors obtained from the reconstruction. The rest of the parameters, $\tau_{q\overline{q}}$, μ_{mean}, S^{main}, S^{tail} and f^{tail}, are obtained from a fit to data outside the signal region, in the sideband.

4.2.7 $q\overline{q}$ Background Suppression

As already mentioned in Section 2.1, around three quarters of all events produced at the $\Upsilon(4\mathrm{S})$ resonance energy are $\mathrm{e^+e^-}\to q\overline{q}$ ($q=\mathrm{u,d,c,s}$) transitions. Their final states usually consist of

two or sometimes more jets, which produce light mesons with high momenta. These mimic the kinematic behaviour of decays such as B $\to \omega$K and are not suppressed neither by the hadronic skim nor by our selection procedure. As a consequence, over 99% of all reconstructed events in data are $q\bar{q}$ background. However, it is possible to reduce the fraction of continuum events by using event-shape variables.

This is illustrated in Figure 4.10. Due to their low mass, the jets have high momenta in opposite directions. The two B mesons are also produced back to back but as their total mass is almost equal to the total energy of the e^+e^- beam, the two particles are almost at rest in the center of mass system. Thus, the momenta of their daughter particles in the CMS are uniformly distributed in all directions. To suppress the continuum, we use a Fisher discriminant [77] based on modified Fox-Wolfram moments [78] and the cosine of the B meson flight direction polar angle $\cos(\theta_B)$, which are combined to a common likelihood ratio. A brief summary of this procedure will be given in the following.

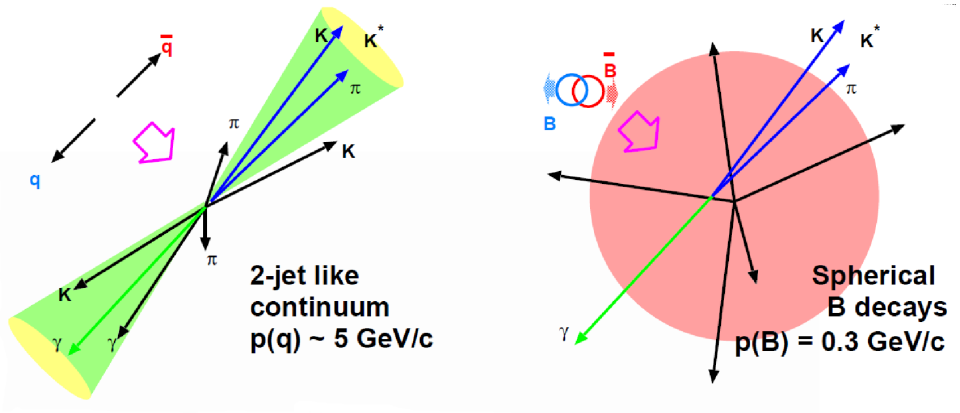

Figure 4.10: Event shape for jet-like (right) and B$\overline{\text{B}}$ (left) events [79].

4.2.7.1 Fisher Discriminant Method

The Fisher linear discriminant is a statistical method aiming to find a linear combination of variables which separate two or more classes of events. The method uses two or more sets of events belonging to exactly one of the classes. It is known what class they are a part of. Using a set of variables, linear borders between the two classes are found. This is referred to as "training". The borders are later applied to a set of event classes with the objective of assigning each of them to one of the classes. In this analysis, the classes are B$\overline{\text{B}}$ (signal) and $q\bar{q}$ and the corresponding sets of events used in the training belong to the signal MC and the sideband data samples. The variables used for separation are modified Fox-Wolfram moments, which will be presented in the next section.

The borders between the two classes are defined by the Fisher coefficients, $\vec{w}$, which maximize the separation $J(\vec{w})$ between the classes. In the case of two classes with variable means $\vec{\mu}_{1,2}$ and covariances $S_{1,2}$, $J(\vec{w})$ is given by the ratio of the variance between the classes, σ_B^2, to the variance within the classes, σ_W^2,

$$J(\vec{w}) = \frac{\sigma_B^2}{\sigma_W^2} = \frac{\vec{w} \cdot (\vec{\mu_2} - \vec{\mu_1})^2}{\vec{w}^T (S_1 + S_2) \vec{w}}. \tag{4.31}$$

4.2.7.2 Fox-Wolfram Moments

The Fox-Wolfram Moments (FWM) were developed for the analysis of event shapes in e^+e^- colliders. They FWM are a set of rotation-invariant observables, given by

$$H_l = \sum_{i,j} \frac{|\overrightarrow{p}_i||\overrightarrow{p}_j|}{s} P_l(\cos\phi_{ij}), \tag{4.32}$$

where $\sqrt{s}$ is the CMS beam energy, $P_l(\cos\phi)$ are the Legendre polynomials and i, j denote two different particles in an event with the angle ϕ_{ij} between the directions of their momenta, $\overrightarrow{p}_i$ and $\overrightarrow{p}_j$. Since ϕ_{ij} is a relative angle, the value of H_l is independent on the coordinate system it is calculated in.

H_l can also be written as

$$H_l = (h_l^{ss} + h_l^{so} + h_l^{oo}) \cdot s, \tag{4.33}$$

with

$$\begin{aligned} h_l^{ss} &= \sum_{i,\bar{i}} (\overrightarrow{p}_i \cdot \overrightarrow{p}_{\bar{i}})\ P_l(\cos\phi_{i\bar{i}}), \\ h_l^{so} &= \sum_{i,k} (\overrightarrow{p}_i \cdot \overrightarrow{p}_k)\ P_l(\cos\phi_{ik}), \\ h_l^{oo} &= \sum_{k,\bar{k}} (\overrightarrow{p}_k \cdot \overrightarrow{p}_{\bar{k}})\ P_l(\cos\phi_{k\bar{k}}), \end{aligned} \tag{4.34}$$

where $i(\bar{i})$ denotes the particles from the B_{CP} candidate and $k(\bar{k})$ – all remaining ones. h_l^{ss} contains information only about B_{CP}; h_l^{so} – about the momentum direction of the B_{CP} with respect to the tag-side; the even h_l^{oo} terms quantify the sphericity of the tag side is and the odd ones contain the B_{tag} kinematics.

On can create a six-variable Fisher discriminant, called the Super Fox-Wolfram (SFW), defined as

$$SFW = \sum_{l=1}^{2} \alpha_{2l} \left(\frac{h_{2l}^{so}}{h_0^{oo}}\right) + \sum_{l=1}^{4} \beta_l \left(\frac{h_l^{oo}}{h_0^{oo}}\right), \tag{4.35}$$

where α and β are the Fisher coefficients. Note that h_l^{ss} is not used, since it is channel dependent and does not allow for a general Fisher discriminant definition.

The separation provided by SFW deteriorates significantly if there are missing particles and with this missing mass in the event. To account for this effect, the Kakuno super Fox-Wolfram moments (KSFW) were introduced [80]. These are derived from SFW and are defined as

$$KSFW = \sum_{l=1}^{4} R_l^{so} + \sum_{l=1}^{4} R_l^{oo} + \gamma \sum_{n=1}^{N_t} |(P_t)_n|, \tag{4.36}$$

where the individual terms have the following content:

- R_l^{so} consists of three parts – "charged", "neutral" and "missing". The first two depend on the charge and momenta of all reconstructed particles, while the "missing" component is a psedo-track containing the missing mass and energy of the event. Each momentum has a weight, which is a Fisher coefficient. In total, there are 11 of them in R_l^{so}.

- R_l^{oo} contains information about the charge and momenta of the tag-side particles. It introduces five Fisher coefficients.
- $\sum_{n=1}^{N_t} |(P_t)_n|$ is the sum of the transverse momenta, P_t, of all particles from both the CP side and the tag side and N_t is their number.

In total, KSFW provide $11 + 5 + 1 = 17$ Fisher coefficients.

4.2.7.3 B Flight Direction $\cos\theta_B$

The cosine of the B meson flight direction polar angle, $\cos\theta_B$, is given by

$$\cos\theta_B = \frac{p_z^{\mathrm{B}}}{|\overrightarrow{p}^{\mathrm{B}}|}, \tag{4.37}$$

where $\overrightarrow{p}^{\mathrm{B}}$ and p_z are the B momentum vector and its z-component in the CMS. The $\cos\theta_B$ shapes for signal and continuum are given in Figure 4.11. To conserve the $\Upsilon(4S)$ spin, which is parallel to the z axis, the spinless B mesons have a momentum that is perpendicular to the z axis. Thus, for $B\overline{B}$ events, $\cos\theta_B$ follows a $1 - \cos\theta_B{}^2$ distribution. For continuum events, $\cos\theta_B$ is distributed uniformly, since there is no angular momentum constraint.

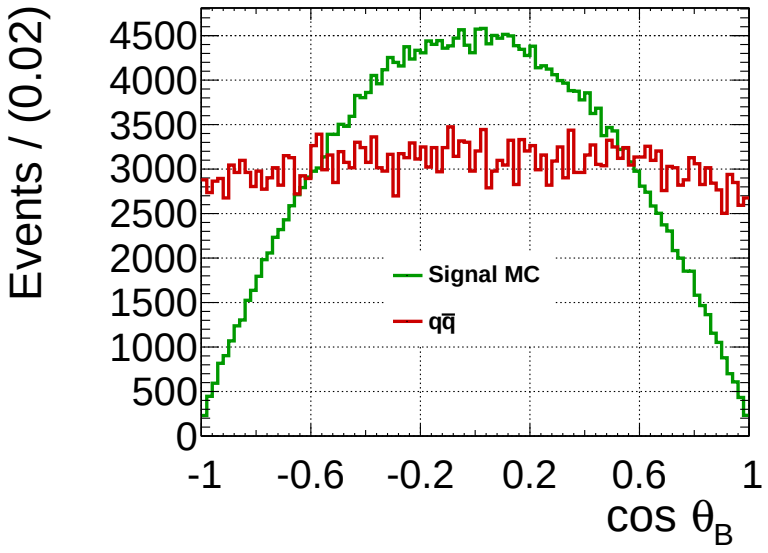

Figure 4.11: $\cos\theta_{\mathrm{B}}$ distribution for $\mathrm{B}^0 \to \omega \mathrm{K}^0_{\mathrm{S}}$ signal MC in green and for continuum in red.

4.2.8 Likelihood Ratio $\mathcal{L}_{B\overline{B}/q\overline{q}}$ and Its Transformation to $\mathcal{F}_{B\overline{B}/q\overline{q}}$

The output of the Fisher discriminant training is a likelihood probability $\mathcal{P}_{\mathrm{B}\overline{\mathrm{B}}(q\overline{q})}(KSFW)$. To further enhance its separation power, it is combined with the $\cos\theta_{\mathrm{B}}$ to a $B\overline{B}/q\overline{q}$ probability, $\mathcal{P}_{\mathrm{B}\overline{\mathrm{B}}(q\overline{q})}(\cos\theta_{\mathrm{B}})$,

$$\mathcal{P}_{\mathrm{B}\overline{\mathrm{B}}(q\overline{q})} = \mathcal{P}_{\mathrm{B}\overline{\mathrm{B}}(q\overline{q})}(KSFW) \times \mathcal{P}_{\mathrm{B}\overline{\mathrm{B}}(q\overline{q})}(\cos\theta_{\mathrm{B}}). \tag{4.38}$$

Using this, a likelihood ratio, $\mathcal{L}_{\mathrm{B\overline{B}}/q\overline{q}}$, is obtained, given by

$$\mathcal{L}_{\mathrm{B\overline{B}}/q\overline{q}} = \frac{\mathcal{P}_{\mathrm{B\overline{B}}}}{\mathcal{P}_{\mathrm{B\overline{B}}} + \mathcal{P}_{q\overline{q}}}. \tag{4.39}$$

The $\mathcal{L}_{\mathrm{B\overline{B}}/q\overline{q}}$ distribution for signal and $q\overline{q}$ background is shown in Fig. 4.12. It ranges between zero and unity, where zero means certitude that an event is a $q\overline{q}$ pair and one – that it is a $\mathrm{B\overline{B}}$ pair.

We apply an arbitrary loose cut on this variable,

$$0.2 \leq \mathcal{L}_{\mathrm{B\overline{B}}/q\overline{q}} \leq 1, \tag{4.40}$$

which reduces the $q\overline{q}$ background by 62% and allows us to retain 94% of the signal events. $\mathcal{L}_{\mathrm{B\overline{B}}/q\overline{q}}$ is one of the variables we use in the final fit to the data to extract the signal yield. In order to make $\mathcal{L}_{\mathrm{B\overline{B}}/q\overline{q}}$ easier to parametrize and later to be able to account for the shape differences between data and MC, we transform it into a Gaussian-like distribution,

$$\mathcal{F}_{\mathrm{B\overline{B}}/q\overline{q}} = \log \frac{\mathcal{L}_{\mathrm{B\overline{B}}/q\overline{q}} - 0.2}{1 - \mathcal{L}_{\mathrm{B\overline{B}}/q\overline{q}}}. \tag{4.41}$$

The $\mathcal{F}_{\mathrm{B\overline{B}}/q\overline{q}}$ distribution for signal and continuum is given in Figure 4.12.

4.2.9 ω Helicity

The consine of the helicity angle of the ω meson, $\cos\theta_{Hel}$, is used as a fit variable in the event model. $\cos\theta_{Hel}$ is defined as the cosine of the angle between the ω flight direction and the normal to the plane in which the three pions decay, as shown in Figure. 4.13. Its disrtribution allows for additional discrimination against continuum.

The decay amplitude of $\mathrm{B} \to \omega\mathrm{K}$ decays with $\omega \to \pi^+\pi^-\pi^0$ is given by

$$\begin{aligned} A(\mathrm{B} \to \omega[\pi^+\pi^-\pi^0]\mathrm{K}) &= A(\omega \to \pi^+\pi^-\pi^0) \cdot A(\mathrm{B} \to \omega\mathrm{K}) \\ &\propto i\epsilon_{\mu\nu\alpha\beta} p^{\beta}_{\pi^+} p^{\alpha}_{\pi^-} p^{\nu}_{\pi^0} \sum_{\lambda} \epsilon^{\mu,\lambda}(p_\omega, m_\omega) \epsilon^{*\delta,\lambda}(p_\omega, m_\omega) p_{\mathrm{K},\delta} \\ &= i\epsilon_{\mu\nu\alpha\beta} p^{\beta}_{\pi^+} p^{\alpha}_{\pi^-} p^{\nu}_{\pi^0} \left(-g^{\mu\delta} + \frac{p^{\mu}_{\omega} p^{\delta}_{\omega}}{m^2_{\omega}} \right) p_{\mathrm{K},\delta} \end{aligned} \tag{4.42}$$

where p_{π^+}, p_{π^-}, p_{π^0}, p_ω and p_K are the π^+, π^-, π^0, ω and K four-momentum vectors; $\epsilon_\omega(p_\omega, m_\omega)$ is the ω polarization vector; $\epsilon_{\mu\nu\alpha\beta}$ is the Levi-Civita anti-symmetric tensor; $\lambda = 0; \pm 1$ denotes the possible intermediate ω polarization states, which are unobservable. To get to the last step of the equation, we use the spin-1 projection operator. Evaluating the square of the amplitude in the ω system of reference, we obtain

$$\left| A(\mathrm{B} \to \omega[\pi^+\pi^-\pi^0]\mathrm{K}) \right|^2 \propto 1 - \cos\theta_{Hel}{}^2. \tag{4.43}$$

It is obvious from this relation that ω mesons originating from $\mathrm{B} \to \omega\mathrm{K}$ decays have a spin which tends to be parallel or anti-parallel to the flight direction of the particle in the B meson reference frame. The ω decays into three spinless pions and must conserve angular momentum,

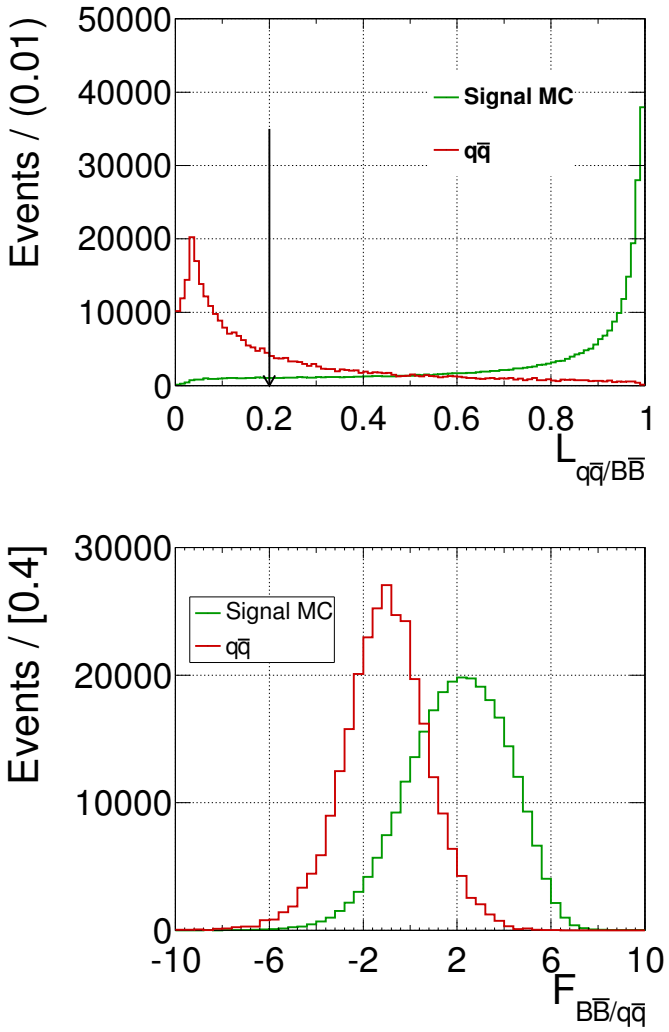

Figure 4.12: $\mathcal{L}_{B\overline{B}/q\bar{q}}$ (up) and $\mathcal{F}_{B\overline{B}/q\bar{q}}$ (down) for signal in green and continuum in red.

which is why the normal of the decay plane of the three pions must be along the flight direction as their mother particle. Thus, the signal $\cos\theta_{Hel}$ distribution peaks at -1 and 1. For continuum, the $\cos\theta_{Hel}$ distribution is Gaussian-like, since the ω candidates are only partially associated with real ω decays and consist mostly of random track combinations. The two distributions are shown in Figure 4.14.

4.2.10 Reconstruction Efficiency and Signal Purity

We study the performance of the reconstruction algorithm using the signal MC sample. Two important characteristics are the signal reconstruction purity, p_{Sig}, given by

$$p_{\mathrm{Sig}} = \frac{\#\text{correctly reconstructed B}}{\#\text{reconstructed B}} \tag{4.44}$$

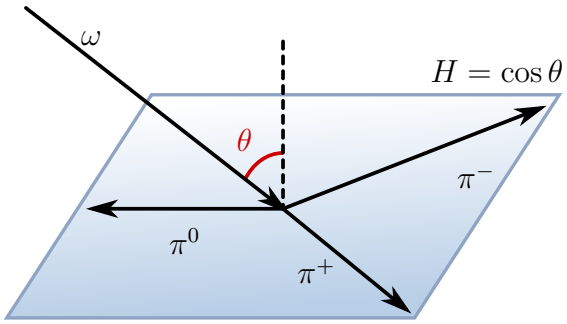

Figure 4.13: Definition of the ω helicity angle, $\cos\theta_{Hel}$.

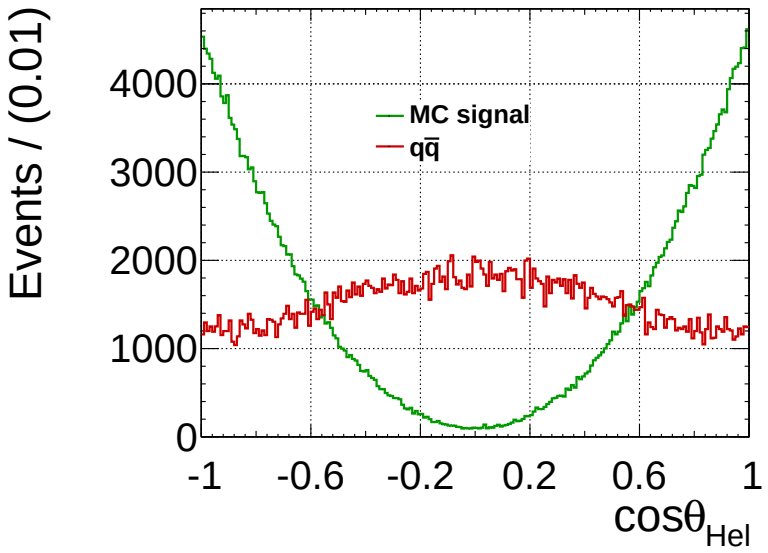

Figure 4.14: The ω helicity angle, $\cos\theta_{Hel}$, distribution for signal MC (green) and $q\overline{q}$ background (red).

and the signal reconstruction efficiency ϵ_{Sig}, given by

$$\epsilon_{Sig} = \frac{\#\text{correctly reconstructed B}}{\#\text{generated events}}. \tag{4.45}$$

The reconstruction efficiency shows what percentage of all $B \to \omega K$ events pass our selection criteria and is an important input variable in the branching fraction calculation (see Eq. 3.4). From the reconstruction purity we extract the relative fraction of the misreconstructed signal events, which is fixed in the event model (see the next section). The signal purity for both decay channels and SVD convigurations is between 98.1% and 98.2%. The signal effeiciencies are summarized in Table 4.4.

Decay	Eff. SVD1 ($\epsilon^{1,d}$)	Eff. SVD2 ($\epsilon^{2,d}$)
$B^0 \to \omega K^0_S$	0.1136 ± 0.0003	0.1454 ± 0.0004
$B^\pm \to \omega K^\pm$	0.1828 ± 0.0004	0.2195 ± 0.0005

Table 4.4: Summary of the detection efficiencies (eff.) for $B^0 \to \omega K^0_S$ and $B^\pm \to \omega K^\pm$. The values are obtained from signal MC.

4.3 Event Model

The two branching fractions

$$\mathcal{B}(B^0 \to \omega K^0_S) \qquad \mathcal{B}(B^\pm \to \omega K^\pm) \tag{4.46}$$

and three CP violation parameters 4.1

$$\mathcal{A}_{\omega K^0_S} \qquad \mathcal{S}_{\omega K^0_S} \qquad \mathcal{A}_{\omega K^\pm} \tag{4.47}$$

are extracted from a sequence of seven-dimensional unbinned extended maximum likelihood fits to

- -0.15 GeV $\leq \Delta E \leq 0.1$ GeV
- 5.25 GeV$/c^2 \leq M_{\rm bc} \leq 5.30$ GeV$/c^2$
- $-10 \leq \mathcal{F}_{B\overline{B}/q\overline{q}} \leq 10$
- 0.73 GeV$/c^2 \leq M_{3\pi} \leq 0.93$ GeV$/c^2$ – mass of the ω candidates
- $-1 \leq \cos\theta_{Hel} \leq 1$
- 70 ps $\leq \Delta t \leq -70$ ps
- $q = \pm 1$,

performed simultaneously on the two data samples, d. Since the resolution of all fit variables except $\cos\theta_{Hel}$ and q depends on the SVD configuration, s, we subdivide the events depending on whether they were recorded with SVD1 or SVD2. To account for a correlation between the flavour-tag quality, r, and the Fisher discriminant, the samples are further divided into seven r-bins (see Table 4.3) with indices $l = 0..6$.

In the first fit, the two branching fractions and the CP parameters of the neutral mode are determined. In two further fits, also simultaneous in $B^0 \to \omega K^0_S$ and $B^\pm \to \omega K^\pm$, the charged data sample is divided into two subsambles depending on the B meson charge. From these two independent fits, two signal yields, $N(B^- \to \omega K^-)$ and $N(B^+ \to \omega K^+)$, are extracted in order to determine $\mathcal{A}_{\omega K^\pm}$ using Eq. 1.62 and 4.6,

$$\begin{aligned} a_{CP}(B^\pm \to \omega K^\pm) \equiv \mathcal{A}_{\omega K^\pm} &= \frac{\Gamma(B^- \to \omega K^-) - \Gamma(B^+ \to \omega K^+)}{\Gamma(B^- \to \omega K^-) + \Gamma(B^+ \to \omega K^+)} \\ &= \frac{N(B^- \to \omega K^-) - N(B^+ \to \omega K^+)}{N(B^- \to \omega K^-) + N(B^+ \to \omega K^+)}. \end{aligned} \tag{4.48}$$

The following categories are considered in the event model:

- correctly reconstructed signal
- misreconstructed signal
- continuum
- neutral charmed B meson decays
- charged charmed B meson decays
- neutral charmless B meson decays
- charged charmless B meson decays
- charmed peaking B meson decays
- charmless peaking B meson decays ($B^{\pm} \to \omega K^{\pm}$ only).

Over 95% of all reconstructed data events in both modes are a part of the continuum background. As shown in Table 4.6, the largest contribution to the B decay background is due to neutral charmless decays for $B^0 \to \omega K^0_S$ and to charged charmless decays for $B^{\pm} \to \omega K^{\pm}$.

Each of these categories has its own model, which is different for $B^0 \to \omega K^0_S$ and $B^{\pm} \to \omega K^{\pm}$. Unless otherwise stated, the probability density function for each category is taken as the product of PDFs of each variable

$$\begin{aligned}\mathcal{P}^{l,s,d}(\Delta E, M_{\rm bc}, \mathcal{F}_{B\overline{B}/q\overline{q}}, M_{3\pi}, \cos\theta_{Hel}, \Delta t, q) \equiv \mathcal{P}^{l,s,d}(\Delta E) \times \mathcal{P}^{l,s,d}(M_{\rm bc}) \times \\ \mathcal{P}^{l,s,d}(\mathcal{F}_{B\overline{B}/q\overline{q}}) \times \mathcal{P}^{l,s,d}(M_{3\pi}) \times \mathcal{P}^{l,s,d}(\cos\theta_{Hel}) \times \mathcal{P}^{l,s,d}(\Delta t, q)\end{aligned} \tag{4.49}$$

in each l, s, d bin as most correlations between the fit observables are negligible. We describe these fit models for each category explicitly in the following sections.

The CP parameters are free in the fit and a part of the Δt distribution. The branching fractions are obtained from the $B^0 \to \omega K^0_S$ and $B^{\pm} \to \omega K^{\pm}$ signal yields, which are also free parameters.

4.3.1 Correctly Reconstructed Signal Events

The correctly reconstructed signal shapes are determined from signal MC events, in which the π^+ and π^- forming the ω candidate are associated with the π^+ and π^- tracks that belong to the generated B_{CP} (see Section 4.2.3.5). In ΔE, $M_{\rm bc}$, $\mathcal{F}_{B\overline{B}/q\overline{q}}$and $M_{3\pi}$, we use the same PDF for both decay channels, sharing the same parameters between them, wherever possible. This is done so that in the fit to the data common correction factors for these observables can be extracted as will be explained in the following. All signal fit projections are shown in Figure 4.15 and in Figure 4.16.

The PDF for ΔE is the sum of three Gaussian functions A.1 and a linear function (1st order Chebyshev polynomial, see Appendix A.6),

$$\begin{aligned}\mathcal{P}^{l,s,d}_{Sig}(\Delta E) \equiv\ & f^s_1 G(\Delta E;\, \mu^{s,d}_1 + \mu^s_C,\, \sigma^{s,d}_1 \sigma^s_C) \\ & + f^s_2 G(\Delta E;\, \mu^s_2 + \mu^{s,d}_1 + \mu^s_C,\, \sigma^s_2 \sigma^{s,d}_1 \sigma^s_C) \\ & + f^s_2 G(\Delta E;\, \mu^s_3 + \mu^s_2 + \mu^{s,d}_1 + \mu^s_C,\, \sigma^s_3 \sigma^s_2 \sigma^{s,d}_1 \sigma^s_C) \\ & + (1 - f^s_1 - f^s_2 - f^s_3)(1 + c^s \Delta E),\end{aligned} \tag{4.50}$$

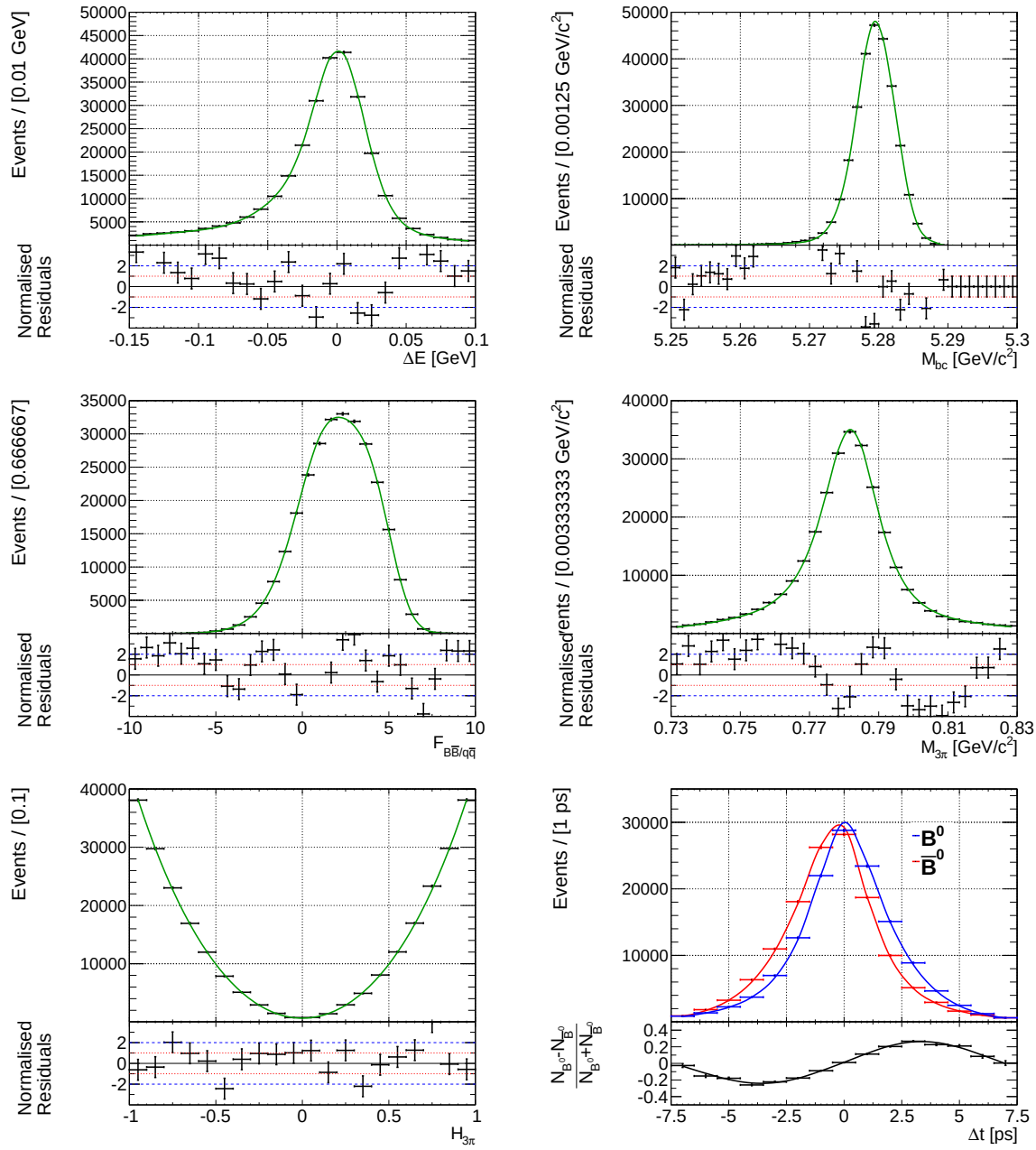

Figure 4.15: Projections of the fit to the $B^0 \to \omega K^0_S$ signal MC for (from top left to right bottom) ΔE, $M_{\rm bc}$, $\mathcal{F}_{B\overline{B}/q\overline{q}}$, $M_{3\pi}$, $\cos\theta_{Hel}$ and Δt. The events were produced assuming $\mathcal{S}_{CP} = 0.689$ and thus the Δt PDFs for $q = \pm 1$ are shifted in respect to each other.

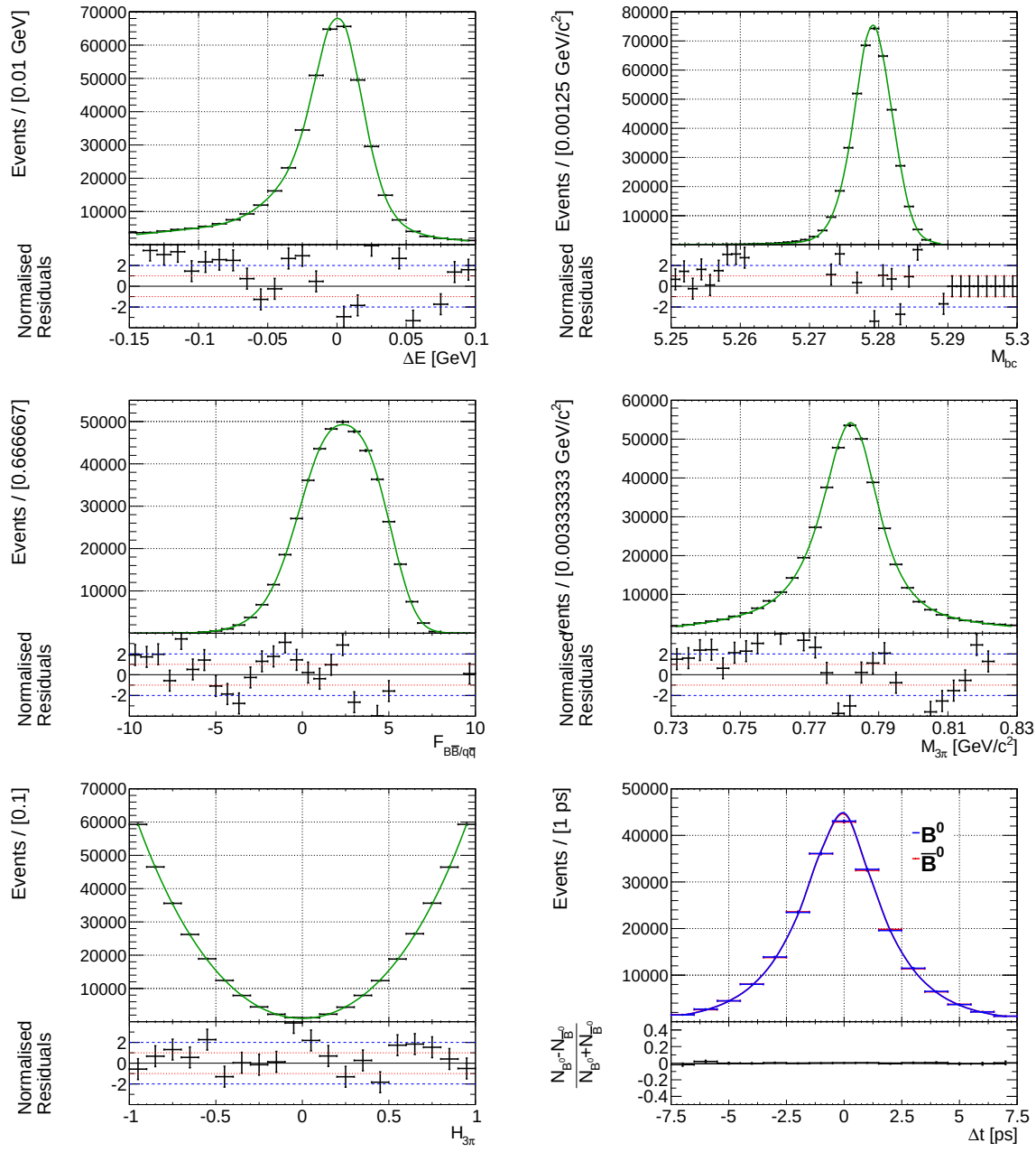

Figure 4.16: Projections of the fit to the $B^{\pm} \to \omega K^{\pm}$ signal MC for (from top left to right bottom) ΔE, M_{bc}, $\mathcal{F}_{\mathrm{B\overline{B}}/q\overline{q}}$, $M_{3\pi}$, $\cos\theta_{Hel}$ and Δt. The PDF with a B^0 and $\overline{B}^0$ tag overlap, since equal amounts of B^+ and B^- were generated.

where the two tail Gaussians are parametrized relative to the main Gaussian. All parameters but the mean and width of the main Gaussian are shared between the two samples. The PDF also incorporates calibration parameters, μ_C^s and σ_C^s, which correct for the difference between data and MC simulation. These parameters calibrate the mean and width of the main Gaussian component. They are fixed to zero and unity, respectively, in the fit to determine the signal model from MC, but are free in the fit to the data. The most accurate way would be to extract them separately from the data for each of the two decay modes. However, because of the low signal yield of the neutral mode, we determine the calibration factors in a simultaneous fit of two decay channels. We avoid extracting the correction parameters from a separate control sample fit. Thus, to first order, we do not need to consider the related systematic uncertainty that arises from the control sample difference between data and MC. Instead, the uncertainty is incorporated in the statistical error of the fit. Because of our definition of correctly reconstructed events, the linear part of the PDF is necessary to describe events where π^0 or K^0_S are incorrectly reconstructed.

ΔE is found to be correlated with M_bc and $M_{3\pi}$. Since the correlation between M_bc and $M_{3\pi}$ is negligible, the total probability of these three observables can be represented by

$$\mathcal{P}_{Sig}^{l,s,d}(\Delta E, M_\mathrm{bc}, M_{3\pi}) = \mathcal{P}_{Sig}^{l,s,d}(M_\mathrm{bc}|\Delta E) \times \mathcal{P}_{Sig}^{l,s,d}(M_{3\pi}|\Delta E) \times \mathcal{P}_{Sig}^{l,s,d}(\Delta E). \tag{4.51}$$

The PDF for M_bc is taken to be the sum of three Gaussians and an ARGUS function A.4. The ARGUS function represents events analogous to those of the linear function models in ΔE. To model the correlation of 4-5% between ΔE and M_bc (see Figure 4.17), the dependency of the main mean and relative fraction of the main Gaussian leads to the parametrization

$$\begin{aligned}\mathcal{P}_{Sig}^{l,s,d}(M_\mathrm{bc}|\Delta E) \equiv\ & (f_1^{s,d} + \alpha^{s,d}|\Delta E|)G(M_\mathrm{bc};\, \mu_1^{s,d} + \mu_C^s + \beta^{s,d}\Delta E,\, \sigma_1^{s,d}\sigma_C^s) \\ & + f_2^{s,d}G(M_\mathrm{bc};\, \mu_2^{s,d} + \mu_1^{s,d} + \mu_C^s + \beta^{s,d}\Delta E,\, \sigma_2^{s,d}\sigma_1^{s,d}\sigma_C^s) \\ & + f_3^{s,d}G(M_\mathrm{bc};\, \mu_3^{s,d} + \mu_2^{s,d} + \mu_1^{s,d} + \mu_C^s + \beta^{s,d}\Delta E,\, \sigma_3^{s,d}\sigma_2^{s,d}\sigma_1^{s,d}\sigma_C^s) \\ & + (1 - [f_1^{s,d} + \alpha^{s,d}|\Delta E|] - f_2^{s,d} - f_3^{s,d})\mathrm{ARGUS}(M_\mathrm{bc}; a^{s,d}),\end{aligned} \tag{4.52}$$

where $\alpha^{s,d}$ and $\beta^{s,d}$ represent the additional correlation parameters and $a^{s,d}$ is the shape parameter of the ARGUS function. In M_bc, only the correction factors between the two samples are shared. M_bc fit projections in slices of ΔE are shown in Figure 4.19 and in Figure 4.20. A clear width and mean dependency on the ΔE region is to be seen. The parametrization we choose describes the inner parts of ΔE the best, where also the most signal events are expected. Although the fit has obvious imperfections, we find the model bias to be small compared to other major systematic uncertainties, as it will be shown further in this thesis. As in ΔE, only the shared calibration parameters are free in the fit to the data.

The $\mathcal{F}_{\mathrm{B\overline{B}}/q\overline{q}}$ PDF is taken to be the sum of three Gaussians in each flavour-tag bin, l,

$$\begin{aligned}\mathcal{P}_{Sig}^{l,s,d}(\mathcal{F}_{\mathrm{B\overline{B}}/q\overline{q}}) \equiv\ & f_1^{l,s,d}G(\mathcal{F}_{\mathrm{B\overline{B}}/q\overline{q}};\, \mu_1^{l,s,d} + \mu_C^{l,s},\, \sigma_1^{l,s,d}\sigma_C^{l,s}) \\ & + f_2^{l,s,d}G(\mathcal{F}_{\mathrm{B\overline{B}}/q\overline{q}};\, \mu_2^{l,s,d} + \mu_1^{l,s,d} + \mu_C^{l,s},\, \sigma_2^{l,s,d}\sigma_1^{l,s,d}\sigma_C^{l,s}) \\ & + f_3^{s,d}G(\mathcal{F}_{\mathrm{B\overline{B}}/q\overline{q}};\, \mu_3^{l,s,d} + \mu_2^{l,s,d} + \mu_1^{l,s,d} + \mu_C^{l,s},\, \sigma_3^{l,s,d}\sigma_2^{l,s,d}\sigma_1^{l,s,d}\sigma_C^{l,s}).\end{aligned} \tag{4.53}$$

The shared calibration parameters depend on l and are free in the fit to the data. Projections of the fit in each r-bin, l, are shown in Figure 4.21 and in Figure 4.22. We observe a clear

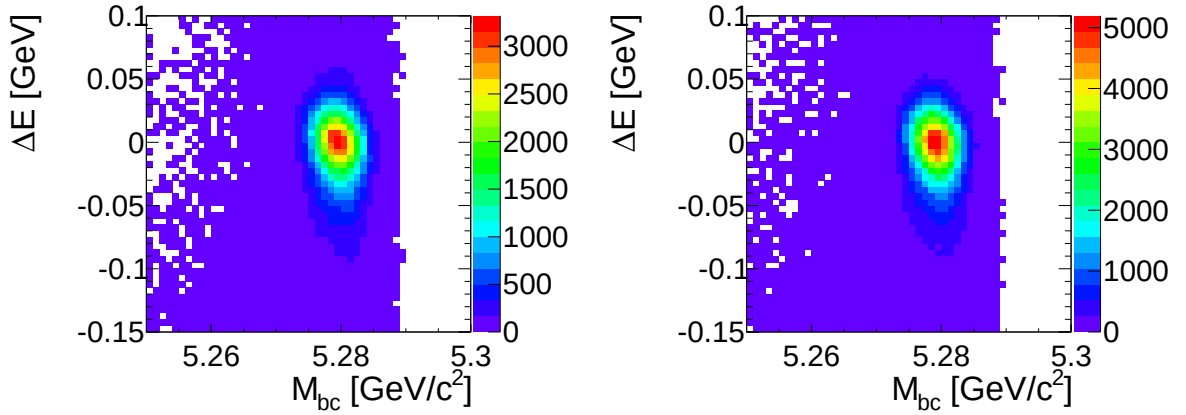

Figure 4.17: Correlation of 4-5% between ΔE and $M_{\rm bc}$ in signal MC for $\mathrm{B}^0 \to \omega \mathrm{K}^0_{\mathrm{S}}$ (left) and $\mathrm{B}^\pm \to \omega \mathrm{K}^\pm$ (right).

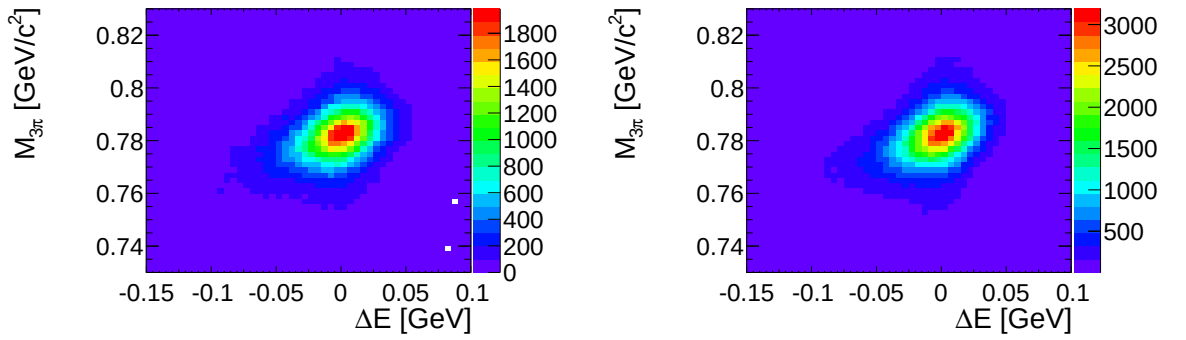

Figure 4.18: Correlation of 27% between ΔE and $M_{3\pi}$ in signal MC for $\mathrm{B}^0 \to \omega \mathrm{K}^0_{\mathrm{S}}$ (left) and $\mathrm{B}^\pm \to \omega \mathrm{K}^\pm$ (right).

correlation between the $\mathcal{F}_{\mathrm{B\overline{B}}/q\overline{q}}$ shape and the r-bin. It is due to a dependency between the missing mass in an event (see Section 4.2.7.2) and its flavour-tag quality, r.

The $M_{3\pi}$ PDF also consists of the sum of three Gaussians, where a correlation of 27% (see Figure 4.18) between ΔE and $M_{3\pi}$ is considered as

$$\begin{aligned}\mathcal{P}^{l,s,d}_{Sig}(M_{3\pi}|\,\Delta E) \;\equiv\; & f_1^{s,d} G(M_{3\pi};\, \mu_1^{s,d} + \mu_C^s + \alpha^{s,d}\Delta E,\, \sigma_1^{s,d}\sigma_C^s + \beta^{s,d}\Delta E^2) \\ & + f_2^{s,d} G(M_{3\pi};\, \mu_2^s + \mu_1^{s,d} + \mu_C^s + \alpha^{s,d}\Delta E,\, \sigma_2^s[\sigma_1^{s,d}\sigma_C^s + \beta^{s,d}\Delta E^2]) \\ & + (1 - f_1^{s,d} - f_2^{s,d}) G(M_{3\pi}; \mu_3^{s,d} + \mu_2^s + \mu_1^{s,d} + \mu_C^s + \alpha^{s,d}\Delta E, \\ & \qquad \sigma_3^{s,d}\sigma_2^s[\sigma_1^{s,d}\sigma_C^s + \beta^{s,d}\Delta E^2]), \end{aligned} \tag{4.54}$$

where $\alpha^{s,d}$ and $\beta^{s,d}$ are the correlation parameters. In $M_{3\pi}$, the correction factors and the mean and width of the second Gaussian are shared between the two decay channels. $M_{3\pi}$ fit projections in slices of ΔE are shown in Figure 4.23 and in Figure 4.24.

The $\cos\theta_{Hel}$ shape is modeled with the sum of symmetric Chebyshev polynomials, C_i (see

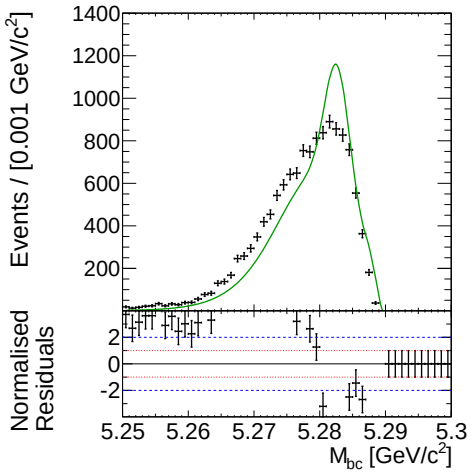

-0.15 GeV $\leq \Delta$E ≤ -0.10 GeV

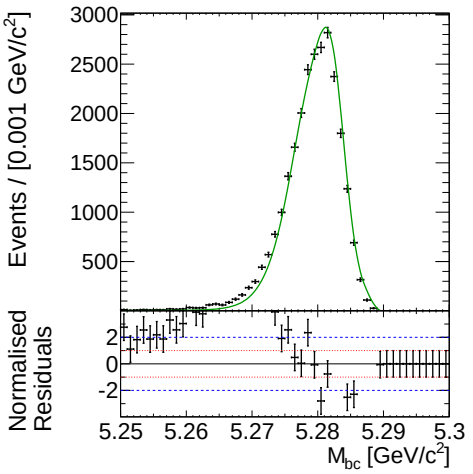

-0.10 GeV $\leq \Delta$E ≤ -0.05 GeV

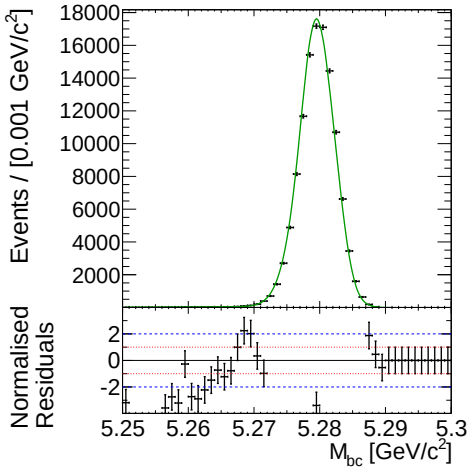

-0.05 GeV $\leq \Delta$E ≤ 0.00 GeV

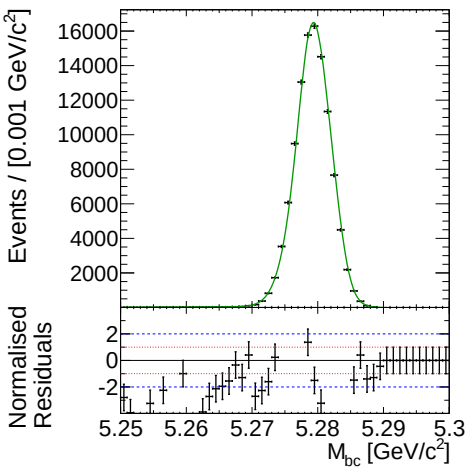

0.00 GeV $\leq \Delta$E $\leq$ 0.05 GeV

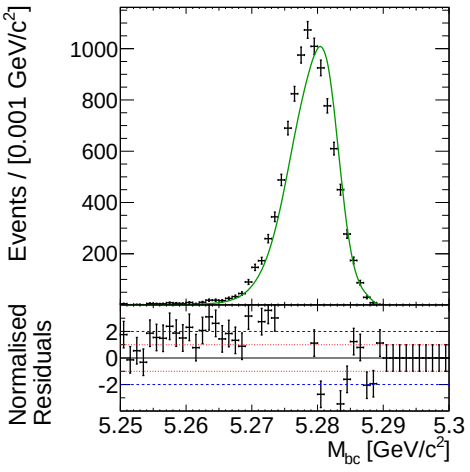

0.05 GeV $\leq \Delta$E $\leq$ 0.10 GeV

Figure 4.19: $M_{\rm bc}$ projections of the $B^0 \to \omega K^0_S$ fit in each of the regions of ΔE.

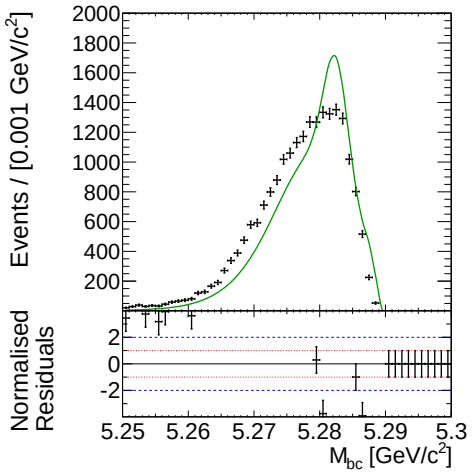

-0.15 GeV $\leq \Delta$E ≤ -0.10 GeV

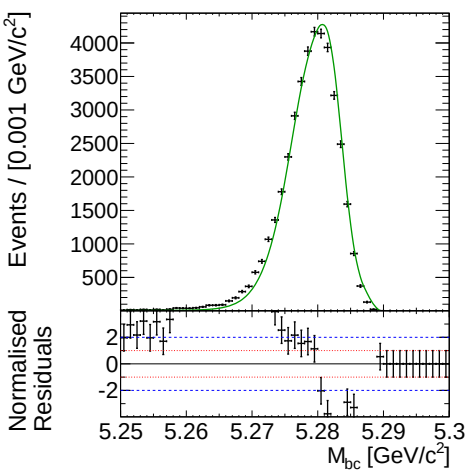

-0.10 GeV $\leq \Delta$E ≤ -0.05 GeV

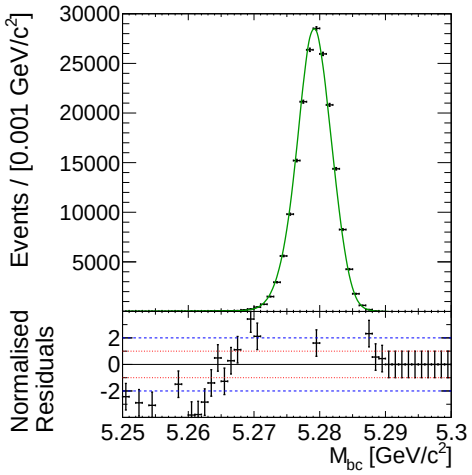

-0.05 GeV $\leq \Delta$E ≤ 0.00 GeV

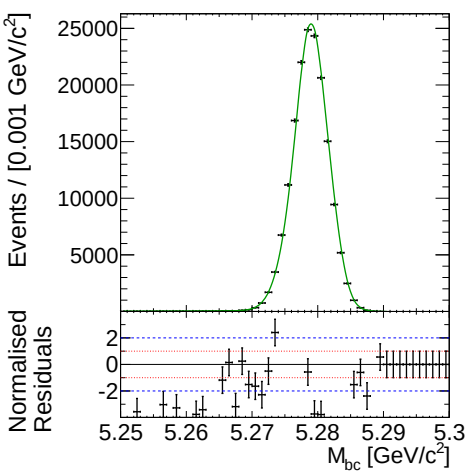

0.00 GeV $\leq \Delta$E ≤ 0.05 GeV

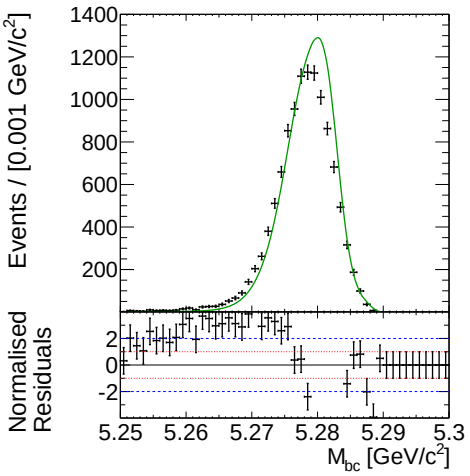

0.05 GeV $\leq \Delta$E ≤ 0.10 GeV

Figure 4.20: $M_{\rm bc}$ projections of the $\mathrm{B}^{\pm} \to \omega \mathrm{K}^{\pm}$ fit in each of the regions of ΔE.

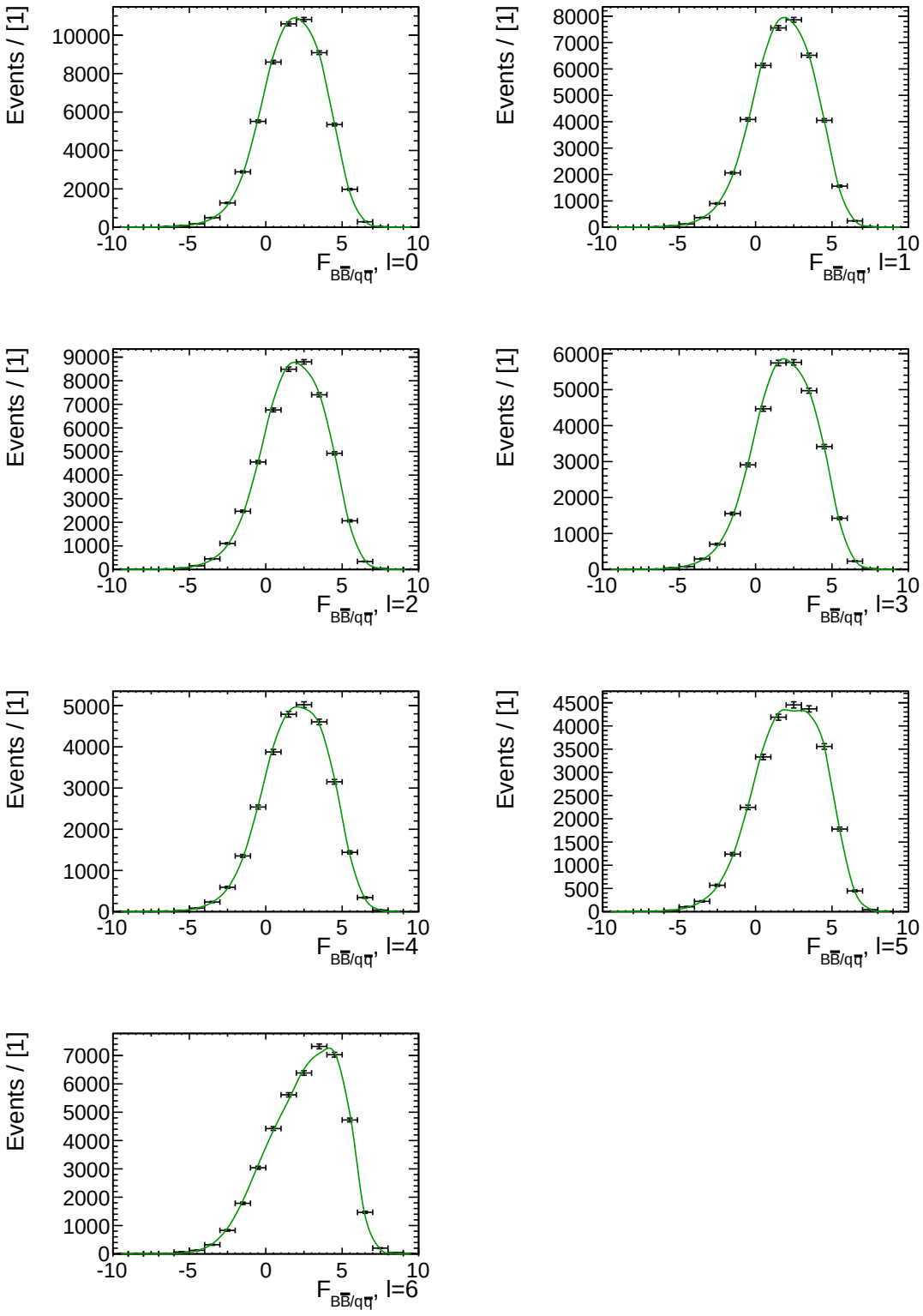

Figure 4.21: $\mathcal{F}_{B\overline{B}/q\bar{q}}$ projections of the $B^0 \to \omega K^0_S$ fit in each of the seven r-bins l.

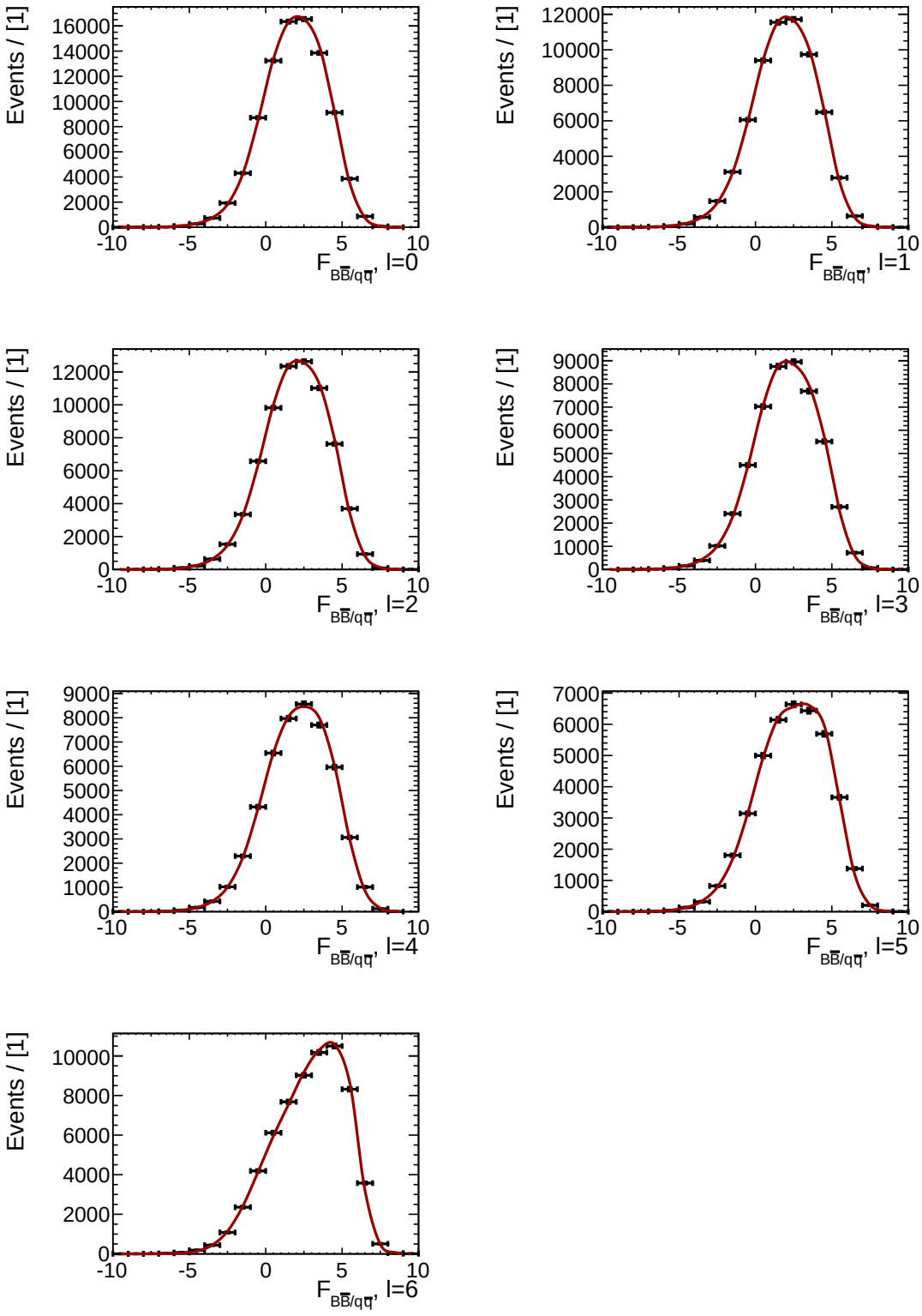

Figure 4.22: $\mathcal{F}_{\mathrm{B\overline{B}}/q\bar{q}}$ projections of the $\mathrm{B}^{\pm} \to \omega \mathrm{K}^{\pm}$ fit in each of the seven r-bins l.

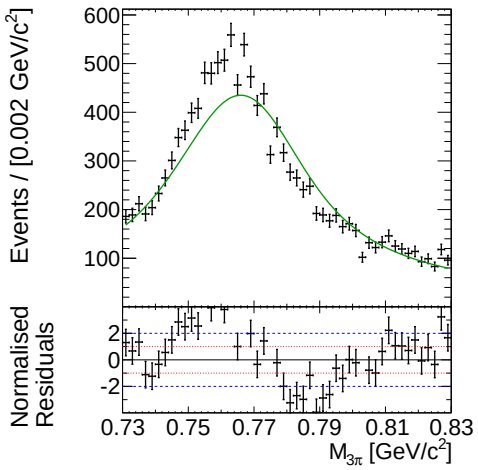

-0.15 GeV $\leq \Delta$E ≤ -0.10 GeV

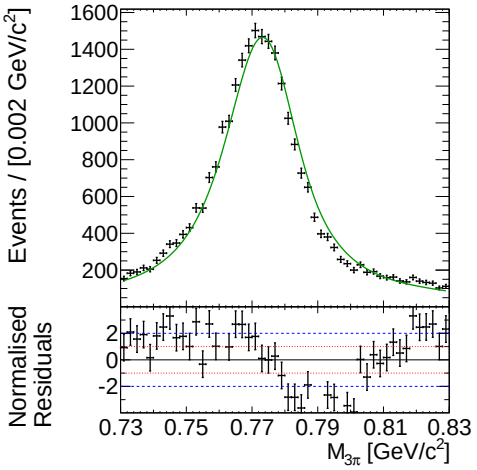

-0.10 GeV $\leq \Delta$E ≤ -0.05 GeV

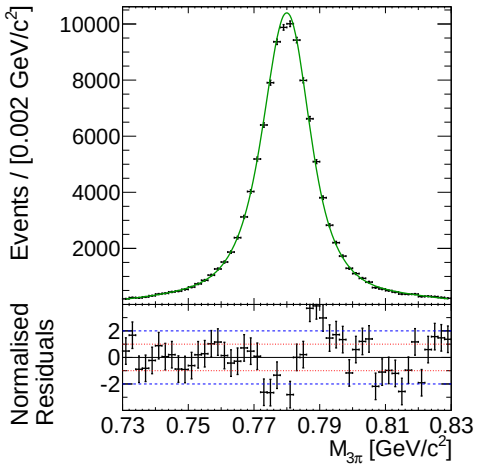

-0.05 GeV $\leq \Delta$E ≤ 0.00 GeV

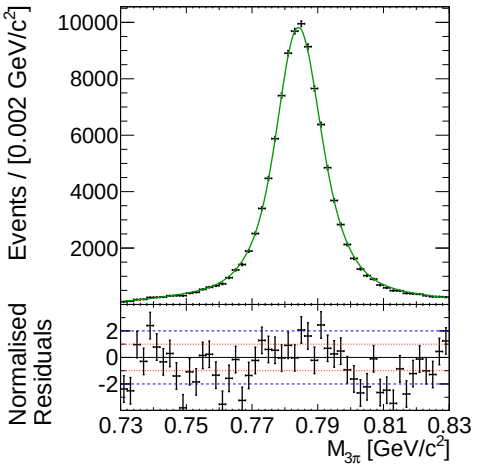

0.00 GeV $\leq \Delta$E ≤ 0.05 GeV

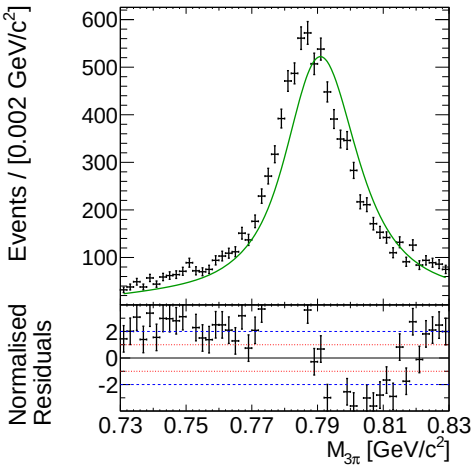

0.05 GeV $\leq \Delta$E ≤ 0.10 GeV

Figure 4.23: $M_{3\pi}$ projections of the $B^0 \to \omega K^0_S$ fit in regions of ΔE.

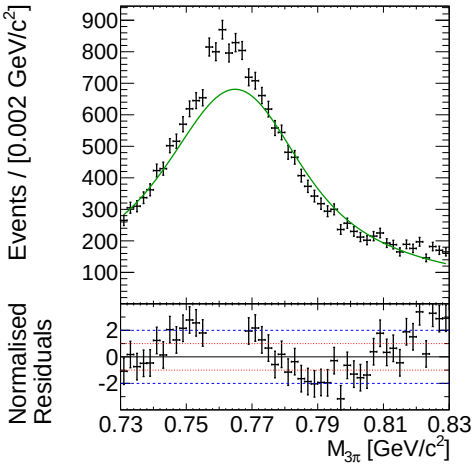

$-0.15\ \text{GeV} \leq \Delta\text{E} \leq -0.10\ \text{GeV}$

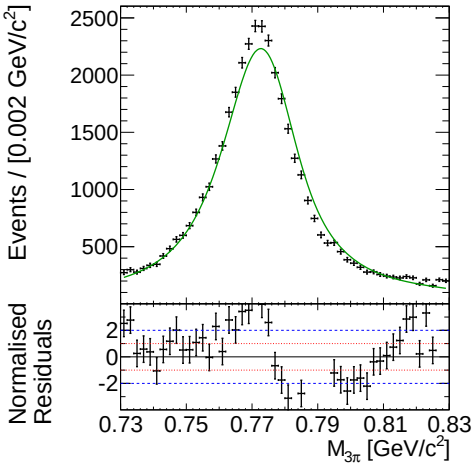

$-0.10\ \text{GeV} \leq \Delta\text{E} \leq -0.05\ \text{GeV}$

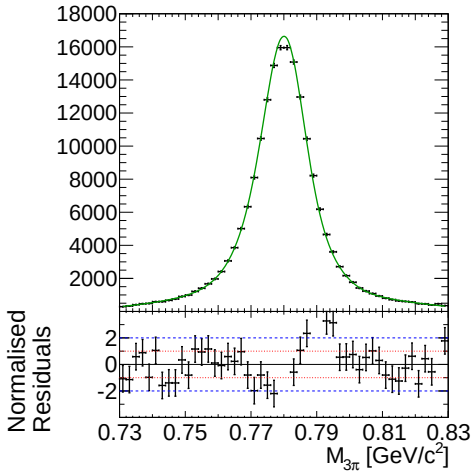

$-0.05\ \text{GeV} \leq \Delta\text{E} \leq 0.00\ \text{GeV}$

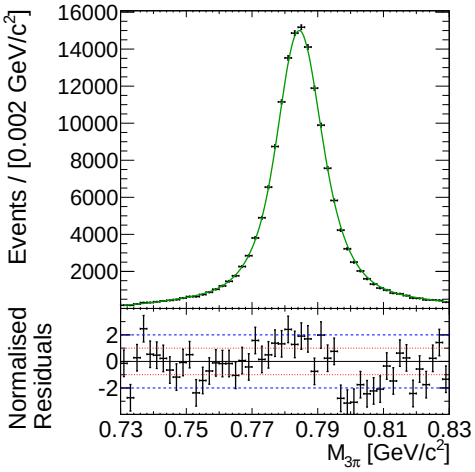

$0.00\ \text{GeV} \leq \Delta\text{E} \leq 0.05\ \text{GeV}$

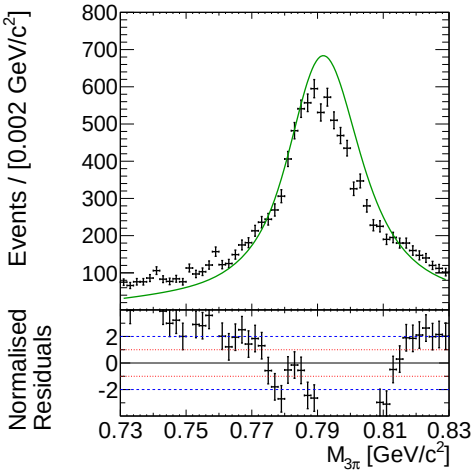

$0.05\ \text{GeV} \leq \Delta\text{E} \leq 0.10\ \text{GeV}$

Figure 4.24: $M_{3\pi}$ projections of the $\text{B}^{\pm} \to \omega\text{K}^{\pm}$ fit in regions of ΔE.

Appendix A), up to fourth order and is determined from MC

$$\mathcal{P}_{Sig}^{l,s,d}(\cos\theta_{Hel}) \equiv 1 + \sum_{i=1}^{2} c_{2i}^{s,d} C_{2i}(\cos\theta_{Hel}). \tag{4.55}$$

One note that $\cos\theta_{Hel}$ follows a theoretically predicted physics distribution that barely depends on the detector resolution and hence does not need to be corrected in the fit to the data.

The PDF of Δt and q for $B^0 \to \omega K^0_S$, as mentioned in Section 4.28, is given by

$$\begin{aligned}\mathcal{P}_{Sig}^{l,s,\omega K^0_S}(\Delta t, q) \equiv (1 - f^s_{Out}) \frac{e^{-|\Delta t|/\tau_B}}{4\tau_B} \quad & \Big\{ \quad 1 - q\Delta w^{l,s} + q(1 - 2w^{l,s}) \times \Big[\mathcal{A}_{\omega K^0_S} \cos\Delta m_d \Delta t \\ & \qquad + \mathcal{S}_{\omega K^0_S} \sin\Delta m_d \Delta t\Big]\Big\} \otimes R^s_{B^0\overline{B}^0}(\Delta t) \\ + f^s_{Out} \frac{1}{2} G(\Delta t; 0, \sigma^s_{Out}).\end{aligned} \tag{4.56}$$

For $B^\pm \to \omega K^\pm$, the PDF is given by

$$\mathcal{P}_{Sig}^{l,s,\omega K^\pm}(\Delta t, q) \equiv (1 - f^s_{Out}) \frac{e^{-|\Delta t|/\tau_{B^+}}}{4\tau_{B^+}} \otimes R^s_{B^+B^-}(\Delta t) + f^s_{Out} \frac{1}{2} G(\Delta t; 0, \sigma^s_{Out}), \tag{4.57}$$

where $\mathcal{R}^s_{B^+B^-}$ is the Δt resolution function for charged B meson decays. The Δt PDFs do not contain any free parameters.

4.3.2 Misreconstructed Signal Events

The misreconstructed signal event shape is determined from signal MC simulation events with an incorrectly reconstructed vertex. The fraction of misreconstructed signal events presented in Section 4.2.3.5 is fixed in the fit to the data. The misreconstructed signal fit projections are shown in Figure 4.25 and in Figure 4.26.

The PDFs for ΔE and $M_{3\pi}$ are the sum of a Gaussian and a linear function, while the $M_{\rm bc}$ PDF is a combination of an asymmetric Gaussian and an ARGUS function. The shape of $\mathcal{F}_{B\overline{B}/q\overline{q}}$ is the same as in the signal model (see Eq. 4.54) and shares most of the parameters including calibration factors; however, the main mean in each flavour-tag bin is determined from the misreconstructed sample. For $\cos\theta_{Hel}$, the sum of symmetric Chebyshev polynomials up to the second order is used. The variables Δt and q are modeled with the same PDF shape as the correctly reconstructed signal events but with an effective lifetime rather than τ_{B^0}/τ_{B^+}. This lifetime is obtained from MC and is necessary due to the presence of a tag-side track in the vertex reconstruction. This has the effect of reducing the average Δz separation between B_{CP} and $B_{\rm tag}$. We found from MC that, although the vertex reconstruction was incorrect, the CP information was mostly retained, so the CP parameters are shared with the signal and are free in the fit to the data. The difference between the generated CP parameters in the MC and the ones obtained from a fit to the misreconstructed signal events is then considered as a systematic uncertainty.

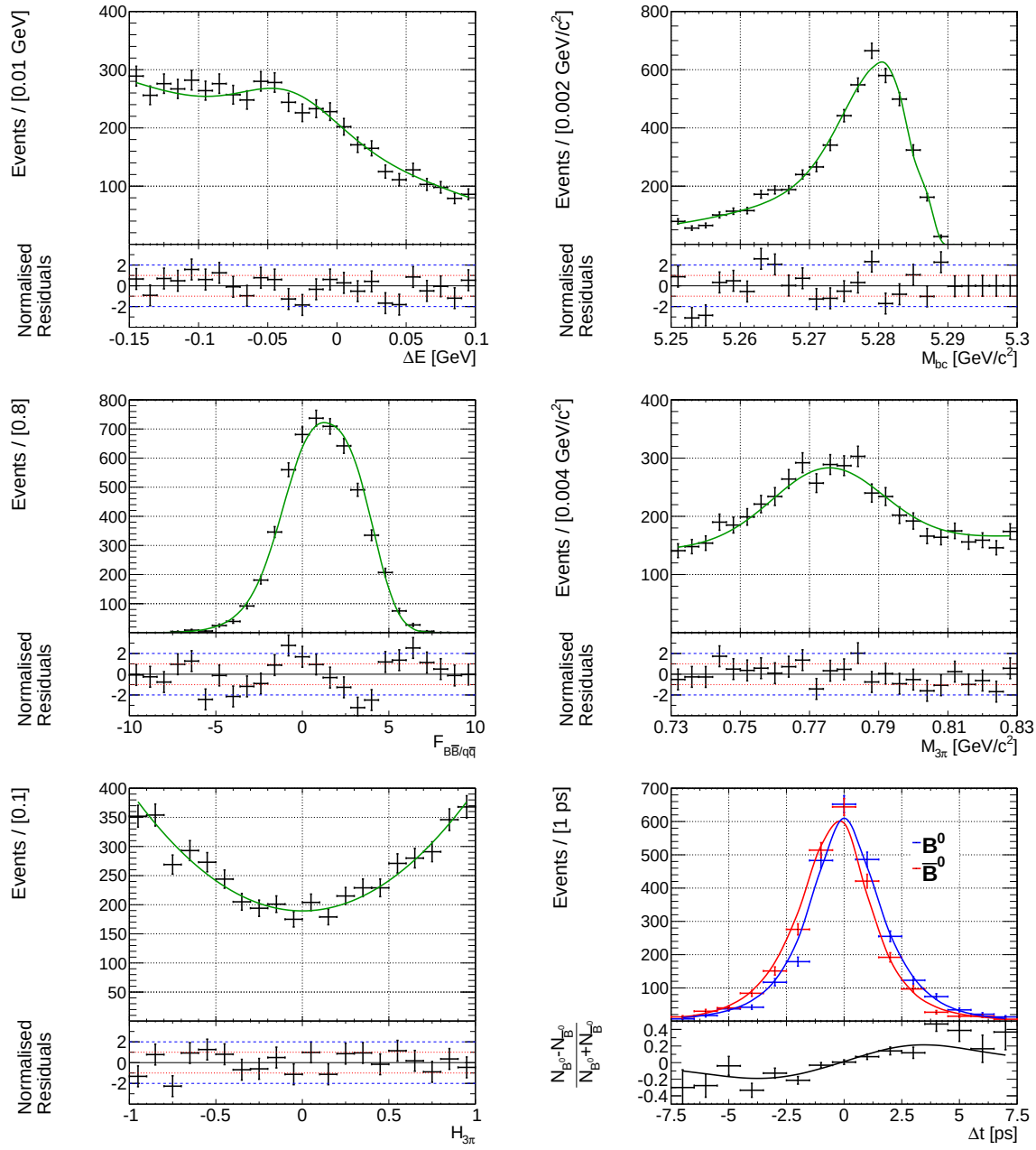

Figure 4.25: Projections of the fit to the $B^0 \to \omega K^0_S$ misreconstructed signal for (from top left to right bottom) ΔE, $M_{\rm bc}$, $\mathcal{F}_{B\overline{B}/q\overline{q}}$, $M_{3\pi}$, $\cos\theta_{Hel}$ and Δt.

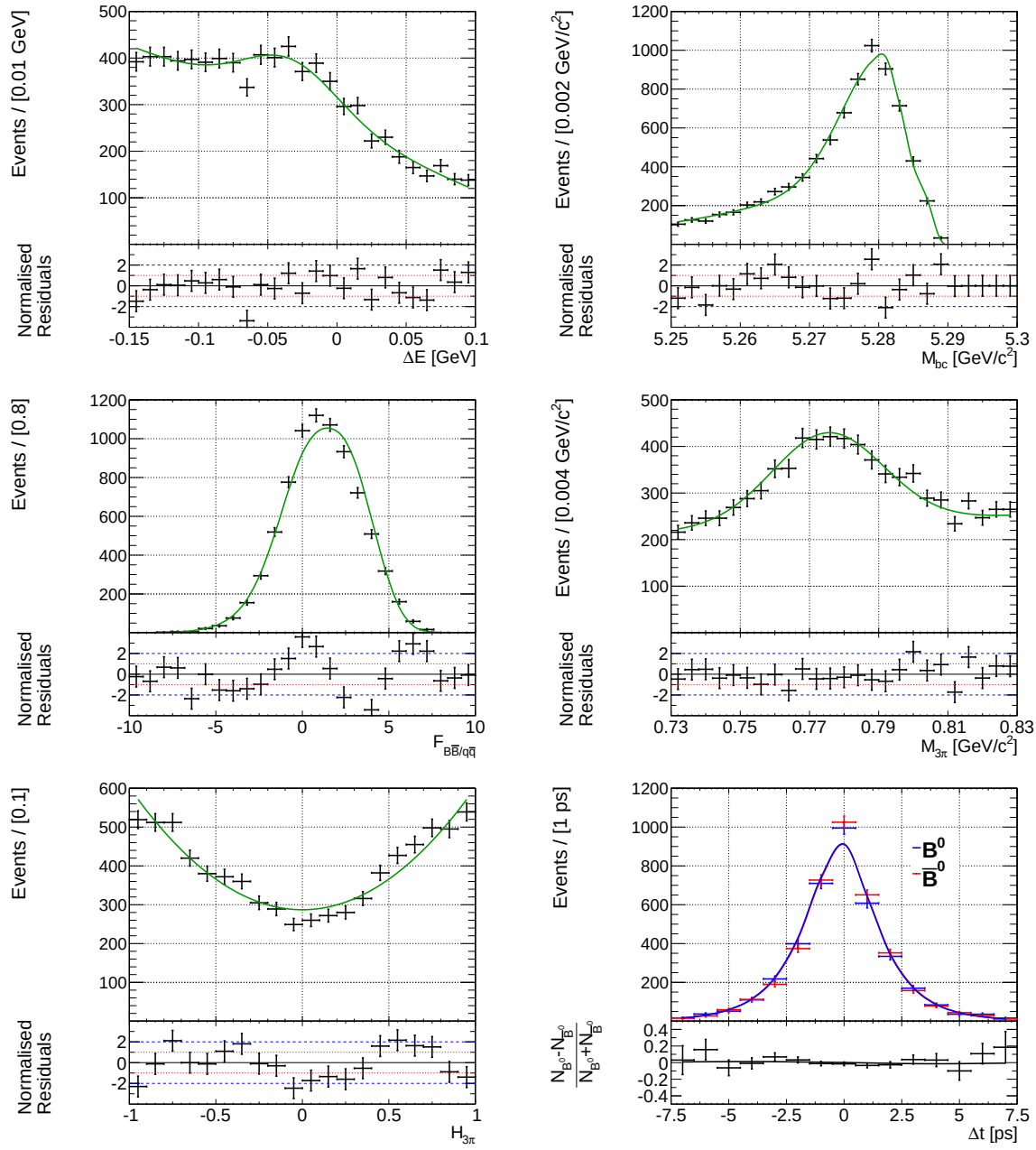

Figure 4.26: Projections of the fit to the $B^{\pm} \to \omega K^{\pm}$ misreconstructed signal for (from top left to right bottom) ΔE, $M_{\rm bc}$, $\mathcal{F}_{B\overline{B}/q\overline{q}}$, $M_{3\pi}$, $\cos\theta_{Hel}$ and Δt.

4.3.3 Continuum Model

The $q\overline{q}$ background is the domininat component in the fit to the data. Its model parametrization is based on the sideband data in the region

$$M_{\rm bc} \leq 5.25\,{\rm GeV}/c^2 \qquad\qquad 0.05\,{\rm GeV} \leq \Delta E \leq 0.20\,{\rm GeV}, \tag{4.58}$$

which is free of B mesons because of the low event mass and high event energy. To obtain a more accurate model, all the shape parameters of ΔE, $M_{\rm bc}$, $\mathcal{F}_{\rm B\overline{B}/q\overline{q}}$, and $M_{3\pi}$ are floated in the fit to the data. The fit observables' projections are shown in Figure 4.27 and in Figure 4.28. ΔE and $M_{\rm bc}$ are modeled by a linear and an ARGUS function, respectively, with parameters defined in bins of s, d. The variable $\mathcal{F}_{\rm B\overline{B}/q\overline{q}}$ is modeled by the sum of either one or two Gaussian functions in each l, s, d bin depending on the amount of data available in each bin. The PDF for $M_{3\pi}$ is a combination of a Gaussian and a linear function, while $\cos\theta_{Hel}$ is the sum of a Gaussian centered around zero and a constant. The parameters of both these PDFs are determined in each s, d bin. The Δt model is fixed from the sideband and is based on Eq. 4.29,

$$\mathcal{P}^{l,s,d}_{q\overline{q}}(\Delta t, q) \equiv \frac{1}{2}\left[(1-f^d_\delta)\frac{e^{-|\Delta t|/\tau^d_{q\overline{q}}}}{2\tau^d_{q\overline{q}}} + f^d_\delta\,\delta(\Delta t - \mu^{s,d}_\delta)\right] \otimes R^{s,d}_{q\overline{q}}(\Delta t). \tag{4.59}$$

4.3.4 B$\overline{\rm B}$ Event Models

After continuum, the next-largest background comes from neutral and charged charm $\mathrm{b} \to \mathrm{c}$ and neutral and charged charmless $\mathrm{b} \to \mathrm{u, d, s}$ decays of the B meson. Some of these B meson decays exhibit peaking structure in the signal region due to the reconstruction of particular channels with identical final states. These modes are modeled separately from the nonpeaking B$\overline{\rm B}$ background so that their shapes can be corrected in the fit to the data using the same correction factors as for the signal. In addition, since their shape similarity to the signal can potentially bias the measured branching fraction, it is important to extract their exact expected yields in the data from the MC.

4.3.4.1 Nonpeaking B$\overline{\rm B}$ Event Models

The charm and charmless B meson background shapes are determined from a large sample of MC simulation events based on $\mathrm{b} \to \mathrm{c}$ and $\mathrm{b} \to \mathrm{u, d, s}$ transitions, respectively. The shape of each of these four nonpeaking B$\overline{\rm B}$ backgrounds is modeled individually and for each SVD to account for the different effective lifetimes in the Δt distribution. In total, there are eleven independent models. Since these have similar shapes, we summarize all of them together in this section.

For all B$\overline{\rm B}$ background shapes except for the charged charm samples, the ΔE distribution is modeled with the sum of a linear function and a Gaussian accounting for six-pion final states from which only five pions were reconstructed. These peak at around $-0.14\,{\rm GeV}/c^2$, which corresponds to one missing pion mass in ΔE. The remaining charged charm samples are modeled with the sum of Chebyshev polynomials up to the second order. We model $M_{\rm bc}$ in the neutral charm category with an ARGUS function and in the charged charm category with a histogram PDF. In the charmless models, the PDF for $M_{\rm bc}$ is the sum of an asymmetric Gaussian and an ARGUS function. A sizable correlation of 12% is found between $M_{\rm bc}$ and $\mathcal{F}_{\rm B\overline{B}/q\overline{q}}$ in the neutral

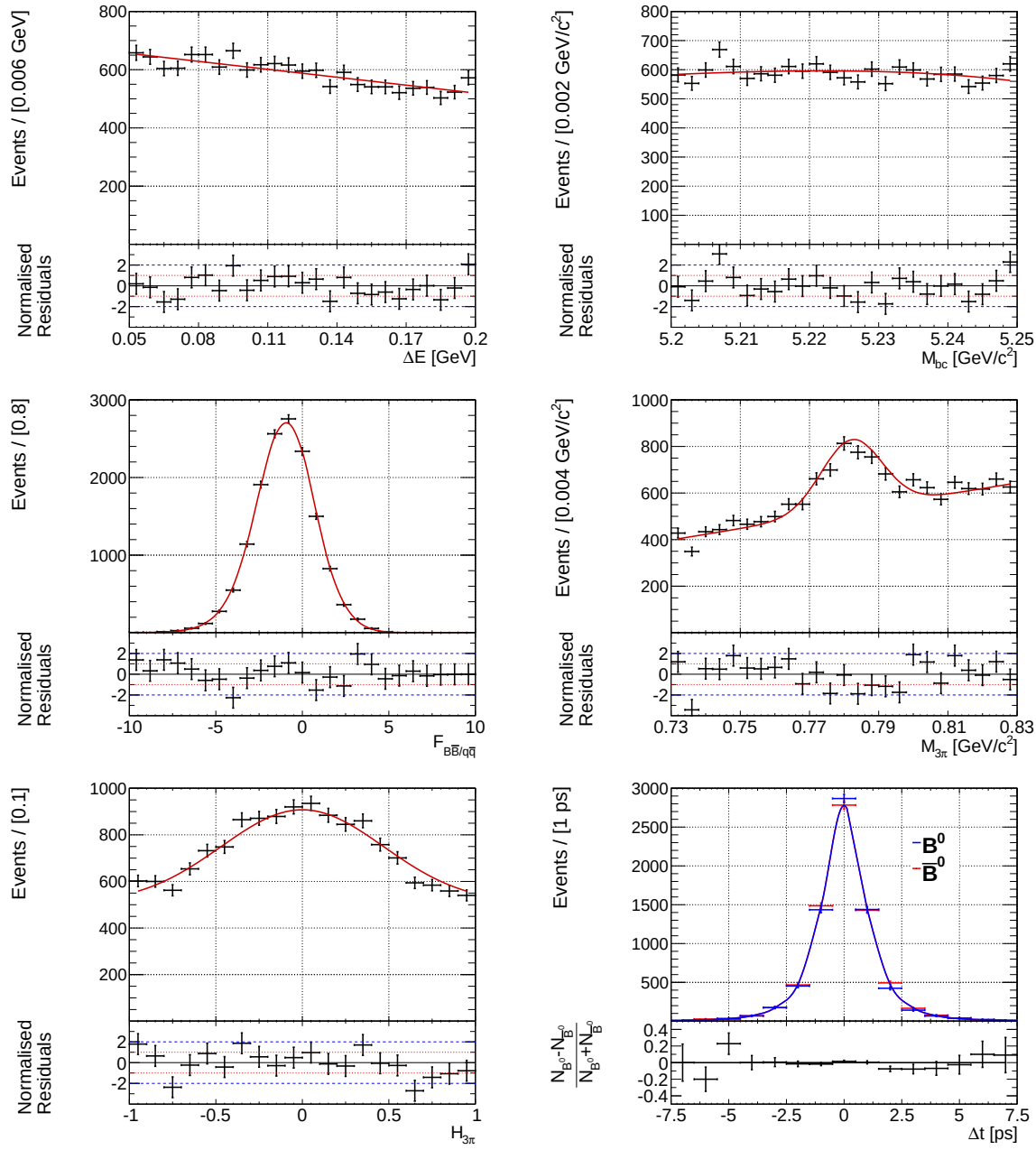

Figure 4.27: Projections of the fit to the $B^0 \to \omega K^0_S$ continuum model for (from top left to right bottom) ΔE, $M_{\rm bc}$, $\mathcal{F}_{B\overline{B}/q\overline{q}}$, $M_{3\pi}$, $\cos\theta_{Hel}$ and Δt.

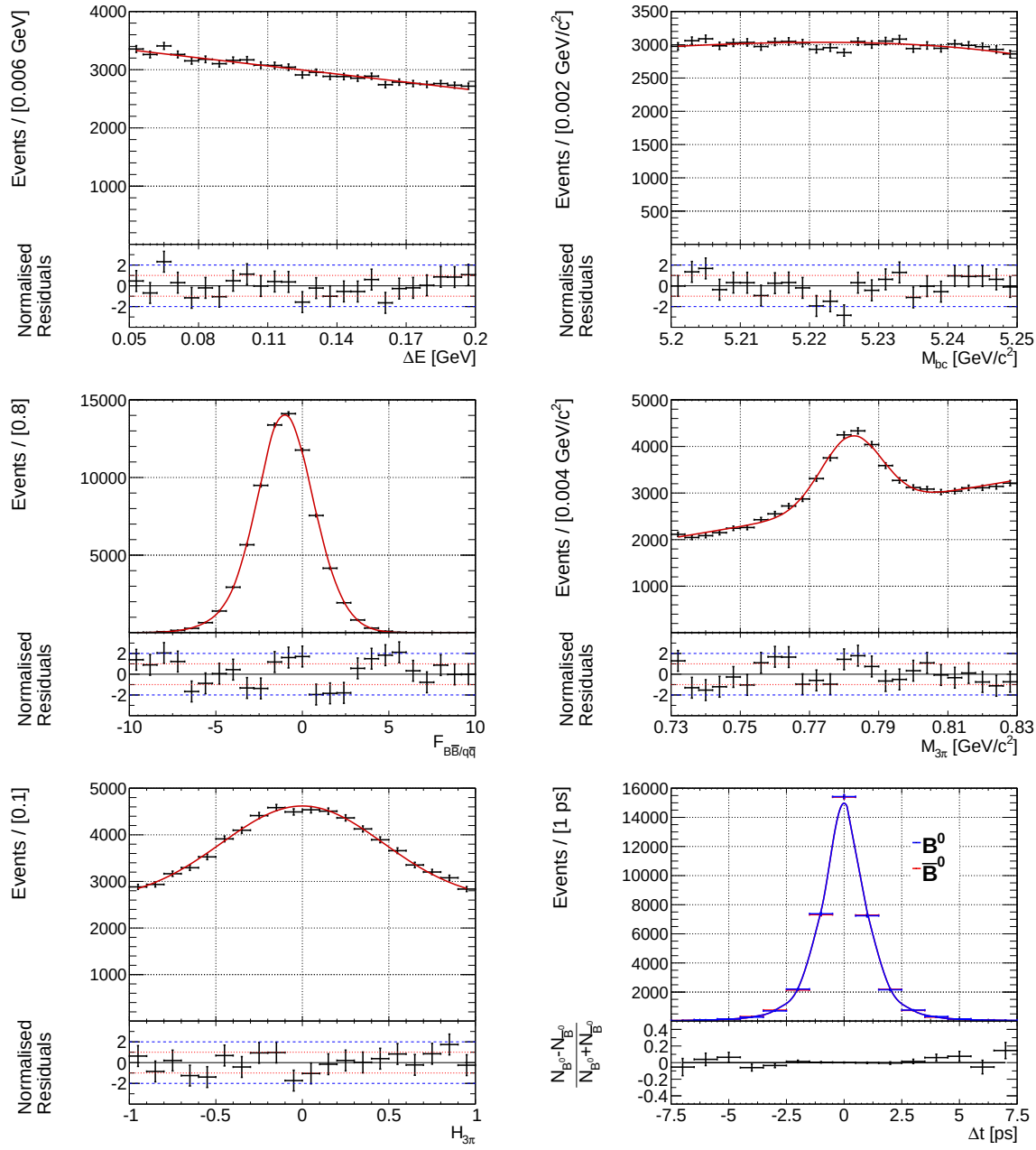

Figure 4.28: Projections of the fit to the $B^{\pm} \to \omega K^{\pm}$ continuum model for (from top left to right bottom) ΔE, M_{bc}, $\mathcal{F}_{\mathrm{B\overline{B}}/q\overline{q}}$, $M_{3\pi}$, $\cos\theta_{Hel}$ and Δt.

charmless model for $B^0 \to \omega K^0_S$ and in the charged charmless model for $B^\pm \to \omega K^\pm$, which is taken into account by further parametrizing this shape of $M_{\rm bc}$ in terms of $\mathcal{F}_{B\overline{B}/q\overline{q}}$ as

$$\begin{aligned}\mathcal{P}^{l,s,d}_{Charmless}(M_{\rm bc}|\,\mathcal{F}_{B\overline{B}/q\overline{q}}) &\equiv f^{s,d}G(M_{\rm bc};\,\mu^{s,d},\,\sigma^{s,d}_l,\,\sigma^{s,d}_r)\\ &+ (1-f^{s,d})A(M_{\rm bc};a^{s,d}+\gamma^{s,d}\mathcal{F}_{B\overline{B}/q\overline{q}},E_{beam}),\end{aligned} \tag{4.60}$$

where $\gamma^{s,d}$ is the correlation parameter. In $\mathcal{F}_{B\overline{B}/q\overline{q}}$, the shape borrows from the signal model where, again, the main mean in each flavour-tag bin is obtained from the relevant $B\overline{B}$ MC simulation sample. In the charm samples, $M_{3\pi}$ is modeled with a linear function; in the charmless samples, an additional Gaussian component is necessary. The variable $\cos\theta_{Hel}$ in the charm sample is taken to be a histogram PDF; in the charmless model, the sum of a Gaussian and a linear function is used. We fit Δt and q with the same lifetime function as for the signal, but instead of the world average for the B meson lifetime, we determine an effective lifetime of the various B meson decays from their respective MC samples. In general, the effective lifetime is smaller than the generated B meson lifetime because a track in B_{CP} can originate from the tag side. The CP parameters are fixed to zero.

Common fit projections for all four models together are shown in Figure 4.29 and in Figure 4.30. The number of charmless events is scaled from 100 to 10 times the expected number in the data to match the number of charm events.

4.3.4.2 Peaking Charm $B\overline{B}$ Event Models

In the neutral decay mode, $B^0 \to \omega K^0_S$, to the charm peaking background contribute $B^0 \to D^{*-}[\overline{D}^0\{K^0_S\pi^0\}\pi^-]\pi^+$, $B^0 \to D^-[K^0_S\pi^-\pi^0]\pi^+$ and $B^0 \to D^-[K^0_S\pi^-]\rho^+[\pi^+\pi^0]$, and their conjugated decays. For the charged decay mode, $B^\pm \to \omega K^\pm$, the charm peaking background includes only $B^+ \to D^0[K^+\pi^-]\rho^+[\pi^+\pi^0]$ and its conjugated decay. Since none of the modes is a CP final state, there is no danger of interference in the Δt distribution that could possibly disturb the value of the measured CP parameters.

The fit projections to the charm peaking background are shown in Figure 4.31 and Figure 4.32. The ΔE PDF consists of a peaking and a combinatorial component. To account for the peaking structure in ΔE, its PDF is taken to be the same as that of the signal (see Eq. 4.50). However, the parameters of the linear component and its relative fraction are determined independently from the peaking charm $B\overline{B}$ MC simulation. The model for $M_{\rm bc}$ is taken to be the combination of a Gaussian function and an ARGUS function. Because of a correlation between ΔE and $M_{\rm bc}$ of up to 12%, the fraction of the Gaussian component is linearly parametrized in terms of ΔE. The variable $\mathcal{F}_{B\overline{B}/q\overline{q}}$ also borrows from the signal model with the main mean and width of the distribution in each flavour-tag bin determined from the peaking charm $B\overline{B}$ MC simulation. In the neutral mode, $\cos\theta_{Hel}$ is modeled with a Gaussian centered around zero; in the charged mode, a symmetrized histogram is used. The variables Δt and q are fitted with a lifetime function with an effective lifetime determined from MC simulation.

4.3.4.3 Peaking Charmless $B\overline{B}$ Event Models

This category only affects the charged decay mode $B^\pm \to \omega K^\pm$, and includes the charmless decays $B^+ \to a_0[\pi^+\pi^-\pi^0]K^+$ and $B^+ \to \omega[\pi^+\pi^-\pi^0]\pi^+$.

The fit projections are shown in Figure 4.33. In ΔE, two peaks are visible in the distribution: one around zero and one shifted to positive values near the difference between the kaon and

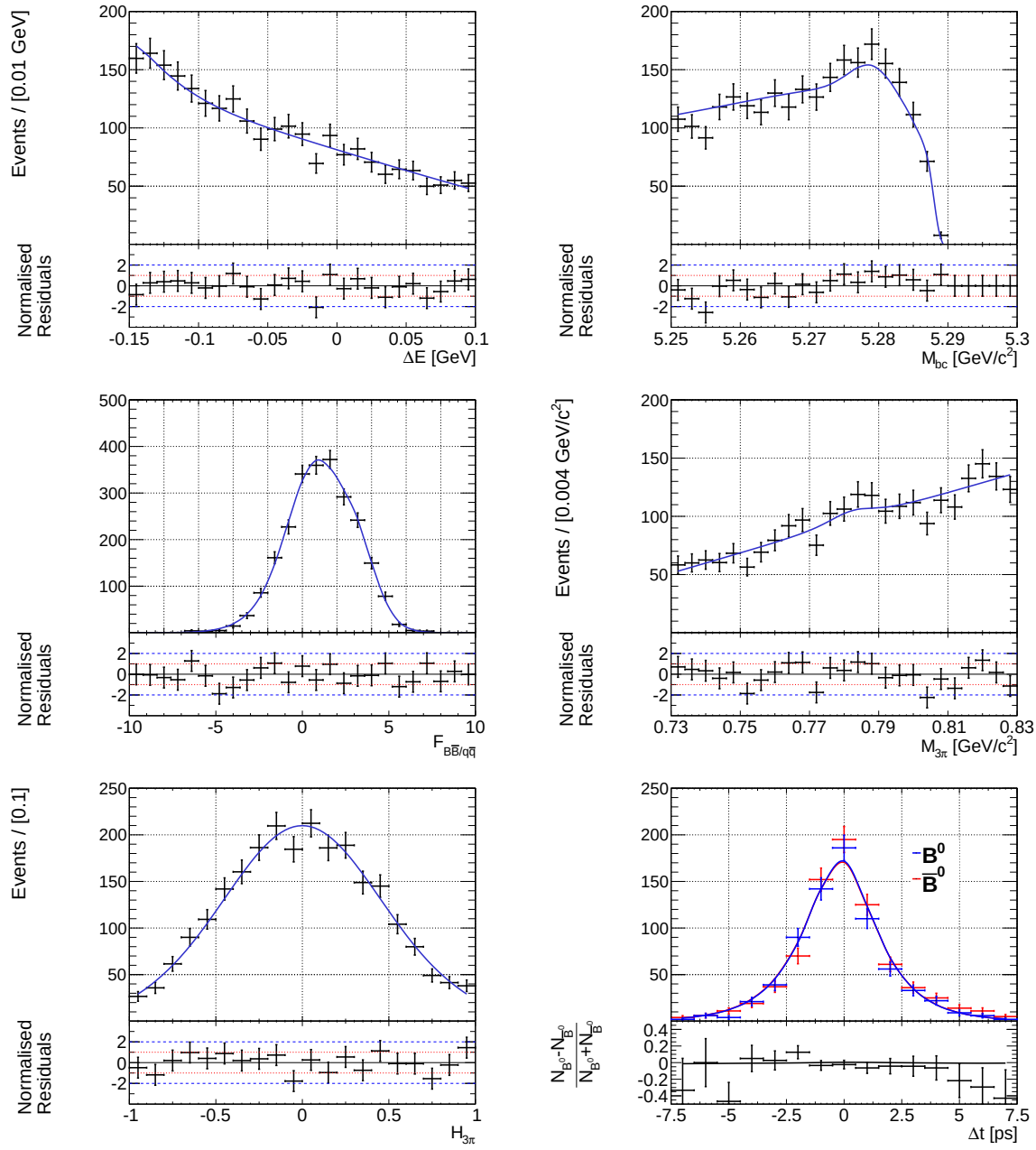

Figure 4.29: Sum of the fit projections of the $B^0 \to \omega K^0_S$ nonpeaking $B\overline{B}$ models for (from top left to right bottom) ΔE, $M_{\rm bc}$, $\mathcal{F}_{B\overline{B}/q\overline{q}}$, $M_{3\pi}$, $\cos\theta_{Hel}$ and Δt.

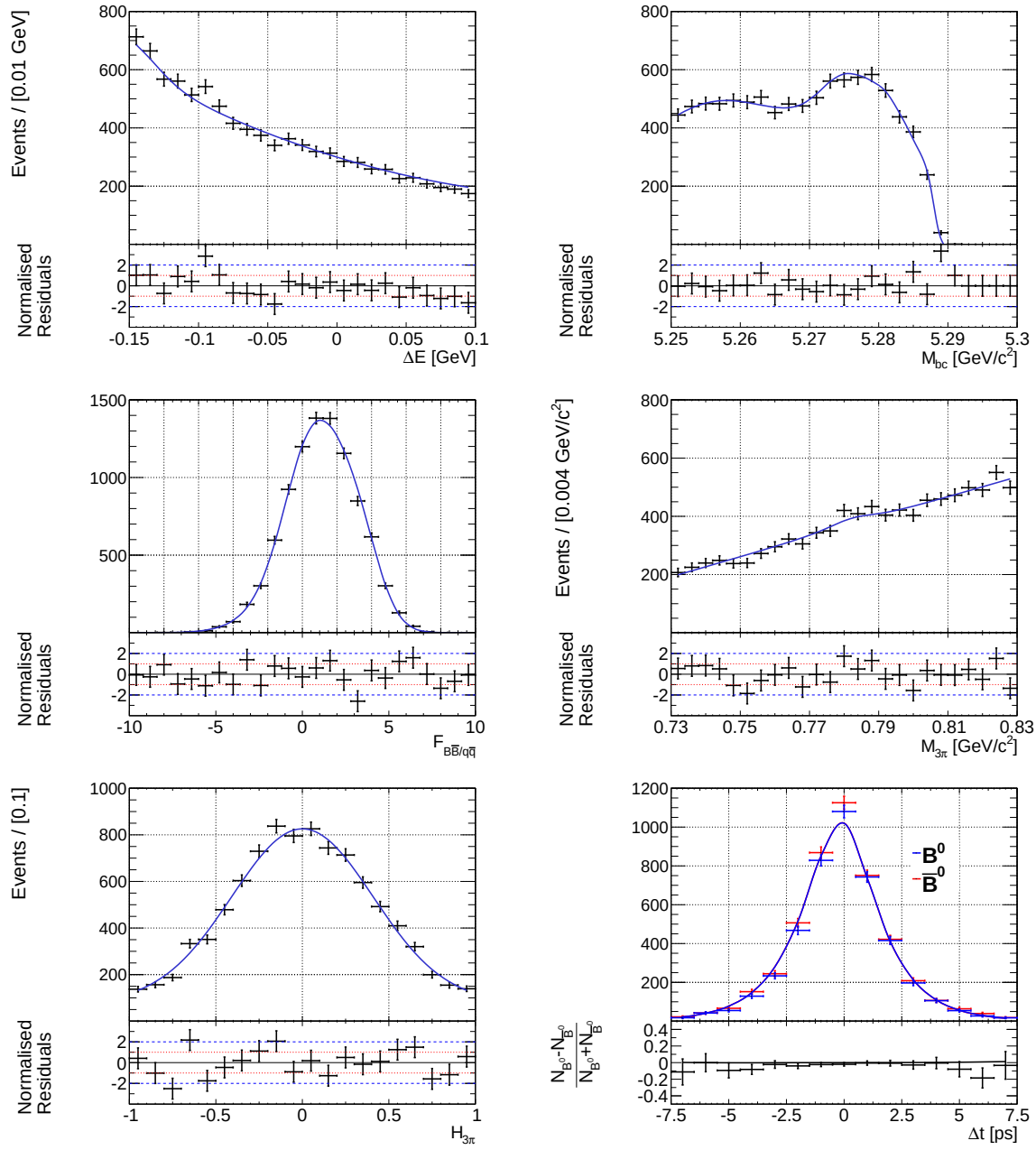

Figure 4.30: Sum of the fit projections of the $B^{\pm} \to \omega K^{\pm}$ nonpeaking $B\overline{B}$ models for (from top left to right bottom) ΔE, $M_{\rm bc}$, $\mathcal{F}_{B\overline{B}/q\overline{q}}$, $M_{3\pi}$, $\cos\theta_{Hel}$ and Δt.

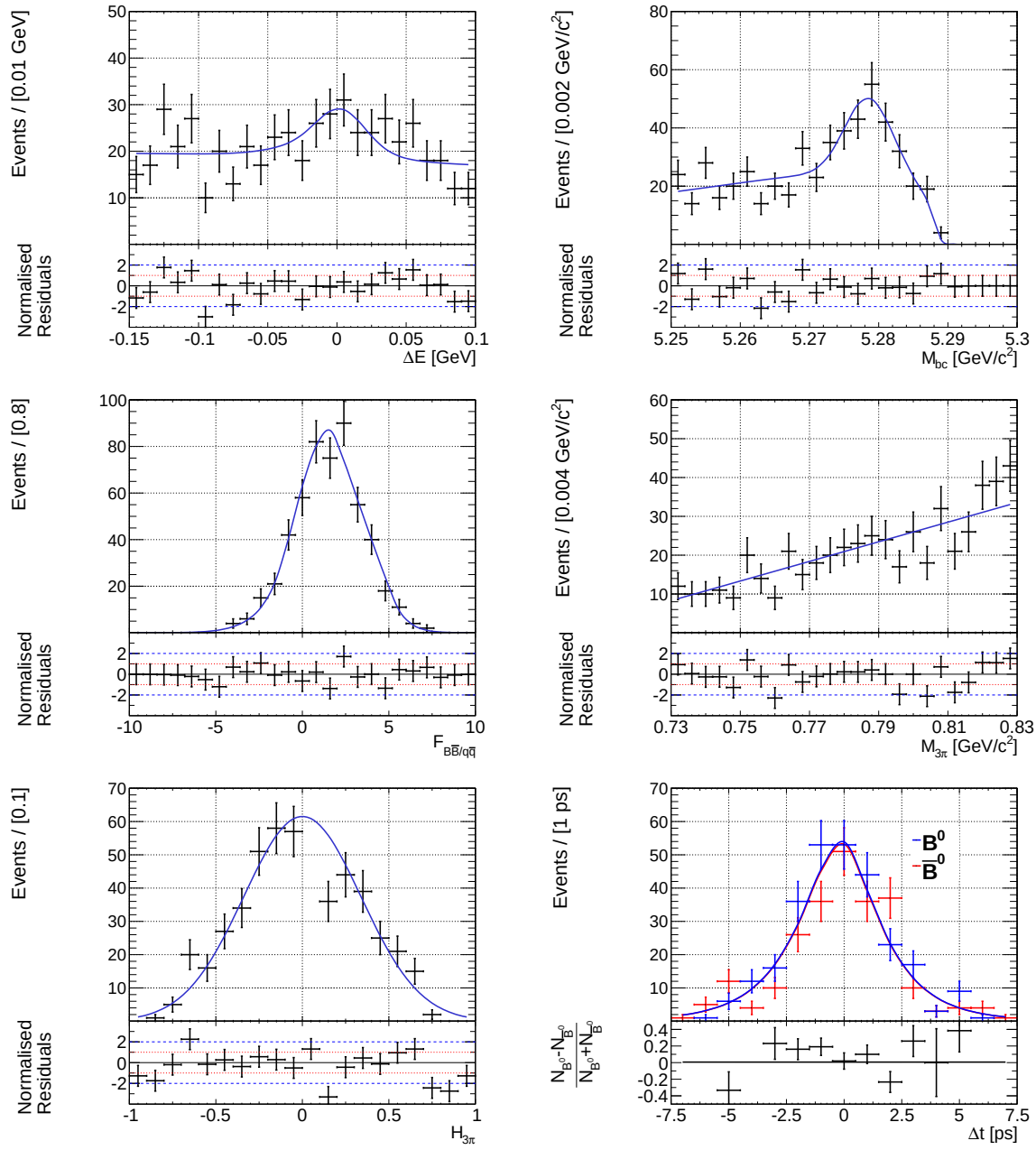

Figure 4.31: Fit projections of the $B^0 \to \omega K^0_S$ peaking charm $B\overline{B}$ model for (from top left to right bottom) ΔE, $M_{\rm bc}$, $\mathcal{F}_{B\overline{B}/q\overline{q}}$, $M_{3\pi}$, $\cos\theta_{Hel}$ and Δt.

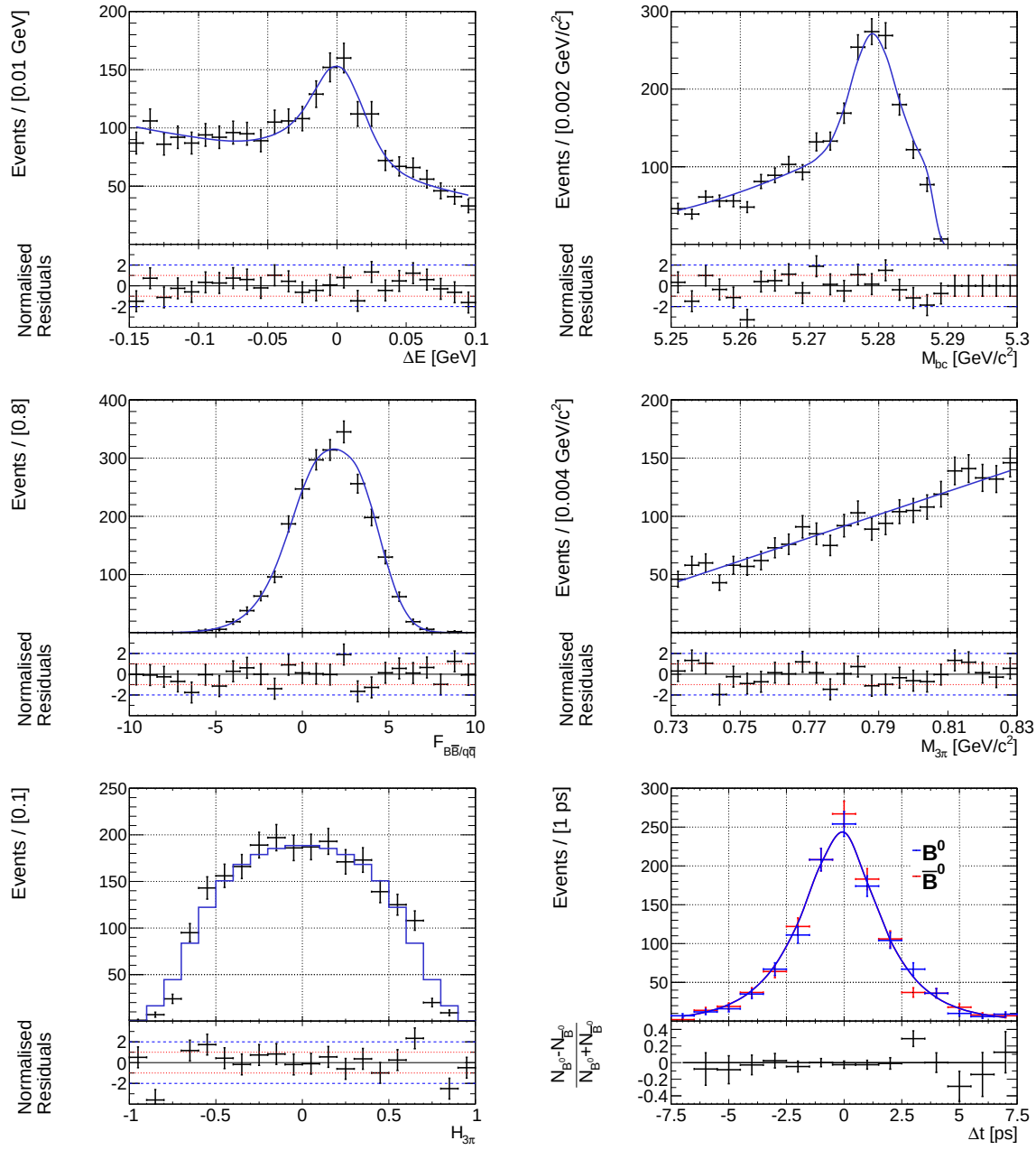

Figure 4.32: Fit projections of the $B^{\pm} \to \omega K^{\pm}$ peaking charm $B\overline{B}$ model for (from top left to right bottom) ΔE, $M_{\rm bc}$, $\mathcal{F}_{B\overline{B}/q\overline{q}}$, $M_{3\pi}$, $\cos\theta_{Hel}$ and Δt.

pion mass, originating from $B^+ \to \omega[\pi^+\pi^-\pi^0]\pi^+$ decays, where a pion is misidentified as a kaon. Both peaks are modeled with the triple Gaussian component of the signal PDF for ΔE, where the mean of the misidentified peak is determined from the peaking charmless $B\overline{B}$ MC simulation. The combinatorial component is modeled with a first-order Chebyshev, for which the shape and fraction are also determined from MC. The model for $M_{\rm bc}$ is the sum of two Gaussians and an ARGUS function. Because of up to a 14% correlation between $M_{\rm bc}$ and ΔE, the main width and fraction of the Gaussian as well as the ARGUS slope parameter are parametrized in terms of ΔE. Once again, $\mathcal{F}_{B\overline{B}/q\overline{q}}$ borrows from the signal model with the main mean and width in each flavour-tag bin determined from peaking charmless $B\overline{B}$ MC simulation. The $\cos\theta_{Hel}$ variable is modeled with the sum of symmetric Chebyshev polynomials up to the fourth order. Finally, Δt and q are fitted with a lifetime function with an effective lifetime determined from MC simulation.

4.3.5 Full Event Model

The total extended likelihood is given by

$$\mathcal{L} \equiv \prod_{l,s,d} \frac{e^{-\sum_j N_j^{s,d} f_j^{l,s,d}}}{N_{l,s,d}!} \prod_{i=1}^{N_{l,s,d}} \sum_j N_j^{s,d} f_j^{l,s,d} \mathcal{P}_j^{l,s,d}(\Delta E^i, M_{\rm bc}^i, \mathcal{F}_{B\overline{B}/q\overline{q}}{}^i, M_{3\pi}{}^i, \cos\theta_{Hel}{}^i, \Delta t^i, q^i), \tag{4.61}$$

which iterates over i data events, j signal and background categories, l flavour-tag bins, s detector configurations, and the d data samples. The fraction of events in each l, s, d bin, for category j, is denoted by $f_j^{l,s,d}$.

In the fit to the data, the $f_j^{l,s,d}$ parameters for the signal and the $B\overline{B}$ background are fixed to their values obtained from the MC. The continuum fit fractions, $f_{q\overline{q}}^{l,s,d}$, are floated, since they cannot be extracted from the sideband fit due to their dependency on $M_{\rm bc}$ and ΔE. In addition, freeing $f_{q\overline{q}}^{l,s,d}$ reduces the systematic uncertainty arising from the model parametrization. The fraction of signal events in each l, s, d bin, $f_{Sig}^{l,s,d}$, is corrected using common correction factors for $B^0 \to \omega K_S^0$ and $B^\pm \to \omega K^\pm$, which are also free parameters in the fit to the data.

Additional free fit parameters include the $N_{q\overline{q}}^{s,d}$ yields. Instead of obtaining separate signal yields for SVD1 and SVD2, $N_{Sig}^{s,d}$, we perform a transformation so that the branching fraction becomes a single free parameter between s samples and is incorporated into the fit with according to Eq. 3.4

$$N_{Sig}^{s,d} = \mathcal{B}^d(B \to \omega K) \times N_{B\overline{B}}^s \epsilon_{Sig}^{s,d} \eta_{Sig}^{s,d}, \tag{4.62}$$

where $N_{B\overline{B}}^s$ is the number of $B\overline{B}$ pairs collected by the Belle detector and $\epsilon_{Sig}^{s,d}$ and $\eta_{Sig}^{s,d}$ are detection efficiencies and selection criteria correction factors, respectively, given in Table 4.5. The efficiencies are calculated by multiplying the detection efficiency from signal MC (see Table 4.4), defined as the fraction of correctly reconstructed events of all produced events, by the world averages for the daughter's branching fractions into the relevant subdecays. The yield of the misreconstructed signal events is fixed with respect to the signal yield with a relative fraction determined from MC. The remaining $N_{B\overline{B}}^s$ yields are fixed with respect to the generic mixed yield from their expected amounts as determined from MC simulation. They are given in Table 4.6. In total, there are 204 free parameters in the fit: 54 belonging to signal and the remaining 150 to the continuum.

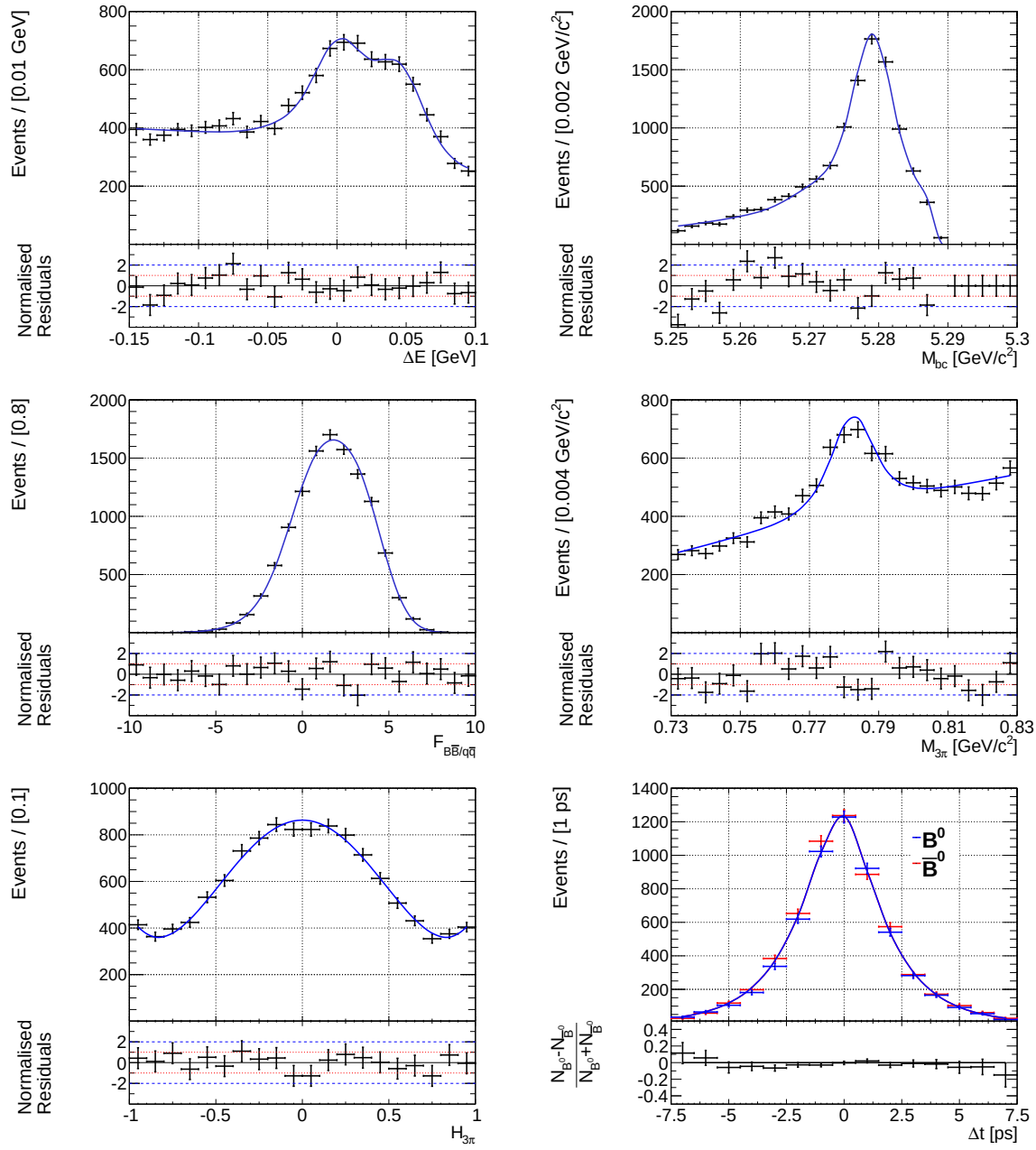

Figure 4.33: Fit projections of the $B^{\pm} \to \omega K^{\pm}$ peaking charmless $B\overline{B}$ model for (from top left to right bottom) ΔE, $M_{\rm bc}$, $\mathcal{F}_{B\overline{B}/q\overline{q}}$, $M_{3\pi}$, $\cos\theta_{Hel}$ and Δt.

Decay	PID SVD1 ($\eta^{1,d}$)	PID SVD2 ($\eta^{2,d}$)
$B^0 \to \omega K^0_S$	0.961 ± 0.010	0.959 ± 0.020
$B^\pm \to \omega K^\pm$	0.948 ± 0.018	0.923 ± 0.028

Table 4.5: Summary of the PID correction factors for $B^0 \to \omega K^0_S$ and $B^\pm \to \omega K^\pm$.

Following this, two additional fits are performed to calculate $\mathcal{A}_{\omega K^\pm}$ by measuring the two terms in Eq. 4.48. In these fits, we divide the $B^\pm \to \omega K^\pm$ sample based on the kaon charge so that we may separately extract $\mathcal{B}(B^+ \to \omega K^+)$ and $\mathcal{B}(B^- \to \omega K^-)$. The only three free parameters in them are the signal branching fraction and the continuum yields, $N^{s,\omega K}_{q\bar{q}}$. The $B\overline{B}$ yields for each $B^\pm \to \omega K^\pm$ subsample are also recalculated as needed based on the relevant kaon charge. All remaining parameters are fixed to those found in the initial fit to the data.

4.3.6 Fit Validation

To test the validity of the fit model, we determine a possible fit bias from a pseudoexperiment MC simulation study in which the signal and the $B\overline{B}$ backgrounds are generated from GEANT-simulated events, while the continuum background is generated from our model of the sideband data extrapolated into the signal region in ΔE and $M_{\rm bc}$. We generate 1000 pseudoexperiments with branching fractions $\mathcal{B}(B^0 \to \omega K^0_S) = 2.5 \times 10^{-6}$ and $\mathcal{B}(B^\pm \to \omega K^\pm) = 6.7 \times 10^{-6}$ and fit them. The pseudoexperiments consist of randomly picked MC signal and $B\overline{B}$ background events with yields corresponding to the ones we expect in the data; the $q\bar{q}$ background events are simulated from the corresponding PDFs extrapolated into the signal region. We build a pull distribution from the fit results. The pull is defined as the error weighted residuals between the fit output and input values, x_{res} and x_{input},

$$\text{Pull}(x_{res}) = \frac{x_{res} - x_{input}}{\Delta x}, \tag{4.63}$$

where Δx is the fit uncertainty. The pull distribution is a measure of the bias to the fit variables introduced by imperfections of the fit model such as badly modeled fit observables and correlations between them. The bias of a fit variable, $\mathcal{O}$, is determined according to

$$\text{Bias}(\mathcal{O}) = \mu\left(\text{Pull}(\mathcal{O})\right) \times \Delta\mathcal{O}, \tag{4.64}$$

where $\mu\left(\text{Pull}(\mathcal{O})\right)$ is the mean of the pull distribution extracted from a fit with a Gaussian function; $\Delta\mathcal{O}$ is the fit uncertainty obtained from the actual fit to the data. This approach is used for both branching fractions and the CP parameters. The branching fraction central value, pull and error distributions for $B^0 \to \omega K^0_S$ and $B^\pm \to \omega K^\pm$ are shown in Figure 4.34 and in Figure 4.35. We find a bias for the branching fraction values of 16% and 45% of their statistical uncertainties for the neutral and charged mode, respectively. We correct the central values by these amounts and assign half the bias as a systematic uncertainty. Using the error propagation method, we extract the $\mathcal{A}_{\omega K^\pm}$ fit bias from the $B^\pm \to \omega K^\pm$ bias.

To determine the bias of the $B^0 \to \omega K^0_S$ CP parameters, a linearity test across the physical $\mathcal{A}_{\omega K^0_S}$-$\mathcal{S}_{\omega K^0_S}$ region is performed. For this, the parameters $\mathcal{A}_{\omega K^0_S}$ and $\mathcal{S}_{\omega K^0_S}$ are varied individually from -1.0 to 1.0 in intervals of 0.25 and 1000 sets of toy MC experiments are generated for each parameter. The results are shown in Figure 4.36 and in Figure 4.37. The distributions are

Yield	SVD1	SVD2
$N^{s,\omega K^0_S}_{Mis}$	$(0.0192 \pm 0.0004) N^{1,\omega K^0_S}_{Sig}$	$(0.0187 \pm 0.0004) N^{2,\omega K^0_S}_{Sig}$
$N^{s,\omega K^0_S}_{Charm\ B^0\overline{B}0}$	12 ± 3	56 ± 7
$N^{s,\omega K^0_S}_{Charm\ B^+B^-}$	$(1.066 \pm 0.094) N^{1,\omega K^0_S}_{Charm\ B^0\overline{B}0}$	$(1.268 \pm 0.048) N^{2,\omega K^0_S}_{Charm\ B^0\overline{B}0}$
$N^{s,\omega K^0_S}_{Charmless\ B^0\overline{B}0}$	$(5.992 \pm 0.216) N^{1,\omega K^0_S}_{Charm\ B^0\overline{B}0}$	$(7.191 \pm 0.109) N^{2,\omega K^0_S}_{Charm\ B^0\overline{B}0}$
$N^{s,\omega K^0_S}_{Charmless\ B^+B^-}$	$(4.537 \pm 0.193) N^{1,\omega K^0_S}_{Charm\ B^0\overline{B}0}$	$(6.295 \pm 0.106) N^{2,\omega K^0_S}_{Charm\ B^0\overline{B}0}$
$N^{s,\omega K^0_S}_{Peaking\ Charm\ B^0\overline{B}0}$	$(0.719 \pm 0.077) N^{1,\omega K^0_S}_{Charm\ B^0\overline{B}0}$	$(0.780 \pm 0.036) N^{2,\omega K^0_S}_{Charm\ B^0\overline{B}0}$

Yield	SVD1	SVD2
$N^{s,\omega K^\pm}_{Mis}$	$(0.0182 \pm 0.0003) N^{1,\omega K^\pm}_{Sig}$	$(0.0182 \pm 0.0003) N^{2,\omega K^\pm}_{Sig}$
$N^{s,\omega K^\pm}_{Charm\ B^0\overline{B}0}$	25 ± 5	147 ± 12
$N^{s,\omega K^\pm}_{Charm\ B^+B^-}$	$(3.334 \pm 0.115) N^{1,\omega K^\pm}_{Charm\ B^0\overline{B}0}$	$(2.808 \pm 0.044) N^{2,\omega K^\pm}_{Charm\ B^0\overline{B}0}$
$N^{s,\omega K^\pm}_{Charmless\ B^0\overline{B}0}$	$(6.000 \pm 0.147) N^{1,\omega K^\pm}_{Charm\ B^0\overline{B}0}$	$(5.556 \pm 0.060) N^{2,\omega K^\pm}_{Charm\ B^0\overline{B}0}$
$N^{s,\omega K^\pm}_{Charmless\ B^+B^-}$	$(9.913 \pm 0.198) N^{1,\omega K^\pm}_{Charm\ B^0\overline{B}0}$	$(8.828 \pm 0.077) N^{2,\omega K^\pm}_{Charm\ B^0\overline{B}0}$
$N^{s,\omega K^\pm}_{Peaking\ Charm\ B^+B^-}$	$(1.504 \pm 0.077) N^{1,\omega K^\pm}_{Charm\ B^0\overline{B}0}$	$(1.300 \pm 0.029) N^{2,\omega K^\pm}_{Charm\ B^0\overline{B}0}$
$N^{s,\omega K^\pm}_{Peaking\ Charmless\ B^+B^-}$	$(7.130 \pm 0.168) N^{1,\omega K^\pm}_{Charm\ B^0\overline{B}0}$	$(6.792 \pm 0.068) N^{2,\omega K^\pm}_{Charm\ B^0\overline{B}0}$

Table 4.6: Summary of yields fixed relative to other yields in the fit for $B^0 \to \omega K^0_S$ (top) and $B^\pm \to \omega K^\pm$ (bottom). The values of the yields and their uncertainties are obtained from MC statistics.

mostly linear with a mostly negligible offset and slope, meaning that the bias is also small and barely dependent on the $\mathcal{A}_{CP}$ and $\mathcal{S}_{CP}$ values.

The pseudoexperiment study indicates 30% improvement in the statistical uncertainty of the branching fractions of $B \to \omega K$, 15-20% improvement in the statistical uncertainty of the $B^0 \to \omega K^0_S$ time-dependent CP parameters and 30% improvement of $\mathcal{A}_{\omega K^\pm}$ over the previous analysis methods. These numbers are calculated by scaling all uncertainties from the previous analyses to that expected with the final data set.

To test the validity of the Δt resolution description and reconstruction procedure, we perform a separate data fit releasing the B^0 and B^+ lifetimes while blinding the physics parameters. We obtain

$$\begin{aligned} \tau_{B^0} &= 1.32 \pm 0.15 \text{ ps}, \\ \tau_{B^+} &= 1.58 \pm 0.08 \text{ ps}, \end{aligned} \tag{4.65}$$

which is in agreement within two standard deviations with the current world averages [27], $\tau_{B^0} = 1.519 \pm 0.007$ ps and $\tau_{B^-} = 1.641 \pm 0.008$ ps.

As a further check of the Δt resolution function and the parameters describing the probability of mistagging, we fit for the time-dependent CP parameters of the $B^\pm \to \omega K^\pm$ sample by substituting Eq. 4.28 for Eq. 4.57; the results are consistent within one standard deviation with $\mathcal{A}_{\omega K^\pm}$ obtained from the nominal fit and with null asymmetry for $\mathcal{S}_{\omega K^\pm}$.

4.3.7 Results

From the fits to the data containing 17860 $B^0 \to \omega K^0_S$ and 88007 $B^\pm \to \omega K^\pm$ candidates, the following branching fractions and CP violation parameters are obtained [2]

$$\begin{aligned} \mathcal{B}(B^0 \to \omega K^0) &= (4.5 \pm 0.4 \text{ (stat)} \pm 0.3 \text{ (syst)}) \times 10^{-6}, \\ \mathcal{B}(B^\pm \to \omega K^\pm) &= (6.8 \pm 0.4 \text{ (stat)} \pm 0.4 \text{ (syst)}) \times 10^{-6}, \\ \mathcal{A}_{\omega K^0_S} &= -0.36 \pm 0.19 \text{ (stat)} \pm 0.05 \text{ (syst)}, \\ \mathcal{S}_{\omega K^0_S} &= +0.91 \pm 0.32 \text{ (stat)} \pm 0.05 \text{ (syst)}, \\ \mathcal{A}_{\omega K^\pm} &= -0.03 \pm 0.04 \text{ (stat)} \pm 0.01 \text{ (syst)}. \end{aligned} \tag{4.66}$$

Here, the first uncertainty is statistical and the second is systematic, which is discussed in the next section. The statistical correlation coefficients between the branching fractions and the CP parameters are below 10^{-5} except for the 0.4% correlation between $\mathcal{A}_{\omega K^0_S}$ and $\mathcal{S}_{\omega K^0_S}$. Signal-enhanced fit projections are shown in Figures 4.38, 4.39, and 4.40. The $B^0 \to \omega K^0_S$ and $B^\pm \to \omega K^\pm$ branching fractions have been bias corrected, corresponding to signal event yields of $N(B^0 \to \omega K^0_S) = 234 \pm 22$ and $N(B^\pm \to \omega K^\pm) = 1114 \pm 59$ where the uncertainties are statistical only. Before the bias correction, the central values of the branching fractions are $\mathcal{B}(B^0 \to \omega K^0) = 4.5 \times 10^{-6}$ and $\mathcal{B}(B^\pm \to \omega K^\pm) = 6.9 \times 10^{-6}$. From the yields obtained in the fit to the data, the relative contributions of each component in the neutral mode are found to be 1.3% for the signal $B^0 \to \omega K^0_S$, 96.5% for the continuum, and 2.2% for the $B\overline{B}$ background. For the charged mode, we obtain 1.3% signal $B^\pm \to \omega K^\pm$, 96.8% continuum and 1.9% $B\overline{B}$. All results are consistent with the previous Belle measurements [63, 64] within two standard

[2] The $B^0 \to \omega K^0$ branching fraction is twice the $B^0 \to \omega K^0_S$ branching fraction, assuming negligible CP asymmetry effects in the kaon system.

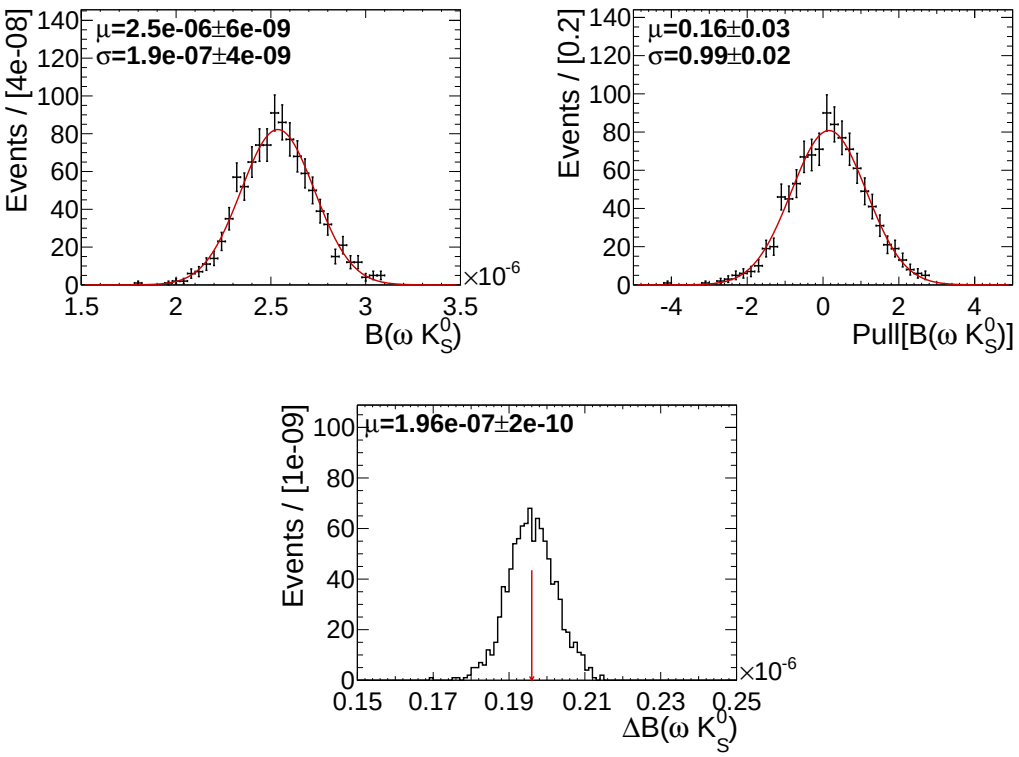

Figure 4.34: The branching fraction central values (top left), pull (top right) and fit uncertainty (bottom) distributions for $B^0 \to \omega K^0_S$. The genrated value is $\mathcal{B}(B^0 \to \omega K^0_S) = 2.5 \times 10^{-6}$.

deviations. The statistical errors obtained in our fit to the data agree with those obtained in the pseudoexperiment study mentioned in the previous section.

These results, apart from $\mathcal{S}_{\omega K^0_S}$, are the world's most precise measurements of the branching fractions and CP violation parameters in B $\to \omega$K decays. To estimate the significance of CP violation, we perform a two-dimensional likelihood scan in the $\mathcal{A}_{\omega K^0_S}$-$\mathcal{S}_{\omega K^0_S}$ plane. This distribution is convolved with a two-dimensional Gaussian with means of zero and widths set to the relevant systematic uncertainty in $\mathcal{A}_{\omega K^0_S}$ and $\mathcal{S}_{\omega K^0_S}$. The resulting distribution is then used to obtain contours in units of significance from which we find the first evidence for CP violation in the $B^0 \to \omega K^0_S$ decay with 3.1 standard deviations, as shown in Figure 4.41. The results of this analysis have been published in [81].

Although the results are constistent with the previous Belle measurements within less than three standard deviations, the question arises of what the origine of the discrepancy between the $\mathcal{S}_{\omega K^0_S}$ central values is. For this, we perform three checks. First, as a test of the accuracy of our result, we perform a fit on the data set containing the first 535×10^6 $B\overline{B}$ pairs, which corresponds to the integrated luminosity used in the previous analysis. We obtain $\mathcal{A}_{\omega K^0_S} = -0.17 \pm 0.24$ and $\mathcal{S}_{\omega K^0_S} = +0.42 \pm 0.40$, which are in agreement with the previous Belle results shown in Table 4.2, considering the new tracking algorithm used in this analysis, the 37% increase in detection efficiency with respect to that given in Ref. [64] and the improved analysis strategy of including $\cos\theta_{Hel}$, which provides powerful discrimination between signal and background.

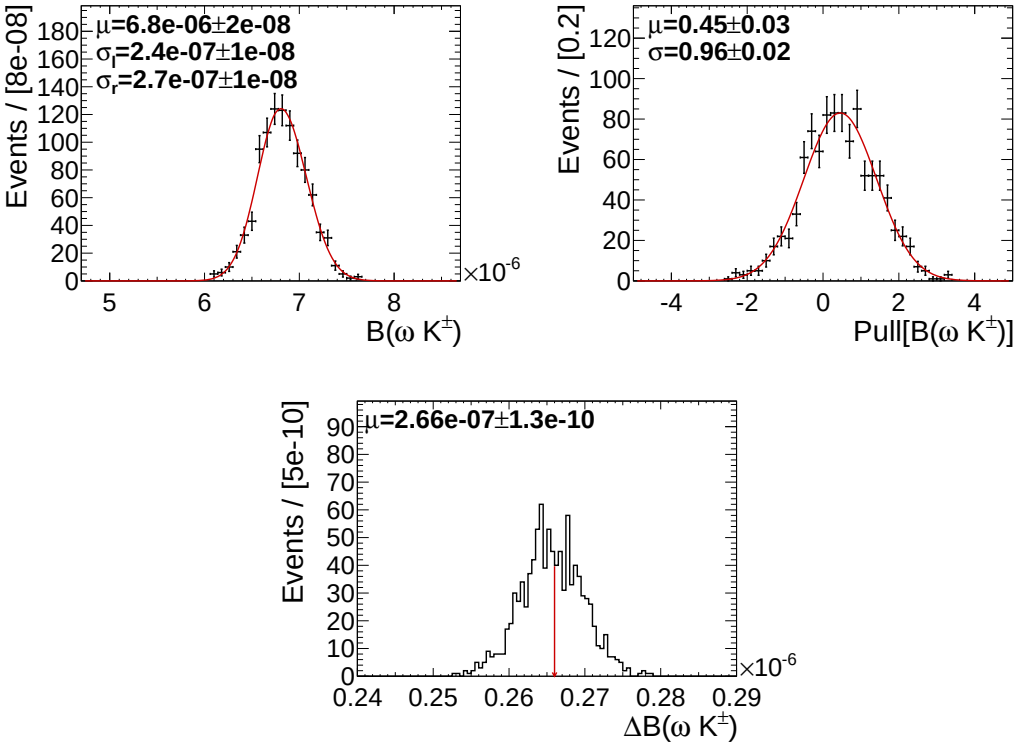

Figure 4.35: The branching fraction central values (top left), pull (top left) and fit uncertainty (bottom) distributions for $B^{\pm} \to \omega K^{\pm}$. The genrated value is $\mathcal{B}(B^{\pm} \to \omega K^{\pm}) = 6.7 \times 10^{-6}$.

Second, we perform a fit to 500 pseudoexperiments based on the 237×10^6 $B\overline{B}$ pairs that are new to this analysis with our results for $\mathcal{A}_{\omega K^0_S}$ and $\mathcal{S}_{\omega K^0_S}$. The two fractions of experiments in which the obtained CP parameters are above $\mathcal{A}_{\omega K^0_S} = -0.09$ and below $\mathcal{S}_{CP} = +0.11$, which are the previous Belle results, give is the two probabilities of a statistical fluctuation in the new data set causing the observed shift in the $\mathcal{A}_{\omega K^0_S}$ and $\mathcal{S}_{\omega K^0_S}$ central values, respectively. For $\mathcal{A}_{\omega K^0_S}$, we obtain a probability of 1.5% and for $\mathcal{S}_{\omega K^0_S}$ – 7%. Third, to find out what the probability of obtaining the previous Belle CP parameters results with using our method is, we do the same pseudoexperiment test with the first 535×10^6 $B\overline{B}$ pairs. We obtain probabilities of 13% for $\mathcal{A}_{\omega K^0_S}$ and 20% for $\mathcal{S}_{\omega K^0_S}$.

In conclusion, a not unlikely statistical fluctuation and the higher efficiency of our method are two possible reasons for the discrepancy between the $\mathcal{S}_{\omega K^0_S}$ central values obtained by us and by the previous Belle analysis.

4.3.8 Improvements Compared to the Previous Belle Analysis

To determine the branching fractions and the CP violation parameters, in contrast to the previous Belle analyses [63, 64], we fit all variables and the two decay channels simultaneously. Extracting common calibration parameters between the two decay modes from the data allows us to neglect systematic uncertainties in the low statistics neutral mode arising from the difference

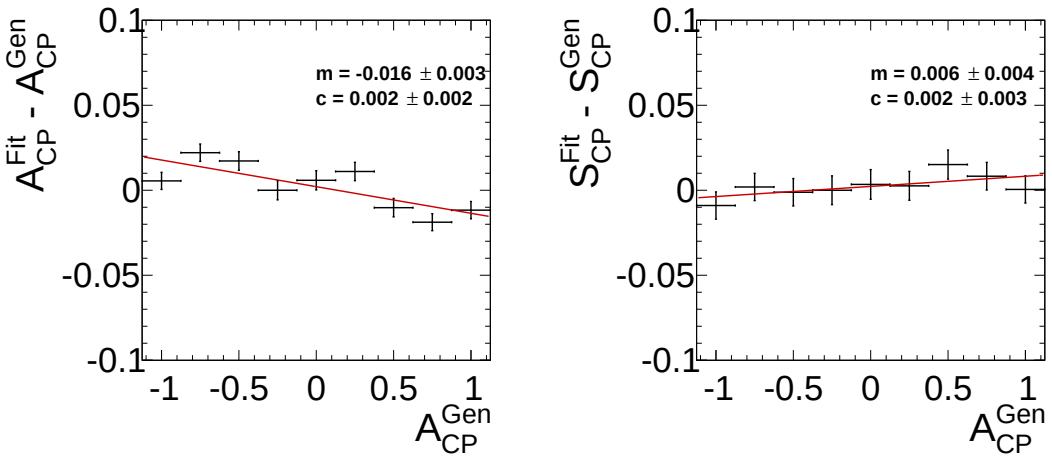

Figure 4.36: Linearity test for the $B^0 \to \omega K_S^0$ time-dependent physics parameters while varying $\mathcal{A}_{CP}$. m and c are the slope and offset of the distributions, respectively.

between data and MC simulation. These are instead absorbed into the statistical error. The advantage of this method becomes clear when using a data set with higher number of signal events, where the statistical uncertainty is negligible compared to the systematic. Our analysis shows that this approach is successful and could be considered in the future by Belle's successor, Belle II.

The reconstruction algorithm used by this analysis has an efficiency that is higher by a factor of 4 for the neutral mode and 2 for the charged mode compared to the previous Belle branching fraction analysis [63]. This is mostly due to looser selection criteria such as the cut on $\mathcal{L}_{B\overline{B}/q\overline{q}}$.

To improve the statistical precision of the branching fraction over the previous measurement, $\mathcal{F}_{B\overline{B}/q\overline{q}}$ has been included in the fit. Another improvement over both previous analyses is the inclusion of the $\cos\theta_{Hel}$ observable into the fit, which significantly improves the background discrimination. To determine the CP parameters, the previous Belle analysis [64] applied a two-step procedure where an initial fit without Δt and q was performed to obtain a signal yield. This allowed the event-dependent probabilities of each component to be determined and then used as input to set the fractions of each component in a fit to Δt and q. Our procedure of combining all variables together in a single fit has the added benefit of further discrimination against the continuum with the Δt variable and makes the treatment of systematic uncertainties more straightforward, at a cost of analysis complexity and longer computational time.

4.3.9 Systematic Uncertainties

Systematic uncertainties from various sources are considered and estimated with both model-specific and -independent studies and cross-checks. All uncertainties are summarized in Table 4.7.

The systematic uncertainty due to the error on the total number of $B\overline{B}$ pairs is calculated from the on- and off-resonance luminosity, taking into account efficiency and luminosity scaling corrections. The major branching fraction systematic uncertainty arises from the π^0 reconstruction and is evaluated by comparing data-MC differences of the yield ratio between

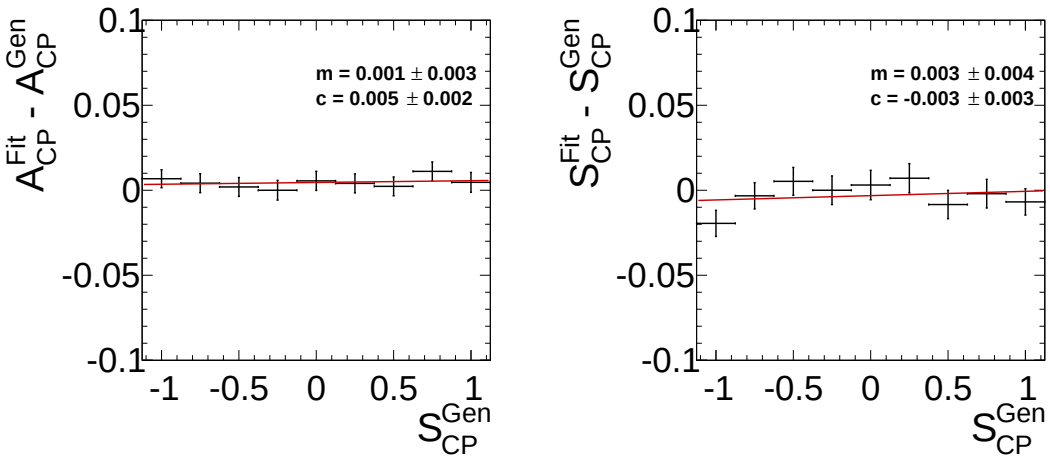

Figure 4.37: Linearity test for the $B^0 \to \omega K_S^0$ time-dependent physics parameters while varying $\mathcal{S}_{CP}$. m and c are the slope and offset of the distributions, respectively.

$\eta \to \pi^0\pi^0\pi^0$ and $\eta \to \pi^+\pi^-\pi^0$. The uncertainties due to K_S^0 reconstruction and tracking efficiencies are calculated by comparing data-MC differences of the reconstruction efficiency of $D^* \to D^0[K^-\pi^+]\pi^0$. The uncertainty due to particle identification efficiency is determined using inclusive $D^{*+} \to D^0[K^-\pi^+]\pi^+$ decays, where the PID of each particle is unambiguously determined by its charge.

The systematic uncertainty of the IP constraint smearing (see Section 4.2.3.5) is estimated by varying its amount by $\pm 10\,\mu m$. The track selection cut values on the tag side are varied by $\pm 10\%$ and the difference in the fit result is taken as a systematic uncertainty. The charged track parametrization errors are corrected by global scaling factors obtained from cosmic rays. The effect of these corrections is studied by looking at the difference in fit results with and without the corrected errors. The requirement of $|\Delta t| < 70$ ps is varied by ± 30 ps. The B vertex quality selection criteria $h < 50$ is varied by $^{+50}_{-25}$ and the z vertex error requirements, $\sigma < 200\,\mu m$ ($500\,\mu m$) for multi- (single-) track vertices, is varied by $\pm 100\,\mu m$. A Δz bias can be caused by an unknown intrinsic misalignment within the SVD or relative misalignment between the SVD and CDC. This scenario is considered by generating MC with and without misalignment effects and taking the difference as a systematic error.

The fit model systematics in the signal PDF include the fixed physics parameters τ_B and Δm_d, which are varied within their world-average uncertainties [27]. It also includes the Δt resolution function parameters of $R^s_{B^0\overline{B}^0}(\Delta t)$ and $R^s_{B^+B^-}(\Delta t)$, as well as the flavour-tagging performance parameters w and Δw, which are varied within $\pm 1\sigma$ of their experimental uncertainties determined from a control sample [72, 82]. The fixed $B\overline{B}$ background yields are also accounted for by varying the nonpeaking background yields within their MC errors. The the peaking background yields are varied by the world-average uncertainties on their branching fractions. The parametric and nonparametric shapes describing the background are varied within their uncertainties. For nonparameteric shapes (*i.e.*, histograms), we vary the contents of the histogram bins by $\pm 1\sigma$. We vary the fractions of the Chebyshev and ARGUS components of the ΔE and M_{bc} signal PDFs by their full amounts in order to estimate the uncertainty due

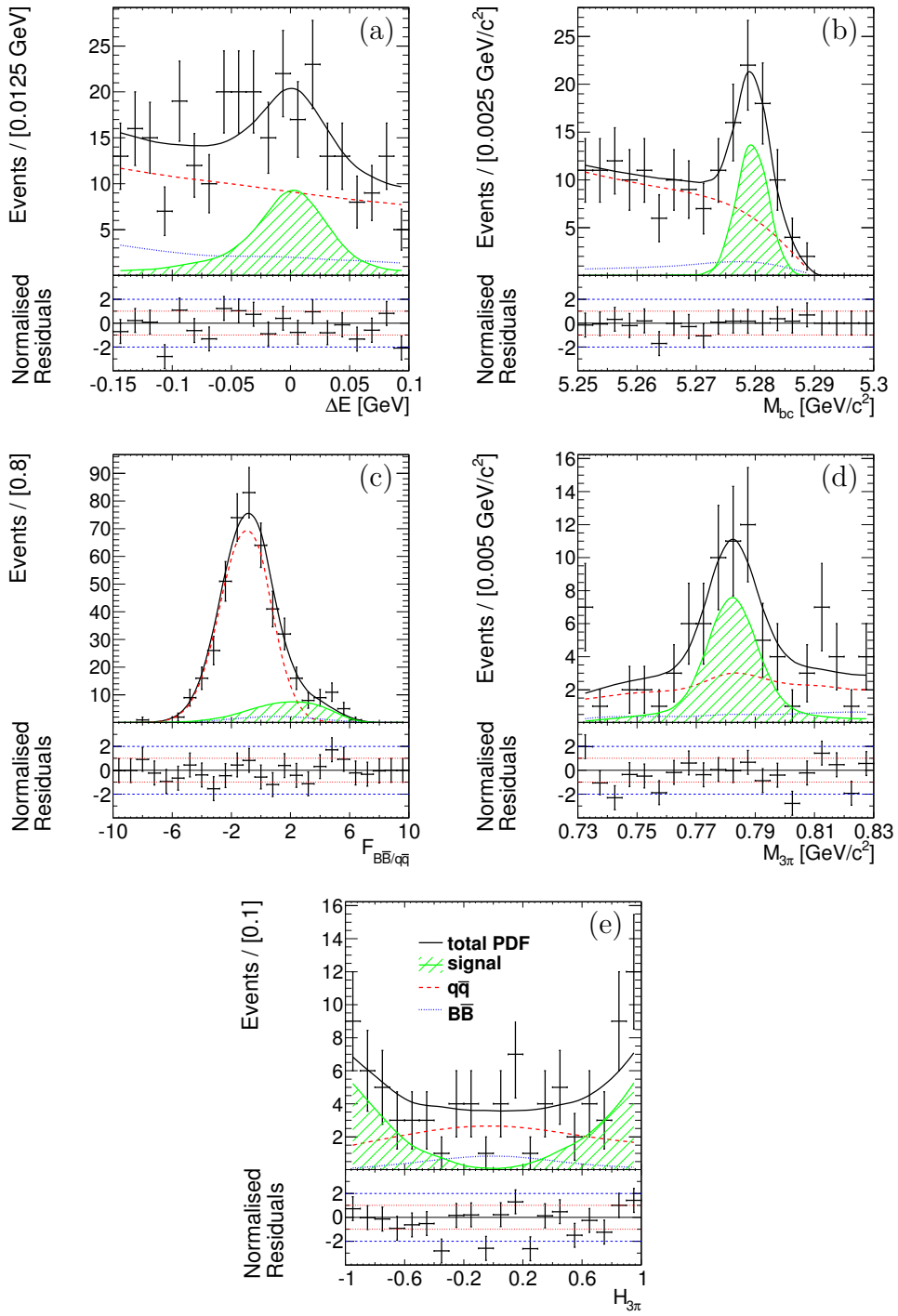

Figure 4.38: Projections of the fit to the $B^0 \to \omega K^0_S$ data enhanced in the signal region. Points with error bars represent the data, and the solid black curves or histograms represent the fit results. The signal enhancements, $-0.04\ \text{GeV} < \Delta E < 0.03\ \text{GeV}$, $M_{\rm bc} > 5.27\ \text{GeV}/c^2$, $\mathcal{F}_{B\overline{B}/q\overline{q}} > 1$, and $r > 0.5$, except for the enhancement of the fit observable being plotted, are applied to each projection. (a), (b), (c), (d), and (e) show the ΔE, $M_{\rm bc}$, $\mathcal{F}_{B\overline{B}/q\overline{q}}$, $M_{3\pi}$, and $\cos\theta_{Hel}$ projections, respectively. Green hatched curves show the $B^0 \to \omega K^0_S$ signal component, dashed red curves indicate the $q\overline{q}$ background and blue dotted curves show the $B\overline{B}$ background component.

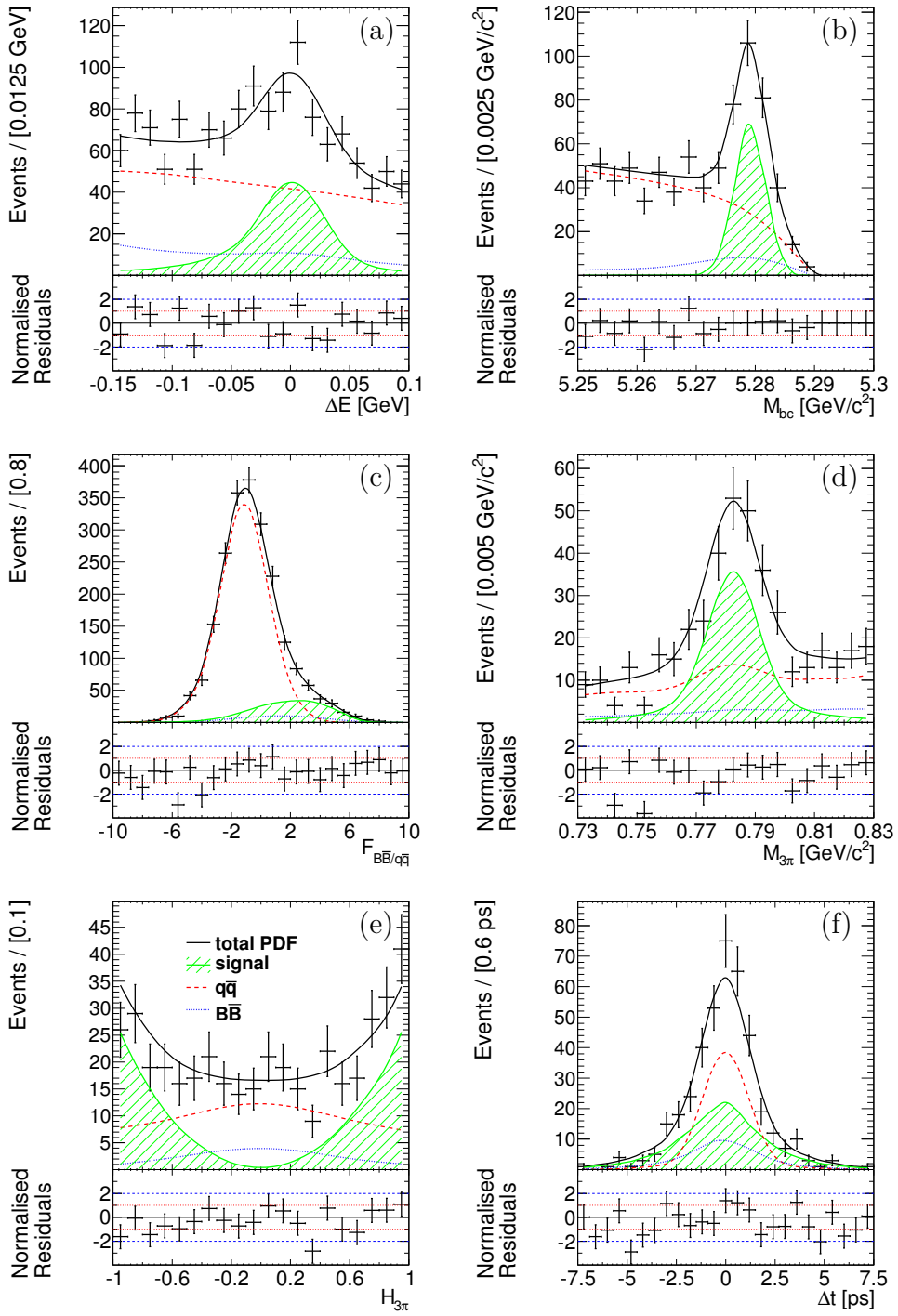

Figure 4.39: Projections of the fit to the $B^{\pm} \to \omega K^{\pm}$ data enhanced in the signal region. Points with error bars represent the data, and the solid black curves or histograms represent the fit results. The signal enhancements, $-0.04\ \text{GeV} < \Delta E < 0.03\ \text{GeV}$, $M_{\text{bc}} > 5.27\ \text{GeV}/c^2$, $\mathcal{F}_{B\overline{B}/q\overline{q}} > 1$, and $r > 0.5$, except for the enhancement of the fit observable being plotted, are applied to each projection. (a), (b), (c), (d), (e), and (f) show the ΔE, M_{bc}, $\mathcal{F}_{B\overline{B}/q\overline{q}}$, $M_{3\pi}$, $\cos\theta_{Hel}$, and Δt projections, respectively. Green hatched curves show the $B^{\pm} \to \omega K^{\pm}$ signal component, dashed red curves indicate the $q\overline{q}$ background and blue dotted curves show the $B\overline{B}$ background component.

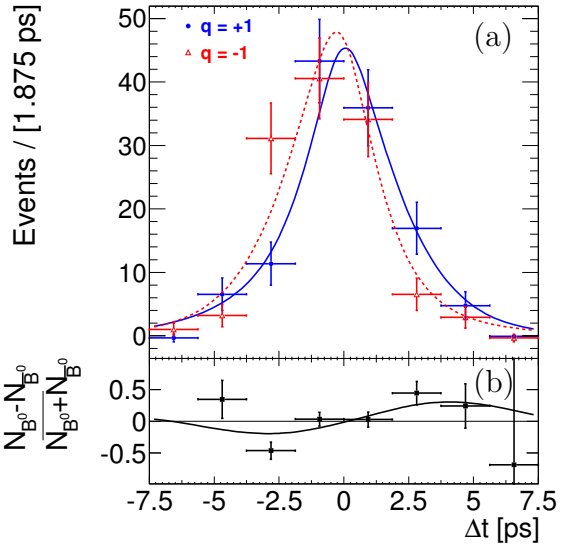

Figure 4.40: Background subtracted time-dependent fit results for $B^0 \to \omega K^0_S$. (a) shows the Δt distribution for each B_{tag} flavour q. The solid blue and dashed red curves represent the Δt distributions for B^0 and $\overline{B}^0$ tags, respectively. (b) shows the asymmetry of the plot above them, $(N_{B^0} - N_{\overline{B}0})/(N_{B^0} + N_{\overline{B}0})$, where N_{B^0} ($N_{\overline{B}0}$) is the measured signal yield of B^0 ($\overline{B}^0$) events in each bin of Δt.

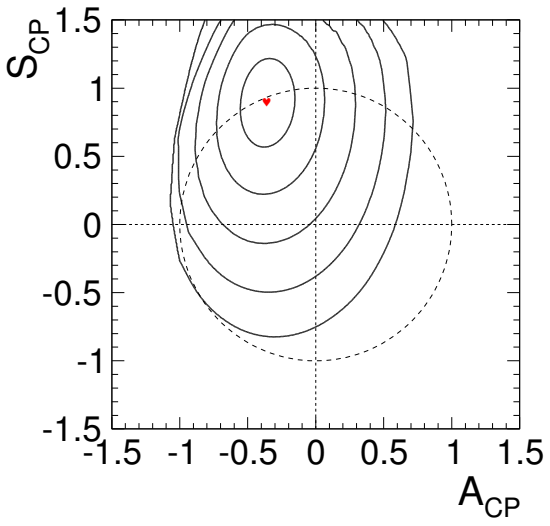

Figure 4.41: Likelihood scan in the $\mathcal{A}_{\omega K^0_S}$-$\mathcal{S}_{\omega K^0_S}$ plane including systematic uncertainties. The dashed circle represents the physical boundary of CP violation. Starting from the red marker in the center that identifies the fit result, the concentric curves represent the contours from 1 to 5 standard deviations from the fit result.

to the presence of misreconstructed π^0 and K^0_S in the signal model. The branching fraction systematic error due to the uncertainty of the relative yield of the misreconstructed signal component is estimated by varying its fraction by the full value estimated from MC simulation. The difference between the generated CP parameters in the MC and the ones obtained from the fit to the misreconstructed signal events is considered as a systematic uncertainty, also labeled as "misreconstructed" in Table 4.7.

We study the uncertainties arising from CP violation in the $B\overline{B}$ background by introducing an artificial CP-violating component, which is set conservatively at 20% of all neutral $B\overline{B}$ events, and vary the CP parameters maximally between $\mathcal{A}_{\omega K^0_S} = \pm 1$ and $\mathcal{S}_{\omega K^0_S} = \pm 1$. Half the fit bias obtained from pseudoexperiment MC studies is taken as an additional systematic uncertainty. A detector bias uncertainty is assigned to $\mathcal{A}_{\omega K^\pm}$, accounting for effects such as asymmetry in PID and tracking efficiencies, material effect using $D^+_s \to \phi[K^+K^-]\pi^+$ and $D^0 \to K^-\pi^+$ samples [83]. Finally, a large number of MC pseudoexperiments are generated, and an ensemble test is performed to obtain possible systematic biases from interference on the tag side arising between the CKM-favored $b\overline{d} \to (c\overline{u}d)\overline{d}$ and doubly CKM-suppressed $\overline{b}d \to (\overline{u}c\overline{d})d$ amplitudes in the final states used for flavour tagging [84].

4.3.10 Outlook to Belle II

The SuperKEKB collider with the Belle II detector [47, 85], scheduled to start operation in 2018, is an upgrade of the original Belle experiment. The SuperKEKB [86, 87] accelarator targets an instant luminosity of 8×10^{35} cm^{-2}s^{-1}, which is almost 40 times higher than its predecessor. A total luminosity of about 50 times the one of Belle is expected to be collected. To exploit it, among other things, a two-layer pixel detector will be added to the Belle detector [86, 88] to improve the SVD vertex resolution. Using this new configuration, an improvement of more than a factor of two for the single track impact parameter resolution compared to Belle is expected.

Assuming that Belle II will collect roughly 50 times the number of $B\overline{B}$ pairs of Belle, it becomes clear that for $B \to \omega K$ it will be able to put the Standard Model to a test.

We have shown that the method presented in this thesis provides superior results than the previous one used by Belle. The improvements are mostly due to the inclusion of additional fit variables such as $\mathcal{F}_{B\overline{B}/q\overline{q}}$ in seven r-bins, $\cos\theta_{Hel}$ and Δt. However, this significantly enhances the complexity of the model and with this also the computation time. With 50 times more events, a model optimization would be inevitable.

The first obvious simplification would be to do the $B^0 \to \omega K^0_S$ and $B^\pm \to \omega K^\pm$ analyses separately, since there will be enough signal events to extract the correction factors to the kinematic observables for each mode individually from the data. Another possible improvement would be to include the ω amplitude in the Fisher discriminant as it is done with the B meson flight direction, as shown in Section 4.2.7.3, which is expected to enhance the the separation between signal and continuum and could help toreduce this dominant background. The same approach could probably be used for $M_{\rm bc}$, with which its discrimination power would be preserved but the amount of fit observables would be lowered. In addition, the significant correlation between $M_{\rm bc}$ and ΔE in the signal would be reduced and the ones between $M_{\rm bc}$ and $\mathcal{F}_{B\overline{B}/q\overline{q}}$ in some $B\overline{B}$ backgrounds would not be present, which would additionally simplify the model.

Not only the analysis technique but also the tools used would need an improvement. For example, an accurate Monte Carlo simulation of the $q\overline{q}$ background would be needed. Due to the lack of it, we model the continuum using sideband data, which is a dangerous approach,

since it is not sensitive to correlations in the signal region.

At Belle II, the B $\to \omega$K measurements will be dominated by their systematic uncertainties. Thus, these will need to be reduced as much as possible. The major systematic uncertainties in this analysis arise from the π^0 reconstruction efficiency and the Δt resolution. To reduce the first one, studies based on hadronic τ decays could be used, in which the observed rates of $\tau^- \to \pi^-\pi^0\nu_\tau$ and $\tau^- \to \pi^-\nu_\tau$ are compared. The branching fractions of the two decays are known with sub-percent precision, allowing a measurement of the π^0 reconstruction efficiency with an uncertainty of the order of 1%. The Δt resolution is expected to be improved by the PXD detector. In addition, developing a better algorithm for the tag-side vertex would further reduce this uncertainty.

Category	$\delta\mathcal{B}(\omega K^0)$ (%)	$\delta\mathcal{A}_{\omega K^0_S}$ (10^{-2})	$\delta\mathcal{S}_{\omega K^0_S}$ (10^{-2})	$\delta\mathcal{B}(\omega K^\pm)$ (%)	$\delta\mathcal{A}_{\omega K^\pm}$ (10^{-2})
$N_{B\overline{B}}$	1.4	N/A	N/A	1.4	N/A
π^0 reconstruction	4.0	N/A	N/A	4.0	N/A
K^0_S reconstruction	0.8	N/A	N/A	N/A	N/A
PID	1.8	N/A	N/A	2.8	N/A
Tracking	0.7	N/A	N/A	1.1	N/A
IP profile	0.4	0.1	1.2	0.2	N/A
B_{tag} track selection	0.5	0.2	0.3	0.2	N/A
Track helix error	0.0	0.0	0.0	0.0	N/A
Δt selection	0.6	0.0	0.1	0.1	N/A
Vertex quality selection	0.9	0.3	0.5	0.9	N/A
Δz bias	N/A	0.5	0.4	N/A	N/A
Misalignment	N/A	0.4	0.2	N/A	N/A
Physics parameters	0.0	0.1	0.1	0.0	0.0
Δt resolution function	0.6	2.6	4.4	0.8	0.7
Flavour tagging	0.0	0.3	0.8	0.0	N/A
Misreconstruction	0.9	0.1	0.3	0.7	0.1
$B\overline{B}$ background yields	0.8	0.2	0.5	0.9	0.3
Parametric shape	1.8	0.5	1.5	1.0	0.5
Nonparametric shape	0.1	0.1	0.2	0.1	0.3
Fit bias	0.6	0.7	0.1	0.9	0.3
Detector bias	N/A	N/A	N/A	N/A	0.3
Background CP violation	N/A	1.5	1.4	N/A	0.1
Tag-side interference	N/A	3.2	0.2	N/A	N/A
Total	5.5	4.6	5.2	5.6	1.0

Table 4.7: Systematic uncertainties of the $B \to \omega K$ branching fractions and CP asymmetries. The uncertainties on the CP parameters are absolute, while those on the branching fractions are given as their percentages.

Chapter 5

Measurement of the $B^0 \to \psi(2S)\pi^0$ Branching Fraction

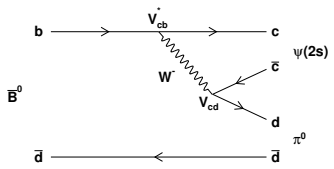

In this chapter, the measurement of the $B^0 \to \psi(2S)\pi^0$ branching fraction is presented. First, the theoretical aspects of the decay are shown. Next, an overview of the reconstruction algorithm is given. Then the event model and its performance are explained. In the end, the results and the main systematic uncertainties are discussed.

5.1 Phenomenology of the $B^0 \to \psi(2S)\pi^0$ Decay

The second analysis presented this thesis is of the decay $B^0 \to \psi(2S)\pi^0$, which has not been observed before. The leading-order decay processes are shown in Figure 5.1. The dominant contribution is a $b \to c\bar{c}d$ tree transition. A $b \to dc\bar{c}$ loop process is also possible but strongly suppressed due to the presence of three gluons in the interaction, which are required for colour and spin conservation reasons.

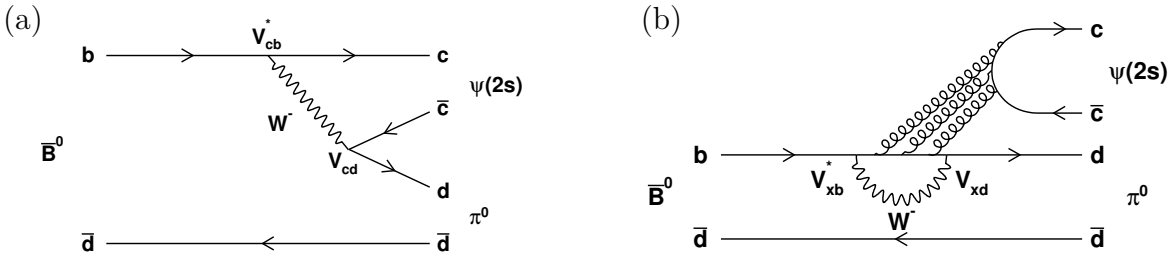

Figure 5.1: Leading-order Feynman diagrams for $B^0 \to \psi(2S)\pi^0$. (a) shows the tree and (b) shows the loop diagram, where the subscript x in V_{xb} denotes the flavour of the intermediate-state up-type quark ($x = u, c, t$).

$\psi(2S)\pi^0$ is a CP final state. Its CP eigenvalue is determined as

$$\eta_{CP} = CP(\psi(2S)) \cdot CP(\pi^0) \cdot (-1)^L = 1 \cdot (-1) \cdot (-1)^1 = 1, \tag{5.1}$$

where $L = 1$ is the relative angular momentum of $\psi(2S)$ and π^0. Assuming only a tree decay contribution and neglecting the loop process, the parameter λ_{CP} is given by

$$\lambda_{CP} = \eta_{CP} \cdot \left(\frac{p}{q}\right)_B \cdot \frac{\bar{A}_{\psi(2S)\pi^0}}{A_{\psi(2S)\pi^0}} = \frac{V_{td}V_{tb}^*}{V_{td}^*V_{tb}} \cdot \frac{V_{cb}V_{cd}^*}{V_{cb}^*V_{cd}} = e^{-2i\phi_1}. \tag{5.2}$$

With this,

$$\mathcal{S}_{CP}(B^0 \to \psi(2S)\pi^0) \equiv \mathcal{S}_{\psi(2S)\pi^0} = \frac{2\,\mathrm{Im}(\lambda_{CP})}{|\lambda_{CP}|^2 + 1} = -\sin 2\phi_1, \tag{5.3}$$

thus, $B^0 \to \psi(2S)\pi^0$ is sensitive to the angle ϕ_1 of the unitarity triangle.

There is no theoretical prediction for the expected branching fraction of $B^0 \to \psi(2S)\pi^0$. However, it is possible to roughly estimate it from the measured branching fractions of other B^0 decays. $B^0 \to \psi(2S)\pi^0$ is a decay that in its leading order process is similar to the "golden channel", $B^0 \to J/\psi K_S^0$. There are two major differences. First, $B^0 \to \psi(2S)\pi^0$ is suppressed by the CKM element $|V_{cd}| \approx \lambda$ (see Section 1.2.2.2), while $B^0 \to J/\psi K_S^0$ has $|V_{cs}| \approx 1$. Since $B^0 \to \psi(2S)\pi^0$ has the same quark content as $B^0 \to \psi(2S)\pi^0$, the $B^0 \to \psi(2S)\pi^0$ branching fraction can give us information about the strength of the CKM suppression. Second, $B^0 \to \psi(2S)\pi^0$ is further suppressed due to the radial excitation in $\psi(2S)$, which can be calculated using the fraction between $\mathcal{B}(B^0 \to \psi(2S)K^0)$ and $\mathcal{B}(B^0 \to J/\psi K^0)$. Taking these two arguments into consideration, we can predict the $B^0 \to \psi(2S)\pi^0$ branching fraction using the ratio

$$\frac{\mathcal{B}(B^0 \to \psi(2S)\pi^0)}{\mathcal{B}(B^0 \to J/\psi\pi^0)} = \frac{\mathcal{B}(B^0 \to \psi(2S)K^0)}{\mathcal{B}(B^0 \to J/\psi K^0)}. \tag{5.4}$$

We obtain $\mathcal{B}(B^0 \to \psi(2S)\pi^0) = 1.25 \times 10^{-5}$.

The decay mode $B^0 \to \psi(2S)\pi^0$ gives model-independent information about the pollution by second-order processes in $B^0 \to \psi(2S)K^0$, constraining the theoretical uncertainty on $\sin 2\phi_1$ and potentially giving information about new physics contribution. The procedure is analogous to the one used for $B^0 \to J/\psi\pi^0$, which is described in [89]. Although Belle is still not sensitive to second-order contributions in $B^0 \to \psi(2S)\pi^0$, Belle II will be. However, an observation of the decay mode would be the first step to the measurement of its properties. We do not attempt a time-dependent measurement at this point due to the low amount of signal events.

5.2 Signal Reconstruction

Just as in the $B \to \omega K$ analysis, the measurement of the $B^0 \to \psi(2S)\pi^0$ branching fraction is based on the blind analysis technique.

5.2.1 Decay Channels

$B^0 \to \psi(2S)\pi^0$ is reconstructed from $\pi^0 \to \gamma\gamma$ and four subdecays of the $\psi(2S)$ resonance:

- $\psi(2S) \to e^+e^-$, with a branching fraction of 7.9×10^{-3}

- $\psi(2S) \to \mu^+\mu^-$, with a branching fraction of 7.9×10^{-3}
- $\psi(2S) \to J/\psi[e^+e^-]\pi^+\pi^-$, with a branching fraction of 2%, taking into account that $\psi(2S) \to J/\psi\pi^+\pi^-$ occurs to 34% and $J/\psi \to e^+e^-$ occurs to 5.9%.
- $\psi(2S) \to J/\psi[\mu^+\mu^-]\pi^+\pi^-$, with a branching fraction of 2%, where $J/\psi \to \mu^+\mu^-$ has a branching fraction of 5.9%.

All branching fractions are taken from [27]. We choose these particular decays because they consist only of charged tracks. With this, we avoid a B meson reconstruction with more than one neutral particle. This has the advantage of little combinatorial background due to multiple pion candidates and less prominent correlations between the fit observables. In the following, we refer to the first two modes as "leptonic" and to the second two modes as "hadronic".

5.2.2 Monte Carlo and Data Samples

The main background originates from other $b \to c\bar{c}q$ decays. There is also a contribution from a combinatorial background, which consists of a mixture of $q\bar{q}$ and other B meson decays. We base our studies on the following MC and data samples.

- Signal MC: It consists of a sample containing exclusively $B^0\overline{B}^0$ pairs, in which one of the B^0 mesons decays as $B^0 \to \psi(2S)\pi^0$ and the other one follows the B meson decay probabilities in PDG. 1 000 000 events were generated for each SVD configuration.
- $b \to c\bar{c}q$ MC: These MC samples contain all known B meson decays occurring via $b \to c\bar{c}q$ transitions, with $q = u, d, s$. There are two $b \to c\bar{c}q$ MC samples – one with neutral and one with charged B meson pairs. The number of events in these MC samples is 100 times their expected contribution to the full data taken by Belle.
- On-resonance data: The full data set of 772×10^6 $B\overline{B}$ events at the $\Upsilon(4S)$ resonance. It is used both for the branching fractions and the study of the combinatorial background shape.

5.2.3 *CP* Side Reconstruction

Just as in the $B \to \omega K$ analysis, we first reconstruct the daughter particles – leptons and pions – and build from them the J/ψ, $\psi(2S)$ and B^0 candidates. In the following, we give an overview of the selection criteria.

5.2.3.1 Continuum Suppression

To suppress continuum events in the data, we apply a cut on the ratio between the second and the zeroth Fox-Wolfram moment [78],

$$R_2 = \frac{H_2}{H_0}, \tag{5.5}$$

where H_0 and H_2 are defined as in Eq. 4.32. We require $R_2 \leq 0.5$. As shown in Figure 5.2, this is a loose cut, which removes around one quarter of the combinatorial background with a negligible loss of signal efficiency. The peak in the background distribution is due to a contribution from B meson decays. After the cut on R_2, their fraction is found the be around 50% of the total background.

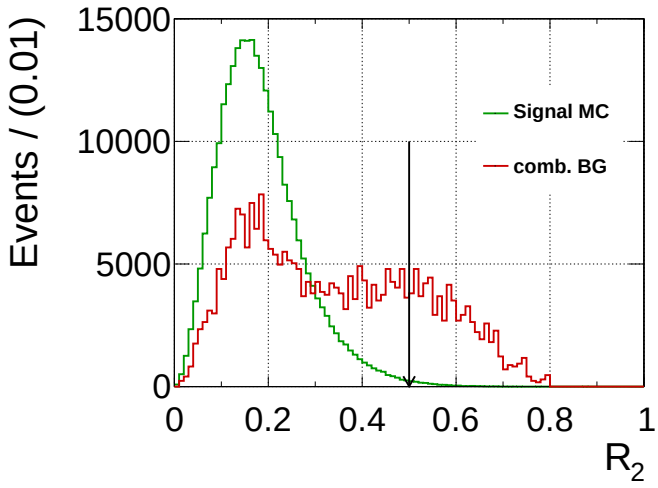

Figure 5.2: R_2 distributions for signal (green) and sideband data (red).

5.2.3.2 π^0 Reconstruction

The neutral pion candidates are reconstructed in the same way as for $B \to \omega K$, which is presented in Section 4.2.3.2. The π^0 candidates' mass distribution is shown in Figure 5.3.

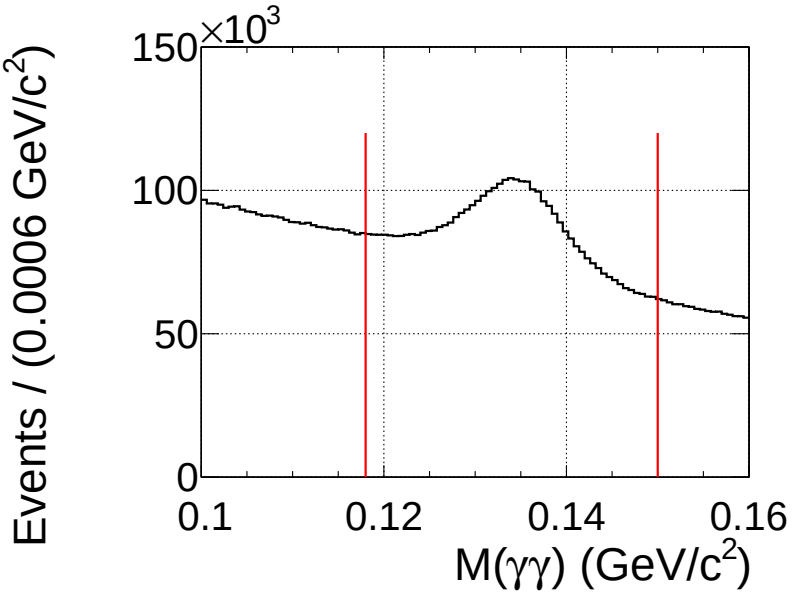

Figure 5.3: Mass distribution of the π^0 candidates in $B^0 \to \psi(2S)\pi^0$ MC before the application of the selection criteria.

5.2.3.3 Charged Track Selection

The charged pions and leptons are required to have a distance of closest approach, dr, between their track and the IP of $dr < 1.5\,\text{cm}$ and a longitudinal distance, dz, of $|dz| < 5\,\text{cm}$.

Lepton Selection
The e^+ and e^- candidates must have an electron ID (see Section 4.2.3.1) $\mathcal{L}_{e/h} > 0.01$. Electrons and positrons radiate photons while propagating through the detector and thus lose a part of their energy. To account for this energy loss, we include to the e^+/e^- four-momentum all photon four-momenta that are in a cone with an opening angle of 50 mrad around the lepton flight direction.

The μ^+ and μ^- candidates are identified using information from the KLM detector with expectations based on extrapolation of the CDC track. For the corresponding likelihood ratio, built using the same principle as the electron and the pion/kaon likelihood ratios, we require $\mathcal{L}_\mu > 0.1$.

Charged Pion Selection
To remove low-energy pion background, only π^+-π^- candidate pairs with a combined mass higher than 400 MeV/c^2 are retained. We also require $\mathcal{L}_{K/\pi} < 0.9$ for each charged pion candidate, where $\mathcal{L}_{K/\pi}$ is defined as in Section 4.2.3.1.

5.2.4 J/ψ Reconstruction

The J/ψ candidates are reconstructed from e^+e^- and from $\mu^+\mu^-$ pairs. On the e^+e^- pair, we place the requirement $-150\ \text{MeV}/c^2 \leq M_{e^+e^-} - M_{J/\psi} \leq 36\ \text{MeV}/c^2$, where $M_{J/\psi} = 3.097\ \text{GeV}/c^2$ [27] is the world average value of the J/ψ mass. This cut is asymmetric to account for the energy loss from bremsstrahlung, which creates a radiative tail in the mass distribution towards lower values. The mass cut on the $\mu^+\mu^-$ pairs is $-60\ \text{MeV}/c^2 \leq M_{\mu^+\mu^-} - M_{J/\psi} \leq 36\ \text{MeV}/c^2$. The J/$\psi$ mass distribution for signal MC events is shown in Figure 5.4. To improve the energy resolution, a kinematic fit is performed on the J/ψ candidates. In this procedure, the energy is obtained from the J/ψ candidate momentum and the world average J/ψ mass value, which is enforced to be the candidate's mass.

5.2.5 ψ(2S) Reconstruction

The ψ(2S) candidates are reconstructed from $\psi(2S) \to e^+e^-$, $\psi(2S) \to \mu^+\mu^-$ and $\psi(2S) \to J/\psi\pi^+\pi^-$. The two leptonic modes are treated in exactly the same was as in the J/ψ reconstruction 5.2.4, with mass cuts of $-150\ \text{MeV}/c^2 \leq M_{e^+e^-} - M_{\psi(2S)} \leq 36\ \text{MeV}/c^2$ and $-60\ \text{MeV}/c^2 \leq M_{\mu^+\mu^-} - M_{\psi(2S)} \leq 36\ \text{MeV}/c^2$, where $M_{\psi(2S)} = 3.686\ \text{GeV}/c^2$ [27] is the world average value of the ψ(2S) mass. Since the J/ψ candidate mass is already constrained, in $\psi(2S) \to J/\psi\pi^+\pi^-$ we only need to cut on the $\pi^+\pi^-$ mass. It is required to be in the range $580\ \text{MeV}/c^2 \leq M_{J/\psi(\ell^+\ell^-)\pi^+\pi^-} - M_{J/\psi} \leq 600\ \text{MeV}/c^2$. The mass cuts are illustrated in Figure 5.5. Just like the J/ψ candidates, the ψ(2S) candidates are also a subject to a kinematic fit.

5.2.6 B^0 Reconstruction

We reconstruct the B^0 meson candidates from a ψ(2S) and a π^0 candidate.

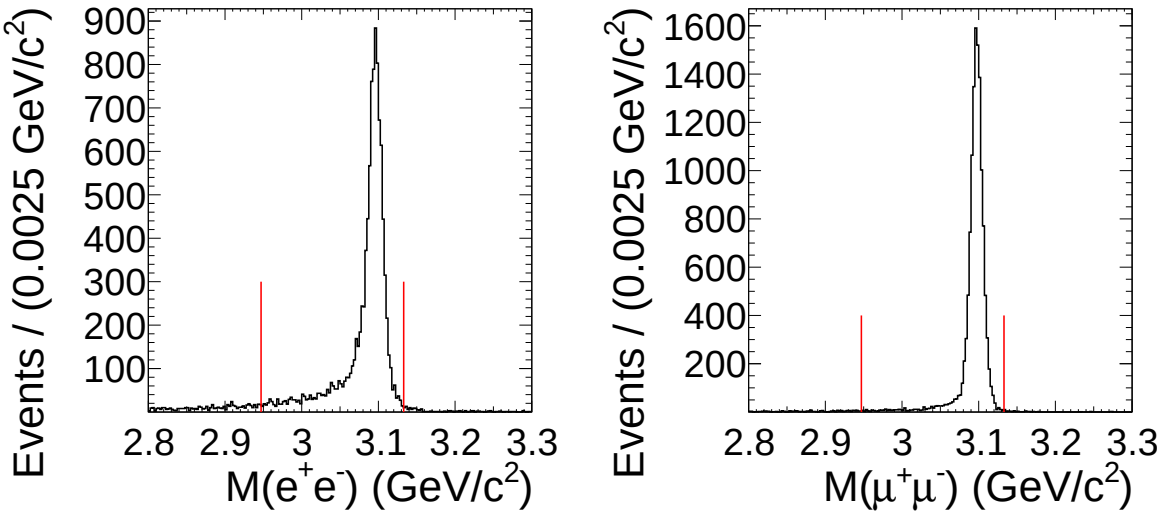

Figure 5.4: J/ψ candidate mass distribution for J/$\psi \to e^+e^-$ (left) and J/$\psi \to \mu^+\mu^-$ (right) from signal MC.

5.2.6.1 ΔE and $M_{\rm bc}$

The B^0 beam-constrained mass, $M_{\rm bc}$, is defined in a similar way as in Section 4.2.3.5. The only difference is that we calculate the π^0 momentum using the $\psi(2S)$ and beam energies $E_{\psi(2S)}$ and E_{beam}, obtaining

$$M_{\rm bc} = \sqrt{E_{beam}^2 - \left| \overrightarrow{p}_{\psi(2S)} + \sqrt{(E_{beam} - E_{\psi(2S)})^2 - M_{\pi^0}^2} \frac{\overrightarrow{p}_{\pi^0}}{|\overrightarrow{p}_{\pi^0}|} \right|^2}, \tag{5.6}$$

where $\overrightarrow{p}_{\psi(2S)}$ and $\overrightarrow{p}_{\pi^0}$ are the $\psi(2S)$ and π^0 momenta, respectively, and M_{π^0} is the world average of the neutral pion mass. Modifying $M_{\rm bc}$ in such a way reduces the correlation between $M_{\rm bc}$ and ΔE from 6-8% to 1-2%, depending on the $\psi(2S)$ decay mode. We require $5.22\ \text{GeV}/c^2 \leq M_{\rm bc} \leq 5.30\ \text{GeV}/c^2$.

We retain only B^0 candidates with $-0.2\ \text{GeV} \leq \Delta E \leq 0.1\ \text{GeV}$, where ΔE is defined as in Section 4.2.3.5.

5.2.6.2 B^0 Meson Vertex

We do not need to reconstruct the vertex of the B^0 meson, since we neither perform a CP analysis nor we use Δt as a fit observable. However, to prepare the reconstruction algorithm for a future measurement of the time-dependent CP parameters, we perform a CP-side vertexing. We use the same procedure as for $B \to \omega K$ (see Section 4.2.3.5), including all charged tracks into the vertex fit. For the leptonic modes, these are the two $\psi(2S)$ daughter leptons and for the hadronic modes – the J/ψ daughter leptons and the two charged pions.

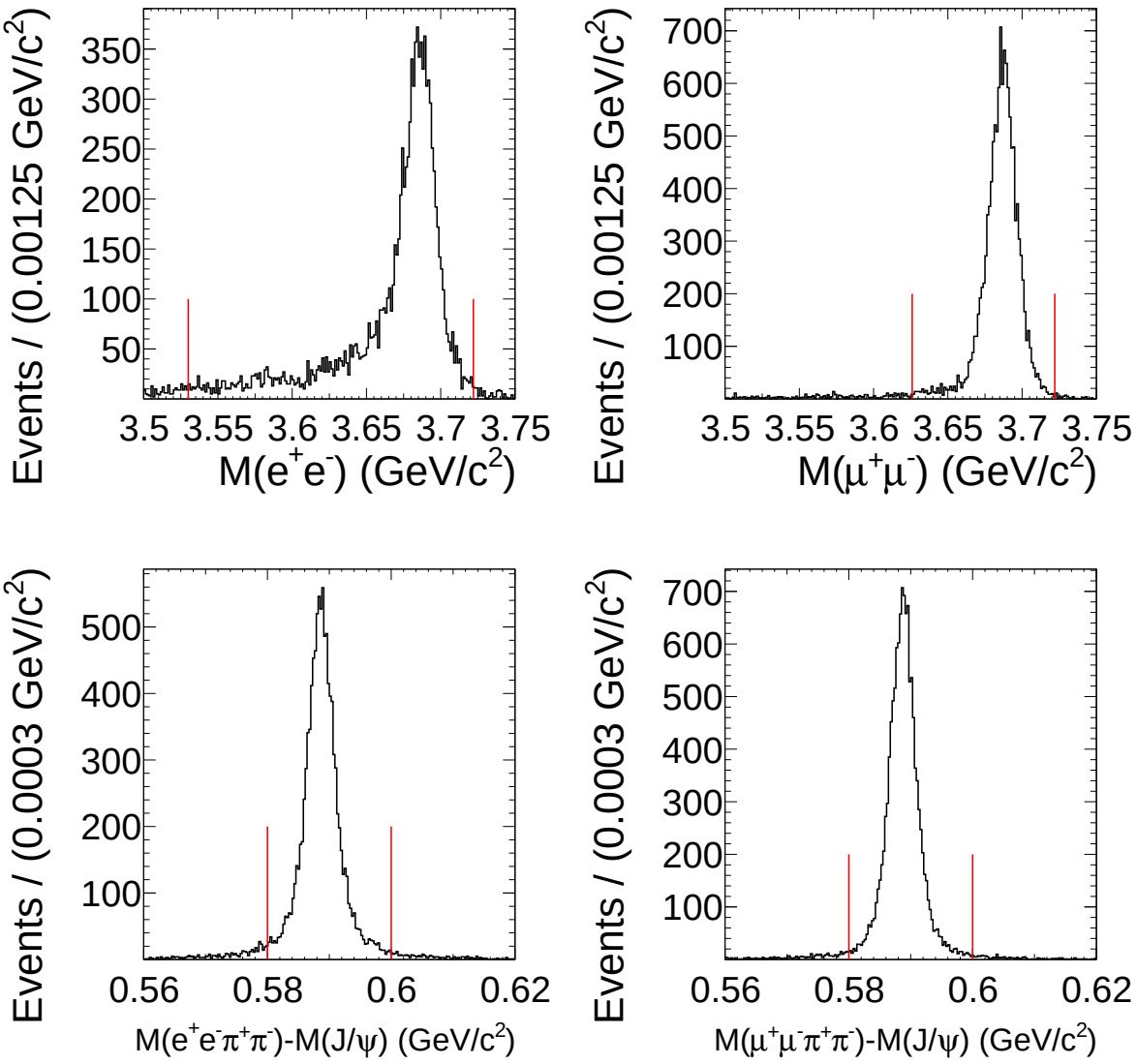

Figure 5.5: $\psi(2S)$ candidate mass distribution for $\psi(2S) \to e^+e^-$ (upper left) and $\psi(2S) \to \mu^+\mu^-$ (upper right). $\pi^+\pi^-$ candidate pair invariant mass distribution for $\psi(2S) \to J/\psi[e^+e^-]\pi^+\pi^-$ (lower left) and $\psi(2S) \to J/\psi[\mu^+\mu^-]\pi^+\pi^-$ (lower right) from signal MC.

5.2.6.3 Best B Candidate Selection

On average, 1.13 B^0 candidates are reconstructed per event. The event multiplicity is shown in Figure 5.6. In each event, we choose the B with the lowest χ^2, defined as

$$\chi^2 = \frac{1}{2}\left[\left(\frac{M_{\bar{\ell}\ell} - M_{\psi(2S)}}{\sigma_{\psi(2S),\bar{\ell}\ell}}\right)^2 + \left(\frac{M_{\gamma\gamma} - M_{\pi^0}}{\sigma_{\gamma\gamma}}\right)^2\right] \tag{5.7}$$

for the $\psi(2S)$ leptonic decay modes and as

$$\chi^2 = \frac{1}{3}\left[\left(\frac{M_{\bar{\ell}\ell} - M_{J/\psi}}{\sigma_{J/\psi,\bar{\ell}\ell}}\right)^2 + \left(\frac{M_{\pi^+\pi^-} - (M_{\psi(2S)} - M_{J/\psi})}{\sigma_{\pi^+\pi^-}}\right)^2 + \left(\frac{M_{\gamma\gamma} - M_{\pi^0}}{\sigma_{\gamma\gamma}}\right)^2\right] \tag{5.8}$$

for $\psi(2S) \to J/\psi\pi^+\pi^-$. $M_{\bar{\ell}\ell}$ denotes the mass of the $\psi(2S)$ (J/ψ) candidate in the first (second) equation, $M_{\gamma\gamma}$ is the mass of the π^0 candidate and $M_{\pi^+\pi^-}$ is the total mass of the two pion candidates in the $\psi(2S)$ hadronic decay modes; $M_{\psi(2S)}$, $M_{J/\psi}$ and M_{π^0} are the world averages for the $\psi(2S)$, J/ψ and π^0 masses, respectively; the $\sigma_{\psi(2S)/J/\psi}$ factors represent mass resolutions of the respective particles, taken from [90] and summarized in Table 5.1. The last quotient in both equations is equivalent to the χ^2 obtained from the π^0 mass fit. The factors 1/2 and 1/3 are a normalization, which accounts for the different number of terms in the two formulae.

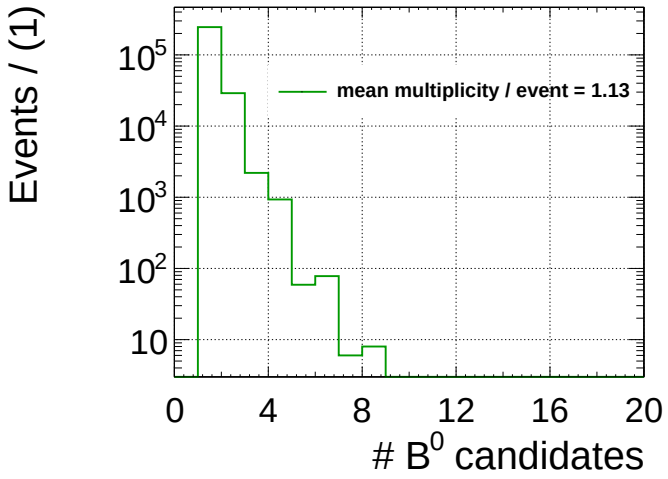

Figure 5.6: Number of reconstructed B^0 candidates per event in $B^0 \to \psi(2S)\pi^0$ signal Monte Carlo.

5.2.7 Tag-Side Reconstruction

For the purposes of a future CP analysis, we reconstruct the tag-side vertex and determine the B^0 flavour using the same algorithm as in presented in Section 4.2.4.

5.2.8 Reconstruction Efficiency and Signal Purity

The reconstruction efficiencies are calculated from the raw efficiency multiplied by the respective subdecay branching fractions of $\psi(2S)$ and J/ψ. A B meson is classified as correctly reconstructed if its vertex is reconstructed from the charged tracks that belong to it. The rest of the events are defined as misreconstructed. The detection efficiency and signal purity (see Section 4.2.10) for the four decay modes are listed in Table 5.2.

5.3 Event Model

The $B^0 \to \psi(2S)\pi^0$ branching fraction, $\mathcal{B}(B^0 \to \psi(2S)\pi^0)$, is obtained from a two-dimensional unbinned extended maximul likelihood fit to

- -0.2 GeV $\leq \Delta E \leq 0.1$ GeV
- 5.22 GeV/$c^2 \leq M_{\rm bc} \leq$ 5.30 GeV/c^2.

We extract a signal yield and determine $\mathcal{B}(B^0 \to \psi(2S)\pi^0)$ according to Eq. 3.4.

The following categories are considered in the event model:

- correctly reconstructed signal
- misreconstructed signal
- $b \to c\bar{c}q$ events
- combinatorial background.

Since a low number of events is expected in the data, we make a common model for the two SVD configurations. However, for reasons to be explained in the next subsection, the correctly reconstructed signal events are divided into other two subcategories – events with a e^+e^- pair and events with a $\mu^+\mu^-$ pair. Each category has its own model. The misreconstructed signal and the combinatorial background are treated in the same way. The $c\bar{c}$ background is subdivided into a leptonic and a hadronic component. Unless otherwise stated, the probability density function for each category is taken as the product of PDFs for each variable,

$$\mathcal{P}^c(\Delta E, M_{\rm bc}) \equiv \mathcal{P}^c(\Delta E) \times \mathcal{P}^c(M_{\rm bc}), \tag{5.9}$$

in each event category, c. The fit models are described in the following subsections.

5.3.1 Correctly Reconstructed Signal Events

Figure 5.7 shows the ratios between the ΔE and $M_{\rm bc}$ shapes of three $\psi(2S)$ decay channels normalized by the remaining one – $\psi(2S) \to e^+e^-$. We find the ΔE shapes to be all very similar; the $M_{\rm bc}$ distributions of the $\psi(2S) \to e^+e^-$ and $\psi(2S) \to J/\psi[e^+e^-]\pi^+\pi^-$ decay channels are alike and so are the ones of the $\psi(2S) \to \mu^+\mu^-$ and $\psi(2S) \to J/\psi[\mu^+\mu^-]\pi^+\pi^-$ decay modes. This is why we divide the signal MC into an electron and a muon component.

The projections of the fit observables are shown in Figure 5.8. The ΔE PDF is a combination of a Crystal Ball function (see Appendix A) and a first-order Chebyshev function,

$$\begin{aligned}\mathcal{P}^c_{Sig}(\Delta E) \equiv\ & f^c{\rm CB}(\Delta E; \alpha,\, n,\, \mu^c + \mu_C,\, \sigma^c\sigma_C) \\ & +(1 - f^c)(1 + c^c\Delta E),\end{aligned} \tag{5.10}$$

where μ_C and σ_C are correction factors obtained from the control sample, $B^\pm \to J/\psi K^{*\pm}$.

The $M_{\rm bc}$ PDF for both modes consists of a Crystal Ball function, combined with an ARGUS distribution to additionally account for the radiative tail towards lower $M_{\rm bc}$ values. Because of a correlation between ΔE and $M_{\rm bc}$, we parametrize the $M_{\rm bc}$ PDF in terms of ΔE,

$$\begin{aligned}\mathcal{P}^c_{Sig}(M_{\rm bc}|\Delta E) \equiv\ & (f^c + \alpha^c\Delta E^2){\rm CB}(M_{\rm bc}; \alpha,\, n,\, \mu^c + \mu_C,\, \sigma^c\sigma_C + \beta^c{\rm fcn}^c(\Delta E)) \\ & +(1 - [f^c + \alpha^c\Delta E^2]){\rm ARGUS}(M_{\rm bc}; a^c),\end{aligned} \tag{5.11}$$

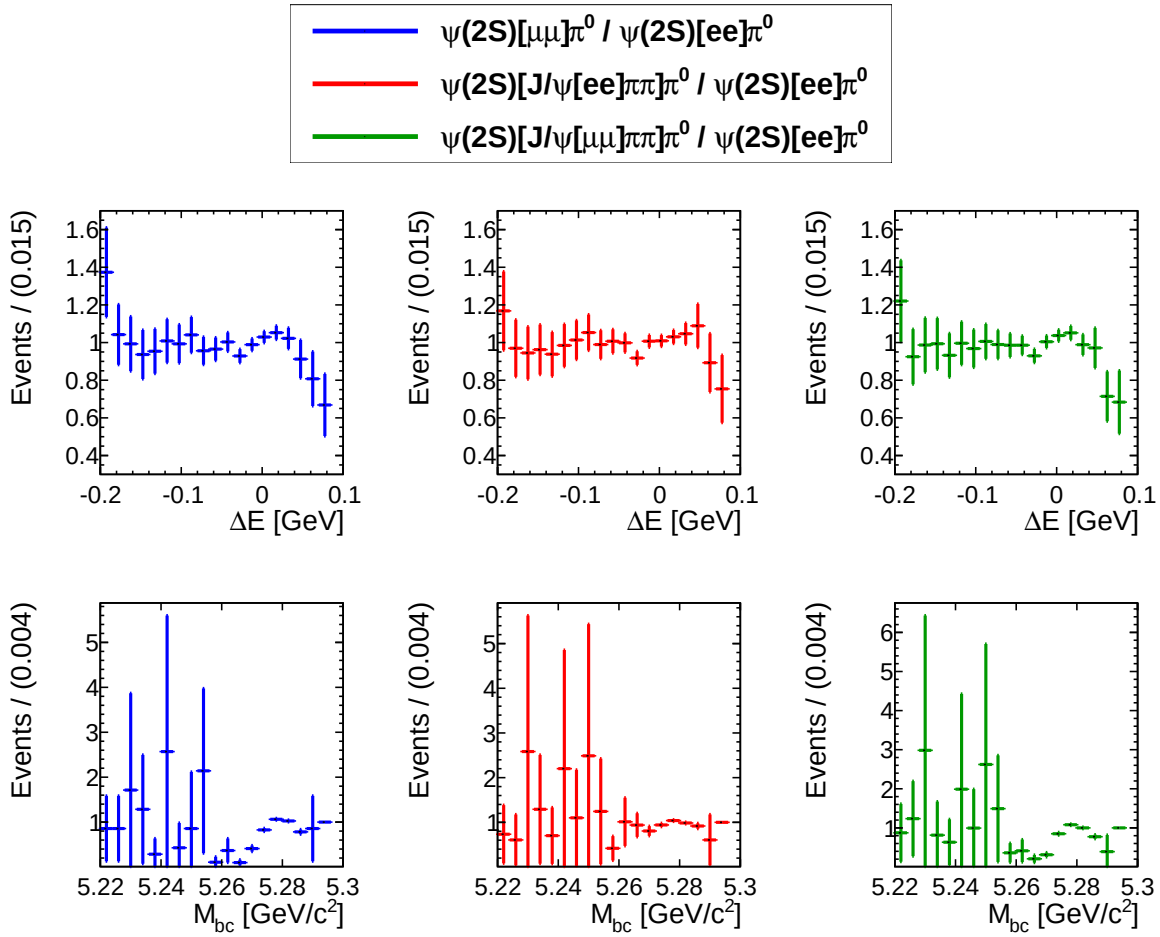

Figure 5.7: $B^0 \to \psi(2S)\pi^0$ signal MC ΔE (up) and $M_{\rm bc}$ (down) ratios between the four $\psi(2S)$ decay channels.

where μ_C and σ_C are correction factors obtained from the control sample; α^c and β^c are correlation factors and $\mathrm{fcn}^c(\Delta E)$ are functions in ΔE,

$$\mathrm{fcn}(\Delta E) = \begin{cases} \Delta E^2, & \text{for} \quad e^+e^- \\ |\Delta E|, & \text{for} \quad \mu^+\mu^- \end{cases}.$$

Projections of $M_{\rm bc}$ in slices of ΔE are shown in Figure 5.9 and in Figure 5.10. Although the correlation is small, the dependecy of $M_{\rm bc}$ on ΔE is visible in the plots.

5.3.2 Misreconstructed Signal Events

While the fraction of misreconstructed signal events is negligible in the leptonic decay modes, they are approximately 10% of the signal events in the two hadronic modes. We fit this component using a two-dimensional histogram in ΔE-$M_{\rm bc}$. This way, we automatically account for the strong correlations of 10-15% between the two fit observables. This approach is only possible for shapes which are not corrected in the fit to the data, which is the case of the misreconstructed signal events. The fit projections are shown in Figure 5.11.

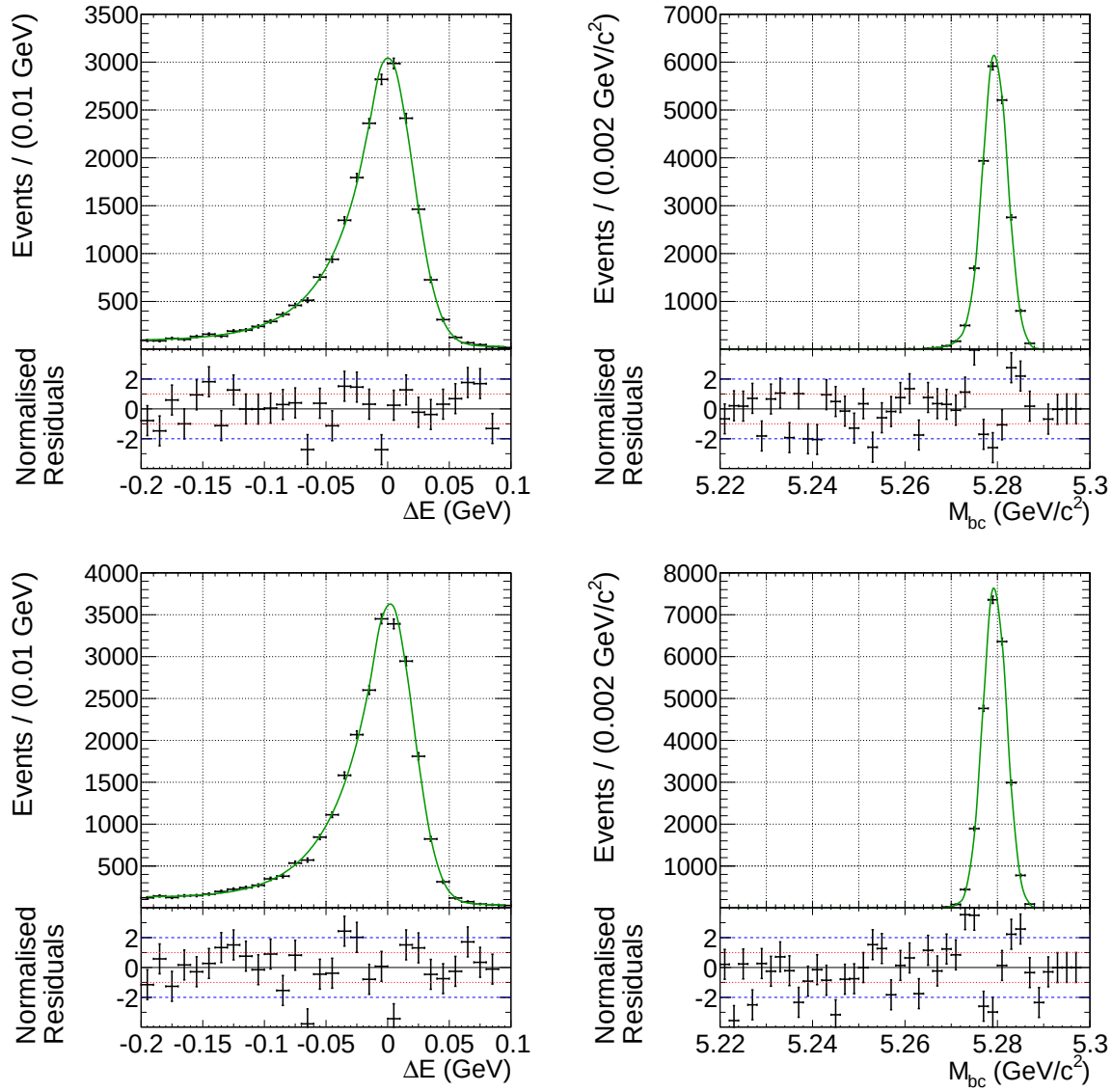

Figure 5.8: $B^0 \to \psi(2S)\pi^0$ ΔE and M_{bc} projections of the fit to the electron (up) and muon (down) signal events.

5.3.3 $c\bar{c}$ Background Events

Figure 5.12 shows the ΔE and M_{bc} ratios between the distributions of the four $\psi(2S)$ decay modes in the $c\bar{c}$ background. Since the two leptonic channels seem to behave in a similar way and the two hadronic ones express the same feautures, we divide the events into a leptonic and a hadronic subsample. Each of them we fit with a two-dimensional histogram in ΔE-M_{bc}, as shown in Figure 5.13.

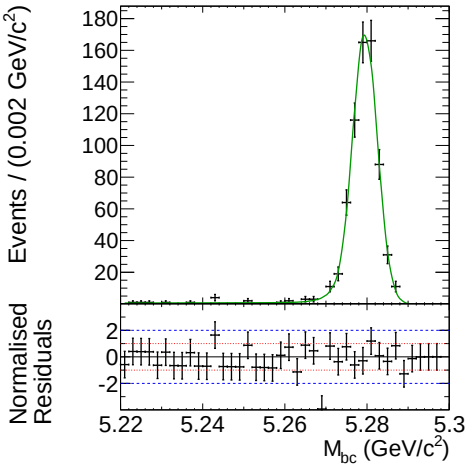

-0.2 GeV $\leq \Delta$E ≤ -0.14 GeV

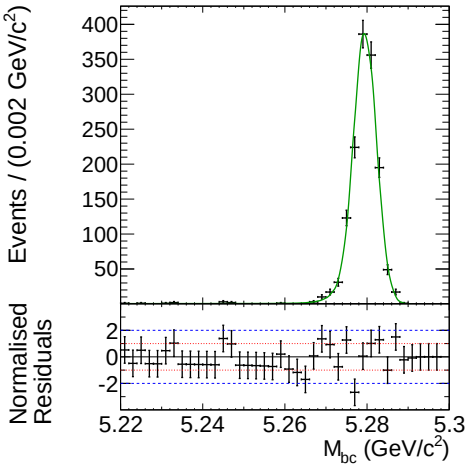

-0.14 GeV $\leq \Delta$E ≤ -0.08 GeV

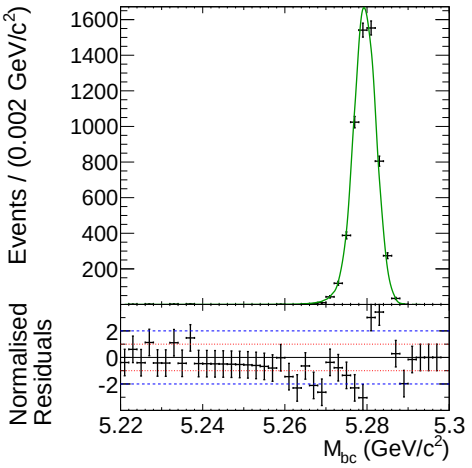

-0.08 GeV $\leq \Delta$E ≤ -0.02 GeV

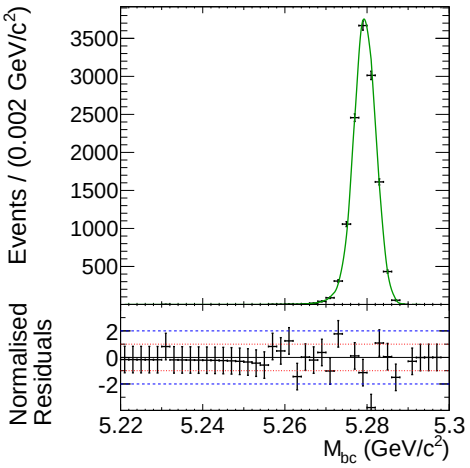

-0.02 GeV $\leq \Delta$E ≤ 0.04 GeV

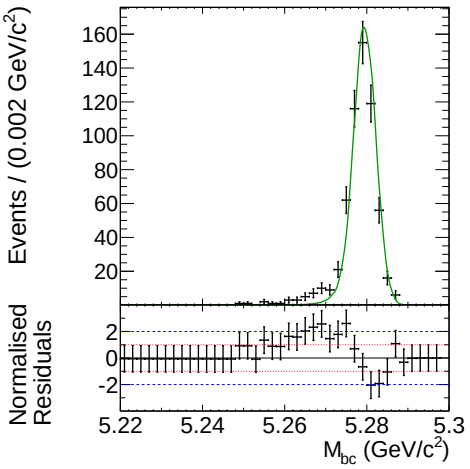

0.04 GeV $\leq \Delta$E ≤ 0.10 GeV

Figure 5.9: $M_{\rm bc}$ projections of the $B^0 \to \psi(2S)\pi^0$ fit in regions of ΔE, electron mode.

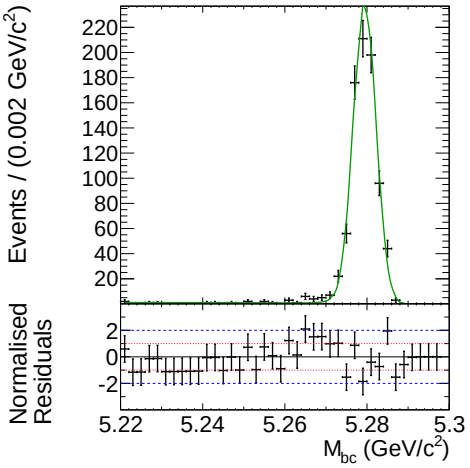

-0.2 GeV $\leq \Delta$E ≤ -0.14 GeV

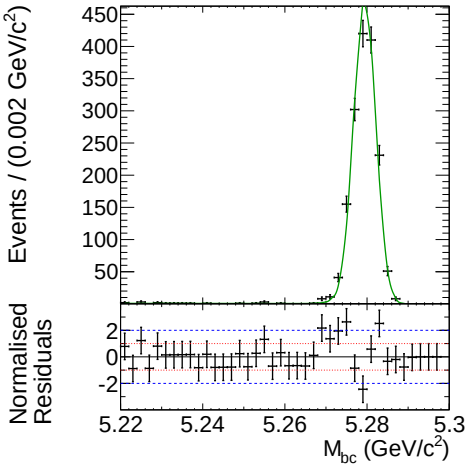

-0.14 GeV $\leq \Delta$E ≤ -0.08 GeV

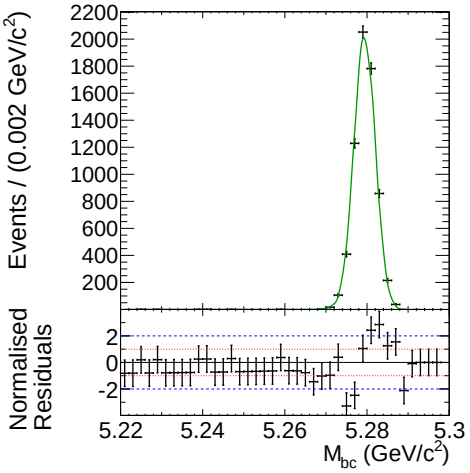

-0.08 GeV $\leq \Delta$E ≤ -0.02 GeV

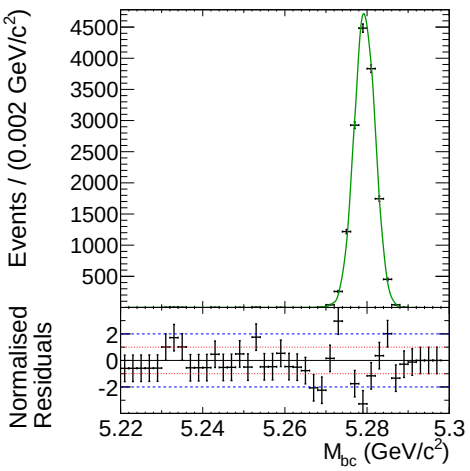

-0.02 GeV $\leq \Delta$E ≤ 0.04 GeV

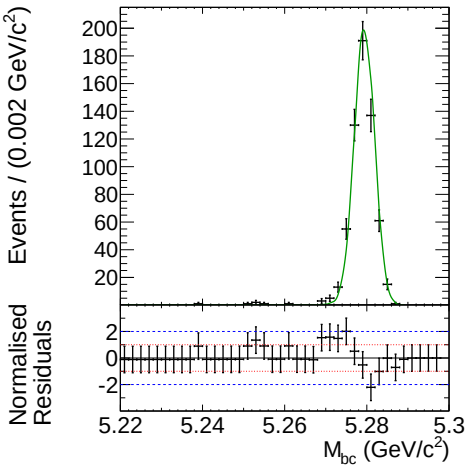

0.04 GeV $\leq \Delta$E ≤ 0.10 GeV

Figure 5.10: M_{bc} projections of the $\mathrm{B}^0 \to \psi(2\mathrm{S})\pi^0$ fit in regions of ΔE, muon mode.

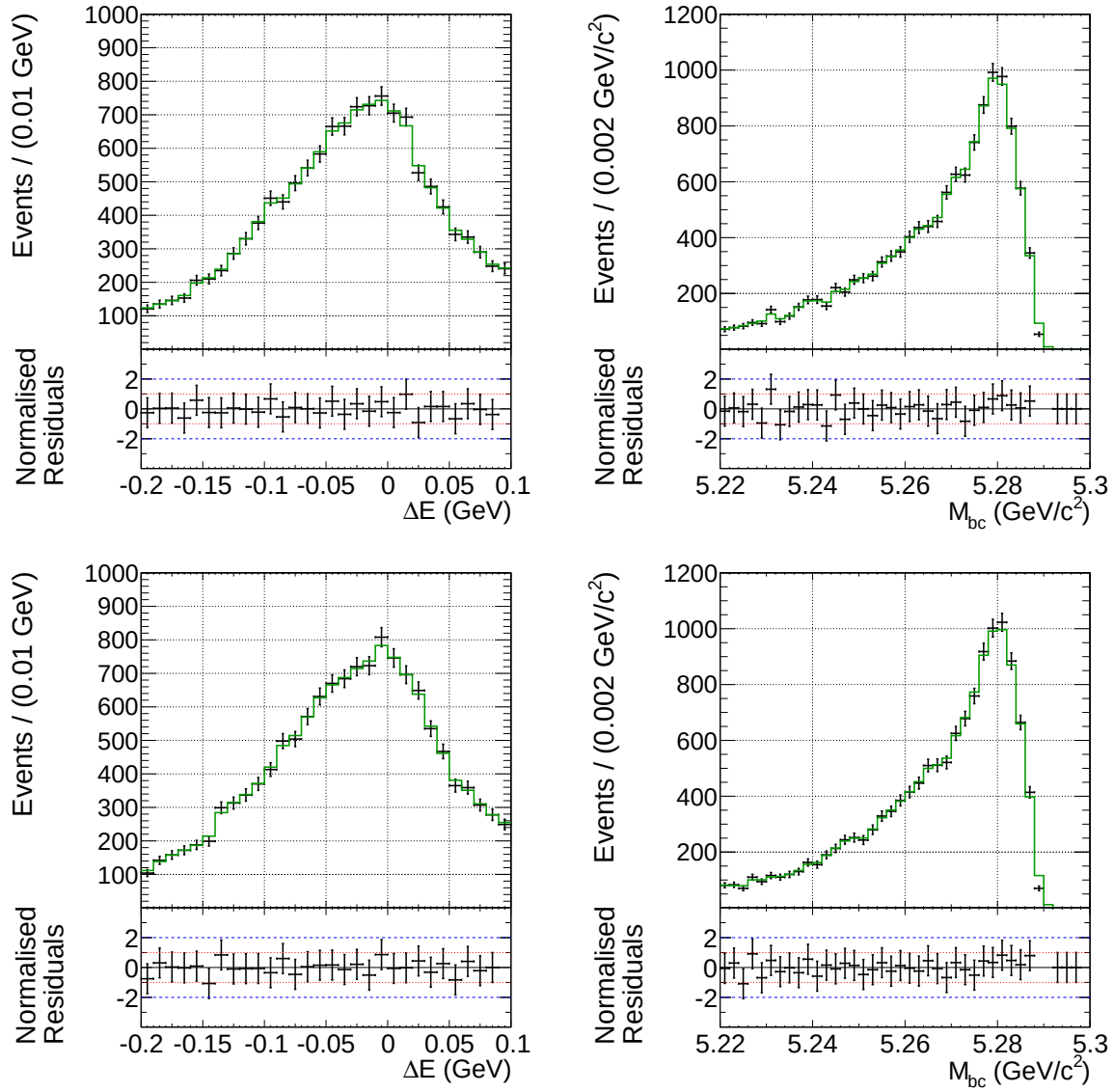

Figure 5.11: ΔE and M_{bc} projections of the $B^0 \to \psi(2S)\pi^0$ fit to the electron (up) and muon (down) misreconstructed signal events.

5.3.4 Sideband Studies and Combinatorial Background Model

No peaking backgrounds, i.e. decays to the same final state as $B^0 \to \psi(2S)\pi^0$ and with this featuring a peak in ΔE, were observed in the $b \to c\bar{c}$ decay modes. Considering the possibility of the presence of peaking combinatorial backgrounds, we study the $B^0 \to \psi(2S)\pi^0$ on-resonance data in the sidebands of $M_{\psi(2S)[\ell\bar{\ell}]}$, $M_{J/\psi}$, and $M_{\psi(2S)[J/\psi\pi^+\pi^-]} - M_{J/\psi}$. The sideband regions are listed in Table 5.3.

We assume that the combinatorial background has non-peaking distributions in ΔE and M_{bc}. In the $M_{\psi(2S)}$ and $M_{J/\psi}$ sidebands, we model ΔE with a Chebyshev polynomial of the first order. The ΔE PDF of the $M_{\psi(2S)} - M_{J/\psi}$ sideband is a sum of Chebyshev polynomials up

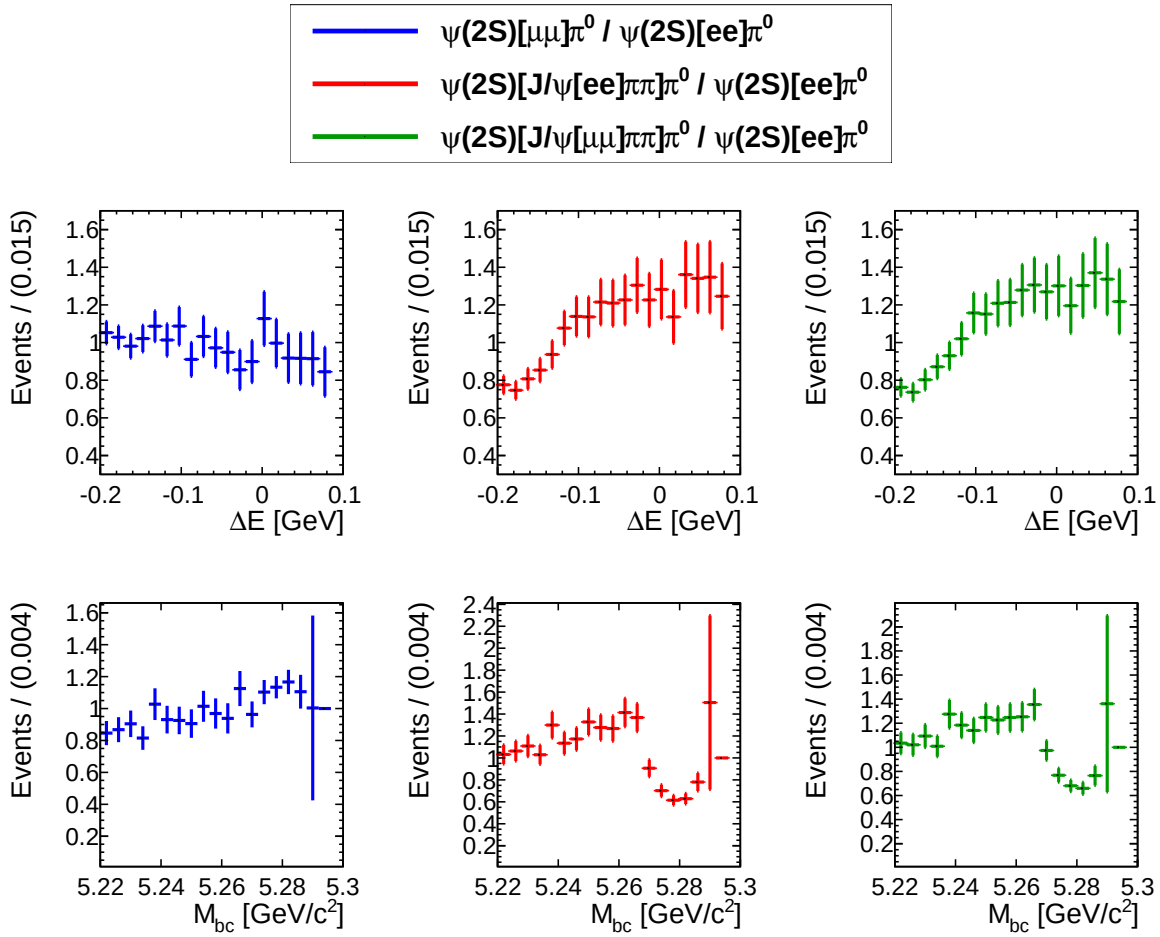

Figure 5.12: $B^0 \to \psi(2S)\pi^0$ $c\bar{c}$ background ΔE (up) and M_{bc} (down) ratios between the four $\psi(2S)$ decay channels.

to the second order. In all sidebands, the M_{bc} PDF is an ARGUS distribution. These shapes are used in the fit to the data, where their parameters are floated to obtain a more accurate result.

We assume a potential peaking background to have the same shape as the correctly reconstructed signal. This is why we combine the combinatorial background shapes with the PDF for the correctly reconstructed signal and extract two yields – combinatorial background yield and peaking background yield. The fit projections are shown in Figure 5.14 and the results are summarized in Table 5.4. For computational reasons, we allow the signal yields to have negative values. In general, the peaking background yield is negligible, except for the muonic signal mode in the $M_{\psi(2S)} - M_{J/\psi}$ sideband, where it has a significance of 3.7σ, determined from the likelihood value. This yield is taken into account as a systematic uncertainty.

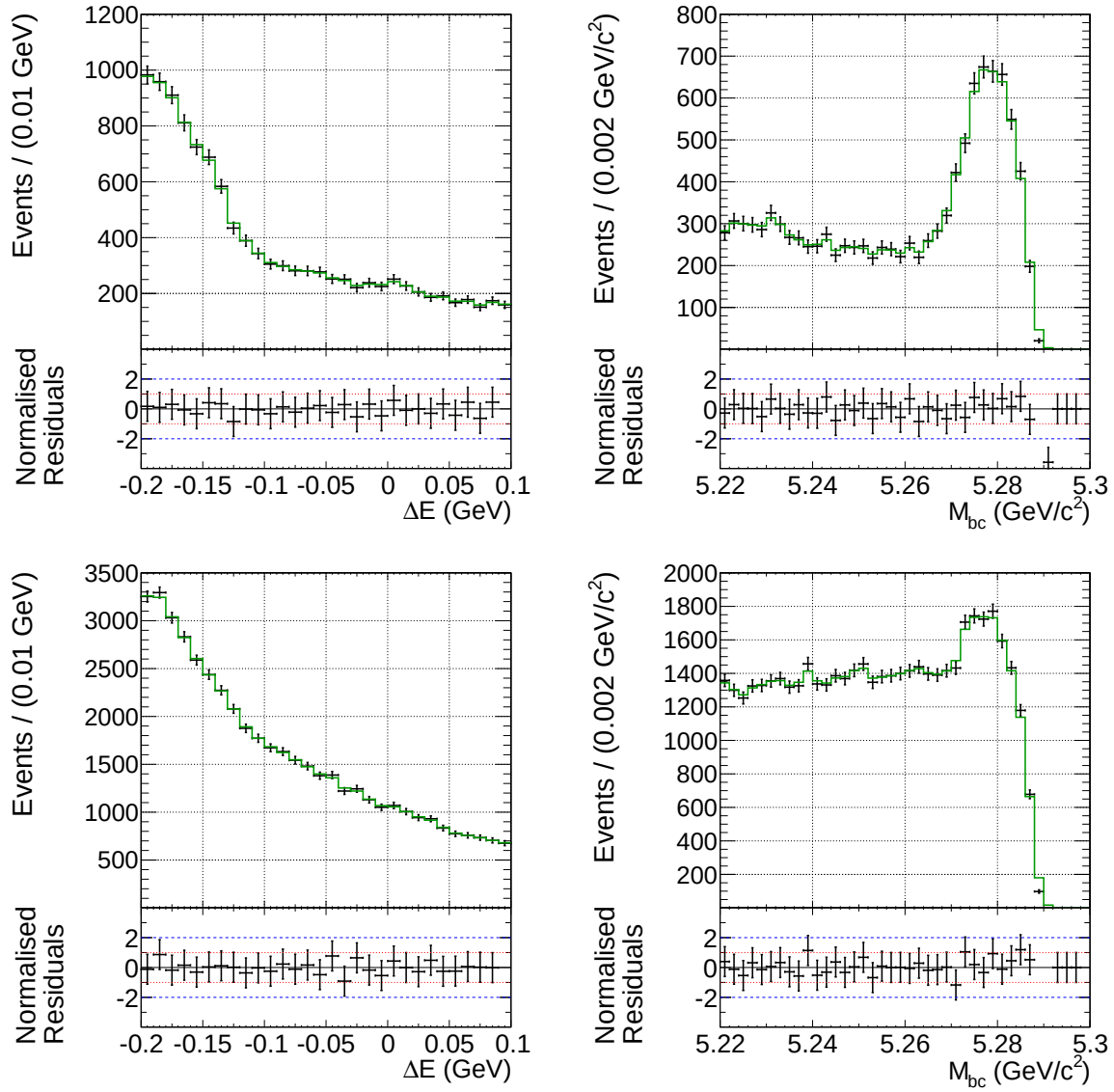

Figure 5.13: $B^0 \to \psi(2S)\pi^0$ ΔE and $M_{\rm bc}$ projections of the fit to the leptonic (up) and hadronic (down) $c\bar{c}$ background events.

5.3.5 Full Event Model

The total extended likelihood is given by

$$\mathcal{L} \equiv \prod_c \frac{e^{-\sum_j N_j^c f_j^c}}{N_c!} \prod_{i=1}^{N_c} \sum_j N_j^c f_j^c \mathcal{P}_j^c(\Delta E^i, M_{\rm bc}^i), \tag{5.12}$$

which iterates over i events, j categories (the different backgrounds) and c subcategories (the four $\psi(2S)$ decay modes). The misreconstructed signal fractions are fixed in respect to the correctly reconstructed events. The fractions of three of the $c\bar{c}$ modes are fixed to the $c\bar{c}$ events in which $\psi(2S) \to J/\psi[e^+e^-]\pi^+\pi^-$. The respective fractions are listed in Table 5.3.5. The

four combinatorial background yields are free as well as both its ΔE and M_{bc} shapes. The $B^0 \to \psi(2S)\pi^0$ branching fraction is extracted from the signal yield according to Eq. 3.4.

5.3.6 Fit Validation

We perform a linearity test on the $B^0 \to \psi(2S)\pi^0$ branching fraction to study a possible bias. We scan the branching fraction region between 0.5×10^{-5} and 3.5×10^{-5} in steps of 0.5×10^{-5}. For each of these seven points, we generate 200 pseudoexperiments. The result is shown in Figure 5.15. The distribution has a slope, m, consistent with zero. This means that the bias depends only slightly on the asolute value of the branching fraction. In total, the bias is expected to be around 10% of the statistical error. The systematic uncertainty due to the bias is small compared to the dominant one, which originates from the neutral pion reconstruction.

5.4 Control Sample $B^{\pm} \to J/\psi K^{*\pm}$

The purpose of the control sample study is to determine the ΔE and M_{bc} correction factors for the $B^0 \to \psi(2S)\pi^0$ decay. The decay kinematics dictates the choice of a control sample, which needs to have a similar topology as $B^0 \to \psi(2S)\pi^0$. With an appropriate set of selection criteria, this can be achieved in the decay channel $B^{\pm} \to J/\psi K^{*\pm}$. To obtain a good precision, it is also necessary that the control sample offers a high statistics as in the case of $B^{\pm} \to J/\psi K^{*\pm}$, which has a branching fraction of the order of 10^{-3}.

5.4.1 Event Reconstruction

We reconstruct the $B^{\pm}$ candidates from a J/ψ and a $K^{*\pm}$ candidate. For J/ψ, we use the same selection criteria as for the $B^0 \to \psi(2S)\pi^0$ mode, described in Section 5.2.4. The $K^{*\pm}$ candidate are reconstructed from a $K^{\pm}$ and a π^0 candidate. For the kaon candidates, we require $\mathcal{L}_{K/\pi} > 0.4$. The π^0 reconstruction is identical to the one described in Section 4.2.3.2.

Since $B^{\pm} \to J/\psi K^{*\pm}$ is a three-body decay, while $B^0 \to \psi(2S)\pi^0$ is only a two-body decay, the pion energy in the control channel is lower on average. To reduce this major difference between the two channels, which strongly affects the ΔE and M_{bc} resolution, we place a helicity angle cut on the π^0 candidate momentum. This is the angle between the π^0 momentum vector in the $K^{*\pm}$ rest frame and the $K^{*\pm}$ momentum vector in the laboratory frame. We require it to be smaller than 1.5 rad. The result is illustrated in Figure 5.16. The remaining π^0 candidates have an energy distribution in a range similar to the π^0 candidates in $B^0 \to \psi(2S)\pi^0$. Only $K^{*\pm}$ candidates in the mass region $0.793\ \mathrm{GeV}/c^2 \leq M_{K^{\pm}\pi^0} \leq 0.990\ \mathrm{GeV}/c^2$ are retained.

We apply the same ΔE and M_{bc} cuts as for $B^0 \to \psi(2S)\pi^0$. The best B candidate is a combination of the kaon with the highest particle ID (see Figure 4.3) and the lowest χ^2 of the rest of the event (π^0 and J/ψ) defined as

$$\chi^2 = \frac{1}{2}\left[\left(\frac{M_{\bar{\ell}\ell} - M_{J/\psi}}{\sigma_{J/\psi,\bar{\ell}\ell}}\right)^2 + \left(\frac{M_{\gamma\gamma} - M_{\pi^0}}{\sigma_{\gamma\gamma}}\right)^2\right], \tag{5.13}$$

which corresponds to the according $B^0 \to \psi(2S)\pi^0$ definition in Eq. 5.7. The respective mass resolutions are listed in Table 5.1.

The reconstruction efficiency and the signal purity (see definition in Section 4.2.10) are summarized in Table 5.6. A correctly reconstructed signal event is defined as such in which the B_{CP} vertex is reconstructed from the charged tracks that belong to it.

5.4.2 Event Model

We divide the events into an electron and a muon categories, depending on the J/ψ decay mode. As in $B^0 \to \psi(2S)\pi^0$, four different components are modeled – correctly reconstructed and misreconstructed signal, $c\bar{c}$ and combinatorial backgrounds. The fit observables are, again, ΔE and $M_{\rm bc}$.

- The correctly reconstructed model for ΔE is the same as the one for $B^0 \to \psi(2S)\pi^0$. Due to a correlation of 13-14% depending on the mode, $M_{\rm bc}$ is parametrized in terms of ΔE

$$\begin{aligned}\mathcal{P}^c_{Sig}(M_{\rm bc}|\Delta E) \equiv\ & (f^c_1 + \alpha^c \Delta E^2)\mathrm{CB}(M_{\rm bc}; \alpha,\, n,\, \mu^c_1 + \mu_C,\, \sigma^c_1\sigma_C + \beta^c|\Delta E|) \\ & +(1 - [f^c_1 + \alpha^c \Delta E^2])\mathrm{ARGUS}(M_{\rm bc}; a^c). \end{aligned} \quad (5.14)$$

  Fit projections to ΔE and $M_{\rm bc}$ are shown in Figure 5.17.

- The misreconstructed signal events are modeled using two-dimensional histograms in ΔE and $M_{\rm bc}$ for each of the two decay modes, as shown in Figure 5.18.

- The $c\bar{c}$ model also consists of two two-dimensional histograms in ΔE and $M_{\rm bc}$, shown in Figure 5.19.

- J/ψ sideband studies are performed as a check for the presence of peaking backgrounds and to model the combinatorial one. The combinatorial background is modeled by a linear function in ΔE and an ARGUS distribution in $M_{\rm bc}$. The same model with shared parameters is used for both J/ψ decay modes. The potential peaking background is assumed to have the same shape as the signal. The results are shown in Table 5.7. The peaking background level is consistent with zero. The fit projections to ΔE and $M_{\rm bc}$ are shown in Figure 5.20.

The total extended likelihood is given by

$$\mathcal{L} \equiv \prod_c \frac{e^{-\sum_j N^c_j f^c_j}}{N_c!} \prod_{i=1}^{N_c} \sum_j N^c_j f^c_j \mathcal{P}^c_j(\Delta E^i, M^i_{\rm bc}), \quad (5.15)$$

which iterates over i events, j categories and c subcategories (the two J/ψ decay modes). The misreconstructed signal fractions are fixed in respect to the correctly reconstructed events. The fraction of muon $c\bar{c}$ events is fixed to the level of electron $c\bar{c}$ events. The two combinatorial background yields are free and so are both its ΔE and $M_{\rm bc}$ shapes. The signal correction factors of the two fit observables are also floated.

Decay mode	Mass resolution [MeV/c^2] $\sigma_{\psi(2S)}$	$\sigma_{J/\psi}$	$\sigma_{\pi^+\pi^-}$
$\psi(2S) \to e^+e^-$	13.2	-	-
$\psi(2S) \to \mu^+\mu^-$	9.7	-	-
$\psi(2S) \to J/\psi[e^+e^-]\pi^+\pi^-$	-	10.8	2.9
$\psi(2S) \to J/\psi[\mu^+\mu^-]\pi^+\pi^-$	-	8.1	2.5

Table 5.1: Mass resolutions used in the best B selection.

Decay mode	Efficiency SVD1	Efficiency SVD2	Purity
$\psi(2S) \to e^+e^-$	0.00166 ± 0.00004	0.00208 ± 0.00005	99.1%
$\psi(2S) \to \mu^+\mu^-$	0.0020 ± 0.0002	0.0023 ± 0.0002	99.8%
$\psi(2S) \to J/\psi[e^+e^-]\pi^+\pi^-$	0.00196 ± 0.00003	0.00268 ± 0.00003	89.8%
$\psi(2S) \to J/\psi[\mu^+\mu^-]\pi^+\pi^-$	0.00216 ± 0.00003	0.00275 ± 0.00004	90.0%

Table 5.2: $B^0 \to \psi(2S)\pi^0$ detection efficiency and signal purity. The efficiency uncertainties are obtained from signal MC and from the errors on the world average values for the daughter branching fractions [27].

Sideband	PDG mass [27] [GeV/c^2]	Lower range [GeV/c^2]	Upper range [GeV/c^2]
$M_{J/\psi}$	3.097	$[2.60; 2.80]$	$[3.20; 3.40]$
$M_{\psi(2S)}$	3.686	$[3.45; 3.53]$	$[3.80; 3.90]$
$M_{\psi(2S)-J/\psi}$	0.589	$[0.49; 0.53]$	$[0.64; 0.68]$

Table 5.3: $B^0 \to \psi(2S)\pi^0$ mass sidebands.

Sideband	N_{sig} (e^+e^-)	N_{sig} ($\mu^+\mu^-$)	N_{BG} (e^+e^-)	N_{BG} ($\mu^+\mu^-$)
$M_{\psi(2S)}$	-2 ± 2	-1 ± 3	192 ± 14	269 ± 16
$M_{J/\psi}$	1 ± 2	0 ± 3	82 ± 9	144 ± 12
$M_{\psi(2S)} - M_{J/\psi}$	0 ± 5	17 ± 6	721 ± 27	608 ± 24

Table 5.4: Combinatorial background yields N_{BG} and peaking background yields N_{sig} obtained from the fit to the $B^0 \to \psi(2S)\pi^0$ mass sidebands.

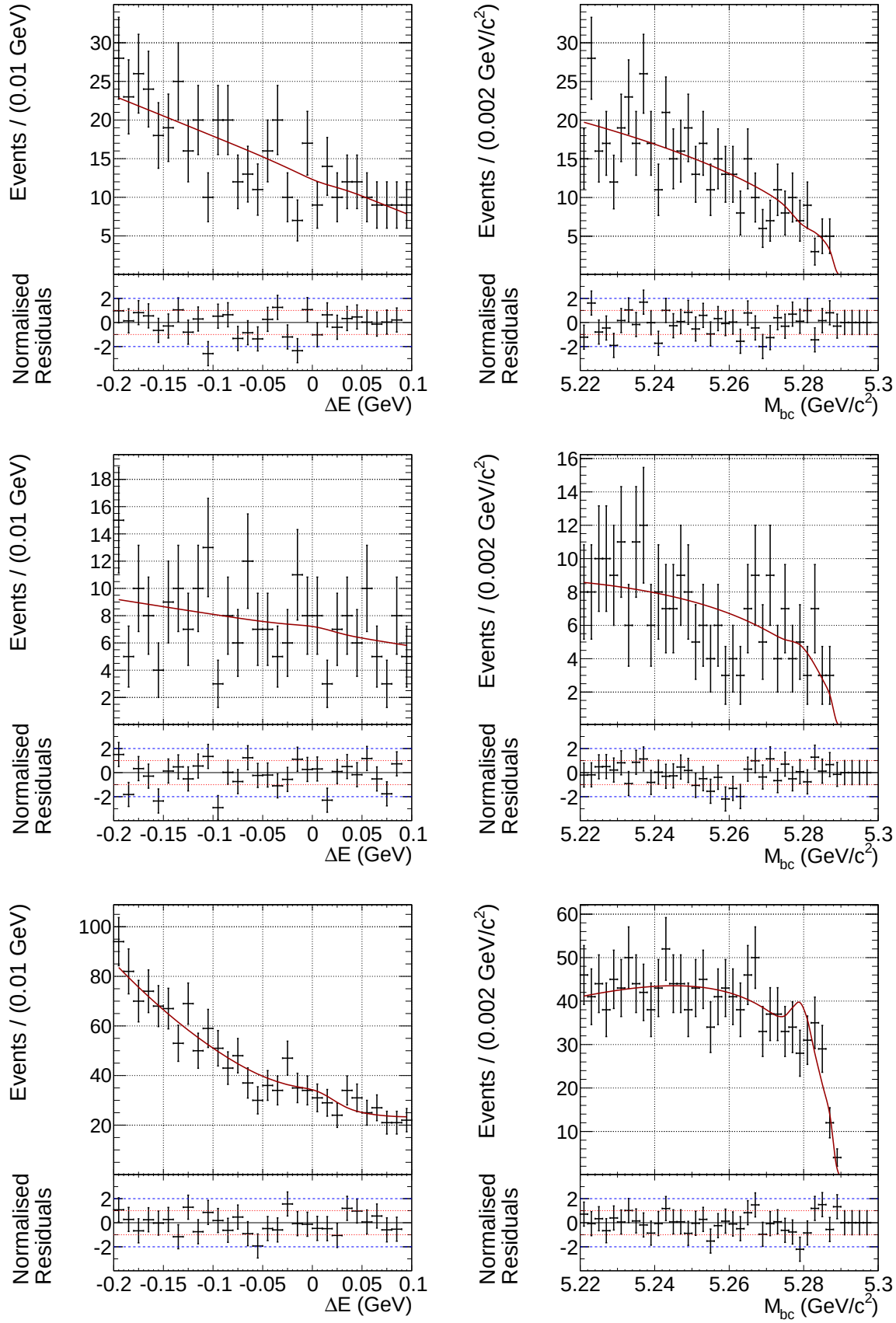

Figure 5.14: ΔE and $M_{\rm bc}$ projections of the fit to the on-resonance sidebands $M_{\psi(2S)}$ (up), $M_{J/\psi}$ (middle) and $M_{\psi(2S)[J/\psi\pi^+\pi^-]} - M_{J/\psi}$ (down), using the $B^0 \to \psi(2S)\pi^0$ reconstruction algorithm.

Decay channel	Yield/Fraction
$\psi(2S) \to e^+e^-$	$(0.2325 \pm 0.004) N_{c\bar{c}}^{\psi(2S)\to J/\psi[\mu^+\mu^-]\pi^+\pi^-}$
$\psi(2S) \to \mu^+\mu^-$	$(0.2523 \pm 0.005) N_{c\bar{c}}^{\psi(2S)\to J/\psi[\mu^+\mu^-]\pi^+\pi^-}$
$\psi(2S) \to J/\psi[e^+e^-]\pi^+\pi^-$	$(0.9753 \pm 0.009) N_{c\bar{c}}^{\psi(2S)\to J/\psi[\mu^+\mu^-]\pi^+\pi^-}$
$\psi(2S) \to J/\psi[\mu^+\mu^-]\pi^+\pi^-$	23966 ± 155

Table 5.5: Summary of $c\bar{c}$ yields fixed relative to the $\psi(2S) \to J/\psi[\mu^+\mu^-]\pi^+\pi^-$ yield $N_{c\bar{c}}^{\psi(2S)\to J/\psi[\mu^+\mu^-]\pi^+\pi^-}$. The values and their uncertainties are obtained from MC statistics.

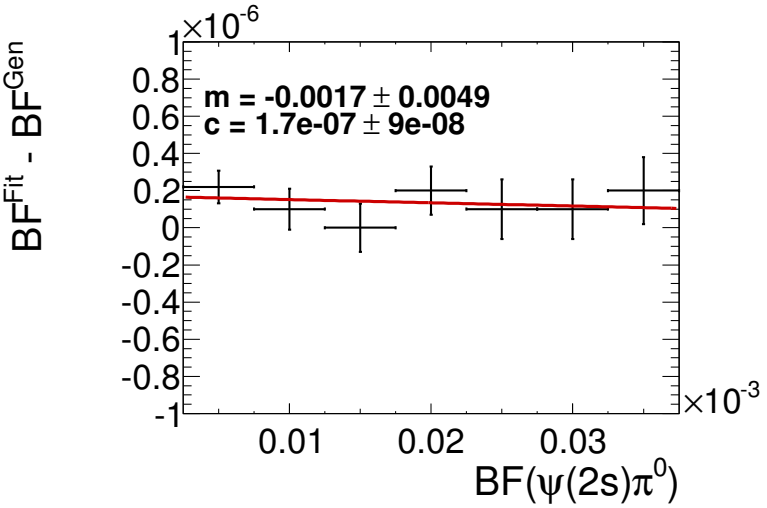

Figure 5.15: Linearity test for the $B^0 \to \psi(2S)\pi^0$ branching fraction. m and c are the slope and offset of the distributions, respectively.

	Efficiency		Purity
Decay mode	SVD1	SVD2	
$J/\psi \to e^+e^-$	0.0008794 ± 0.000009	0.00108 ± 0.00001	89.9%
$J/\psi \to \mu^+\mu^-$	0.00098 ± 0.00001	0.00109 ± 0.00001	90.0%

Table 5.6: $B^{\pm} \to J/\psi K^{*\pm}$ detection efficiency and signal purity. The efficiency uncertainties are obtained from signal MC and from the errors on the world average values for the daughter branching fractions [27].

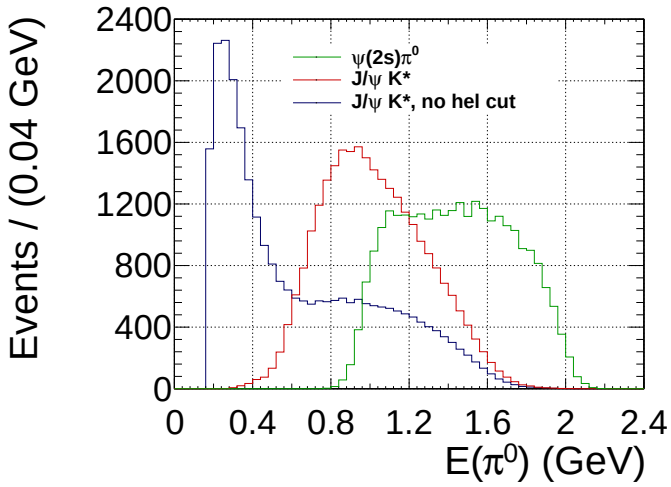

Figure 5.16: Energy of the π^0 candidates in $B^0 \to \psi(2S)\pi^0$ (green) and $B^\pm \to J/\psi K^{*\pm}$ before (blue) and after (red) the helicity cut.

Sideband	N_{sig} (e^+e^-)	N_{sig} ($\mu^+\mu^-$)	N_{BG} (e^+e^-)	N_{BG} ($\mu^+\mu^-$)
$M_{J/\psi}$	5 ± 8	-4 ± 8	1955 ± 45	2810 ± 54

Table 5.7: Combinatorial background yields N_{BG} and peaking background yields N_{sig} obtained from the fit to the $B^\pm \to J/\psi K^{*\pm}$ mass sidebands.

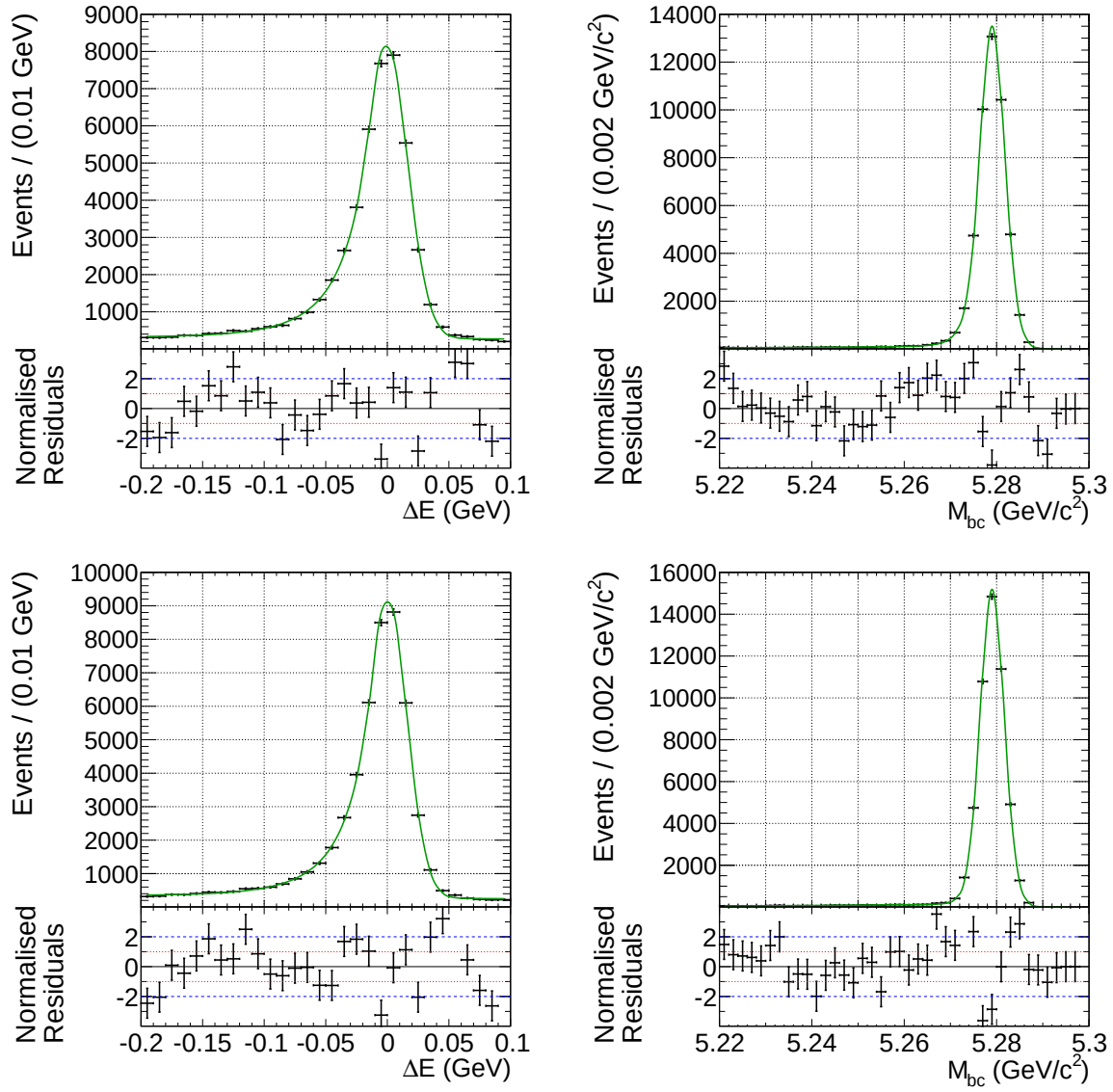

Figure 5.17: $B^{\pm} \to J/\psi K^{*\pm}$ ΔE and $M_{\rm bc}$ projections of the fit to the electron (up) and muon (down) signal events.

5.4.3 Correction Factors for the Difference between Data and Monte Carlo

We extract 3681 signal events from the data. The ΔE and $M_{\rm bc}$ fit projections are shown in Figure 5.21. The common correction factors for the two decays modes are listed in Table 5.8. The electron (muon) mode correction factors are used to calibrate the $B^0 \to \psi(2S)\pi^0$ electron (muon) mode signal shape in $B^0 \to \psi(2S)\pi^0$.

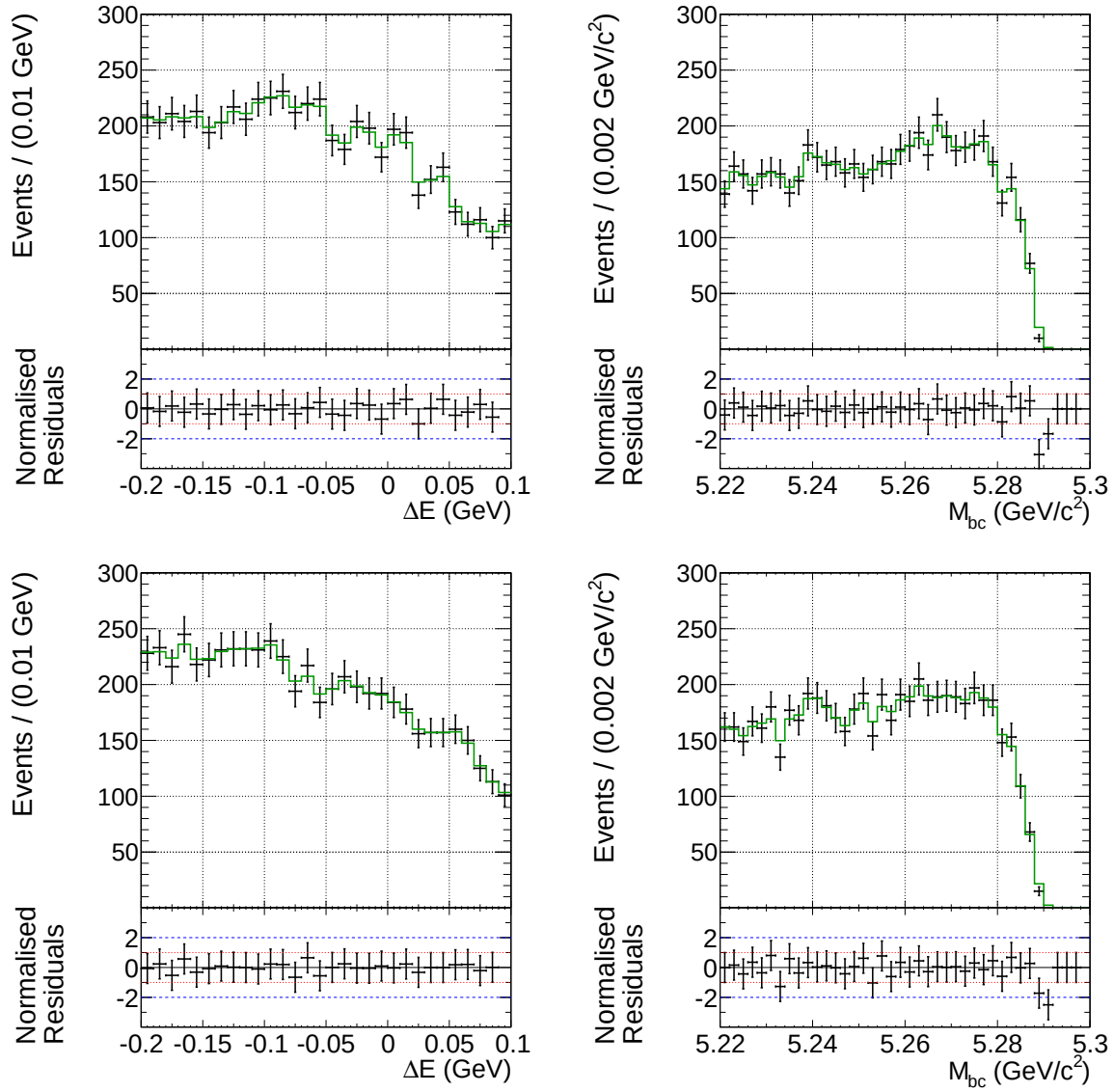

Figure 5.18: $B^{\pm} \to J/\psi K^{*\pm}$ ΔE and M_{bc} projections of the fit to the electron (up) and muon (down) misreconstructed signal events.

5.5 Results

From the fit to the data containing 1090 $B^0 \to \psi(2S)\pi^0$ candidates, we obtain the branching fraction

$$\mathcal{B}(B^0 \to \psi(2S)\pi^0) = (1.17 \pm 0.18\ (\mathrm{stat}) \pm 0.08\ (\mathrm{syst})) \times 10^{-5}, \tag{5.16}$$

where the first uncertainty is statistical and the second is systematic. The branching fraction is bias corrected and corresponds to 85 signal events, of which 38 are leptonic and 47 are hadronic. 628 events originate from other $b \to c\bar{c}q$ decays and 377 events belong to the combinatorial background. Data fit projections are shown in Figure 5.22. The result is consistent with our theoretical prediction presented in Section 5.1.

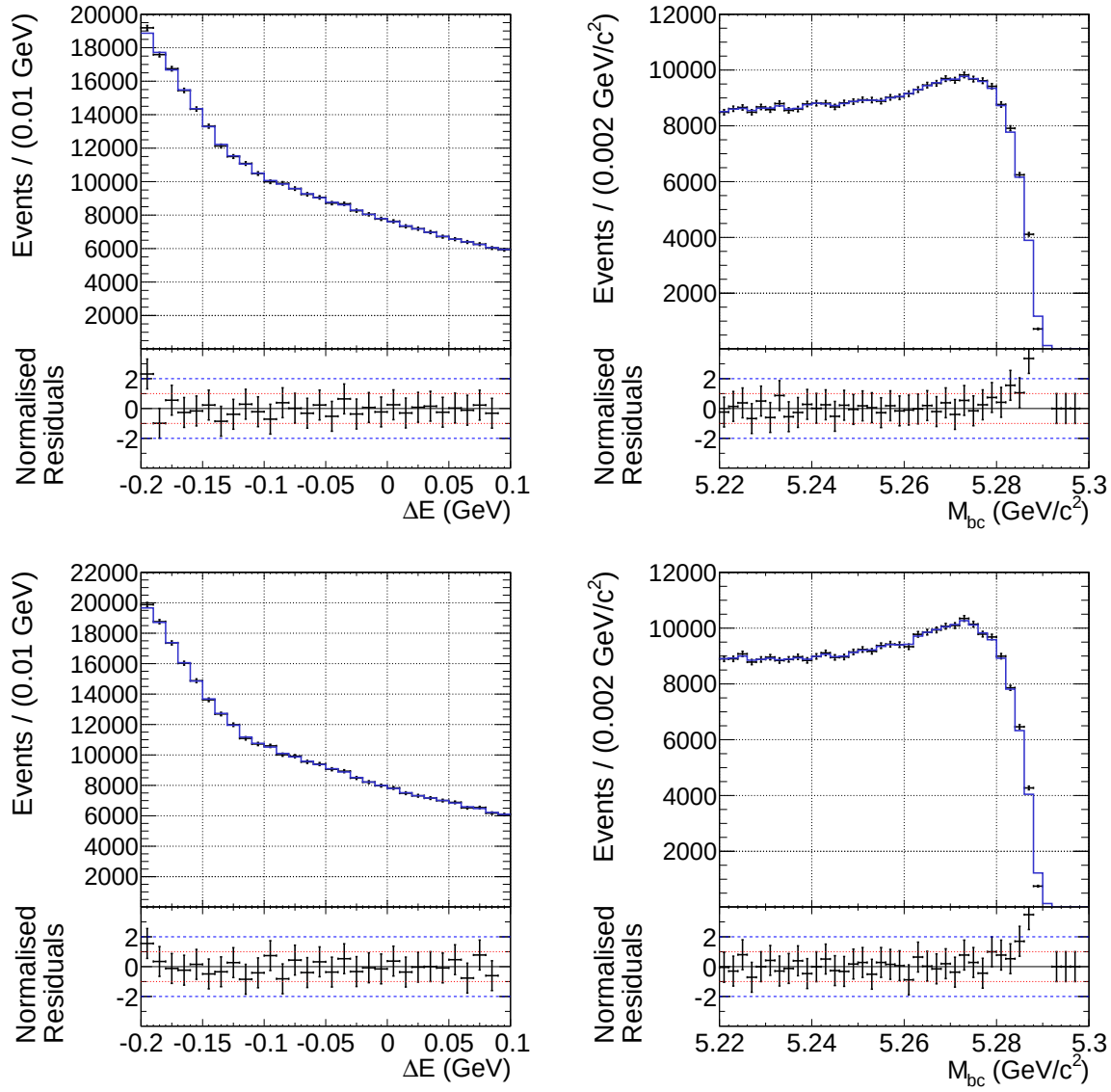

Figure 5.19: $B^{\pm} \to J/\psi K^{*\pm}$ ΔE and $M_{\rm bc}$ projections of the fit to the electron (up) and muon (down) $c\bar{c}$ background events.

5.6 Systematic Uncertainties

The $\mathcal{B}(B^0 \to \psi(2S)\pi^0)$ systematic uncertainties are summarized in Table 5.9. The way the $N_{B\overline{B}}$, π^0 reconstruction, PID, tracking, parametric shape, nonparametric shape and the fit bias uncertainties are obtained was explained in Section 4.3.9. In addition, we consider the systematic uncertainties originating from the $\psi(2S)$ decay branching fractions used in this analysis, $\mathcal{B}(\psi(2S) \to \ell\bar{\ell})$, $\mathcal{B}(\psi(2S) \to J/\psi\pi^+\pi^-)$ and $\mathcal{B}(J/\psi \to \ell\bar{\ell})$. They are taken to be equal to the experimental percentage uncertainty listed in [27]. The electron (EID) and muon (MuID) identification reconstruction efficiency uncertainties were obtained from a Belle study of the two-photon processes $e^+e^- \to e^+e^-\ell\bar{\ell}$, where $\ell = e, \mu$. The misreconstructed signal uncertainty

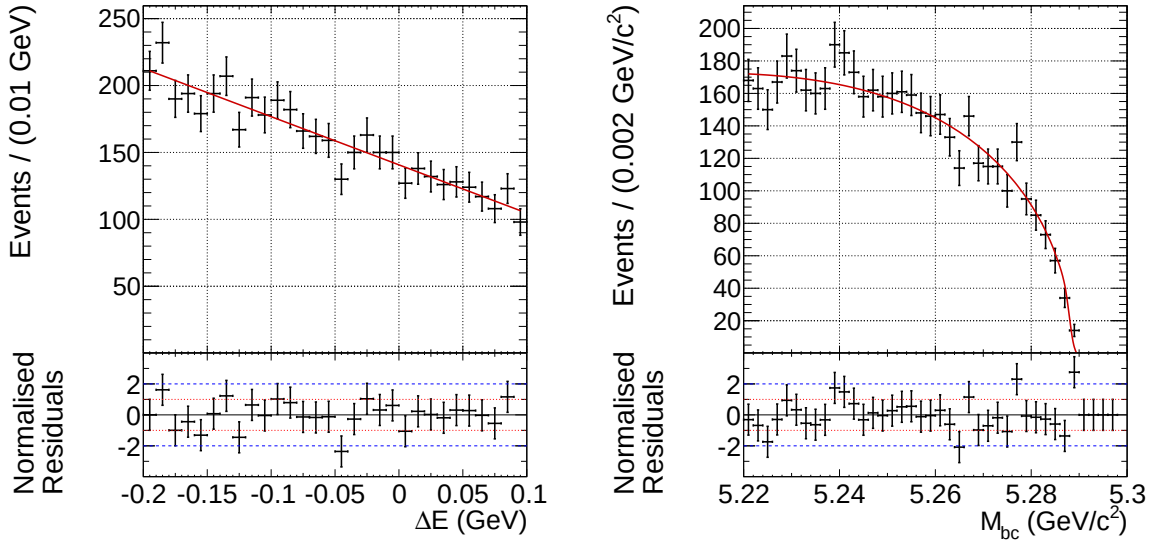

Figure 5.20: $B^{\pm} \to J/\psi K^{*\pm}$ ΔE and $M_{\rm bc}$ projections of the fit to the J/ψ sideband events.

$M_{\rm bc}$ [MeV/c^2]		ΔE [MeV/c^2]	
Offset	Fudge factor	Offset	Fudge factor
0.20 ± 0.06	1.03 ± 0.02	-1.15 ± 0.54	1.14 ± 0.03

Table 5.8: Results for the correction factors from the $B^{\pm} \to J/\psi K^{*\pm}$ fit to the data. The given uncertainties are statistical.

is obtained by varying the misreconstructed fraction by 20%, which is a conservative estimate. The number of peaking background events is varied by one standard deviation and the branching fraction difference is assigned as a systematic uncertainty. The same approach is used for the ΔE and $M_{\rm bc}$ correction factors. The total systematic uncertainty is 7.14% of the $B^0 \to \psi(2S)\pi^0$ branching fraction.

5.7 Statistical Significance

We perform a likelihood scan to obtain the statistical significance of our branching fraction measurement. For this, the branching fraction is fixed to a value between 0 and 2 times the result from Eq. 5.16 in steps of 0.01. Then the fit to the data is repeated and the likelihood value of each point, $-2\log\mathcal{L}$, is recorded. In addition, the $\mathcal{L}$ distribution is convoluted with a Gaussian with zero mean and a width equal to the systematic error. The statistical significance, σ, is defined as

$$\sigma = \sqrt{2(\log\mathcal{L}_0 - \log\mathcal{L}_{fit})}, \tag{5.17}$$

where $\mathcal{L}_0$ is the likelihood value at 0, consistent with no signal, and $\mathcal{L}_{fit}$ is the likelihood value obtained at the result branching fraction. The $2(\log\mathcal{L}_0 - \log\mathcal{L}_{fit})$ distribution is shown in

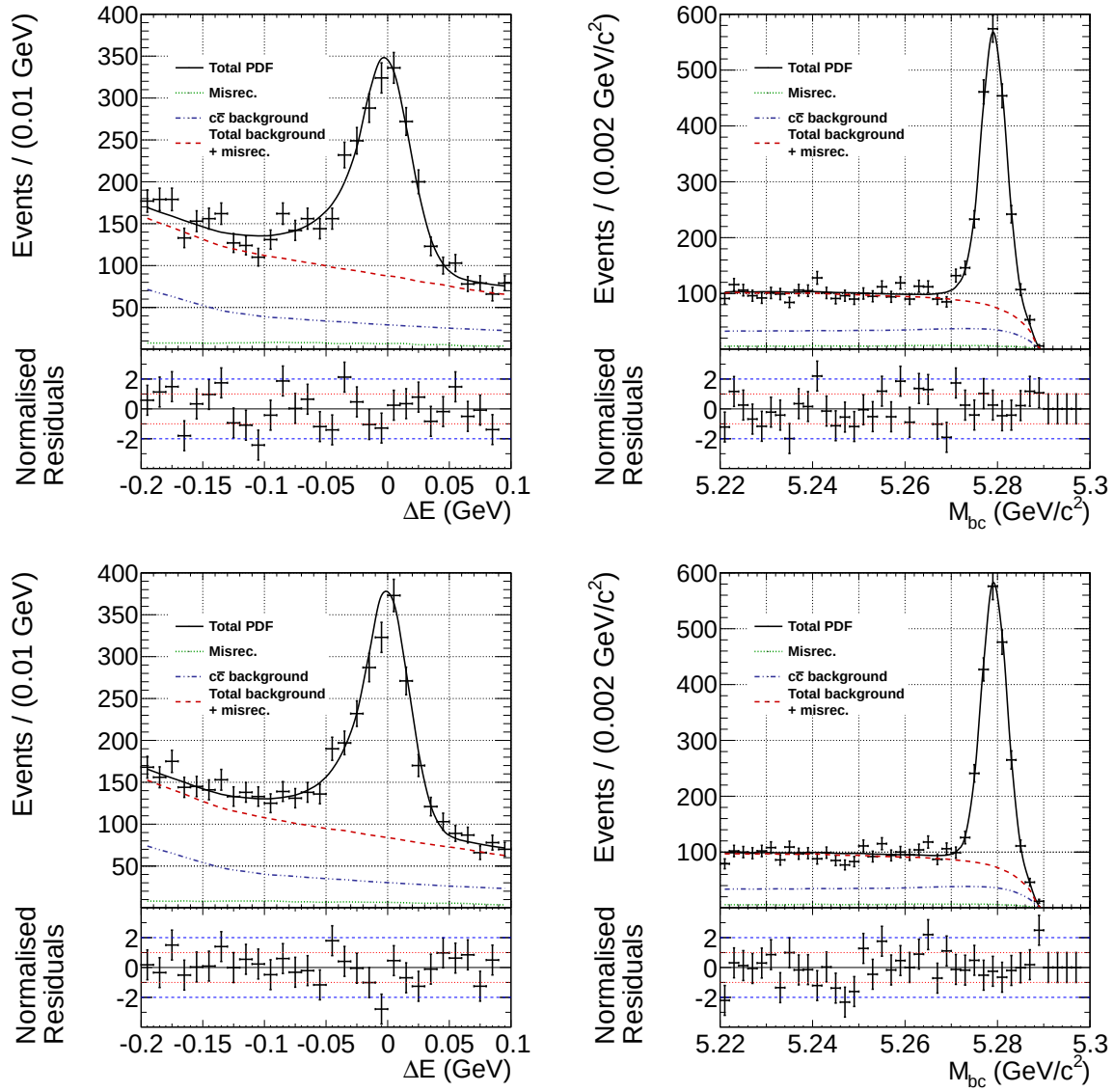

Figure 5.21: $B^{\pm} \to J/\psi K^{*\pm}$ ΔE and $M_{\rm bc}$ projections of the fit to the data for the electron (up) and the muon (down) decay modes.

Figure 5.23. We obtain a statistical significance of 7.2 standard deviations. With this, our result could be the first observation of the decay $B^0 \to \psi(2S)\pi^0$. However, at the time of the submission of this thesis, the result is still not officially acknowledged by the Belle collaboration and should be regarded as preliminary.

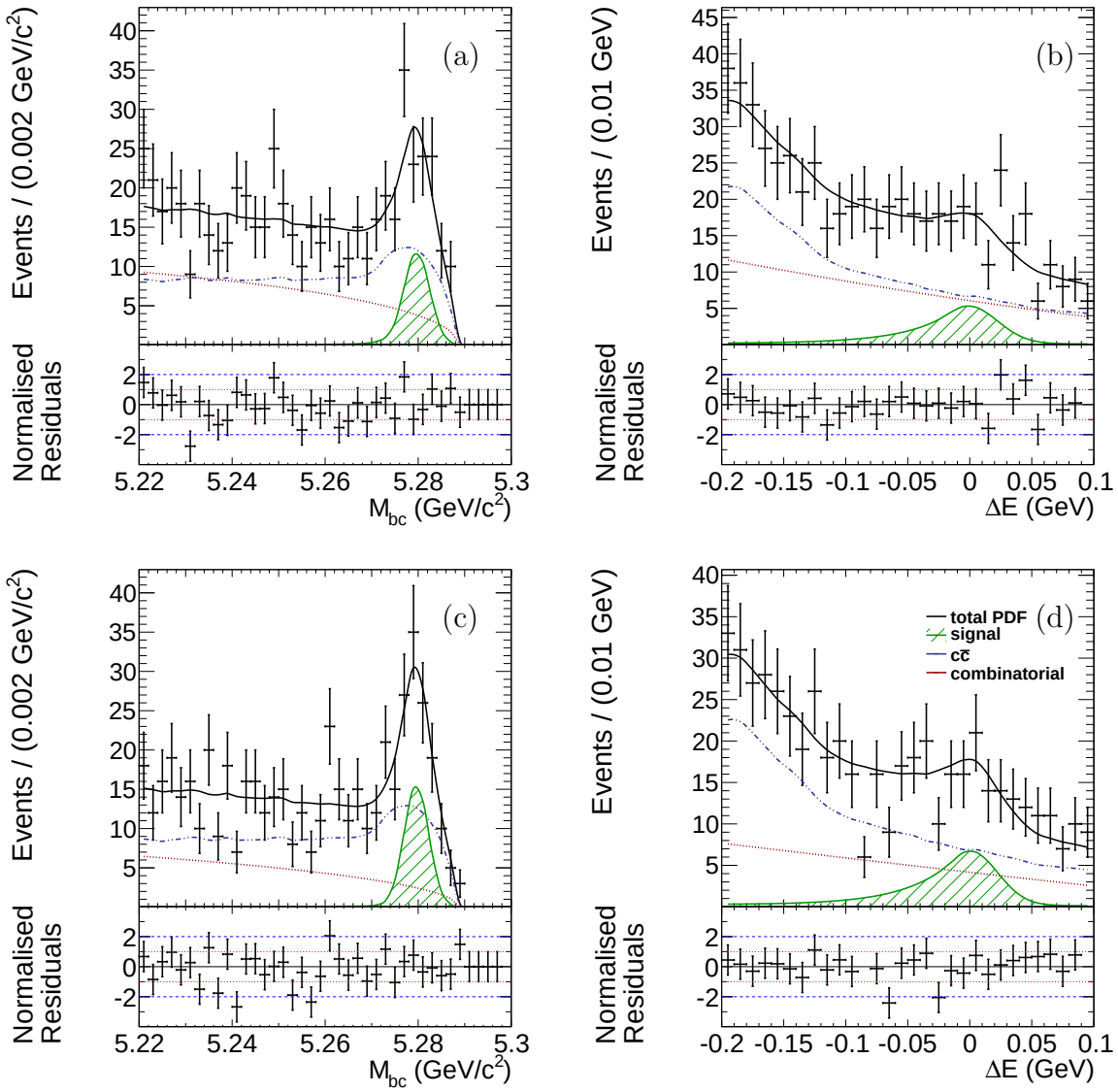

Figure 5.22: Projections of the fit to the $B^0 \to \psi(2S)\pi^0$ data. Points with error bars represent the data, and the solid black curves or histograms represent the fit results. (a) and (b) are $M_{\rm bc}$ and ΔE projections for the two electron modes, respectively; (c) and (d) are $M_{\rm bc}$ and ΔE projections for the two muon modes. Green hatched curves show the $B^0 \to \psi(2S)\pi^0$ signal component, blue dash-dotted curves show the $c\bar{c}$ background component and red dotted curves indicate the combinatorial background.

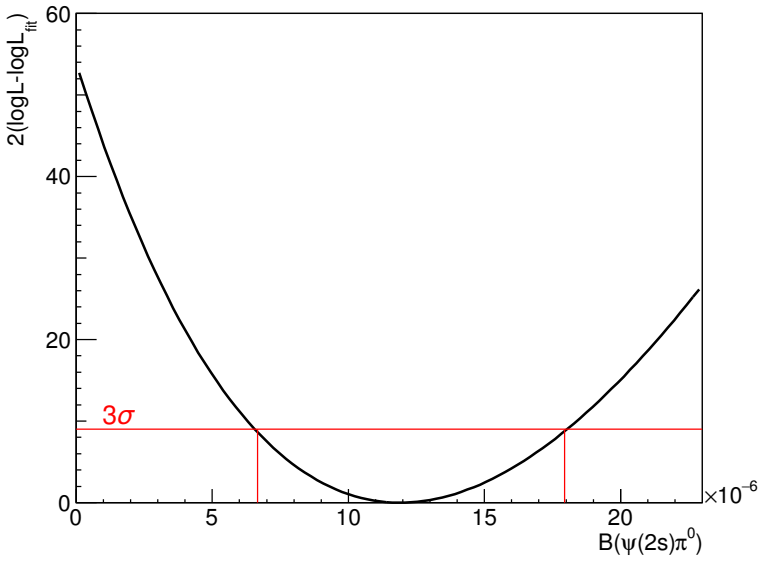

Figure 5.23: $\mathcal{B}(\mathrm{B}^0 \to \psi(2\mathrm{S})\pi^0)$ likelihood scan.

Category	$\delta\mathcal{B}(\psi(2S)\pi^0)$ (%)
$N_{B\overline{B}}$	1.37
π^0 reconstruction	4.00
$\mathcal{B}(\psi(2S) \to \ell\overline{\ell})$	2.99
$\mathcal{B}(\psi(2S) \to J/\psi\pi^+\pi^-)$	0.66
$\mathcal{B}(J/\psi \to \ell\overline{\ell})$	0.55
EID	1.56
MuID	1.69
PID	2.33
Tracking	1.66
Misreconstruction	0.34
Peaking background	2.22
Parametric shape	0.88
Nonparametric shape	1.38
Correction factors	0.85
Fit bias	0.63
Total	7.14

Table 5.9: Systematic uncertainties of the $B^0 \to \psi(2S)\pi^0$ branching fraction.

Conclusion

Two measurements based on the full Belle data set containing 772 million $B\overline{B}$ pairs are presented in this thesis: The $B \to \omega K$ branching fractions and CP asymmetry and the $B^0 \to \psi(2S)\pi^0$ branching fraction. All parameters were obtained from unbinned maximum likelihood fits, using a blind analysis technique.

The $B^0 \to \omega K^0_S$ decay is a loop-dominated $b \to s q\overline{q}$ transition sensitive to the angle ϕ_1 of the unitarity triangle. The loop process allows contributions from heavy particles beyond the reach of the LHC and with this makes the indirect search for new physics effects possible. From the $B \to \omega K$ study, we obtain

$$\begin{aligned}
\mathcal{B}(B^0 \to \omega K^0) &= (4.5 \pm 0.4\ (\text{stat}) \pm 0.3\ (\text{syst})) \times 10^{-6}, \\
\mathcal{B}(B^\pm \to \omega K^\pm) &= (6.8 \pm 0.4\ (\text{stat}) \pm 0.4\ (\text{syst})) \times 10^{-6}, \\
\mathcal{A}_{\omega K^0_S} &= -0.36 \pm 0.19\ (\text{stat}) \pm 0.05\ (\text{syst}), \\
\mathcal{S}_{\omega K^0_S} &= +0.91 \pm 0.32\ (\text{stat}) \pm 0.05\ (\text{syst}), \\
\mathcal{A}_{\omega K^\pm} &= -0.03 \pm 0.04\ (\text{stat}) \pm 0.01\ (\text{syst}).
\end{aligned}$$

These results are in agreement within up to three standard deviations with the previous measurements of Belle and BaBar. They are compatible with the theoretical predictions based on the Standard Model. However, the precision of our results is not sufficient to challenge it – something that the Belle successor, Belle II, will be in the position to do.

The results of the two branching fractions and of the two $\mathcal{A}_{CP}$ parameters are the most accurate measurement to date. The method used in the analysis includes more fit observables than the previous one performed by Belle, allowing for a higher reconstruction efficiency and a lower statistical error. In addition, the simultaneous study of the two different decay channels reduced the systematic uncertainty.

We find the first evidence for CP violation in the $B^0 \to \omega K^0_S$ decay with a significance of 3.1 standard deviations. The measurement was officially published in the Physical Review D journal in 2014 [81] as the final Belle result.

The $B^0 \to \psi(2S)\pi^0$ decay is a tree-dominated $b \to c\bar{c}d$ process, which is also sensitive to ϕ_1, just like the "golden channel", $B^0 \to J/\psi K^0_S$. Additionally, a strongly suppressed loop transition contributes to the decay. The $B^0 \to \psi(2S)\pi^0$ branching fraction and CP asymmetries could be used to determine the second-order process pollution to $B^0 \to \psi(2S)K^0_S$ decay and with this to precisely determine the $\sin 2\phi_1$ value. This study, however, would only be possible with a larger data set. For the $B^0 \to \psi(2S)\pi^0$ branching fraction, we obtain

$$\mathcal{B}(B^0 \to \psi(2S)\pi^0) = (1.17 \pm 0.18\ (\text{stat}) \pm 0.08\ (\text{syst})) \times 10^{-5},$$

which has a significance of 7.2 standard deviations and, once officially verified by the Belle

collaboration, would be the first observation of the $B^0 \to \psi(2S)\pi^0$ decay. The result is consistent with our theoretical prediction shown in Section 5.1.

Appendix A

Probability Density Functions

A probability density function (PDF) describes the relative likelihood for a continuous random variable to take a given value. As such, a PDF is non-negative and its integral over the entire space is normalized to one. In the following, the most common PDFs used in the event model are presented.

A.1 Gaussian Distribution

The standard Gaussian PDF is defined as

$$G(x;\mu,\sigma) = \frac{1}{N} \cdot e^{-\frac{(x-\mu)^2}{2\sigma}}, \tag{A.1}$$

where μ is the mean and σ is the width of the distribution; N is a constant normalization factor. In certain cases, we use a bifurcated Gaussian

$$G_b(x;\mu,\sigma_L,\sigma_R) = \frac{1}{N} \cdot e^{-\frac{(x-\mu)^2}{2\sigma}}, \quad \sigma = \begin{cases} \sigma_L & \text{if } x \leq \mu, \\ \sigma_R & \text{otherwise,} \end{cases} \tag{A.2}$$

which is and asymmetric Gaussian distribution with widths σ_L and σ_R on the left or right side of the mean, respectively.

A.2 ARGUS Distribution

The ARGUS distribution is an empirical function introduced by the ARGUS collaboration [91] and is used to model the invariant mass of the continuum background, in the case of Belle the M_{bc} distribution. ARGUS is defined as

$$\mathrm{ARGUS}(x;a,c) = \frac{1}{N} \cdot x \cdot \sqrt{1-\frac{x^2}{c^2}}\, e^{a\cdot\left(1-\frac{x^2}{c^2}\right)}, \tag{A.3}$$

with the curvature parameter $a < 0$, the cutoff energy $c > 0$ with a normalization factor N. In the case of the Belle experiment, the cutoff parameter is the beam energy, which is an event dependent variable, and hence we use the notation

$$\mathrm{ARGUS}(x;a) = \mathrm{ARGUS}(x;a,E_{beam}) \tag{A.4}$$

A.3 Chebychev Polynomials

The Chebychev Polynomials [92] are an orthogonal set of polynomials which can be used to approximate any function in a given interval using a sufficiently high order. We use Chebychev polynomials of the first kind defined as

$$\mathrm{Cheb}_n(x; c_1, c_2, \ldots, c_n) = \frac{1}{N} \cdot \left(C_0(x) + \sum_{i=1}^{n} c_i \cdot C_i(x) \right), \tag{A.5}$$

where N is a normalization factor, n is the order of the polynomial and $C_i(x)$ are defined using the recurrence relation

$$C_0(x) = 1 \qquad C_1(x) = x \qquad C_{n+1}(x) = 2x \cdot C_n(x) - C_{n-1}(x) \tag{A.6}$$

A.4 Crystal Ball Function

The Crystal Ball function, named after the Crystal Ball Collaboration, is a probability density function commonly used to model physics distributions featuring a low-end tail. It consists of a Gaussian core component and a power-law tail, below a certain threshold. The function is given by

$$CB(x; \alpha, n, \bar{x}, \sigma) = \begin{cases} \exp -\frac{(x-\bar{x})^2}{2\sigma^2}, & \text{for} \quad \frac{x-\bar{x}}{\sigma} > -\alpha \\ A \cdot \left(B - \frac{x-\bar{x}}{\sigma}\right)^{-n}, & \text{for} \quad \frac{x-\bar{x}}{\sigma} \leq -\alpha \end{cases},$$

where

$$\begin{aligned} A &= \left(\frac{n}{|\alpha|}\right)^n \cdot \exp\left(-\frac{|\alpha|^2}{2}\right), \\ B &= \frac{n}{|\alpha|} - |\alpha| \\ N &= \frac{1}{\sigma(C+D)} \\ C &= \frac{n}{|\alpha|} \cdot \frac{1}{n-1} \cdot \exp\left(-\frac{|\alpha|^2}{2}\right) \\ D &= \sqrt{\frac{\pi}{2}} \left(1 + \mathrm{erf}\left(\frac{|\alpha|}{\sqrt{2}}\right)\right). \end{aligned} \tag{A.7}$$

List of Figures

List of Tables

Bibliography

[1] A. D. Sakharov. "Violation of CP Invariance, C Asymmetry, and Baryon Asymmetry of the Universe". *JETP Lett.* 5 (1967), p. 24. URL: http://www.jetpletters.ac.ru/ps/1643/article_25089.pdf.

[2] J. H. Christenson et al. "Evidence for the 2π Decay of the K_2^0 Meson". *Phys. Rev. Lett.* 13 (4 July 1964), pp. 138–140. DOI: 10.1103/PhysRevLett.13.138.

[3] N. Cabibbo. "Unitary Symmetry and Leptonic Decays". *Phys. Rev. Lett.* 10 (12 June 1963), pp. 531–533. DOI: 10.1103/PhysRevLett.10.531.

[4] M. Kobayashi and T. Maskawa. "CP-Violation in the Renormalizable Theory of Weak Interaction". *Prog. Theor. Phys.* 49.2 (1973), pp. 652–657. DOI: 10.1143/PTP.49.652.

[5] S. L. L. Glashow. "Partial-symmetries of weak interactions". *Nuclear Physics* 22.4 (1961), pp. 579–588. ISSN: 0029-5582. DOI: 10.1016/0029-5582(61)90469-2.

[6] A. Salam and N. Svartholm. "Elementary Particle Physics: Relativistic Groups and Analyticity, Almqvist and Wiksell (1968)". *Proceedings of the eighth Nobel symposium* (1968), p. 367.

[7] S. Weinberg. "A Model of Leptons". *Phys. Rev. Lett.* 19 (21 Nov. 1967), pp. 1264–1266. DOI: 10.1103/PhysRevLett.19.1264.

[8] F. J. Hasert et al. "Observation of neutrino-like interactions without muon or electron in the Gargamelle neutrino experiment". *Nuclear Physics B* 73.1 (1974), pp. 1–22. ISSN: 0550-3213. DOI: 10.1016/0550-3213(74)90038-8.

[9] F. D. Abe et al. "Observation of Top Quark Production in $\overline{p}p$ Collisions with the Collider Detector at Fermilab". *Phys. Rev. Lett.* 74 (14 Apr. 1995), pp. 2626–2631. DOI: 10.1103/PhysRevLett.74.2626.

[10] S. Abachi et al. "Search for High Mass Top Quark Production in $p\overline{p}$ Collisions at $\sqrt{s} = 1.8$ TeV". *Phys. Rev. Lett.* 74 (13 Mar. 1995), pp. 2422–2426. DOI: 10.1103/PhysRevLett.74.2422.

[11] K. Kodama et al. "Observation of tau neutrino interactions". *Phys. Lett. B* 504.3 (2001), pp. 218–224. ISSN: 0370-2693. DOI: 10.1016/S0370-2693(01)00307-0.

[12] ATLAS collaboration. "Observation of a new particle in the search for the Standard Model Higgs boson with the ATLAS detector at the LHC". *Phys. Lett. B* 716.1 (2012), pp. 1–29. ISSN: 0370-2693. DOI: 10.1016/j.physletb.2012.08.020.

[13] CMS collaboration. "Observation of a new boson at a mass of 125 GeV with the CMS experiment at the LHC". *Phys. Lett. B* 716.1 (2012), pp. 30–61. ISSN: 0370-2693. DOI: 10.1016/j.physletb.2012.08.021.

[14] G. Hinshaw et al. "Nine-Year Wilkinson Microwave Anisotropy Probe (WMAP) Observations: Cosmological Parameter Results". *Astrophys. J.* 208 (Oct. 2013), pp. 19–43. DOI: 10.1088/0067-0049/208/2/19.

[15] P. A. R. Ade et al. "Planck 2013 results. I. Overview of products and scientific results" (2013). arXiv: 1303.5062 [astro-ph.CO].

[16] I. I. Bigi and A. I. Sanda. "Notes on the observability of CP violations in B decays". *Nucl. Phys. B* 193.1 (1981), pp. 85–108. ISSN: 0550-3213. DOI: 10.1016/0550-3213(81)90519-8.

[17] A. B. Carter and A. I. Sanda. "CP Nonconservation in Cascade Decays of B Mesons". *Phys. Rev. Lett.* 45 (12 Sept. 1980), pp. 952–954. DOI: 10.1103/PhysRevLett.45.952.

[18] A. B. Carter and A. I. Sanda. "CP violation in B-meson decays". *Phys. Rev. D* 23 (7 Apr. 1981), pp. 1567–1579. DOI: 10.1103/PhysRevD.23.1567.

[19] B. Aubert et al. "The BABAR detector". *Nucl. Instrum. Methods Phys. Res. Sect. A* 479.1 (2002), pp. 1–116. ISSN: 0168-9002. DOI: 10.1016/S0168-9002(01)02012-5.

[20] A. Abashian et al. "The Belle detector". *Nucl. Instrum. Methods Phys. Res. Sect. A* 479.1 (2002), pp. 117–232. ISSN: 0168–9002. DOI: 10.1016/S0168-9002(01)02013-7.

[21] The LHCb Collaboration. "The LHCb Detector at the LHC". *J. Instrum.* 3.08 (2008), S08005. URL: http://stacks.iop.org/1748-0221/3/i=08/a=S08005.

[22] K. Abe et al. "Observation of large CP violation in the neutral B meson system". *Phys. Rev. Lett.* 87 (2001), p. 091802. DOI: 10.1103/PhysRevLett.87.091802.

[23] B. Aubert et al. "Observation of CP Violation in the B Meson System". *Phys. Rev. Lett.* 87.9 (Aug. 2001), p. 091801. DOI: 10.1103/PhysRevLett.87.091801.

[24] W. N. Cottingham and D. A. Greenwood. *An Introduction to the Standard Model of Particle Physics*. Cambridge University Press, 2007.

[25] F. Englert and R. Brout. "Broken Symmetry and the Mass of Gauge Vector Mesons". *Phys. Rev. Lett.* 13 (9 Aug. 1964), pp. 321–323. DOI: 10.1103/PhysRevLett.13.321.

[26] P .W. Higgs. "Broken Symmetries and the Masses of Gauge Bosons". *Phys. Rev. Lett.* 13 (16 Oct. 1964), pp. 508–509. DOI: 10.1103/PhysRevLett.13.508.

[27] K. Olive et al. *Chin.Phys.* C38 (2014), p. 090001. DOI: 10.1088/1674-1137/38/9/090001.

[28] E. Noether. "Invariante Variationsprobleme". *Nachr. d. König. Gesellsch. d. Wiss. zu Göttingen* (1918), pp. 235–257.

[29] T. D. Lee and C. N. Yang. "Question of parity conservation in weak interactions". *Phys. Rev.* 104 (1956), pp. 254–258.

[30] C. S. Wu et al. "Experimental test of parity conservation in beta decay". *Phys. Rev.* 105 (1957), pp. 1413–1415.

[31] M. Goldhaber, L. Grodzins, and A. W. Sunyar. "Helicity of Neutrinos". *Phys. Rev.* 109 (3 Feb. 1958), pp. 1015–1017. DOI: 10.1103/PhysRev.109.1015.

[32] B. Aubert et al. "Observation of *CP* Violation in the B^0 Meson System". *Phys. Rev. Lett.* 87 (9 Aug. 2001), p. 091801. DOI: 10.1103/PhysRevLett.87.091801.

[33] K. Abe et al. "Observation of Large *CP* Violation in the Neutral *B* Meson System". *Phys. Rev. Lett.* 87 (9 Aug. 2001), p. 091802. DOI: 10.1103/PhysRevLett.87.091802.

[34] T. Nakada. "Physics of CP Violation and B Decays" (2008). URL: http://nakada.web.cern.ch/nakada/epfl.

[35] L. Wolfenstein. "Parametrization of the Kobayashi-Maskawa Matrix". *Phys. Rev. Lett.* 51 (21 Nov. 1983), pp. 1945–1947. DOI: 10.1103/PhysRevLett.51.1945.

[36] C. Jarlskog. "Commutator of the Quark Mass Matrices in the Standard Electroweak Model and a Measure of Maximal *CP* Nonconservation". *Phys. Rev. Lett.* 55.10 (Aug. 1985), pp. 1039–1042. DOI: 10.1103/PhysRevLett.55.1039.

[37] J. Charles et al. "CP violation and the CKM matrix: Assessing the impact of the asymmetric B factories". *Eur.Phys.J.* C41 (2005). Updated results and plots available at: http://ckmfitter.in2p3.fr, pp. 1–131. DOI: 10.1140/epjc/s2005-02169-1. arXiv: hep-ph/0406184 [hep-ph].

[38] V. F. Weisskopf and E. P. Wigner. "Calculation of the natural brightness of spectral lines on the basis of Dirac's theory". *Z. Phys.* 63:54-73 (1930).

[39] M. Thomson. *Modern Particle Physics*. Cambridge University Press, 2013. ISBN: 9781107034266.

[40] R. N. Cahn and G. Goldhaber. *The Experimental Foundations of Particle Physics, Second Edition*. Cambridge University Press, 2009.

[41] *Using Crab Cavities, KEKB Breaks Luminosity World Record*. URL: http://www.kek.jp/intra-e/press/2009/KEKBluminosity2.html.

[42] *Belle Collaboration Homepage*. URL: http://belle.kek.jp/.

[43] T. E. Browder and K. Honscheid. "B mesons". *Prog. Part. Nucl. Phys.* 35 (1995), pp. 81–219. ISSN: 0146-6410. DOI: 10.1016/0146-6410(95)00042-H.

[44] T. Abe et al. "Achievements of KEKB". *Prog. Theor. Exp. Phys.* 2013.3 (2013). 03A001 (2013) and following articles up to 03A011. DOI: 10.1093/ptep/pts102.

[45] S. Kurokawa and E. Kikutani. "Overview of the KEKB accelerators". *Nucl. Instrum. Methods Phys. Res. Sect. A* 499.1 (2003). And other papers included in this Volume. ISSN: 0168-9002. DOI: 10.1016/S0168-9002(02)01771-0.

[46] J. Brodzicka et al. "Physics achievements from the Belle experiment". *Prog. Theor. Exp. Phys.* 2012.1 (2012). DOI: 10.1093/ptep/pts072.

[47] K. Abe et al. *Letter of Intent for KEK Super B Factory. Part II: Detector*. Tech. rep. KEK Report 04-4, 2004. URL: http://superb.kek.jp/documents/loi/img/LoI_detector.pdf.

[48] R. Abe et al. *Nucl. Instrum. Methods Phys. Res. Sect. A* 535.1–2 (2004). Proceedings of the 10th International Vienna Conference on Instrumentation, pp. 379–383. ISSN: 0168-9002. DOI: 10.1016/j.nima.2004.07.156.

[49] Y. Ushiroda et al. "Development of the central trigger system for the BELLE detector at the KEK B-factory". *Nucl. Instrum. Methods Phys. Res. Sect. A* 438.2–3 (1999), pp. 460–471. ISSN: 0168-9002. DOI: 10.1016/S0168-9002(99)00823-2.

[50] F. James and M. Roos. "Minuit: A System for Function Minimization and Analysis of the Parameter Errors and Correlations". *Comput.Phys.Commun.* 10 (1975), pp. 343–367. DOI: 10.1016/0010-4655(75)90039-9.

[51] C. C. Calame et al. "Large-angle Bhabha scattering and luminosity at flavour factories". *Nucl. Phys. B* 584 (2000), pp. 459–479. DOI: 10.1016/S0550-3213(00)00356-4.

[52] S. Uehara. "Devellopment study of zero-degree luminosity monitor using a GSO scintillator for the Belle experiment". *Belle Note 174, accessible only by Belle members* (1997).

[53] V. Zhilich. "Offline luminosity measurements from the Belle detector". *Belle Note 453, accessible only by Belle members* (2001).

[54] D. Beylin. "Online luminosity measurements from the Belle detector". *Belle Note 465, accessible only by Belle members* (2001).

[55] B. Casey. "HadronB". *Belle Note 390, accessible only by Belle members* (2001).

[56] D. J. Lange. "The EvtGen particle decay simulation package". *Nucl. Instrum. Methods Phys. Res. Sect. A* 462 (2001), pp. 152–155.

[57] R. B. Brun et al. "GEANT 3.21". *CERN Report DD/EE/84-1* (1984).

[58] Heavy Flavor Averaging Group (HFAG). "Averages of b-hadron, c-hadron, and tau-lepton properties as of early 2012" ().

[59] A. G. Akeroyd, C.-H. Chen, and C.-Q. Geng. "$B \to \eta'(l^-\nu_l, l^+l^-, K, K^*)$ decays in the quark-flavor mixing scheme". *Phys. Rev. D* 75 (5 Mar. 2007), p. 054003. DOI: 10.1103/PhysRevD.75.054003.

[60] H.-n. Li and S. Mishima. "Penguin-dominated $B \to PV$ decays in NLO perturbative QCD". *Phys. Rev. D* 74 (9 Nov. 2006), p. 094020. DOI: 10.1103/PhysRevD.74.094020.

[61] H.-Y. Cheng and C.-K. Chua. "Revisiting charmless hadronic $B_{u,d}$ decays in QCD factorization". *Phys. Rev. D* 80 (11 Dec. 2009), p. 114008. DOI: 10.1103/PhysRevD.80.114008.

[62] W. Wang et al. "Charmless two-body $B_{(s)} \to VP$ decays in soft collinear effective theory". *Phys. Rev. D* 78 (3 Aug. 2008), p. 034011. DOI: 10.1103/PhysRevD.78.034011.

[63] C.-M. Jen, P. Chang, et al. "Improved measurements of branching fractions and CP partial rate asymmetries for $B \to \omega K$ and $B \to \omega\pi$". *Phys. Rev. D* 74 (11 Dec. 2006), p. 111101. DOI: 10.1103/PhysRevD.74.111101.

[64] Y. Chao et al. "Measurements of time-dependent CP violation in $B^0 \to \omega K_S^0$, $f_0(980)K_S^0$, $K_S^0\pi^0$ and $K^+K^-K_S^0$ decays". *Phys. Rev. D* 76 (9 Nov. 2007), p. 091103. DOI: 10.1103/PhysRevD.76.091103.

[65] B. Aubert et al. "Branching fraction and CP-violation charge asymmetry measurements for B-meson decays to $\eta K^\pm$, $\eta\pi^\pm$, $\eta' K^\pm$". *Phys. Rev. D* 76 (3 Aug. 2007), p. 031103. DOI: 10.1103/PhysRevD.76.031103.

[66] B. Aubert et al. "Measurement of time dependent CP asymmetry parameters in B^0 meson decays in ωK_S^0, $\eta' K_S^0$, and $\pi^0 K_S^0$". *Phys. Rev. D* 79 (5 Mar. 2009), p. 052003. DOI: 10.1103/PhysRevD.79.052003.

[67] S. W. Lin, P. Chang, and H. C. Huang. "Study of π^0 systematics using inclusive η (78 fb^{-1})". *Belle Note 586, accessible only by Belle members* (2002).

[68] F. Fang. "Study of $K_S^0 \to \pi^+\pi^-$ selection". *Belle Note 323, accessible only by Belle members* (2000).

[69] J. Tanaka. "Kinematic Fitting". *Belle Note 194, accessible only by Belle members* (2000).

[70] H. Tajima et al. "Proper-time resolution function for measurement of time evolution of B mesons at the KEK B-Factory". *Nucl. Instrum. Methods Phys. Res. Sect. A* 533.3 (2004), pp. 370–386. DOI: 10.1016/j.nima.2004.07.199.

[71] T. Browder and S. Swain. "Beam-Energy Calibration". *Belle Note 567, accessible only by Belle members* (2002).

[72] H. Kakuno et al. "Neutral B flavor tagging for the measurement of mixing-induced CP violation at Belle". *Nucl. Instr. and Meth. in Phys. Res. A* 533.3 (2004), pp. 516–531. DOI: 10.1016/j.nima.2004.06.159.

[73] A. Bevan et al. *Physics of the B Factories*. Springer, 2015. ISBN: 9783662449905.

[74] T. Higuchi. *Resolution Function Study*. Belle Analysis Meeting. Accessible only by Belle members. 2010. URL: http://kds.kek.jp/getFile.py/access?contribId=63&resId=0&materialId=slides&confId=4932.

[75] T. Higuchi. *Time-Dependent CP Violation*. Belle Analysis School. Accessible only by Belle members. 2012. URL: http://kds.kek.jp/getFile.py/access?contribId=8&resId=1&materialId=slides&confId=9641.

[76] G. Punzi. "Comments on Likelihood fits with variable resolution". *ArXiv e-prints* (2004). arXiv: physics/0401045.

[77] R. A. Fisher. "The Use of Multiple Measurements in Taxonomic Problems". *Annals of Eugenics* 7 (1936), pp. 179–188. DOI: 10.1111/j.1469-1809.1936.tb02137.x.

[78] G. C. Fox and S. Wolfram. "Observables for the analysis of event shapes in e^+e^- annihilation and other processes". *Phys. Rev. Lett.* 41 (1978), pp. 1581–1585. DOI: 10.1103/PhysRevLett.41.1581.

[79] K. Nishimura. *Time-Dependent CP Violation*. Belle Analysis School. Accessible only by Belle members. 2011. URL: http://kds.kek.jp/getFile.py/access?contribId=7&resId=0&materialId=slides&confId=6516.

[80] H. Ishino et al. "Measurement of the CP-Violating Parameters in $B \to \pi^+\pi^-$ Decay With a 253 fb^{-1} Data Sample". *Belle Note 663, accessible only by Belle members* (2005).

[81] V. Chobanova et al. "Measurement of branching fractions and CP violation parameters in $B \to \omega K$ decays with first evidence of CP violation in $B \to \omega K^0_S$". *Phys. Rev. D* 90 (1 2014), p. 012002. DOI: 10.1103/PhysRevD.90.012002.

[82] I. Adachi et al. "Precise Measurement of the CP Violation Parameter $\sin 2\phi_1$ in $B^0 \to (c\bar{c})K^0$ Decays". *Phys. Rev. Lett.* 108 (2012), p. 171802. DOI: 10.1103/PhysRevLett.108.171802.

[83] K. Sakai et al. "Search for CP-violating charge asymmetry in $B \to J/\psi K^\pm$ decays". *Phys. Rev. D* 82 (9 2010), p. 091104. DOI: 10.1103/PhysRevD.82.091104.

[84] O. Long et al. "Impact of tag-side interference on time-dependent CP asymmetry measurements using coherent B^0B^0 pairs". *Phys. Rev. D* 68 (3 2003), p. 034010. DOI: 10.1103/PhysRevD.68.034010.

[85] T. Aushev et al. "Physics at Super B Factory". *ArXiv e-prints* (Feb. 2010). arXiv: 1002.5012 [hep-ex].

[86] T. Abe et al. "Belle II Technical Design Report". *ArXiv e-prints* (Nov. 2010). arXiv: 1011.0352.

[87] J. W. Flanagan and other. *Letter of Intent for KEK Super B Factory. Part III: Accelerator Design*. Tech. rep. KEK Report 04-4, 2004. URL: http://superb.kek.jp/documents/loi/img/LoI_accelerator.pdf.

[88] S. Hashimoto et al. *Letter of Intent for KEK Super B Factory. Part I: Physics*. Tech. rep. KEK Report 04-4, 2004. URL: http://superb.kek.jp/documents/loi/img/LoI_physics.pdf.

[89] M. Ciuchini, M. Pierini, and L. Silvestrini. "Effect of Penguin Operators in the $B^0 \to J/\psi K^0$ CP Asymmetry". *Phys. Rev. Lett.* 95 (22 Nov. 2005), p. 221804. DOI: 10.1103/PhysRevLett.95.221804.

[90] S. Sahoo, V. Bhardwaj, and K. Trabelsi. "Measurement of time-dependent CP violation in $B^0 \to \psi(2S)K^0_S$ and $B \to \chi_{c1}K^0_S$ decays". *Belle Note 1175, accessible only by Belle members* (2011).

[91] H. Albrecht et al. “Exclusive hadronic decays of B mesons”. *Z. Phys. C* 48.4 (1990), pp. 543–551. ISSN: 0170–9739. DOI: 10.1007/BF01614687.

[92] P. L. Chebyshev. *Théorie des mécanismes connus sous le nom de parallélogrammes*. 1854.

Acknowledgements

I would like to thank my Ph.D. supervisor, Prof Dr Christian Kiesling, for his support and guidance throughout the years.

I wish to express gratitude to Dr Frank Simon for giving me the opportunity to work in the Belle group of the Max Planck Institute and for the feedback on this thesis.

I am much obliged to Dr Jeremy Dalseno for teaching me the nitty-gritty of data analysis and for the continuous encouragement during the tough times of my doctorate.

To Dr Martin Ritter I am grateful for solving my computer issues. And also for all the whisky.

I thank Dr Luigi Li Gioi for proof-reading this work.

For the pleasant atmosphere at the institute and the nice discussions, I thank my colleagues from the Belle and ILC groups: Dr Kolja Prothmann, Dr Pit Vanhoefer, Marco Szalay, Miroslav Gabriel and Dr Michal Tesar.

The analyses presented in this thesis would not have been possible without the contribution from my Belle experiment colleagues. I am especially thankful to the ICPV group and my referees: Prof Dr Peter Krizan, Dr Torben Ferber and Assoc Prof Hideki Miyake; Prof Dr Vishal Bhardwaj, Dr Zbynek Drasal and Dr Pablo Goldenzweig.

I am grateful to the MPI administration for all the assistance with the various aspects of the life in Munich, especially to Mrs Katharina Henning and Mrs Jördis Scholz.

Last but not least, I would like to thank my family for their support throughout the years of pursuing a physics career.